

**DISTRIBUTION STATEMENT A**  
Approved for Public Release  
Distribution Unlimited

MATERIALS RESEARCH SOCIETY  
SYMPOSIUM PROCEEDINGS VOLUME 724

**Biological and Biomimetic  
Materials—Properties to Function**

Symposium held April 1-5, 2002, San Francisco, California, U.S.A.

**EDITORS:**

**Joanna Aizenberg**  
Bell Labs, Lucent Technologies  
Murray Hill, New Jersey, U.S.A.

**Joanna M. McKittrick**  
University of California-San Diego  
La Jolla, California, U.S.A.

**Christine A. Orme**  
Lawrence Livermore National Laboratory  
Livermore, California, U.S.A.

**ADDITIONAL SYMPOSIUM ORGANIZER**

**Peter G. Vekilov**  
University of Houston  
Houston, Texas, U.S.A.



**Materials Research Society**  
Warrendale, Pennsylvania

THIS DOCUMENT CONTAINED  
BLANK PAGES THAT HAVE  
BEEN DELETED

20030812 223

**BEST AVAILABLE COPY**

**Biological and Biomimetic  
Materials—Properties  
to Function**

Single article reprints from this publication are available through  
University Microfilms Inc., 300 North Zeeb Road, Ann Arbor, Michigan 48106

**CODEN: MRSPDH**

Copyright 2002 by Materials Research Society.  
All rights reserved.

This book has been registered with Copyright Clearance Center, Inc. For further information, please  
contact the Copyright Clearance Center, Salem, Massachusetts.

Published by:

Materials Research Society  
506 Keystone Drive  
Warrendale, PA 15086  
Telephone (724) 779-3003  
Fax (724) 779-8313  
Web site: <http://www.mrs.org/>

Manufactured in the United States of America

## CONTENTS

Preface.....	xi
Materials Research Society Symposium Proceedings.....	xii

### *MATERIALS IN NATURAL BIOLOGICAL TISSUES*

Extracellular Matrix Molecules Involved in Barnacle Shell Mineralization .....	3
María S. Fernández, Italo Vergara, Alejandro Oyarzún, José I. Arias, Renato Rodríguez, Juan P. Wiff, Víctor M. Fuenzalida, and José L. Arias	
* Molecular Mechanism of Bacterial Magnetite Formation and Its Application .....	11
Tadashi Matsunaga and Yoshiko Okamura	

### *IMAGING AND CHARACTERIZATION TECHNIQUES*

Mechanical and Microstructural Properties of Stratum Corneum .....	27
Kenneth S. Wu, William W. Van Osdol, and Reinhold H. Dauskardt	

### *ORGANIC BIOMATERIALS— PROTEINS AND PEPTIDES*

Biologically-Based Self-Assembling Hydrogels .....	37
Brandon L. Seal and Alyssa Panitch	
Self-Assembly of a Modular Polypeptide Based on Blocks of Silk-Mimetic and Elastin-Mimetic Sequences .....	43
Chrystelle S. Cazalis and Vincent P. Conticello	

### *INTERFACE ENGINEERING, PATTERNING AND BIOCOMPATIBILITY*

In Vitro Vascular Cell Adhesion and Proliferation on Alkaline Degraded Poly-lactic/glycolic Acid Polymers.....	51
Thomas J. Webster, Derick C. Miller, Anil Thapa, and Karen M. Haberstroh	

\*Invited Paper

---

<b>Nanoscale Patterning of Antigen on Silicon Substrate to Examine Mast Cell Activation .....</b>	<b>57</b>
Reid N. Orth, Min Wu, Theodore G. Clark, David A. Holowka, Barbara A. Baird, and Harold G. Craighead	
<b>Formation, Characterization, Protein Resistance, and Reactivity of <math>\text{Cl}_3\text{Si}(\text{CH}_2)_{11}(\text{OCH}_2\text{CH}_2)_3\text{OH}</math> Self-Assembled Monolayers .....</b>	<b>63</b>
Jiehyun Seong, Seok-Won Lee, and Paul E. Laibinis	
<b>Helical, Disordered, and What That Means: Structural Characterization of a New Series of Methyl 1-Thiaoligo(ethylene Oxide) Self-Assembled Monolayers.....</b>	<b>69</b>
David J. Vanderah, Jennifer Arsenault, Hongly La, Vitalii Silin, Curtis W. Meuse, and Richard S. Gates	
<b>Selectivity of Polypeptide Binding to Nanoscale Substrates .....</b>	<b>75</b>
Steven R. Lustig and Anand Jagota	

***COMPOSITE BIOMATERIALS—  
BONES AND TEETH I***

<b>* Developing Bio-Stable and Biodegradable Composites for Tissue Replacement and Tissue Regeneration.....</b>	<b>83</b>
Min Wang	
<b>Effects of Counterface Roughness and Conformity on the Tribological Performance of Crosslinked and Non-Crosslinked Medical-Grade Ultra-High Molecular Weight Polyethylene .....</b>	<b>95</b>
A.D. Chawan, A.M. Chakravartula, J. Zhou, L.A. Pruitt, M. Ries, and K. Komvopoulos	

***COMPOSITE BIOMATERIALS—  
BONES AND TEETH II***

<b>* Effects of Ionic Flow and Amelogenins on the Lengthwise Growth of Octacalcium Phosphate Crystals in a Model System of Tooth Enamel Formation.....</b>	<b>103</b>
M. Iijima, Y. Moriwaki, H.B. Wen, T. Takagi, A.G. Fincham, and J. Moradian-Oldak	

\*Invited Paper

## **BIOMATERIALS**

<b>Magnetic Material Arrangement in <i>Apis Mellifera</i> Abdomens .....</b>	<b>113</b>
Darcy M.S. Esquivel, Eliane Wajnberg, Geraldo R. Cernicchiaro, Daniel Acosta-Avalos, and B.E. Garcia	
<b>Microstructure and Thermal Expansion Properties of Ostrich Eggshell .....</b>	<b>117</b>
A. Heredia, L. Lozano, C.A. Martinez-Matias, M.A. Peña-Rico, A. Rodriguez-Hernández, E. Villarreal, A. Martinez, M.V. García-Garduño, V.A. Basiuk, L. Bucio, and E. Orozco	
<b>Thermal Properties of Mineralized and Non-Mineralized Type I Collagen in Bone .....</b>	<b>123</b>
L.F. Lozano, M.A. Peña-Rico, H. Jang-Cho, A. Heredia, E. Villarreal, J. Ocotlán-Flores, A.L. Gomez-Cortes, F.J. Aranda-Manteca, E. Orozco, and L. Bucio	
<b>Tissue Engineering of Fibroblast Constructs and Anisotropic Collagen Gels.....</b>	<b>129</b>
Sarah Calve, Ellen Arruda, Robert Dennis, Karl Grosh, and Krystyna Pasyk	
<b>The Investigation on Preparation and Physicochemical Process of Nanosized Hydroxyapatite Powder.....</b>	<b>135</b>
Yunjing Song, Shulin Wen, and Musen Li	
<b>Spatio-Temporal Patterns in Ferritin Crystal Growth .....</b>	<b>141</b>
Olga Gliko and Peter G. Vekilov	
<b>Influence of DNA, Alginate, Lysozyme and Bovine Serum Albumin on Sodium Silicate Condensation.....</b>	<b>147</b>
Thibaud Coradin, Aurélie Coupé, and Jacques Livage	
<b>Colorimetric Biosensor Vesicles for Biotechnological Applications.....</b>	<b>153</b>
Revital Halevy, Sofiya Kolusheva, Robert E.W. Hancock, and Raz Jelinek	

## **TISSUE ENGINEERING I**

<b>Self-Assembly of Hydrogels From Elastin-Mimetic Block Copolymers.....</b>	<b>161</b>
Elizabeth R. Wright, R. Andrew McMillan, Alan Cooper, Robert P. Apkarian, and Vincent P. Conticello	

---

<b>Lipid Exchange Rates of Conventional and Polymer Stabilized Liposomes .....</b>	<b>167</b>
Awad Ahmed, Nicole Heldt, Gregory Slack, and Yuzhuo Li	
<b>Synthesis of Biocompatible Surfaces by Different Techniques .....</b>	<b>173</b>
E. Garreta, T. Fernández, S. Borrós, J. Esteve, C. Colominas, and L. Kempf	
<b>Antimicrobial Coatings Obtained in an Atmospheric Pressure Dielectric Barrier Glow Discharge .....</b>	<b>179</b>
Sabine Paulussen, Dirk Vangeneugden, Olivier Goossens, and Erik Dekempeneer	
<b>Calcium Carbonate Reinforced Natural Polymer Composite For Bone Grafts .....</b>	<b>185</b>
Samar J. Kalita, Susmita Bose, Howard L. Hosick, Steve A. Martinez, and Amit Bandyopadhyay	

***BIOMIMETICS, SENSORS AND NANOTECHNOLOGY***

<b>Biomimetic Networks for Selective Recognition of Biomolecules .....</b>	<b>193</b>
Mark E. Byrne, Kinam Park, and Nicholas A. Peppas	
<b>Microcontact Printing Via a Polymer-Induced Liquid-Precursor (PILP) Process .....</b>	<b>201</b>
Yi-yeoun Kim and Laurie B. Gower	

***MATERIALS FOR DRUG AND GENE DELIVERY***

<b>The Effects of Charge Separation in Quaternary Ammonium, DABCO-Containing Polymers on In Vitro Toxicity and Gene Delivery .....</b>	<b>209</b>
Theresa M. Reineke and Mark E. Davis	
<b>Oral Administration of Chemotherapeutic Agents Using Complexation Hydrogels .....</b>	<b>215</b>
James Blanchette, Kinam Park, and Nicholas A. Peppas	

---

**TISSUE ENGINEERING II**

<b>Poly(glycerol sebacate)—A Novel Biodegradable Elastomer for Tissue Engineering .....</b>	<b>223</b>
Yadong Wang, Barbara J. Sheppard, and Robert Langer	
<b>Honeycomb Films of Biodegradable Polymers for Tissue Engineering.....</b>	<b>229</b>
Takehiro Nishikawa, Keiko Arai, Junko Hayashi, Masahiko Hara, and Masatsugu Shimomura	
<b>Author Index .....</b>	<b>235</b>
<b>Subject Index.....</b>	<b>237</b>

## **PREFACE**

Symposium N, "Biological and Biomimetic Materials—Properties to Function," held April 2–5 at the 2002 MRS Spring Meeting in San Francisco, California, had sessions on natural biological tissues, imaging and characterization techniques, inorganic and organic biomaterials, biocompatibility, interface issues, tissue engineering, sensors, nanotechnology and materials for drug and gene delivery. Twenty-four invited talks, 47 contributed talks and 43 posters were presented in this well-attended symposium.

The symposium also had a Sunday tutorial entitled "In-situ and Ex-situ Characterization Techniques and Imaging of Biomaterials," presented by instructors James De Yoreo (LLNL), Alexander Chernov (Universities Space Research Association) and William Landis (Northeastern Ohio Universities College of Medicine). The tutorial had a large audience and was well received.

The organizers wish to thank the Lawrence Livermore National Laboratory for their generous financial support.

### **Editors**

Joanna Aizenberg  
Joanna M. McKittrick  
Christine A. Orme

### **Additional Symposium Organizer**

Peter G. Vekilov

October 2002

---

## MATERIALS RESEARCH SOCIETY SYMPOSIUM PROCEEDINGS

Volume 686— Materials Issues in Novel Si-Based Technology, W. En, E.C. Jones, J.C. Sturm, S. Tiwari, M. Hirose, M. Chan, 2002, ISBN: 1-55899-622-2

Volume 687— Materials Science of Microelectromechanical Systems (MEMS) Devices IV, A.A. Ayon, S.M. Spearing, T. Buchheit, H. Kahn, 2002, ISBN: 1-55899-623-0

Volume 688— Ferroelectric Thin Films X, S.R. Gilbert, Y. Miyasaka, D. Wouters, S. Trolier-McKinstry, S.K. Streiffer, 2002, ISBN: 1-55899-624-9

Volume 689— Materials for High-Temperature Superconductor Technologies, M.P. Paranthaman, M.W. Rupich, K. Salama, J. Mannhart, T. Hasegawa, 2002, ISBN: 1-55899-625-7

Volume 690— Spintronics, T.J. Klemmer, J.Z. Sun, A. Fert, J. Bass, 2002, ISBN: 1-55899-626-5

Volume 691— Thermoelectric Materials 2001—Research and Applications, G.S. Nolas, D.C. Johnson, D.G. Mandrus, 2002, ISBN: 1-55899-627-3

Volume 692— Progress in Semiconductor Materials for Optoelectronic Applications, E.D. Jones, M.O. Manasreh, K.D. Choquette, D. Friedman, 2002, ISBN: 1-55899-628-1

Volume 693— GaN and Related Alloys—2001, J.E. Northrup, J. Neugebauer, S.F. Chichibu, D.C. Look, H. Ricchert, 2002, ISBN: 1-55899-629-X

Volume 695— Thin Films: Stresses and Mechanical Properties IX, C.S. Ozkan, R.C. Cammarata, L.B. Freund, H. Gao, 2002, ISBN: 1-55899-631-1

Volume 696— Current Issues in Heteroepitaxial Growth—Stress Relaxation and Self Assembly, E. Stach, E. Chason, R. Hull, S. Bader, 2002, ISBN: 1-55899-632-X

Volume 697— Surface Engineering 2001—Fundamentals and Applications, W.J. Meng, A. Kumar, Y-W. Chung, G.L. Doll, Y-T. Cheng, S. Veprek, 2002, ISBN: 1-55899-633-8

Volume 698— Electroactive Polymers and Rapid Prototyping, Y. Bar-Cohen, D.B. Chrisey, Q.M. Zhang, S. Bauer, E. Fukada, S.C. Danforth, 2002, ISBN: 1-55899-634-6

Volume 699— Electrically Based Microstructural Characterization III, R.A. Gerhardt, A. Washabaugh, M.A. Alim, G.M. Choi, 2002, ISBN: 1-55899-635-4

Volume 700— Combinatorial and Artificial Intelligence Methods in Materials Science, J. Takeuchi, C. Buelens, H. Koinuma, E.J. Amis, J.M. Newsam, L.T. Wille, 2002, ISBN: 1-55899-636-2

Volume 702— Advanced Fibers, Plastics, Laminates and Composites, F.T. Wallenberger, N. Weston, K. Chawla, R. Ford, R.P. Wool, 2002, ISBN: 1-55899-638-9

Volume 703— Nanophase and Nanocomposite Materials IV, S. Komarneni, R.A. Vaia, G.Q. Lu, J-I. Matsushita, J.C. Parker, 2002, ISBN: 1-55899-639-7

Volume 704— Nanoparticle Materials, R.K. Singh, R. Partch, M. Muhammed, M. Senna, H. Hofmann, 2002, ISBN: 1-55899-640-0

Volume 705— Nanopatterning—From Ultralarge-Scale Integration to Biotechnology, L. Merhari, K.E. Gonsalves, E.A. Dobisz, M. Angelopoulos, D. Herr, 2002, ISBN: 1-55899-641-9

Volume 706— Making Functional Materials with Nanotubes, P. Nikolaev, P. Bernier, P. Ajayan, Y. Iwasa, 2002, ISBN: 1-55899-642-7

Volume 707— Self-Assembly Processes in Materials, S. Moss, 2002, ISBN: 1-55899-643-5

Volume 708— Organic and Optoelectronic Materials, Processing and Devices, S. Moss, 2002, ISBN: 1-55899-644-3

Volume 709— Advances in Liquid Crystalline Materials and Technologies, P.T. Mather, D.J. Broer, T.J. Bunning, D.M. Walba, R. Zentel, 2002, ISBN: 1-55899-645-1

Volume 710— Polymer Interfaces and Thin Films, C.W. Frank, 2002, ISBN: 1-55899-646-X

Volume 711— Advanced Biomaterials—Characterization, Tissue Engineering and Complexity, 2002, ISBN: 1-55899-647-8

## MATERIALS RESEARCH SOCIETY SYMPOSIUM PROCEEDINGS

Volume 712— Materials Issues in Art and Archaeology VI, P.B. Vandiver, M. Goodway, J.R. Druzik, J.L. Mass, 2002, ISBN: 1-55899-648-6

Volume 713— Scientific Basis for Nuclear Waste Management XXV, B.P. McGrail, G.A. Cagnolino, 2002, ISBN: 1-55899-649-4

Volume 714E—Materials, Technology and Reliability for Advanced Interconnects and Low-k Dielectrics II, S. Lahiri, 2002, ISBN: 1-55899-650-8

Volume 715— Amorphous and Heterogeneous Silicon-Based Films—2002, J.R. Abelson, J.B. Boyce, J.D. Cohen, H. Matsumura, J. Robertson, 2002, ISBN: 1-55899-651-6

Volume 716— Silicon Materials—Processing, Characterization and Reliability, J. Veteran, D.L. O'Meara, V. Misra, P. Ho, 2002, ISBN: 1-55899-652-4

Volume 717— Silicon Front-End Junction Formation Technologies, D.F. Downey, M.E. Law, A. Claverie, M.J. Rendon, 2002, ISBN: 1-55899-653-2

Volume 718— Perovskite Materials, K. Poepelmeier, A. Navrotsky, R. Wentzcovitch, 2002, ISBN: 1-55899-654-0

Volume 719— Defect and Impurity Engineered Semiconductors and Devices III, S. Ashok, J. Chevallier, N.M. Johnson, B.L. Sopori, H. Okushi, 2002, ISBN: 1-55899-655-9

Volume 720— Materials Issues for Tunable RF and Microwave Devices III, S.C. Tidrow, J.S. Horwitz, J. Levy, X. Xi, 2002, ISBN: 1-55899-656-7

Volume 721— Magnetic and Electronic Films—Microstructure, Texture and Application to Data Storage, P.W. DeHaven, D.P. Field, S.D. Harkness IV, J.A. Sutliff, J.A. Szpunar, L. Tang, T. Thomson, M.D. Vaudin, 2002, ISBN: 1-55899-657-5

Volume 722— Materials and Devices for Optoelectronics and Microphotonics, R.B. Wehrspohn, S. Noda, C. Soukoulis, R. März, 2002, ISBN: 1-55899-658-3

Volume 723— Molecularly Imprinted Materials—Sensors and Other Devices, K.J. Shea, M.J. Roberts, M. Yan, 2002, ISBN: 1-55899-659-1

Volume 724— Biological and Biomimetic Materials—Properties to Function, J. McKittrick, J. Aizenberg, C. Orme, P. Vekilov, 2002, ISBN: 1-55899-660-5

Volume 725— Organic and Polymeric Materials and Devices—Optical, Electrical and Optoelectronic Properties, G.E. Jabbour, N.S. Sariciftci, S.T. Lee, S. Carter, J. Kido, 2002, ISBN: 1-55899-661-3

Volume 726— Organic/Inorganic Hybrid Materials—2002, R.M. Laine, C. Sanchez, S. Yang, C.J. Brinker, 2002, ISBN: 1-55899-662-1

Volume 727— Nanostructured Interfaces, G. Duscher, J.M. Plitzko, Y. Zhu, H. Ichinose, 2002, ISBN: 1-55899-663-X

Volume 728— Functional Nanostructured Materials through Multiscale Assembly and Novel Patterning Techniques, Steven C. Moss, 2002, ISBN: 1-55899-664-8

Volume 729— BioMEMS and Bionanotechnology, L.P. Lee, J.T. Borenstein, R.P. Manginell, M. Okandan, P.J. Hesketh, 2002, ISBN: 1-55899-665-6

Volume 730— Materials for Energy Storage, Generation and Transport, G. Ceder, S.A. Ringel, R.B. Schwarz, 2002, ISBN: 1-55899-666-4

Volume 731— Modeling and Numerical Simulation of Materials Behavior and Evolution, V. Tikare, E.A. Olevsky, A. Zavaliangos, 2002, ISBN: 1-55899-667-2

Volume 732E—Chemical-Mechanical Planarization, S.V. Babu, R. Singh, N. Hayasaka, M. Oliver, 2002, ISBN: 1-55899-668-0

Volume 733E—Polymer Nanocomposites, S. Nutt, R. Vaia, W. Rodgers, G.L. Hagnauer, G.W. Beall, 2002, ISBN: 1-55899-669-9

**Materials in Natural  
Biological Tissues**

### Extracellular Matrix Molecules Involved in Barnacle Shell Mineralization

Maria S. Fernández, Italo Vergara, Alejandro Oyarzún, José I. Arias, Renato Rodríguez, Juan P. Wiff, Víctor M. Fuenzalida, José L. Arias  
Faculty of Veterinary Sciences and Center for Advanced Interdisciplinary Research in Materials, Universidad de Chile, Santiago, Chile.

#### ABSTRACT

*Austromegabalanus psittacus* is a large (normally up to 30 cm high) sessile balanomorph barnacle from the coast of Chile and South Peru. Its hard shell is composed of twelve calcareous side plates, six parietes and six radii, joined in the form of a truncated cone opened at the top. Plates rest on a basal disk firmly cemented to the substratum. Although the crystalline microstructure of barnacle's shell has been studied to some extent, its organic composition and the mechanisms governing the biomineralization of such highly ordered nanocomposite have remained obscure. By using X-ray diffraction, infrared spectrometry, SEM and TEM electron microscopy, histochemistry, immuno-histochemistry and -ultrastructure, biochemistry and a crystallization assay, we have studied the cell-shell interactions, the crystalline microstructure of the inorganic moiety and the localization of particular macromolecules, and tested their influence on crystallization. The mineral of the plates and basal disk was calcite showing a (104) preferential orientation. Plates were not solid but porous. While parietes have longitudinal canals (from the base to the apex), radii have transversal canals arranged parallel to the base. These canals are not in the center of the plates but displaced to the outside of the shell delimiting a thinner solid outer lamina and a thicker inner one. The inner lamina consisted of parallel calcified layers separated by organic sheets. These sheets showed autofluorescence and consisted of chitin surrounded by proteoglycans and other minor proteins, which seems to be responsible for the fluorescent behaviour. These organic sheets were also organized as several concentric rings around the canals. The shell matrix obtained after decalcification, which surrounded the crystals, also contained a loose net of such proteoglycans. Mantle epithelial cells covered the entire surface of the inner side of the inner lamina and extend to the plate canals. While isolated chitin did not promote or alter calcite crystallization, the proteoglycan-rich fraction dramatically modified crystal morphology and size. As we have demonstrated in another model of biomineralization, such as the eggshell, hereby we suggest that these structured polyanionic proteoglycan moieties could also be part of the regulatory mechanisms of the barnacle shell mineralization.

#### INTRODUCTION

Fabrication of mineralized structures is a widespread phenomenon among living beings [1-3]. Although a great number of these structures are mainly made out of calcium carbonate, they result in the formation of products of unique morphologies and properties. These naturally fabricated bioceramics are composites and are assembled from readily available materials, usually in aqueous solution, at ambient conditions, and to net shape [4]. These particular characteristics reflect the controlling activity of a relatively small repertoire and minute quantities of organic macromolecules which regulate the formation of these structures [5-10]. Some of these macromolecules, obtained from different biomineralization model such as mollusks, crustacea,

echinoderms and avian eggshells, are well characterized, while their role on the control of crystal nucleation, growth and shape is still far from a full understanding [11-13]. While mollusk's shell grows continuously without any spatial restriction, crustacea exoskeleton grows step by step between molting periods. Although being crustacea, showing molting cycle, these Thoraceca barnacles build a quite stable and heavily mineralized wall made out of a series of thick plates that completely surround the animal, which is firmly cemented to the substratum. This makes barnacles an interesting model for studying processes of biomimicry. Since Darwin's pioneering studies [14], there have been several studies on barnacle's shell formation, general structure or microstructure [see 15], but only a few have been concerned with the chemical characterization of the organic matrix of its shell [16]. In this study we therefore examined the shell structure and chemical composition and spatial distribution of its organic matrix.

## MATERIALS AND METHODS

For light microscopy, pieces of shells were polished to obtain thin sheets, mounted on slides and examined with an epifluorescent microscope. For SEM, pieces of shell were polished to obtain thin sheets, decalcified for 15, 30 and 50 sec with 37% orthophosphoric acid, dehydrated, coated with gold and observed in a Tesla BS 343 A scanning electron microscope. For TEM, samples were decalcified in 10% formic acid for 48 h at room temperature, dehydrated in a graded acetone series and embedded in Poly Bed 812 (Polysciences Inc., Warrington, PA). Ultrathin sections (70-90 nm) were cut with a Porter Bloom MT2-B ultramicrotome. Bulk ultrastructural visualization of proteoglycans was done by using polyethyleneimine [17]. For precise proteoglycan determination by immunogold localization, sections were incubated with one of the primary monoclonal anti-glycosaminoglycan antibodies listed below and then incubated with gold conjugated second antibody (Ted Pella, CA). Observation were made with a Zeiss EM-109 electron microscope.

Antibodies: 2B6 (IgG): recognize dermatan sulfate or chondroitin-4-sulfate after chondroitinase digestion [18]; 5D4 (IgG): recognize a hypersulfated hexasaccharide of keratan sulfate [19].

For organic matrix extraction and *in vitro* crystallization assays, pieces of shell were decalcified using Dowex resin in a rotating glass tube [6] for 3 days at room temperature, dialyzed (Spectra/Por membrane tubing MWCO 3,500) and lyophilized. Organic matrix (soluble and insoluble fractions) obtained was assayed for their crystallization properties. The crystallization experiment were done using a chamber consisting of 85 mm plastic Petri dish having a central hole in its bottom glued to a plastic cylindrical vessel. Inside the chamber, microbridges were filled with 35  $\mu$ l of 200 mM calcium chloride solution in 200 mM TRIS buffer pH 9. The cylindrical vessel contained 25 mM ammonium carbonate. Control samples contained only calcium chloride solution, while 64  $\mu$ g/ml of organic matrix from shells were added to the experimental ones. All experiments were carried out inside the petri dish at 20° C for variable periods of time (6-24 h). Precipitation of calcium carbonate results from the diffusion of carbon dioxide vapor into the buffered  $\text{CaCl}_2$  solution [20]. The crystals were observed in a Tesla BS 343 A scanning electron microscope. The FTIR spectrum was obtained by using a 1% KBr pellet, in the 400- to 4000  $\text{cm}^{-1}$  region from crude organic matrix treated with 10% NaOH (standard method for obtaining pure deproteinized chitin) at room temperature compared to standard chitin. For X-ray diffraction analysis, pieces of shell were ground into fine powder, applied to a holder,

and scanned at 6°C/min with a step size of 0.01°, with an operating voltage of 40KV and current of 35 mA in a Siemens D5000 diffractometer.

## RESULTS AND DISCUSSION

Specimens of *Austromegabalanus psittacus* are seen in figure 1a. Barnacle's shell is composed of twelve calcitic plates, six parietes and six radii, joined in the form of a truncated cone opened at the top, and resting on a basal disk (figure 1b). While parietes have longitudinal canals (from the base to the apex), radii have transversal canals arranged parallel to the base (figure 1b). These canals are displaced to the outside of the shell delimiting a thinner solid outer lamina and a thicker inner one. The inner lamina consists of parallel calcitic layers separated by organic sheets, which also organize as many concentric rings around the canals (figure 1c and d). These sheets and rings showed autofluorescence (figure 1e and f) and consisted of  $\beta$  chitin (figure 2a). This fluorescence disappeared after mild treatment with NaOH, indicating that some undefined proteins associated to chitin are involved in this phenomenon. Partially decalcified shells show numerous apparently disoriented planar aggregated fusiform calcite crystals located between chitin sheets intermixed with an organic material which eventually collapsed after complete decalcification remaining as a granular sheet (figures 2b and 3a). Chitin sheets showed a parallel fibrillar structure and a less electron-dense granular material between them was observed (figure 3b). A higher magnification of this granular material stained with a cationic dye (polyethyleneimine) showed the occurrence of a net-shape arrangement of proteoglycans (figure 3b, insert). Immunogold studies of this organic matrix showed a positive reaction with anti-keratan sulfate antibody (5D4) around the chitin sheets (figure 3c), while the granular material between the chitin sheets showed a positive reaction with anti-dermatan sulfate antibody (2B6) (figure 3d).

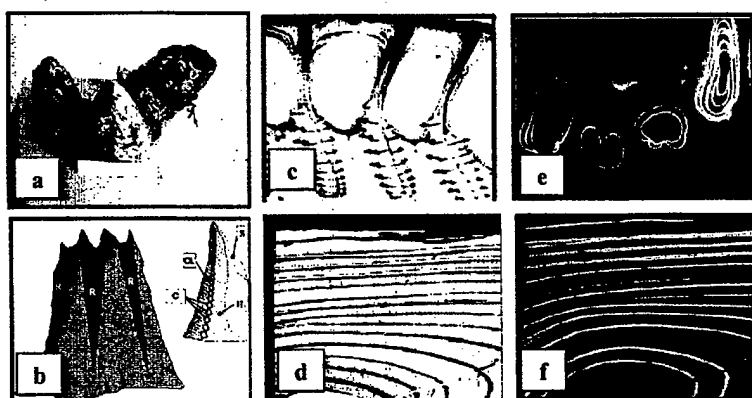


**Figure 1.** a) Live *A. psittacus* specimens from central coast of Chile, bar: 10 cm ; b) Schematic illustration of barnacle's shell wall showing parietes (P) and radii (R), and a longitudinal section of a radius showing canals (C), outer and inner lamina (OL and IL), and sheath (S); c) and d) Light microscopy of polished transversal section of a paries showing canals and inner lamina respectively, 400X; e) and f) Same as c) and d) but observed under the fluorescence microscopy, showing autofluorescent rings around canals and sheets layering the inner lamina, 400X.

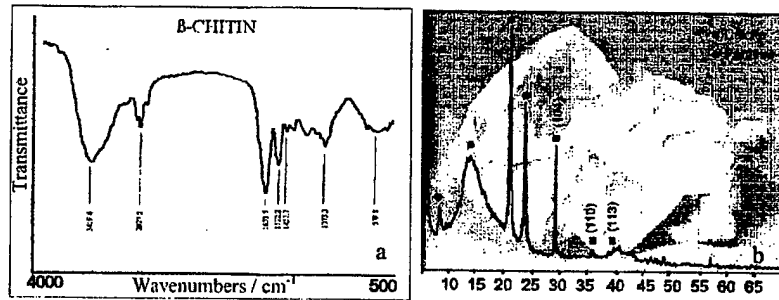


**Figure 2.** a) FTIR spectrum of the insoluble organic matrix extracted from barnacle's shell corresponding to  $\beta$  chitin; b) Powder XRD pattern showing preferred orientation of calcite crystals obtained from barnacle's shell

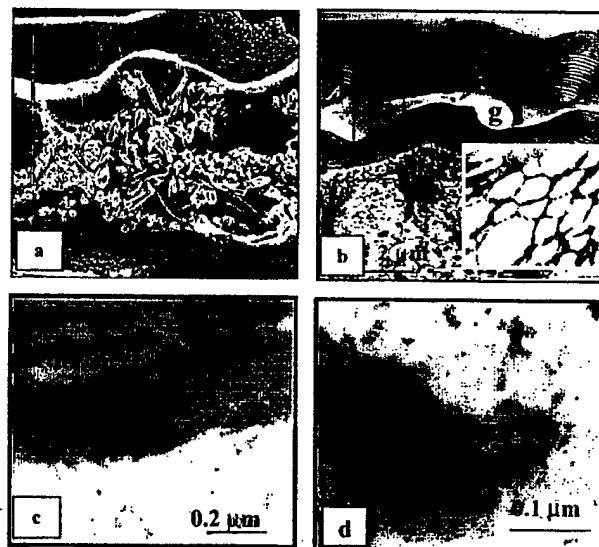


**Figure 3.** a) SEM of partially decalcified shell showing elongated crystals associated to granular organic material between chitin sheets (g); b) TEM of a decalcified shell showing laminated sheets of chitin and a granular material between them (g). Insert: granular material positive to cationic dye indicating proteoglycan occurrence (g); c) immunogold positive reaction with anti-keratan sulfate antibody around chitin fibers; d) immunogold positive reaction with anti-dermatan sulfate antibody on the granular material located between chitin sheets.

When crystallization assays were carried out in the absence of any organic additive, regular calcite crystals showing the {104} faces were obtained (figure 4a). However, when a mixture of soluble and insoluble fractions of shell organic matrix containing chitin, proteoglycans and some proteins was added, a time-depending modification of the calcite morphology was observed. In the first 8 h, crystals seem to nucleate from the chitin fibers, and the corners of the rhombohedra became rough and started to develop curved faces (figure 4b). Between 8 to 20 h, helical aggregations of rounded crystals compacted each other (figure 4c), and after 20 h these rounded crystals appear to be composed of helically ordered planar aggregates of elongated crystals (figure 4d).

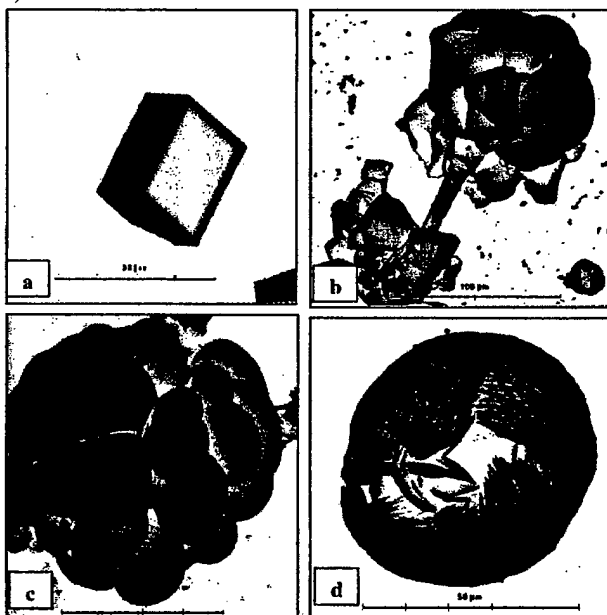


**Figure 4.** SEM micrographs showing the morphology of calcite crystals grown *in vitro* with or without shell organic matrix soluble plus insoluble fractions at different incubations times: a) Control experiment showing the {104} faces; b) incubation with the fractions for 6-8 h; c) incubations with the fractions for 8-20 h; d) incubations with the fractions for 20-24 h.

Although we can not discard the occurrence of undefined proteins in the barnacle's shell, we do show the occurrence and precise localization of particular proteoglycans. The same proteoglycans have been observed in the avian eggshell where a keratan sulfate-rich proteoglycan (mammillan) has a role in the nucleation of the first calcite crystals, and a dermatan sulfate-rich proteoglycan (ovoglycan) regulates the growth and orientation of the later forming crystals [21-22]. The proposed structure of the nacreous organic matrix of mollusks includes layers of chitin (with patches of associated anionic-rich proteins) separated by a silk fibroin gel [23]. Barnacle's shell appeared to have a similar general structure, and here we provide evidence of the occurrence of an additional kind of polyanionic, highly hydrophilic and gelatinous molecules, one closely

associated to the chitin fibers (keratan sulfate proteoglycans) and other in the granular material located between them (dermatan sulfate proteoglycans), both localized where the calcite crystals were before decalcification. Foregoing experiments could answer the precise effect of these sulfated molecules in crystal nucleation and growth. However, the extracted barnacle shell organic matrix, containing these sulfated polymers, shows dramatic effects on the morphology of calcite crystals. We suggest that these sulfated macromolecules, because their acidic nature, could be also responsible for controlling the processes of biomineralization of barnacle shell.

#### ACKNOWLEDGEMENTS

This work was supported by FONDAP 11980002 granted by the Chilean Council for Science and Technology (CONICYT).

#### REFERENCES

1. H.A. Lowenstam and S. Weiner, *On Biomimetication*, (Oxford University Press, Oxford, 1989) p. 324.
2. S. Mann, J. Webb and R.J.P. Williams, *Biomimetication*, (VCH, Weinheim, 1989) p. 490.
3. K. Simkiss and K.M. Wilbur, *Biomimetication*, (Academic Press, San Diego, 1989) p. 337.
4. A.H. Heuer, D.J. Fink, V.J. Laraia, J.L. Arias, P.D. Calvert, K. Kendall, G.L. Messing, J. Blackwell, P.C. Rieke, D.H. Thompson, A.P. Wheeler, A. Veis and A.I. Caplan, *Science* **255**, 1098 (1992).
5. J. Aizenberg, A. Tkachenko, S. Weiner, L. Addadi and G. Hendl, *Nature* **412**, 819 (2001).
6. S. Albeck, S. Weiner and L. Addadi, *Chem. Eur. J.* **2**, 278 (1996).
7. A.M. Belcher, X.H. Wu, R.J. Christensen, P.K. Hansma, G.D. Stucky and D.E. Morse, *Nature* **381**, 56 (1996).
8. G. Falini, S. Albeck, S. Weiner and L. Addadi, *Science* **271**, 67 (1996).
9. J.B. Thompson, G.T. Paloczi, J.H. Kindt, M. Michenfelder, B.L. Smith, G. Stucky, D.E. Morse and P.K. Hansma, *Biophys. J.* **79**, 3307 (2000).
10. C.A. Orme, A. Noy, A. Wierzbicki, M.T. McBride, M. Grantham, H.H. Teng, P.M. Dove and J.J. DeYoreo, *Nature* **411**, 775 (2001).
11. Y. Nys, M.T. Hincke, J.L. Arias, J.M. García-Ruiz and S.E. Solomon, *Poultry Avian Biol. Rev.* **10**, 143 (1999).
12. Y. Dauphin, *Int. J. Biol. Macromol.* **28**, 293 (2001).
13. I.M. Weiss, W. Góhring, M. Fritz and K. Mann, *Biochem. Biophys. Res. Comm.* **285**, 244 (2001).
14. C. Darwin, *A monograph on the sub-class cirripedia*, (Ray Soc., London, 1854)
15. E. Bourget, *Le Natur. Canadien* **104**, 281 (1977).
16. H.A. Lowenstam, S. Weiner and W.A. Newman, in *Chemistry and Biology of Mineralized Tissues*, edited by H. Slavkin and P. Price (Excerpta Medica, Amsterdam, 1992) pp. 73-84.
17. Y.M.H.F. Sauren, R.H.P. Micremet, C.G. Groot, H.K. Koerten and J.P. Scherft, *J. Histochem Cytochem.* **39**, 331 (1991).
18. B. Caterson, J.E. Christner, J.R. Baker, and J.R. Couchman, *Fed. Proc. Fed. Am. Soc. Exp. Biol.* **44**, 386 (1985).
19. H. Mehmet, P. Sculder, P.W. Tang, F.F. Hounsell and B. Caterson, *Eur. J. Biochem.* **157**, 385 (1986).

---

20. J.I. Arias, C. Jure, J.P. Wiff, M.S. Fernandez, V. Fuenzalida and J.L. Arias, presented at the 2001 MRS Fall Meeting, Boston, MA, 2001 (Mater. Res. Soc. Proc. in press).
21. M.S. Fernandez, A. Moya, L. Lopez and J.L. Arias, *Matrix Biol.* **19**, 793 (2001).
22. J.L. Arias and M.S. Fernandez, *World's Poultry Sci. J.* **57**, 349 (2001).
23. Y. Levi-Kalisman, G. Falini, L. Addadi and S. Weiner, *J. Struct. Biol.* **135**, 8 (2001).

### **Molecular Mechanism of Bacterial Magnetite Formation and Its Application**

Tadashi Matsunaga and Yoshiko Okamura

Department of Biotechnology, Tokyo University of Agriculture and Technology  
Naka-Cho, Koganei, Tokyo 184-8588, Japan

#### **ABSTRACT**

Nano-technology has been identified as an area which will bring about new evolutions in materials, devices and processes. The challenges of nano-biotechnology entail manufacturing more sophisticated and highly efficient biosensors and biomaterials at the nano-scale level for use in interdisciplinary fields. Here, we introduce a biomaterial produced by magnetic bacteria, bacterial magnetic particles (BMPs), and the molecular architecture technique we have used for its application.

Magnetic bacteria synthesize intracellular magnets which are encapsulated by lipid bilayer membranes. Sizes of BMPs vary from 50 - 100 nm in diameter, and number over 10 per cell. BMPs are composed of magnetite ( $Fe_3O_4$ ) with a single magnetic domain. Easy aqueous dispersion of BMPs enable development of highly sensitive chemiluminescence enzyme immunoassays by the chemical coupling of antibodies on BMP surfaces. BMPs can likewise be used as drug delivery systems employing magnetoliposomes with high capture volumes. We previously reported a technique for preparing recombinant BMPs on which proteins were displayed by gene-fusion. We furthermore applied such recombinant BMPs to biotechnologically-important issues, including novel bioassay platforms for medicine and environmental management. We envisage the production of more refined chemicals and agents through expression on BMPs by gene-fusion followed by simple purification using magnet.

---

## INTRODUCTION

The use of magnetic particles in immunoassays enables the separation of bound and free analytes by applying a magnetic field. For example, proteins can be attaching covalently to solid supports, such as magnetic particles, preventing the desorption of antibodies during assaying. Because these particles disperse evenly throughout the reaction mixture, they allow rapid reaction kinetics without the need for continuous mixing or shaking, enable coupling antibodies, and facilitate ease of use. Magnetic particles serve as both solid supports and a means of separation in the assay system.

Magnetic bacteria have been isolated from freshwater and marine sediments, and are known to produce magnetite particles which are aligned in chains of around 20 particles per cell [1-4]. Bacterial magnetic particles (BMPs) are nano-size and disperse well in aqueous solution due to their stable lipid membranes [5]. On the basis of these properties, BMPs have been utilized in fluoroimmunoassays [6-8], mRNA recovery [9] and as DNA carriers [10]. Because of their fastidious characteristics and undefined metabolism, pure cultures of magnetic bacteria are very difficult to achieve. However, the successful isolation, cultivation and colony formation of the magnetic bacteria, *Magnetospirillum magneticum* AMB-1 [3] and MGT-1 [2], which are tolerant to oxygen, have allowed development of conjugative gene transfer and transposon mutagenesis systems [11]. Several recent findings and the mechanism of magnetite particle formation have been ascertained through studies with AMB-1. Thus, we describe here the molecular, genetic and biotechnological characteristics of magnetic bacteria and bacterial magnetic particles, revealed mainly from our recent studies with respect to the

genetic engineering of magnetic bacteria and advanced applications of bacterial magnets based on molecular architecture.

## MAGNETIC BACTERIA

Magnetic bacteria are a heterogeneous group of gram-negative prokaryotes with both diverse morphologies and habitats [12-20]. Various morphological types of magnetic bacteria including cocci, rods, vibrio, and spirilla have been isolated from sediments, e.g. marine, rivers, lakes, ponds, beaches, rice paddies, drains, wet soil [21], deep sea [22] and estuaries. Most magnetic bacteria produce nano-sized magnetite with species- or strain- specific morphologies [23-26]. The alignment of BMPs in chains confers a magnetic dipole and magnetotaxis to cells allowing bacterial orientation along geomagnetic field lines. The successful isolation and cultivation of a facultative aerobic magnetic bacterium, *Magnetospirillum magneticum* AMB-1 (Fig.1a), has enabled us to conduct genetic manipulations to elucidate the mechanism of BMP formation, and to optimize culturing for industrial-scale production of BMPs. We have also isolated a novel sulfate-reducing magnetic bacterium, *Desulfovibrio magneticus* (sp. nov.) (Fig.1b), formerly known as RS-1, which grows and synthesizes BMPs under strict anaerobic conditions [4].

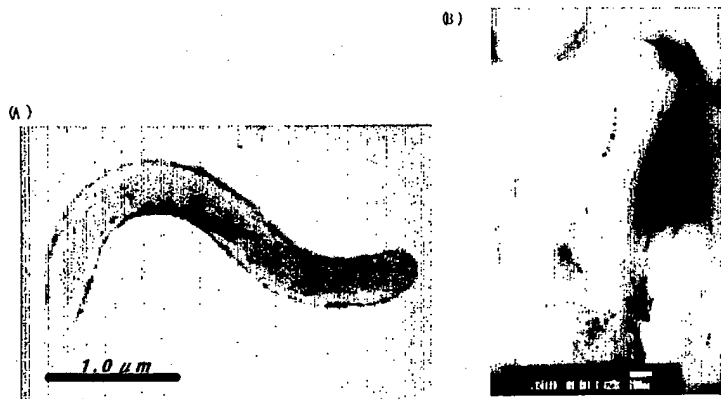


Fig. 1 Transmission electron micrographs of *Magnetspirillum magneticum* AMB-1 (A) and *Desulfovibrio magneticus* RS-1 (B).

## BACTERIAL MAGNETIC PARTICLES

Transmission electron microscopy shows BMPs to be encapsulated by a biomembrane (Fig.2). The membrane is approximately 2-4 nm in thickness. Analysis of membrane components has been carried out mainly on strain AMB-1. Results indicate that BMP membrane consists of lipid containing phospholipids (comprising 58-65% of the total lipids) of which about 50% contains phosphatidylethanolamine [6, 27-28]. Moreover, the fatty acid make up of BMP membrane is similar to the cytoplasmic membrane in strain AMB-1. Almost all of the proteins expressed in the cytoplasmic membrane were also found in the BMP membrane. However, five proteins were shown to be specific to BMP membrane fractions. [29, 30].



Fig. 2 Bacterial magnetic particle from *Magnetspirillum magneticum* AMB-1.

## GENETIC ANALYSES OF *MAGNETOSPIRILLUM MAGNETICUM* AMB-1

Isolation and characterization of the genes that mediate magnetite formation in bacteria are prerequisite for determining the mechanisms of magnetic particle biosynthesis. In order to identify specific genes involved in magnetite synthesis, transposon mutagenesis was conducted with strain AMB-1 [11]. Numerous non-magnetic mutants were successfully obtained and *magA* gene was subsequently isolated from one of the numerous mutants (strain NM5) by analyzing of the transposon disrupted gene (Fig. 3). The *magA* gene has homology with the  $\text{Na}^+ / \text{H}^+$  antiporter, NapA, from *Enterococcus hirae*. The iron up-take activity of MagA protein was determined using inverted vesicles prepared from fragmented membrane expressing MagA protein in *Escherichia coli* (Fig. 4). Addition of ATP initiated accumulation

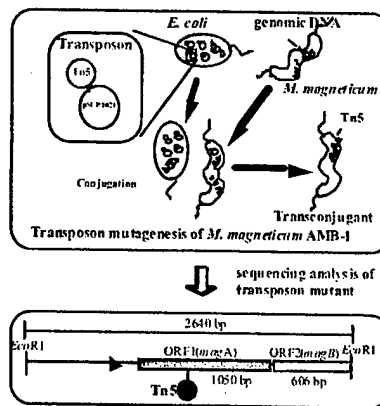


Fig. 3 Transposon mutagenesis of *Magnetospirillum magneticum* AMB-1 and isolation of *magA*.

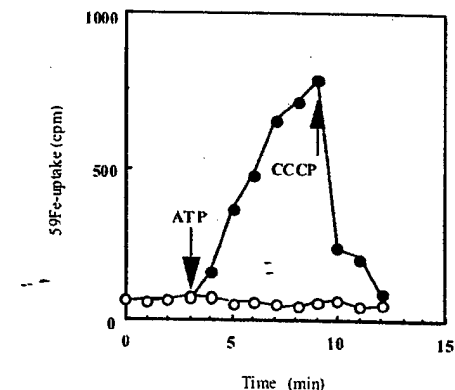


Fig. 4 Iron uptake into inverted vesicles. Arrowhead indicated the point of addition of ATP or CCCP.  
● ; the vesicles expressed MagA  
○ ; control

of ferrous ion in vesicles and the ion was released by adding of carbonyl cyanide m-chlorophenylhydrazone (CCCP) known as protonophore. The activity was also observed under artificial proton gradient without ATP. These results suggests that MagA protein is a proton-driving  $H^+$  / Fe(II) antiporter [31]. Additionally, intracellular localization of the MagA protein was examined using a MagA-Luciferase fusion protein, indicating that MagA is localized on both the cytoplasmic and BMP membranes, where it appears to transport iron into BMP vesicles [32]. Therefore, MagA is considered to play an essential role in the bacterial formation of magnetite crystals.

Presupposing that proteins expressed on BMP membranes play a direct role in regulating magnetite crystallization, a number of distinct BMP-specific proteins have since been identified. Protein fractions prepared from cellular and BMP membranes and cytoplasm were separated by SDS-polyacrylamide gel electrophoresis, reveal five specific proteins in BMP membrane fractions (Fig. 5). Utilizing 2D-electrophoresis, 4 of these proteins were

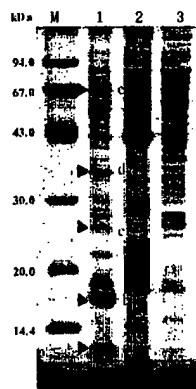


Fig. 5 Protein profiles by SDS-PAGE. 40 $\mu$ g of protein from each fraction was applied. Lane 1: BMP membrane solubilysate; lane 2: membrane solubilysate; lane 3: cytoplasmic fraction; M: standard markers.

separated for amino acid sequencing. On the basis of the N-terminal amino acid sequences determined, oligonucleotide primers were designed to perform polymerase chain reactions (PCR) to amplify DNA sequences of the target proteins. Subsequently, *mpsA* encoding a 36 kDa protein and *mms16* encoding a 16 kDa protein were isolated. DNA sequences of these two genes were analyzed and protein homology was examined. The amino acid sequence of MpsA was

proven to be highly homologous with that of *E. coli* acetyl-CoA carboxylase [29], and the *mms16* gene encodes for a GTPase [33]. Mms16 protein was found to be the most abundantly expressed of the five BMP specific proteins. We hypothesize that Mms16 is a GTPase with properties similar to eukaryotic small GTPases which control vesicle trafficking. Thus, we conducted inhibition experiments on GTPase by aluminum fluoride.  $\text{AlF}_4^-$  prevents BMP synthesis suggesting that GTPase activity is required for BMP synthesis [33]. Thus, we hypothesize that magnetosomes arise through invagination of the cytoplasmic membrane and processes similar to those of eukaryotic vesicle formation.

#### **PROPOSED MECHANISM FOR MAGNETITE FORMATION**

We have hypothesized that the BMP membrane is derived from the cytoplasmic membrane and formed through the invagination process. Transmission electron microscopy of *M. magnetotacticum* MS-1 reveals that BMP envelopes appear prior to the crystallization of magnetite [28]. The mechanism of envelope formation, however, still remains unclear. Previous studies on vesicle formation by invagination of the cytoplasmic membrane have been performed using eukaryotes. It is possible that magnetic bacteria have similar mechanisms of vesicle formation. We propose that Mms16 mediates the priming of invagination and MpsA mediates the acylation of Mms16 to anchor the BMP membrane. Moreover, MagA on BMP membranes, transfers Fe ions into intracellular vesicles. Various proteins associated with the BMP membrane may play functional roles involved in magnetite

generation inside BMP envelopes. These include: 1) the accumulation of supersaturating iron concentrations and maintenance of reductive conditions; and 2) the oxidation of iron to induce mineralization, or the partial reduction and dehydration of ferrihydrite to magnetite (Fig. 6).

#### FUNCTIONAL BMP BASED ON MOLECULAR ARCHITECTURE

MagA, MpsA and Mms16 are all

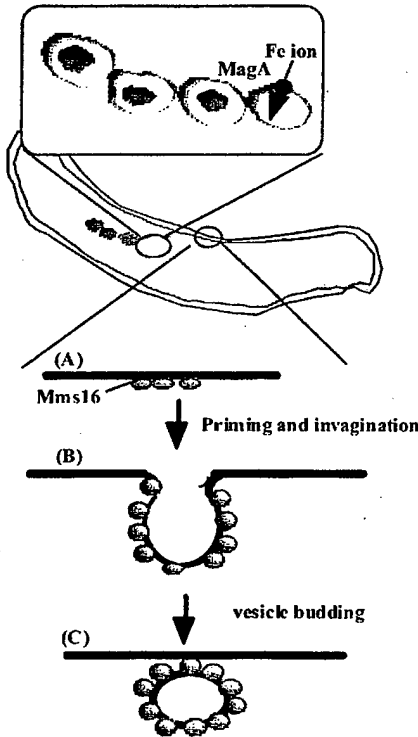


Fig. 6 Postulated mechanism of bacterial magnetic particle formation.

localized on the membranes of BMPs.

These proteins could therefore be utilized as anchor proteins, allowing a variety of functional proteins to function on BMPs, i.e., enzymes or antibodies can be displayed on BMP membrane surfaces. For instance, employing the firefly luciferase *luc* gene, a *magA-luc* fusion gene was cloned into plasmid pRK415 and introduced into *M. magneticum* AMB-1 (Fig. 7) [32]. Extracted BMPs from recombinant AMB-1 cells expressed luciferase activity. In such a way, MagA protein acts as a workable anchor for the site-specific display of functional foreign proteins. Similarly, immunoglobulin (IgG) binding cell wall protein and proteinA,

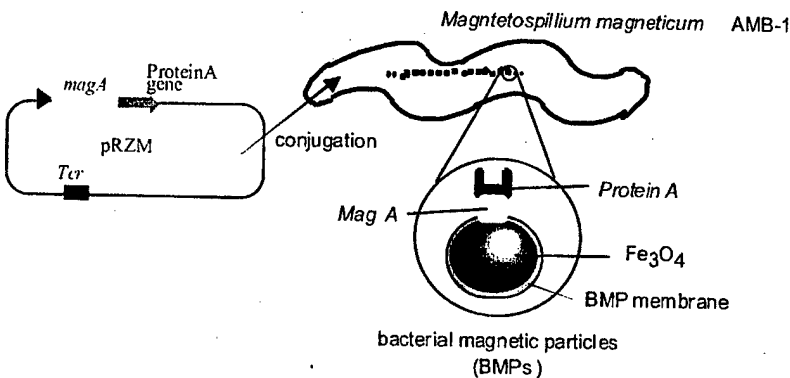


Fig. 7 Display of protein A onto bacterial magnetic particle using *magA* gene fusion.

were introduced to BMP membranes, using a *proteinA-magA* hybrid gene [34]. Using antibody bound proteinA-BMP complexes together with a chemiluminescence enzyme immunoassay, we have developed a rapid and highly sensitive diagnostic method for detecting human immunoglobulin G (IgG) [35]. Also, the feasibility of Mms16 as an anchor molecule was established by manifesting the estrogen receptor hormone binding domain (ERHBD) on BMP membranes. ERHBD-BMP complexes function as practical receptor binding assays for estrogen-like compounds. Upscale production of functionally active antibodies or enzymes expressed on BMP membranes is effectively accomplished by fed-batch culturing techniques [36]. Further, we constructed a high copy number plasmid pUMG in AMB-1 for a more efficient display of functional foreign proteins on BMP.

#### APPLICATIONS OF FUNCTIONAL BMP

We have examined the functional uses of BMPs in immunoassay systems to detect various biological markers. A chief advantage of using BMPs, compared with other

conventional immunoassay methods, is the easy separation of membrane-bound and free fractions by applying a magnetic field. ProteinA-BMP complexes have viable applications in the detection of human IgG, insulin, HbA1 and glycated albumin from serum [37]. Antibodies conjugated with BMPs by chemical cross-linking methods are also valuable tools for detecting a wide variety of substances.

We have investigated various environmental pollutants, including endocrine disruptors, alkylphenol ethoxylates (APE), bisphenol A (BPA), and linear alkylbenzene sulfonates (LAS), using monoclonal antibodies immobilized on BMP and a fully automated detection system. The automated sandwich immunoassay system developed (fig. 8) comprises a reaction station, a tip rack, and an automated eight-channel pipet bearing a retractable magnet mounted close to the pipet tip and conterminous with a microtiter plate (96 wells). A single rack holds 8X3 tips for reaction. Our data show that this fully-automated system provides rapid detection (in 15 min), and efficiently determines concentrations of APE, BPA, and LAS with detection limits of 6.6 ppb, 0.023 ppt, and 35 ppt, respectively. The advantages

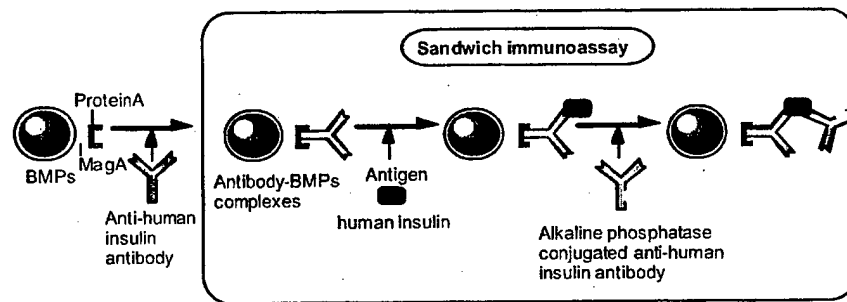


Fig. 8 Schematic diagram of sandwich immunoassay using ProteinA-BMP complexes and alkaline phosphatase-conjugated antibody.

afforded by this automated detection system should be practicable to other assay systems utilizing functional BMP.

### CONCLUSION

In conclusion, BMP formation has been examined at the molecular level, although further studies are required to elucidate the whole mechanism of BMP formation and its highly controlled biominerization process. However, recent progress in molecular biology will help enable more highly organized and systematic studies toward the elucidation of bacterial magnetite formation. In addition, improved analysis and identification of BMP specific factors will facilitate the use of biominerization as a biomimetic technique for in vitro production of highly controlled biocrystals.

### REFERENCES

1. R. P. Blakemore, *Science* **190**, 377 (1975).
2. T. Matsunaga, F. Tadokoro and N. Nakamura, *IEEE Trans. Magn.*, **26**, 1557 (1991).
3. T. Matsunaga, T. Sakaguchi and F. Tadokoro, *Appl. Microbiol. Biotechnol.* **35**, 651 (1991).
4. T. Sakaguchi, J. G. Burgess and T. Matsunaga, *Nature* **365**, 47 (1993).
5. D. L. Balkwill, D. Maratea and R. P. Blakemore, *J. Bacteriol.* **141**, 1399 (1980).

6. N. Nakamura, K. Hashimoto and T. Matsunaga, *Anal. Chem.* **63**, 268 (1991).
7. N. Nakamura, J. G. Burgess, K. Yagiuda, K. kudo, S. Sakaguchi and T. Matsunaga, *Anal. Chem.* **65**, 2036 (1993).
8. N. Nakamura and T. Matsunaga, *Anal. Chim. Acta*, **281**, 585 (1993).
9. K. Sode, S. Kudo, T. Sakaguchi, N. Nakamura and T. Matsunaga, *Biotechnol. Tech.* **7**, 688 (1993).
10. H. Takeyama, A. Yamazawa, C. Nakamura and T. Matsunaga, *Biotechnol. Tech.* **9**, 355 (1995).
11. T. Matsunaga, C. Nakamura, J. G. Burgess and K. Sode, *J. Bacteriol.* **174**, 2748 (1992).
12. R. P. Blakemore and N. A. Blakemore, in *Iron biominerals*, ed. R. B. Frankel and R. P. Blakemore (Plenum Press, 1991) pp. 51-67.
13. R. P. Blakemore, *Ann. Rev. Microbiol.* **36**, 217 (1982).
14. R. P. Blakemore, N. A. Blakemore, D. A. Bazylinski and T. T. Moench, in *Bergey's manual of systematic bacteriology*, vol. 3, edited by J. T. Staley, M. P. Bryant, N. Pfennig and J. G. Holt, (Williams & Wilkins, Baltimore, 1989) pp. 1882-1889.
15. D. M. S. Esquivel and H. G. P. Linns de Barros, *J. Exp. Biol.* **121**, 153 (1986).
16. S. Mann, N. H. C. Sparks and R. G. Borad, *Adv. Microb. Physiol.* **31**, 125 (1990).
17. M. Oberhack, R. Sussmuth and H. Frank, *Z. Naturforsch.* **42c**, 300 (1987).
18. N. H. C. Sparks, L. Courtaux, S. Mann, and R. G. Borad, *FEMS Microbiol. Lett.* **37**, 305 (1986).
19. T. Matsunaga and S. Kamiya, *Appl. Microbiol. Biotechnol.* **26**, 328 (1987).

20. R. H. Thornhill, J. G. Burgess, T. Sakaguchi and T. Matsunaga, *FEMS Microbiol. Lett.* **115**, 169 (1993).

21. J. W. E. Fassbinder H. Stanjek and H. Vail, *Nature* **343**, 161 (1990).

22. J. F. Stolz, S. -B. R. Chang and J. L. Kirschvink, *Nature* **321**, 849 (1986).

23. D. Schuler and E. Baeuerlein, in *Transition metals in microbial metabolism*, ed. G Winkelmann and C. J. Carrano (Harwood Academic Publishers, Amsterdam, The Netherlands, 1997)

24. J. F. Stolz, *J. Gen Microbiol.* **139**, 1663 (1993).

25. D. A. Bazylinski, *ASM News* **61**, 337 (1995).

26. D. Schuler and R. B. Frankel, *Appl. Microbiol. Biotechnol.* **52**, 464 (1999).

27. T. Matsunaga, T. Sakaguchi, K. Sode, S. Kudo and N. Nakamura, in *Proceedings of the 3rd IUMRS international conference on advanced materials*, edited by H. Aoki et al. (Advanced materials '93 II/A, Kawasaki, Japan, 1993) pp. 449-454.

28. Y. A. Gorby, T. J. Beveridge and R. P. Blakemore, *J. Bacteriol.* **170**, 834 (1988).

29. T. Matsunaga, N. Tsujimura, Y. Okamura and H. Takeyama, *Biochem. Biophys. Res. Commun.* **268**, 932 (2000).

30. Y. Okamura, H. Takeyama and T. Matsunaga, *Appl. Biochem. Biotech.* **84-86**, 441 (2000).

31. C. Nakamura, J. G. Burgess, K. Sode and T. Matsunaga, *J. Biol. Chem.* **270**, 28392 (1995).

32. C. Nakamura, T. Kikuchi, J. G. Burgess and T. Matsunaga, *J. Biochem.* **118**, 23 (1995).

33. Y. Okamura, H. Takeyama and T. Matsunaga, *J. Biol. Chem.* **276**, 48183 (2001).
34. T. Matsunaga, R. Sato, S. Kamiya, T. Tanaka and H. Takeyama, *J. Magn. Magn. Mater.* **194**, 126 (1999).
35. T. Tanaka and T. Matsunaga, *Anal. Chem.* **72**, 3518 (2000).
36. C. -D. Yang, H. Takeyama, T. Tanaka and T. Matsunaga, *Enz. Microb. Technol.* **29**, 13 (2001).
37. T. Tanaka and T. Matsunaga, *Biosens. & Bioelectronics*, **16**, 1089 (2001).

**Imaging and  
Characterization Techniques**

### Mechanical and Microstructural Properties of Stratum Corneum

Kenneth S. Wu<sup>1</sup>, William W. Van Osdol<sup>2</sup>, and Reinhold H. Dauskardt<sup>3</sup>

<sup>1</sup>Department of Mechanical Engineering, Stanford University, Stanford, CA 94305-2205

<sup>2</sup>ALZA Corporation, Mountain View, CA 94039-7210

<sup>3</sup>Department of Materials Science and Engineering, Stanford University, Stanford, CA 94305-2205

#### ABSTRACT

A mechanics approach is presented to study the intercellular delamination resistance and mechanical behavior of stratum corneum (SC) tissue in the direction normal to the skin surface. The effects of temperature and hydration on debonding behavior were also explored. Such understanding, which includes the relationship of mechanical behavior to the underlying SC cellular structure, is essential for emerging transdermal drug delivery technologies. Fracture mechanics-based cantilever-beam specimens were used to determine reproducibly the energy release rates to quantify the cohesive strength of human SC. The debond resistance of fully hydrated SC was found to decrease with increasing temperature, while dehydrated SC exhibited a more complex variation with temperature. Stress-separation tests showed that fracture energies and peak separation stresses decreased with increasing temperature and hydration, although the SC modulus varied only marginally with temperature and hydration. Results are described in terms of microstructural changes associated with hydrophilic regions and intercellular lipid phase transitions.

#### INTRODUCTION

As the most externally exposed organ in the human body, the skin provides mechanical protection and a controlled permeable barrier to the external environment to maintain internal homeostasis. The layered construction of the skin represents a composite material in which the components possess specialized functionalities to accommodate a variety of conditions from mechanical stresses to variable ambient moisture and to resist the presence of toxic chemicals, pathogens, and radiation.<sup>1</sup> The top layer of the skin, the epidermis, consists of epithelial cells bound together via various cell-adhesion mechanisms including intercellular proteins and lipids. The top most-layer of the epidermis, the stratum corneum (SC), consists of layered anucleated cells that mature and subsequently detach in a natural renewing process. The disk-shaped SC cells, composed largely of aligned keratin filaments, create a regular interdigitating structure held together by lipid and protein structures as illustrated in Fig. 1.

The SC is the first structure to provide resistance to abrasion and penetration of foreign objects and must provide this protection under highly variable temperature, humidity, and chemical conditions which bodily self-regulation or external environments may induce. In the case of emerging transdermal drug delivery technologies, the application and removal of adhesive drug delivery devices necessitates an appropriate balance between patch adhesive strength and SC cohesive strength in the direction normal to the skin surface. While previous investigators have examined in-plane properties of SC to determine modulus and fracture phenomena and dependencies upon environmental conditions, surprisingly little quantitative work has examined properties of the SC in the direction normal to the skin surface.<sup>2,3,4,5,6,7</sup> The resistance of SC to delamination is not well characterized, and virtually no quantitative data or reproducible test methods are available.

In the present study, a mechanics approach to examine the SC intercellular delamination resistance and out-of-plane mechanical behavior and their relationship to SC cellular structure is presented. The delamination resistance of human SC was examined as a function of selected testing and preconditioning temperature and moisture conditions and related to underlying structure. Fracture resistance was quantified in terms of the energy required to propagate a crack or debond and defined in terms of the strain energy release rate  $G$ , measured in units of  $J/m^2$ . Furthermore, stress-separation tests were performed to examine the out-of-plane mechanical behavior of the SC.

## EXPERIMENTAL

### Double-cantilever beam (DCB)

The debond resistance of human cadaver SC tissue was examined using fracture mechanics techniques developed to measure the adhesive properties of highly viscoelastic pressure sensitive adhesives.<sup>8</sup> Similar techniques have been employed to measure the adhesive properties of polymer bone cements.<sup>9</sup> The technique involves sandwiching the SC between two elastic polycarbonate substrates with cyanoacrylate adhesive to form fracture-mechanics based double-cantilever beam (DCB) specimens. The SC was separated from the underlying epidermis via a trypsin enzymatic digest then stored at 4°C in a fully hydrated state on water-moistened filter paper. The transparent polycarbonate beams facilitated optical inspection of the inner sandwich structure during sample preparation and testing. Substrate dimensions were chosen to ensure purely elastic deformation of the substrates during testing to enable the use of linear elastic fracture mechanics to determine the strain energy release rates.<sup>8,9</sup> Two sets of DCB specimens were prepared containing SC that was either fully hydrated (FH) or room-humidity dehydrated (DH) in 100% R.H. or 45% R.H. environments, respectively.

To fabricate the specimens, a thin layer of cyanoacrylate adhesive was applied to the face of a 40 mm x 10 mm x 3.175 mm polycarbonate substrate leaving a 7-10 mm region of the beam end uncoated. The substrate was pressed against the SC on the filter paper backing and a scalpel was used to cut around the substrate to detach the adhered SC from surrounding tissue. Another substrate coated with adhesive in the same manner was pressed against the SC face on the complimentary beam with adhesive-free ends aligned to form the final sandwich structure. Excess adhesive along the sandwich edges was removed with a scalpel to ensure that only SC was binding the two halves of the sandwich structure together.

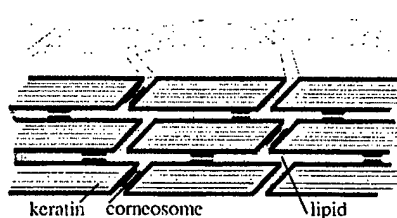


**Figure 1.** Schematic of the stratum corneum showing cellular structure including aligned keratin filaments as well as lipid intercellular space with corneosomes.

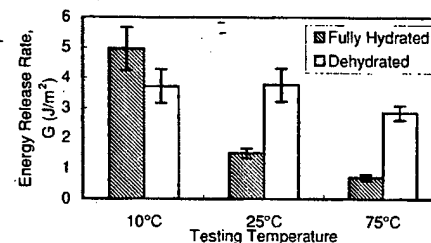


**Figure 2.** SC debond resistance values measured at selected temperatures after being fully hydrated or dehydrated. Error bars represent standard error of the mean.

Specimens were placed in an environmental chamber at selected temperature (10, 25, 75°C) and relative humidity (45 and 85% RH) conditions and allowed to equilibrate for ~10 min. Subsequently, the samples were loaded, via attached loading tabs, to propagate a debond within the SC layer. The specimens were tested in a custom-built mechanical test system with a computer controlled DC servoelectric actuator operated in displacement control. Tests were performed at a constant displacement rate of 2  $\mu\text{m/s}$ . Corresponding loads were measured using a 222 N load cell and the debond length was determined using compliance techniques. Debond resistance was determined from critical values of the strain energy release rate,  $G_c$ .<sup>8,9</sup>

#### Stress-separation (SS)

Structures containing the SC sandwiched between polycarbonate substrates were fabricated in a similar manner to the DCB specimens. The substrate dimensions were 10 mm x 10 mm x 3.175 mm. The specimens were loaded normal to the SC face via attached loading tabs in an environmental chamber with controlled temperature and humidity. Testing was conducted at a constant displacement rate of 1  $\mu\text{m/s}$ , yielding a strain rate of ~0.025  $\text{s}^{-1}$  in the SC for a SC thickness of 40  $\mu\text{m}$ . The SS measurements were performed using the same apparatus as that for DCB experiments. The specimens were allowed to equilibrate for ~20 min. before testing.

#### Scanning electron microscopy (SEM)

Both DCB and SS samples were examined after mechanical testing using SEM to characterize the debond surface morphologies. Selected specimens were allowed to dry in a desiccator and then gold coated and examined in an SEM operating at 15 keV. Two specimens from each testing condition were inspected to ensure representative characterization.

## RESULTS

Debond resistance values,  $G_c$ , for specimens containing DH and FH SC measured at selected temperatures are presented in Fig. 2. All reported results are from testing utilizing a single sheet of SC to avoid tissue variations. The specimens exhibited constant debond energy with debond extension suggesting that the varying strain rates obtained during debond extension did not significantly effect the debond fracture resistance. Such behavior was subsequently verified by varying the testing displacement rate from 2 to 8  $\mu\text{m/s}$  with no systematic effect on  $G_c$  values. The hydrated state of the SC had only a small effect on  $G_c$  values measured at 10°C where the average  $G_c$  value for the FH specimen was ~1  $\text{J/m}^2$  (or 25%) higher than the DH specimen. At elevated temperatures, the FH specimens exhibited markedly lower debond energy with increasing test temperature. In contrast, the DH samples lacked a pronounced change with temperature although a marginal decrease was apparent at 75°C. At the elevated temperatures,  $G_c$  values for the DH specimens were markedly higher than those of the FH specimens.

Stress-separation tests performed on DH and FH specimens under the same environmental conditions as the DCB tests are shown in Fig. 3(a). The SS tests resulted in linear loading up to a peak stress after which the stress catastrophically dropped essentially to zero. Any residual stresses decayed to zero with continued displacement. For the FH specimens tested at 75°C, the SS curves do not show the marked drop in stress but rather decrease more gradually from the peak stresses toward zero. The area enclosed by the SS curve represents the total work required to cause failure of the SC and resulting fracture energy values calculated from the SS curves are presented in Fig. 3(b). Similar to the DCB results, the SS fracture energy values of the FH specimens decreased markedly with increasing temperature while the DH specimens

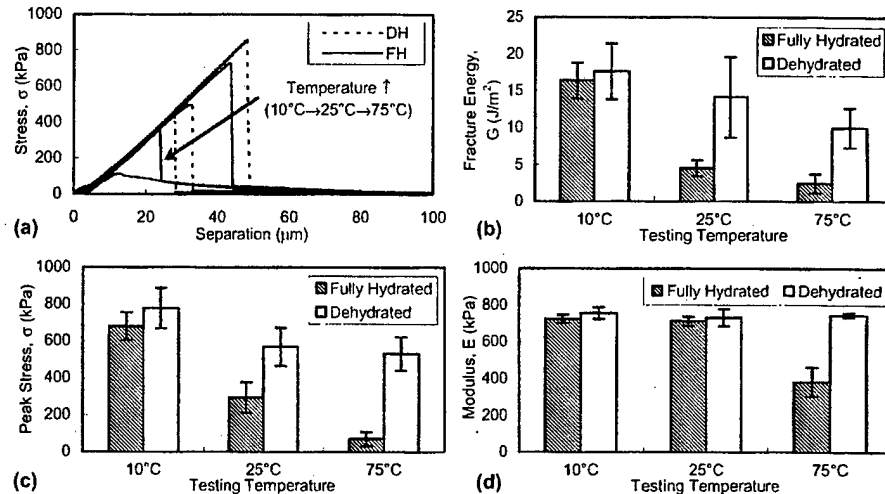


**Figure 3.** Stress-separation measurements conducted at selected temperatures showing (a) representative stress-separation curves, (b) fracture energy values determined from the area enclosed by the curves, (c) peak stresses, and (d) the initial loading modulus.

decreased less dramatically. Peak stress values obtained from the SS curves are shown in Fig. 3(c). Similar to the fracture energy values, both the peak stresses and corresponding strains were observed to decrease with increasing hydration and testing temperature.

The initial stiffnesses (or moduli) of the SC in the out-of-plane orientation for the selected testing conditions are shown in Fig. 3(d). The SC modulus measured was  $\sim 0.7$  MPa and was constant over the range of temperatures and hydrations tested with the exception of the FH specimens at 75°C where the modulus was  $\sim 0.4$  MPa.

Representative SEM micrographs of the fracture surfaces of tested DCB specimens containing FH and DH SC are shown in Fig. 4. Similar micrographs were obtained for all testing types and conditions. The FH specimens revealed comparatively little surface morphology and individual SC cells were difficult to discern (Fig. 4(a)). The DH specimens all revealed partial pullout of individual SC cells to varying degrees producing more debond surface roughness. The SS tests reveal similar trends to those seen in the DCB specimens in which the DH specimens exhibit SC cell pullout while the FH specimens lack similar cellular features.

## DISCUSSION

The marked decrease in fracture energy (Fig. 2) apparent with increasing temperature for the FH SC tissue are most likely related to a corresponding decrease in the peak cohesive strength (Fig. 3(c)) measured using the SS tests. Other energy dissipation mechanisms such as plasticity in the SC are also expected to scale with the peak cohesive strength. However, it should be noted that plastic deformation will be restricted in these specimens due to the thin film nature of the samples and the plane strain constraint of the DCB test configuration. The similarly constrained SS test geometries also limit plasticity. With restricted plastic zone formation, the SS data primarily represent properties of the cohesive mechanisms operating in

the SC layers. The limited influence of plasticity-type effects is seen by the similar trends in both DCB and SS fracture energy measurements and plastic zone calculations of  $\sim 0.1$ - $0.5$   $\mu\text{m}$ . In the case of strong plasticity, one might expect to observe increasing  $G$ -values with hydration and temperature for the DCB tests. Therefore, the decreases in peak stresses and total work to failure with increasing temperature in SS tests correlate with lowered SC cohesive strength.

In comparison to the FH specimens, the DH SC exhibited far smaller changes in fracture energy and peak cohesive strength with increasing temperature, suggesting that the cohesive strength is strongly hydration dependent and more weakly associated with testing temperature. One possible explanation is related to the microstructure of the SC layer itself. In a simplistic model of the SC structure proposed by Elias et al.<sup>10</sup>, the cells are viewed as highly keratinized bricks surrounded by a lipid mortar as represented in Fig. 1. In this model, behavior of the SC is presumed to be dominated by the properties of the lipids, particularly since the composition of the extracellular components are estimated to be at least 80 wt.% lipid.

Examination of the SEM micrographs reveals little overall difference in the extent of cellular pullout for the DH SC tissue tested at different temperatures suggesting that this feature of the debonding process is temperature independent. The FH specimen surfaces consistently remained quite featureless throughout the range of testing temperatures despite a large decrease in  $G_c$  values with increasing temperatures. Clearly, cellular pullout during debonding is therefore dependent on the initial hydration of the SC tissue. However, the lack of any significant morphological changes on the fracture surfaces of the FH specimens despite a correspondingly strong decrease in debond energy suggests that temperature must affect underlying processes that control the peak cohesive strength.

To better understand the possible effects of underlying SC structure upon the observed mechanical behavior, selected studies are briefly reviewed. X-ray diffraction (XRD) analysis of human SC revealed a crystalline structure associated with the lipids sheathing the keratin filaments that lie in the plane of the SC layer.<sup>11</sup> These results together with in-plane dynamical mechanical analysis (DMA) revealed hydration independent transitions that are attributed to lipid conformational changes from a crystalline to more disordered state.<sup>2</sup> Additionally, differential scanning calorimetry (DSC) analyses suggest that the presence of strong endothermic dips in the gathered data indicate transitions in the SC due to variations in water content; the in-plane modulus was also observed to decrease with increased testing humidity.<sup>3</sup> From the DSC analysis these changes were attributed to keratin fiber relaxation due to substitution of existing protein-protein hydrogen bonds with water-mediated bonding facilitating greater fiber mobility, as these bond substitutions would lead to a reduction in modulus with increasing hydration level.

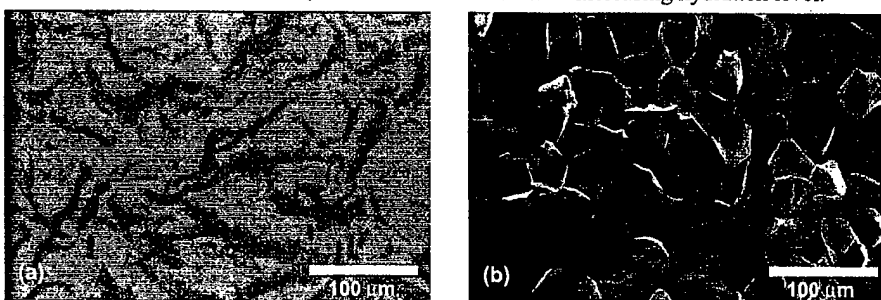


Figure 4. Scanning electron micrographs of DCB specimens: Fully hydrated (a) and Dehydrated (b) samples tested at 25°C.

While the mechanisms responsible for the out-of-plane properties are different, some insight can be gathered from the analyses reported above. As suggested by Papir et al.<sup>3</sup>, the ability of water molecules to substitute for existing hydrogen bonds may lead to strength degradation. Thus, while the lipid transitions may be hydration independent as indicated by XRD tests, mechanical degradation may require the presence of water to facilitate loss of structural integrity and cohesive strength; so, the proportionally smaller decreases in fracture energies and peak stresses in the DH samples may be explained by the lack of hydration available to mediate weakening mechanisms. Additionally, the decreases in fracture energy with increasing temperature may be a result of greater accessibility of hygroscopic sites to water molecules leading to bond substitution as the lipid structure becomes more disorganized.

Furthermore, in contrast to in-plane modulus data, the moduli measured during SS testing reveal a behavior that is quite distinct from the changes observed during in-plane testing.<sup>3,4</sup> The modulus values shown in Fig. 3 indicate little variation with hydration or temperature although the cohesive strengths of the samples decrease as seen in the reported total work to failure. While the abrupt decrease in out-of-plane modulus (Fig. 3(d)) may seem anomalous, the measured value can be explained upon closer examination of the SS curves. The SC exhibits an increase in stiffness for separations less than  $\sim 10 \mu\text{m}$ , but due to substantially decreased cohesive strength, the FH SC tested at  $75^\circ\text{C}$  begins to fail before stiffening occurs.

Comparing in-plane with out-of-plane mechanical properties reveals that the simplistic model proposed by Elias et al.<sup>10</sup> requires refinement to explain the results presented here. For example, the in-plane tensile tests performed by Papir et al.<sup>3</sup> on newborn rat SC led to measurements of decreasing elastic moduli ranging from  $\sim 8.87 \text{ GPa}$  to  $12 \text{ MPa}$  with increasing humidity at constant temperature while similar tests by Wildnauer et al.<sup>4</sup> upon human SC revealed moduli decreasing from  $\sim 45 \text{ MPa}$  to  $10 \text{ MPa}$ , assuming a SC thickness of  $40 \mu\text{m}$ . Similar decreases in modulus with increasing temperature were observed as well.<sup>3</sup> These values are starkly different from the out-of-plane measurements of  $\sim 0.7 \text{ MPa}$ . Furthermore, only limited work to measure in-plane fracture properties of human SC as a function of varying environmental conditions has been performed. Koutroupi and Barbenel<sup>5</sup> have measured mean fracture energies of  $3600 \text{ J/m}^2$  for  $\sim 76\%$  RH conditioned SC samples in a tearing configuration, and subsequent work by Nicolopoulos et al.<sup>6</sup> suggests that debond energy increases with increasing hydration, a trend not generally observed in the DCB or SS specimens. Intuitively, the in-plane fracture energy is expected to be higher than that of the natural delamination mode. However, that the fracture energy is orders of magnitude greater than the  $\sim 1-6 \text{ J/m}^2$  measured in delamination tests is surprising.

In the bricks-and-mortar model, the mechanical characteristics of the SC should be the same in both orientations provided the mortar is isotropic. However, the data discussed above indicate that the SC exhibits much tougher in-plane mechanical characteristics as compared to those out-of-plane. While mechanical anisotropy is evident, the mechanisms causing the differences are unclear but may be related to additional SC microstructure. In transmission electron microscope (TEM) studies, remnants of desmosomal structures, or corneosomes, are evident between SC cells.<sup>12</sup> Structurally important in the lower levels of the epidermis, these structures are located where intermediate filaments such as keratin fibers terminate in one cell wall and bridge the intercellular space to connect to adjacent cells. Although the corneosomes are thought to be degraded desmosomes, these structures may facilitate the transmission of tensile forces between cells leading to the greater stiffnesses and higher fracture energies observed in this orientation. Furthermore, considering the alignment of the keratin fibers in the

plane of the SC layer, increased mobility of the fibers with increasing hydration as postulated by Papir et al.<sup>3</sup> represents a reasonable mechanism leading to decreased modulus with increased fiber sliding. Further exploration remains necessary to determine the precise microstructural mechanisms that lead to the observed mechanical properties; however, the bricks and mortar model needs refinement (Fig. 1) in order to capture the true mechanical properties of the SC.

## CONCLUSION

A fracture-mechanics based approach using DCB specimens was developed to examine quantitatively the delamination properties of stratum corneum. In conjunction with out-of-plane stress-separation measurements, a decrease in debond energy with increasing temperature was observed in fully hydrated SC tissue. Little effect of testing temperature was observed for dehydrated SC tissue. The observed decrease in debond energy was associated with a reduction in SC cohesive strength due to hydration-mediated processes. While fracture energy decreases with increasing hydration for tests above 25°C, it remains unclear why G-values are higher for the fully hydrated samples at 10°C. Measurements of modulus obtained while varying temperature and hydration reveal that SC stiffness in this mode is much lower than that reported in-plane. The fracture energy and modulus data reveal that a simple bricks and mortal model requires refinement to explain the highly anisotropic mechanical behavior exhibited by the SC.

## ACKNOWLEDGMENTS

The authors would like to thank Nieves Crisologo and Mrudula Patel from ALZA Corporation for their technical assistance in providing the stratum corneum specimens. K.W. supported by a Stanford Graduate Fellowship.

## REFERENCES

1. A.J. Thody and P.S. Friedmann in *Scientific Basis of Dermatology: A Physiological Approach*, edited by A.J. Thody and P.S. Friedmann (Churchill Livingstone, Inc., London, 1986), p. 1-5.
2. G.L. Wilkes and R.H. Wildnauer, *Biochimica et Biophysica Acta* **304**, 276 (1973).
3. Y.S. Papir, K.-H. Hsu, and R.H. Wildnauer, *Biochimica et Biophysica Acta* **399**, 170 (1975).
4. R.H. Wildnauer, J.W. Bothwell, and A.B. Douglass, *The Journal of Investigative Dermatology* **56**, 72 (1971).
5. K.S. Koutroupi and J.C. Barbenel, *Journal of Biomechanics* **23**, 281 (1990).
6. C.S. Nicolopoulos, P.V. Giannoudis, K.D. Glaros, and J.C. Barbenel, *Archives of Dermatological Research* **290**, 638 (1998).
7. M.A. Wolfram, N.F. Wolejsza, and K. Laden, *The Journal of Investigative Dermatology* **59**, 421 (1973).
8. M. B. Taub and R. H. Dauskardt in *Biomaterials for Drug Delivery and Tissue Engineering*, edited by S. Mallapragada, R. Korsmeyer, E. Mathiowitz, B. Narasimhan, and M. Tracy, (Mater. Res. Soc. Proc. **662**, Warrendale, PA, 2001) pp. NN4.9.1-NN4.9.6.
9. K.L. Ohashi, A.C. Romero, P.D. McGowan, W.J. Maloney, and R.H. Dauskardt, *J. Ortho. Res.*, **16**, 705 (1998).
10. P.M. Elias, S. Grayson, M.A. Lampe, M.L. Williams, and B.E. Brown in *Stratum Corneum*, edited by R. Marks and G. Plewig (Springer-Verlag, Berlin, 1983), p. 53-67.
11. G.L. Wilkes, A.-L. Nguyen, and R. Wildnauer, *Biochimica et Biophysica Acta* **304**, 267 (1973).
12. J. Vičanová, A.M. Mommaas, A.A. Mulder, H.K. Koerten, and M. Ponec, *Cell Tissue Research* **286**, 115 (1996).

---

**Organic Biomaterials—  
Proteins and Peptides**

### Biologically-Based Self-Assembling Hydrogels

Brandon L. Seal and Alyssa Panitch  
Department of Bioengineering, Arizona State University  
Tempe, AZ 85287-9709, U.S.A.

#### ABSTRACT

We have developed polymers, which borrowing from biology, assemble into networks. The self-assembly regions of fibrinogen were cloned to form a scaffolding that either interacts with fibrin or assembles independently. Peptides consisting of a binding pocket (BP), ligand (L), and/or a Factor XIIIa substrate were synthesized and conjugated to methacrylated dextran or acrylated poly(ethylene glycol). Peptide-conjugated dextran was added to polymerizing fibrin, and the resulting hydrogels were evaluated rheologically. These conjugates significantly affected the mechanical properties of fibrin while the addition of unconjugated dextran did not. The BP and L peptides were conjugated to PEG star polymer. Mixtures of conjugated PEG-BP and PEG-L were found to assemble. This work shows that peptides directing assembly can be designed using motifs found in proteins. The peptides in this study not only alter the mechanical properties of fibrin, but also allow a mechanism for creating a self-assembling network.

#### INTRODUCTION

As material scientists, we stand to learn a lot from nature as biological molecules form precise structures and geometries. With respect to proteins, the primary structure defines the overall three-dimensional architecture. The resulting secondary, tertiary and, in some cases, quaternary structures are necessary to affect intermolecular interactions and protein function. However, examples exist that suggest that short peptides also can be used to affect biological activity including self-assembly.

Material assembly via peptide motifs has been demonstrated. Petka et al. showed how recombinant coiled-coils flanking a random coil polyelectrolyte induced gelation [1]. Gelation was based on the self-assembly of the coiled-coil regions at a controlled pH or temperature. Wang et al. used coiled-coil homotetramers containing histidine tails, copolymers of methacrylic acid, acrylamide, and N-isopropyl acrylamide, and  $\text{Ni}^{++}$  to form gels. By tailoring the amino acid sequence of the coiled-coil, they could control the gel response to temperature and pH [2].

We have taken another approach. Our goal was to use biological ligand and receptor interactions to guide the assembly of synthetic polymers. By synthesizing short peptide sequences from fibrinogen that are active in the assembly of fibrin from fibrinogen, we have developed molecules that either can assemble with fibrin or can self-assemble to form three-dimensional complexes.

Fibrinogen is a plasma glycoprotein that participates in the coagulation cascade. The mature protein consists of a dimer of two identical subunits composed of  $\alpha$ ,  $\beta$  and  $\gamma$  associated chains; three chains associate through a coiled-coil trimer to form a subunit, and two of these subunits associate to form the mature dimer. The assembly of the three chains [3-4], the mature fibrinogen [5], and polymerization of fibrin from fibrinogen [6-8] have been well characterized.

The crystal structure and essential amino acids of the binding pocket for the  $\alpha$ -chain-ligand also have been characterized. Oxela and Budzynski found that amino acids 373-410 from

the  $\gamma$ -chain inhibited fibrin polymerization by entrapping the  $\alpha$ -chain-ligand; this  $\gamma$ -chain peptide is sufficient to form the binding pocket for the  $\alpha$ -chain with a  $k_D = 1.45 \times 10^{-6}$  M for the peptide versus  $1 \times 10^{-4}$  M for the intact molecule [9]. Horwitz et al. studied a shorter peptide consisting of amino acids 374-396 of the  $\gamma$ -chain and found that this domain does not contain the platelet binding peptide. In addition, this shorter peptide bound to the N-terminal ligand of the  $\alpha$ -chain and was sufficient for formation of the binding pocket [7].

Lorand et al. synthesized a double-headed glycine-proline-arginine-proline, (part of the  $\alpha$ -chain ligand) PEG molecule; they found that this molecule induced dimerization of the D proteolytic fragment, which contains the binding pocket, of fibrinogen [10]. This result indicates that PEG molecules containing this tetrapeptide will associate with the binding pocket.

We describe peptide-conjugated polymers that contain blocks of ligand peptide or binding-pocket peptide. These polymers assemble with ligand and binding pocket on fibrinogen or with ligand and binding pocket peptides coupled to other synthetic polymers. Figure 1 shows a schematic of the proposed artificial protein assembly.

## MATERIALS AND METHODS

### Methacrylation of dextran

Methacrylated dextran was synthesized using published methods [11]. Dextran (MW 40kD) and dimethylaminopyridine (Sigma) were dissolved in dimethylsulfoxide (Sigma) under nitrogen at room temperature. Glycidyl methacrylate (GMA) (Sigma) was added to the mixture to produce GMA-derivatized dextran (dex-GMA). The product was purified by solvent removal and size exclusion chromatography. Aqueous solutions of methacrylated dextran were frozen, lyophilized, and stored at  $-80^{\circ}\text{C}$ . The degree of substitution of the purified product was determined by NMR.

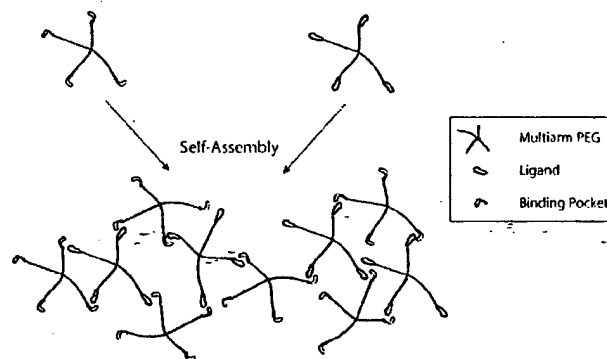


**Figure 1.** A schematic representation of self-assembly using peptide motifs found within fibrinogen. Multifunctional polymers, such as 4-arm poly(ethylene glycol) can be covalently coupled to ligand or binding pocket peptides inspired by motifs in fibrinogen. A combination of PEG-ligand and PEG-binding pocket will form a three-dimensional physical gel that self-assembles in a manner that mimics fibrinogen to fibrin assembly.

### Peptide synthesis

Peptides encoding the binding pocket (BP) from the  $\gamma$ -chain and the ligand from the  $\alpha$ -chain of human fibrinogen as well as substrates for factor XIIIa (Fa XIIIa) (Table I) were synthesized using solid-state Fmoc chemistry in the Arizona State University Protein Chemistry Laboratory. All peptides were purified with a C4 reverse phase preparatory column on an ÄTKA FPLC using a water/acetonitrile gradient. Following elution, the peptides were lyophilized and stored at  $-80^{\circ}\text{C}$ . Peptide identity was confirmed using MALDI-TOF mass spectrometry (Vestec PerSeptive Biosystems).

### Conjugation of peptides to dextran

The following procedure was used to conjugate cysteine-terminated peptide to methacrylated dextran via Michael addition. In separate reactions, a 10 molar excess of each of these peptides was coupled to methacrylated dextran (31% degree of substitution; 40 kD MW) under the following conditions: A solution of dextran was prepared in phosphate buffered saline, 1.5 mM EDTA, pH 7.4. A 10 molar excess of peptide was added to the dextran to create a 20% (w/v) solution. Due to the solubility of the BP peptide, 6 M urea was added to the buffer to allow coupling of BP to dextran. The conjugation reaction proceeded for 2 hours at  $37^{\circ}\text{C}$ . Then, the reaction mixture was dialyzed in 8,000 MWCO dialysis tubing (Spectrum) against MilliQ purified water for 24 hours to remove urea.

### Fibrin gel studies

Bovine fibrinogen (Sigma) was dissolved in deionized water and dialyzed against Tris-buffered saline, pH 7.4. A Bradford assay was used to determine the concentration of the fibrinogen solution. Fibrin gels were made to a final volume of 500  $\mu\text{l}$ , and the final fibrinogen concentration of each gel was 0.6%. BP-conjugated dextran was added to 0.5, 1 or 2%. Dextran-LFaXIIIa and dextran-iLFaXIIIa each were added to a final concentration of 2%. For each gel,  $\text{CaCl}_2$  to 2.5 mM, 1 unit thrombin (Sigma), and 6  $\mu\text{g}$  of factor XIIIa (Enzyme Research Laboratories) were added, and the gels polymerized for 15 minutes at  $37^{\circ}\text{C}$ . Control gels consisted of unmodified 0.6% fibrin gels and 0.6% fibrin gels containing 2% methacrylated dextran that had not been conjugated to peptide. Dynamic mechanical properties were measured using a 20 mm acrylic parallel plate geometry on a TA Instruments AR 1000 rheometer under a 1 Pa stress throughout a 0.1-100 rad/s frequency sweep [12-13]. The mechanical properties of four gels of each type were compared to determine statistical significance using  $\alpha = 0.05$ .

**Table I.** Fibrinogen derived peptides for assembly.

Peptide Function	Amino Acid Sequence*
Binding Pocket (BP)	CGTATWKGSTRWYSMKKTTMKIIPFNRLTIGE
Ligand (L)	<b>G</b> PRPGGC
Ligand + FaXIIIa (LFaXIIIa)	<u>E</u> GGGV <u>R</u> G <u>P</u> RP <u>N</u> <u>Q</u> E <u>Q</u> V <u>S</u> PLPC
Inactive Ligand+FaXIIIa (iLFaXIIIa)	CG <u>Q</u> E <u>Q</u> V <u>S</u> PL <u>G</u> PR <u>P</u> EGGVR

\* Bold letters represent binding pocket or ligand motifs from human fibrinogen. Italicized letters show an amino acid sequence that acts as a substrate for Fa XIIIa. Underlined amino acids indicate a sequence serving as a protective cap (cleaved by thrombin) for the ligand domain.

### Acrylation of poly(ethylene glycol)

Poly(ethylene glycol)-tetraacrylate was prepared from PEG 4-arm star polymer (Shearwater, Inc.,  $M_w = 10,000$ ) using published methods [14]. Briefly, 25 g 4-arm PEG was dried by azeotropic distillation in 100 mL toluene for 4 hours using a Dean-Stark trap. After cooling, the PEG was resuspended in 25 mL dry dichloromethane (Aldrich). The mixture was placed in an ice bath, and 2 equiv. of triethylamine (Aldrich) was added. Then, 1.7 equiv. of acryloyl chloride (Aldrich) was added to initiate the reaction. The reaction continued with stirring overnight in the dark under nitrogen. The resulting solution was extracted twice with 0.1 N HCl, and the organic phase was precipitated by dropwise addition to diethyl ether (ECM) in an ice bath. After recovery by filtration, the precipitate was dried *in vacuo* and stored under nitrogen at -80°C. NMR analysis confirmed complete derivatization of the 4-arm PEG.

### PEG-peptide studies

The synthetic peptide L was combined with acrylated PEG in phosphate-buffered saline, 1.5 mM EDTA, pH 8.0 in a 4:1 molar ratio of peptide to PEG to yield a 1:1 molar ratio of peptide to acrylate group. The peptide BP was conjugated to acrylated PEG in a similar manner; however, the reaction buffer required 6 M urea (Sigma). Each reaction proceeded for 2 hours at 37°C and then was dialyzed against MilliQ water in 8 kD MWCO membrane to remove any unreacted peptide. PEG-BP and PEG-L were combined to make a 5% (w/v) solution that contained equimolar amounts of the two molecules.

## RESULTS

### Fibrin gel studies

Dynamic mechanical properties were measured on fibrin gels and fibrin gels containing dextran or peptide-conjugated dextran. Dextran alone did not significantly affect the mechanical properties of fibrin (Figure 2). For all concentrations studied, the addition of BP-conjugated dextran significantly disrupted the integrity of the fibrin gels indicating association of the BP with the ligand in fibrin (Figure 2). Increasing the amount of BP-conjugated dextran decreased the storage modulus,  $G'$ , of the gel in a dose-dependent manner. Similarly, at 2% concentration, dex-iLFaXIIIa significantly disrupted the integrity of the fibrin gels indicating association of the ligand-conjugated dextran with the binding pocket in fibrin (Figure 2). At 2%, dex-iLFaXIIIa significantly increased  $G'$  of the fibrin gels to 160% base value, indicating association of the Fa XIIIa substrate-conjugated dextran with the fibrin (Figure 2). The increase in  $G'$  with the addition of Fa XIIIa substrate-conjugated dextran is expected based on results by Schense and Hubbell demonstrating that synthetic peptides can be conjugated to fibrin via Fa XIIIa [15]. Since the C-terminal protective cap of iLFaXIIIa cannot be cleaved by thrombin, the ligand domain cannot associate with binding pocket in fibrin. Thus, the Fa XIIIa substrate in dex-iLFaXIIIa serves as the only active domain within the peptide. Although dex-LFaXIIIa contains a Fa XIIIa substrate, the substrate appears not to be crosslinked into the fibrin gel suggesting that the ligand/binding pocket interaction dominates. The lack of Fa XIIIa activity of LFaXIIIa may be due to spatial constraints within the peptide

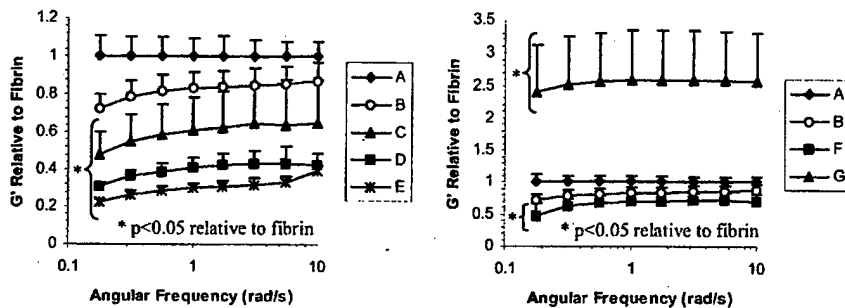


**Figure 2.** The two plots show the elastic modulus,  $G'$ , of the fibrin gels, with or without peptide-conjugate dextran, relative to fibrin as a function of angular frequency for the linear viscoelastic region of 0.6% fibrin gels. For both plots, A=0.6% Fibrin; B=2% Dextran; C=0.5% Dex-BP; D=1% Dex-BP; E=2% Dex-BP; F=2% Dex-LFaXIIIa; G=2% Dex-iLFaXIIIa. As shown in the panel on the left, the BP-conjugated dextran significantly decreased the modulus of fibrin in a dose dependent manner. Dextran alone did not significantly alter  $G'$ . In the panel on the right, the dex-LFaXIIIa significantly disrupted the fibrin gel by competitively binding to the native binding pocket in fibrin. The dex-iLFaXIIIa significantly increased the modulus of fibrin through chemical crosslinking via the transglutaminase activity of factor XIIIa.

limiting the ability of the Fa XIIIa substrate to interact with complementary domains within fibrin. These results suggest that proper ratios of ligand-, BP- and Fa XIIIa substrate-conjugated dextran will associate with and affect the mechanical properties of fibrin clots.

#### PEG-peptide studies

As seen in Figure 3, 5% solutions (w/v) containing only PEG-BP or PEG-L (image not shown) show no evidence of assembly. In contrast, when a 5% solution (w/v) containing equimolar amounts of PEG-BP and PEG-L was observed on a glass microscope slide, the two materials interacted to create a cloudy, viscous suspension. These results suggest a physical self-assembly of the PEG-BP and PEG-L through receptor-ligand interactions. Complete characterization of the association between PEG-BP and PEG-L is ongoing.

#### **CONCLUSIONS**

This work provides the first demonstration that peptide sequences directing ligand-receptor interactions in nature can be used to direct assembly of synthetic polymers. We have shown that synthetic polymers can assemble with other synthetic polymers and biologically-derived macromolecules. Future work will involve the optimization of polymer and peptide content to achieve assembly into hydrogels and other useful motifs.

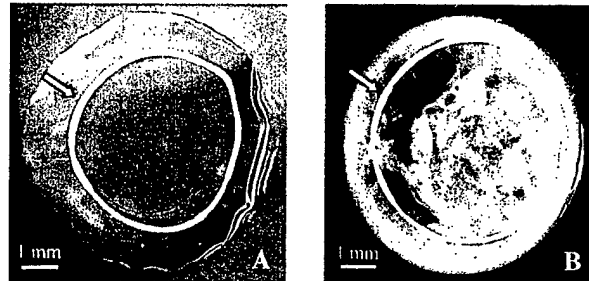


**Figure 3.** Two stereoscopic images of PEG-peptide solutions on a glass slide. Panel A depicts an image of a 5% PEG-BP solution, and panel B shows an image of a 5% solution containing equimolar amounts of PEG-BP and PEG-L. In both A and B, the white circular rings, denoted by the white arrows, are optical artifacts created by the light source of the stereoscope. As panel B shows, a mixture of PEG-BP and PEG-L results in a physical association.

#### ACKNOWLEDGMENTS

This work was supported through the Arizona Disease Control Research Commission contract No. 6018 and a graduate fellowship from the Whitaker Foundation.

#### REFERENCES

1. Petka, W. A., J. L. Harden, K. P. McGrath, D. Wirtz and D. A. Tirrell. *Science* **281**: 389-392 (1998).
2. Wang, C., R. J. Stewart and J. Kopecek. *Nature* **397**: 417-420 (1999).
3. Huang, S., E. R. Mulvihill, D. H. Farrell, D. W. Chung and E. W. Davies. *J. Biol. Chem.* **268**(12): 8919-8926 (1993).
4. Xu, W.-f., D. W. Chung and E. W. Davie. *J. Biol. Chem.* **271**(44): 27948-27953 (1996).
5. Zhang, J.-Z. and C. M. Redman. *J. Biol. Chem.* **271**(21): 12674-12680 (1996).
6. Shimizu, A., G. M. Nagel and R. F. Doolittle. *Proc. Nat. Acad. Sci.* **89**: 2888-2892 (1992).
7. Horwitz, B. H., A. Varadi and H. A. Scheraga. *Proc. Nat. Acad. Sci.* **81**: 5980-5984 (1994).
8. Cote, H. C. F., K. P. Pratt, E. W. Davie and D. W. Chung. *J. Biol. Chem.* **272**(38): 23792-23798 (1997).
9. Olexa, S. A. and A. Z. Budzynski. *J. Biol. Chem.* **256**(7): 3544-3549 (1981).
10. Lorand, L., K. N. Parameswaran and S. N. P. Murthy. *Proc. Nat. Acad. Sci.* **95**: 537-541 (1998).
11. van Dijk-Wolthuis, W., M. van Steenbergen, W. Underberg and W. Hennink. *J. Pharm. Sci.* **86**: 413-417 (1997).
12. Chambon, F. and H. H. Winter. *Pol. Bul.* **13**: 499-503 (1985).
13. Tung, C.-Y. M. and P. J. Dynes. *J. Appl. Poly. Sci.* **27**: 569-574 (1982).
14. Hastyberg, S., A. Panitch, S. Rizzi, H. Hall and J. A. Hubbell. *Biomacromolecules* In Press (2002).
15. Schense, J. C. and J. A. Hubbell. *Bioconj. Chem.* **10**(1): 75-81 (1999).

### Self-Assembly of a Modular Polypeptide based on Blocks of Silk-Mimetic and Elastin-Mimetic Sequences

Chrystelle S. Cazalis, and Vincent P. Conticello\*  
Department of Chemistry, Emory University, Atlanta, GA 30322

#### ABSTRACT

Spider dragline silk fiber displays a unique and technologically significant combination of high tensile and compressive strength. The structural origin of these properties arises from the alternating sequence of crystalline alanine-rich domains and amorphous glycine-rich domains, which undergo microscopic phase separation in the silk fiber. We previously reported the synthesis and the self-assembly of a novel polypeptide 1, which emulates the modular structure of crystalline and amorphous elastomeric domains in dragline silk proteins. The sequence of this polypeptide comprises an alternating arrangement of a self-complementary, amphiphilic silk-mimetic oligopeptide (Ala-Glu-Ala-Glu-Ala-Lys-Ala-Lys) and environmentally-responsive elastin-mimetic segment (Val-Pro-Gly-Val-Gly). We report herein the synthesis and the self-assembly of an analogous polypeptide (2) with a higher content of elastin mimetic pentapeptides. A synthetic gene encoding four repeats of the alternating sequence was expressed in *E. coli* strain BL21(DE3) as a C-terminal fusion to a decahistidine leader sequence to afford a polypeptide with a molar mass of approximately 39 kDa. The regularly alternating pattern of elastin-mimetic and silk-mimetic blocks within the protein allowed the copolymer to spontaneously self-assemble upon heating above the phase transition of the elastin-mimetic block. The self-assembly process was studied using a combination of CD and solid-state NMR spectroscopy, which suggested that the alanine-rich domains undergo a conformational rearrangement from  $\alpha$ -helix to  $\beta$ -sheet. This rearrangement coincides with the macromolecular phase transition of the elastin-mimetic domains, which resulted in irreversible aggregation of the polypeptide above the  $T_g$  of the elastin-mimetic domains.

#### INTRODUCTION

Spider dragline silk fiber has attracted much scientific interest due to its unique and technologically significant combination of high tensile and compressive strength<sup>1</sup>. Dragline silk proteins are composed of alternating sequences of conservatively substituted alanine-rich and glycine-rich oligopeptide segments<sup>2</sup>. Recent spectroscopic<sup>3,4</sup> and X-ray diffraction<sup>5</sup> studies of *N. clavipes* dragline fiber suggest that individual chain segments of the silk fibroins segregate into conformationally asymmetric domains and that this mosaic structure underlies the tensile properties of the fiber<sup>6</sup>. The alanine-rich domains adopt a  $\beta$ -strand<sup>4,7</sup> conformation that may aggregate into either weakly oriented individual sheets or highly oriented crystallites within the fiber. In contrast, the glycine-rich domains form a flexible, amorphous matrix that is responsible for the elasticity of the fiber<sup>7</sup>. The well-defined modular structure of these proteins<sup>8</sup> suggests potential opportunities for engineering of novel protein polymers based on dragline silk sequences that emulate the properties of natural materials while enhancing the *in vitro* processing characteristics. We have previously reported the design and biosynthesis of a hybrid silk in which the native alanine-rich domain of *A. diadematus* fibroin 3 was replaced with the

amphiphilic oligopeptide sequence [(Ala-Glu-Ala-Glu-Ala-Lys-Ala-Lys)<sub>2</sub>]<sup>9</sup>. This oligopeptide segment undergoes an irreversible rearrangement from  $\alpha$ -helix to  $\beta$ -strand, which drives the self-assembly of the polypeptide into a macroscopic membrane. Later we reported the synthesis and self-assembly of a copolymer incorporating this cross-linkable module (**HB**) into an elastin-mimetic polypeptide sequence (**SB**)<sup>10</sup>. We describe herein the synthesis of a analogous block copolymer (**2**) with a molar mass of approximately 39 kDa, using recombinant DNA techniques and bacterial protein expression, that self-assembles through formation of  $\beta$ -sheet segments mediated by the amphiphilic peptides. This polypeptide differs from the previously reported material in that the ratio of elastin-mimetic domains to silk-mimetic domains within the repeat sequence has been increased in order to assess the effect of relative composition on the self-assembly process.

## EXPERIMENTAL DETAILS

All chemical reagents were purchased from either Fisher Scientific (Pittsburgh, PA) or Sigma Chemical Corporation (St. Louis, MO) unless otherwise specified. All enzymes were obtained from New England Biolabs, Inc. (Beverly, MA). Plasmid pZErO<sup>TM</sup>-1.1, *E.coli* strain TOP10F' and Zcycin<sup>TM</sup> were purchased from Invitrogen Corporation (Carlsbad, CA). Plasmid pET-19b and *E.coli* strain BL21(DE3) were obtained from Novagen (Madison, WI). Synthetic oligonucleotides were from Genosys Biotechnologies, Inc. (The Woodlands, TX). TALON metal affinity resin was purchased from CLONTECH Inc. (Palo Alto, CA). The isotopically labeled amino acid [ $1-^{13}\text{C}$ ]alanine was obtained from Cambridge Isotope Laboratories, Inc. (Andover, MA).

DNA sequences analyses were performed on a Perkin-Elmer ABI Prism model 377 DNA sequencer. Amino acid compositional analyses were obtained from the Microchemical Facility of the Winship Cancer Center at Emory University. MALDI-TOF mass spectrometry data were performed on an Applied Biosystem Voyager-DE<sup>TM</sup> STR Biospectrometry<sup>TM</sup> Workstation MALDI-TOF Mass Spectrometer. Protein electrophoresis was performed on 10-15% gradient discontinuous SDS polyacrylamide gels on a PhastSystem from Amersham Pharmacia Biotech and visualized via a silver staining procedure.

Circular dichroism (CD) spectra were recorded on a Jasco J-715 spectropolarimeter. Protein samples were dissolved in sterile water at a concentration of 0.6 mg/mL. Spectra were obtained from 260 nm to 180 nm at a scanning rate of 20 nm/min with a resolution of 0.1 nm and a path length of 0.05 cm.

Solid-state CP/MAS <sup>13</sup>C spectra were recorded on a Bruker DSX 400 spectrometer (100.6 MHz, <sup>13</sup>C). Solid-state <sup>13</sup>C chemical shifts were referenced to the methylene carbons of external adamantane (31.26 ppm) and reported relative to the methyl resonances of an external sample of aqueous 2,2-dimethyl-2-silapentane-5-sulfonate (DSS) (0 ppm).

## DISCUSSION

### Biosynthesis of the protein copolymer

The protein copolymer was biologically synthesized as previously described<sup>10</sup>. Briefly, self-ligation of DNA encoding for elastin-mimetic block (Figure 1d) afforded a population of

concatemeric genes, encoding fragments with termini that were compatible with the proximal (Figure 1b) and distal (Figure 1c) HB fragments. The concatemers were joined together with the HB fragments and inserted into the plasmid pZErO-1.1. A recombinant clone was isolated that encoded three repeats of the SB sequence between the HB segments, which was verified by DNA sequence analysis. The DNA monomer cassette was excised by restriction digestion with endonuclease *Sap* I. Self-ligation of the monomer afforded a population of concatemers, which were inserted between the *Sap* I sites of a modified polylinker (Figure 1e) introduced into expression plasmid pET-19b. A recombinant clone was isolated that encoded four repeats of the monomer, which was verified by DNA sequence analysis. The plasmid encoding the copolymer gene was introduced into competent cells of *E. coli* strain BL21(DE3). Expression under the induction of 1 mM IPTG in LB medium afforded the target protein as a C-terminal fusion to a short leader sequence containing a decahistidine tag. Electrophoretic analysis of the whole cell lysate as a function of time indicated the gradual accumulation of new protein during a 3 hr induction period. The fusion protein was isolated from the bacterial cell lysate by immobilized metal affinity chromatography and the homogeneity of the protein was confirmed via 10-15% gradient discontinuous SDS polyacrylamide gel electrophoresis. The yield of lyophilized protein is 35 mg per liter cell culture. Amino acid compositional analysis and MALDI-TOF mass spectrometry were consistent with the expected sequence of the protein polymer.

**a**  
 Ala-Glu-Ala-Glu-Ala-Lys-Ala-Lys-(Ser-Glu-Ala-Glu-Ala-Lys-Ala-Gly-Gly-Val-[Pro-Gly-Val-Gly-Val-Pro-Gly-Val-Gly-Ile-Pro-Gly-Phe-Gly-Val-(Pro-Gly-Val-Gly-Val)<sub>2</sub>]<sub>3</sub>-Pro-Gly-Val-Gly-Gly-Ala-Glu-Ala-Glu-Ala-Lys-Ala-Lys)-Ser-Glu-Ala-Glu-Ala-Lys-Ala-Ala

**b**  
 Ser Glu Ala Glu Ala Lys Ala Lys Ala Gly Gly Val  
 AGCCTC CGA CTT CGA TTC CGC TTT CGA CCG CCA CAT  
 TCGGAG GCT GAA GCT AAG GCG AAAG GCT GGC GGT GTA

**c**  
 Pro Gly Val Gly Gly Ala Glu Ala Lys Ala Lys  
 CCTGGT GTT GGC GGT GCA GAA GCT GAA GCC AAG GCT AAG  
 GGACCA CAA CCG CCA CGT CTT CGA CTT CGG TTC CGA TTC

**d**  
 Pro Gly Val Gly Val Pro Gly Val Gly Ile Pro Gly  
 CCT GGT GTT GGC GAT CGGGGT GTT GGC ATC CCA GGC  
 GGACCA CAA CCG CTA GGC CCA CAA CCG TAG GGT CCG

**e**  
*Nde* I site  
 5'- CAT ATG GCA GAA GCT GAA GCC AAG GCT AAG TCG  
 TA TAC CGT CTT CGA CTT CGG TTC CGA TTC ACT  
 Ala Glu Ala Glu Ala Lys Ala Lys Ser  
*Sap* I site *Sap* I site  
 TGA AGA GCG GTA CCA TGC TCT TCA TCG GAG GCT GAA  
 ACT TCT CGC CAT GGT ACG AGA AGT AGC CTC CGA CTT  
 Stop Arg Ala Asp Pro Cys Ser Ser Glu Ala Glu  
*Bam* H I site  
 GCT AAG GCG AAA GCT TGA GGA TCC -3'  
 CGA TTG CGC TTT CGA ACT CCT AG  
 Ala Lys Ala Lys Ala Stop

**Figure 1.** Amino acid sequence of protein 2 (a), and the double stranded DNA sequences of silk-mimetic HB blocks (b and c), elastin-mimetic SB block (d), and the adaptor gene (e).

### Temperature-Dependent Phase Behavior

Elastin-mimetic protein polymers  $[(\text{Val-Pro-Gly-Xaa-Gly})_n]$  in aqueous solution display reversible phase separation above a lower critical solution temperature  $T_c$ . This process coincides with a conformational rearrangement of the pentapeptide segments from random coil to type II  $\beta$ -turn. The turbidimetric profiles of the protein **2** in aqueous solution at 400 nm (3°C/min) show that the protein is soluble at 25°C, but aggregated as the temperature was raised (Figure 2). The development of turbidity depended on the concentration of **2** as was observed for elastin-mimetic protein polymers (Figure 3)<sup>11</sup>. A linear dependence between  $T_{\text{onset}}$  and the logarithm of the concentration was observed, which indicated that the transition involves more than one polypeptide chain<sup>12</sup> (Figure 3). These results suggested that the elastin-mimetic segments of protein polymer **2** undergo conformational rearrangement upon heating above  $T_c$ . However, the inverse temperature transition is irreversible since the precipitated polymer does not redissolve at temperatures below  $T_c$ . The hydrophobic collapse of the elastin-mimetic blocks above  $T_c$  apparently drives an irreversible conformational modification within the silk-mimetic blocks. The overall transition temperature of protein **2** is much higher than that observed for protein **1**<sup>10</sup>. For example, at a concentration of 1 mg/ml, the onset of phase separation occurs at 38°C for protein **1** but at 50°C for protein **2**. This difference may be due to the lower molar mass of **2**, which corresponds to a lower total content of elastin-mimetic pentapeptides in comparison to **1** (61 pentapeptides per chain *versus* 111 pentapeptides per chain).

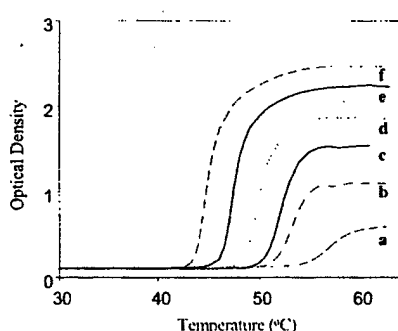


**Figure 2.** Temperature-dependent turbidity profiles for solutions of protein **2** in water at 400 nm (3°C/min) at different concentration: (a) 0.25 mg/ml, (b) 0.50 mg/ml, (c) 0.66 mg/ml, (d) 1.00 mg/ml, (e) 2.00 mg/ml, (f) 3.40 mg/ml.

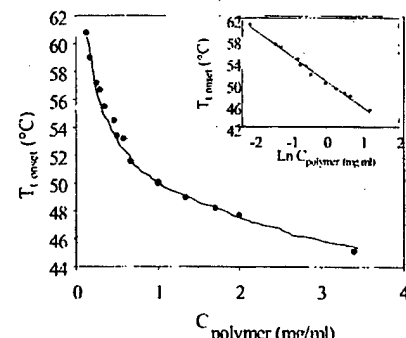


**Figure 3.** Correlation of the  $T_{\text{onset}}$  with the concentration of protein **2** in water ( $C_{\text{polymer}}$  (mg/ml)). Turbidimetry experiments were recorded at 400nm with a scan rate of 3°C/min.

### Conformational behavior of polypeptide **2**

*In situ* CD studies were performed on a solution of the protein polymer **2** in water at various temperatures to interrogate the conformational behavior of the polypeptide as the temperature is raised through the phase transition (Figure 4). The CD spectrum initially displayed absorptions that corresponded to those that are typically observed in the spectra of  $\alpha$ -helical proteins<sup>13</sup>. As the temperature was raised to 65°C, the CD spectra changed significantly in

a manner that was consistent with formation of  $\beta$ -sheet structure<sup>14</sup>. Moreover, specimen did not revert back to the original spectrum upon cooling to ambient temperature, but remained in the  $\beta$ -sheet conformation that was characteristic of the CD spectra at higher temperatures (58°C and 65°C). These data suggest that segments with polypeptide 2 undergo an irreversible  $\alpha$ -helix to  $\beta$ -sheet transition that coincides with the phase transition in the elastin-mimetic domains.

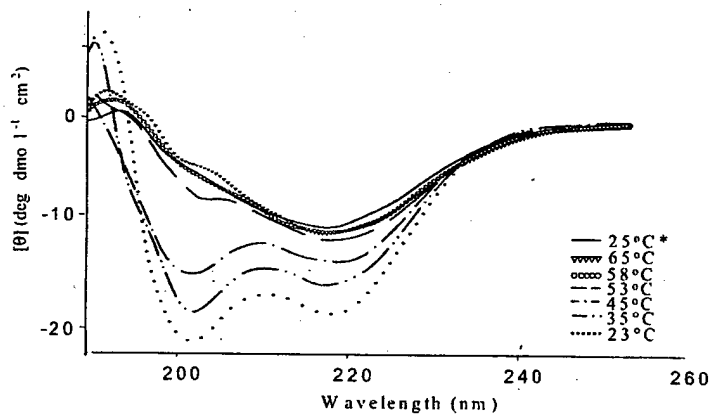


**Figure 4.** Circular dichroism spectra of protein 2 in water (0.6 mg/ml) as a function of temperature.

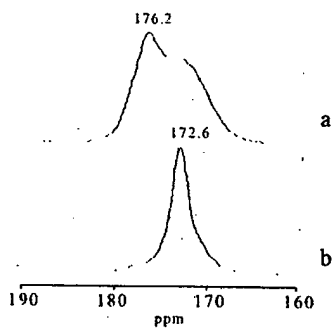


**Figure 5.** Expansion of the amide carbonyl region within the solid state <sup>13</sup>C CP/MAS NMR spectra of lyophilized specimen of 2 (a) and the corresponding heat-treated material (b).

CP/MAS NMR spectroscopy was employed to study the conformation of structural domains within 2 that were site-specifically labeled with NMR-active isotopes. Protein 2 was labeled with the <sup>13</sup>C isotope at carbonyl positions of the alanine residues using a procedure similar to that employed for the unlabeled polypeptides. The solid-state <sup>13</sup>C NMR spectrum of a nascent specimen of protein 2 revealed a resonance at 176.2 ppm (Figure 5), which is within the expected range for an  $\alpha$ -helical conformation for the alanine residues within the silk-mimetic

---

domains (cf.  $\alpha$ -polyalanine, 176.4 ppm)<sup>14,4</sup>. This result was consistent with the previous CD spectroscopic results, which indicated the presence of  $\alpha$ -helices prior to self-assembly. The upfield shoulder of this resonance may reflect the contribution of lyophilization-induced  $\beta$ -sheet formation, which has been observed for similarly treated dragline silk proteins<sup>4</sup>. The  $^{13}\text{C}$  CP/MAS NMR spectrum of a specimen of protein 2 heated above the phase transition of the clastin-mimetic domain indicated that the alanine carbonyl resonance had shifted upfield to 172.6 ppm, which is within the expected range for a  $\beta$ -sheet conformation (cf. polyalanine 171.8 ppm)<sup>14</sup>. These data suggested that the alanine rich block experienced on the  $\alpha$ -to- $\beta$  transition, as consequence of the phase transition of the clastin-mimetic domains.

## CONCLUSIONS

A polypeptide multiblock copolymer 2 based on elastin- and silk-mimetic peptide sequences was successfully synthesized via genetic engineering methodology. The elastin-mimetic domains undergo a phase transition in aqueous solution as the temperature is increased. The onset of the phase transition depends on the concentration of the polypeptide. The phase separation of the elastin-mimetic domains induces a conformational transition in the silk-mimetic domains, which results in irreversible aggregation of the polypeptide.

## ACKNOLEGDMENTS

The authors acknowledge the support of NSF grant CHE-9875776.

## REFERENCES

1. L. W. Jelinski, *Biomaterials*, **3**, 237 (1998)
2. (a) R. Beckwwitt, S. Arcidiacono, R. Stote, *Insect Biochem. Mol. Biol.*, **28**, 121 (1998). (b) P. A. Guerette, D. G. Ginzinger, B. H. F. Weber, J. M. Gosline, *Science*, **272**, 112 (1996).
3. (a) D. H. Hijirida, K. G. Do, S. Wong, D. Zax, L. W. Jelinski, *Biophys. J.*, **71**, 3442, (1996). (b) A. H. Simmons, C. A. Michal, L. W. Jelinski, *Science*, **271**, 84 (1996). (c) A. H. Simmons, E. Ray, L. W. Jelinski, *Macromolecules*, **27**, 5235 (1994).
4. C.A. Michal, L. W. Jelinski, *J. Biomol. NMR* **12**, 231 (1998).
5. D. T. Grubb, L. W. Jelinski, *Macromolecules*, **30**, 2860 (1997).
6. Y. Termonia, *Macromolecules*, **27**, 7378 (1994).
7. J. O. Warwicker, *J. Mol. Biol.*, **2**, 350 (1960).
8. C. Y. Hayashi, N. H. Shipley, R. V. Lewis, *Int. J. Biol. Macromol.*, **24** 271(1999).
9. Y. Qu, S. C. Payne, R. P. Apkarian, V. P. Conticello, *J. Am. Chem. Soc.*, **122**, 5014 (2000)
10. C. Cazalis, V. P. Conticello, *Abstr. Pap. Am. Chem. Soc.* 211: 591-PMSE Part 2 (2001).
11. D. W. Urry, T. L. Trapani, K. U. Prasad, *Biopolymers*, **24**, 2345 (1985).
12. L. A. Marky, K. J. Breslauer, *Biopolymers*, **26**, 1601 (1987).
13. C. W. Jr. Johnson, *Proteins*, **7**, 205 (1990)
14. H. Saito, *J. Biomol. NMR*, **5**, 67 (1995).

**Interface Engineering,  
Patterning and Biocompatibility**

### **In Vitro Vascular Cell Adhesion and Proliferation on Alkaline Degraded Poly-lactic/glycolic Acid Polymers**

Thomas J. Webster, Derick C. Miller, Anil Thapa, and Karen M. Haberstroh  
Department of Biomedical Engineering, Purdue University  
West Lafayette, IN 47907-1296

#### **ABSTRACT**

The objective of the present in vitro study was to determine vascular endothelial and smooth muscle cell responses to poly(lactic-co-glycolic acid) (PLGA) films that were exposed *a priori* to various degrees of alkaline degradation. To model the alkaline environment of blood in arteries, PLGA films were separately soaked in select concentrations (from 0.1 – 10 N) of NaOH for various periods of time (from 10 minutes to 1 hour). Vascular endothelial and smooth muscle cells were then separately allowed to adhere and/or proliferate on the different PLGA degraded surfaces. Results provided the first evidence that smooth muscle adhesion and proliferation increased with larger amounts of alkaline PLGA degradation. In contrast, endothelial cell adhesion and proliferation decreased with increasing amounts of alkaline PLGA degradation. In this manner, the present in vitro study suggests a possible mechanism for insufficient endothelialization on PLGA vascular implants *in vivo*.

#### **INTRODUCTION**

Biodegradable polymers (such as poly(lactic acid), poly(glycolic acid), and poly(lactic-co-glycolic acid)) have become attractive candidates in vascular tissue engineering [1-4]. Such polymeric scaffolds can be easily shaped into grafts to serve as three-dimensional substrates capable of promoting vascular tissue ingrowth. Moreover, it is hoped that these biologically resorbable scaffolds will dissolve *in situ* and leave behind a regenerated neo-vascular conduit. Unfortunately, to date, polymer scaffolds containing poly(lactic acid) have not lived up to their potential [1, 2]. Formation of fibrovascular tissue in the intima of implanted grafts often leads to intimal hyperplasia which has resulted in occlusion of the regenerated vascular tissue [1, 2]. Since an endothelial cell lining often fails to develop on the luminal surface of polymers that contain poly(lactic acid), no regulatory mechanisms exist to minimize fibrovascular tissue ingrowth [1]. Clearly, the inability of poly(lactic acid) containing polymers to promote sufficient endothelialization presents serious limitations for this polymer as a successful vascular prosthetic material [1, 2]. The goal of this research was to determine, for the first time, in vitro vascular endothelial and smooth muscle cell responses (specifically, adhesion and proliferation) to poly(lactic-co-glycolic acid) at various stages of alkaline degradation, similar to the degradation which would be experienced *in vivo*, in order to better understand cellular events that lead to previously observed [2] insufficient endothelialization.

---

## MATERIALS AND METHODS

### Substrates

#### *Poly(lactic-co-glycolic acid) (PLGA)*

PLGA (50/50 weight % poly(lactic acid)/poly(glycolic acid), Polysciences, Inc.) samples were prepared by dissolving (at 50-60 °C) 0.5g of PLGA in 8ml chloroform. This solution was poured into glass petri dishes, allowed to sit overnight, and then transferred to a vacuum (15mm Hg) oven for 2 days at room temperature. The resulting film was cut into either 0.5 cm x 1 cm or 1 cm x 1 cm strips. The polymer strips were treated in three ways to simulate various stages of biodegradation: untreated (non-degraded); 0.1 N NaOH for 10 minutes (partially degraded); and 10 N NaOH for 1 hour (extensively degraded). Polymer strips were sterilized by exposure to UV light for 2 hours followed by soaking in ethanol for 24 hours.

#### *Glass*

Borosilicate glass coverslips (Fisher) were used as a reference substrate in experiments with cells. Coverslips were degreased in acetone and ethanol, etched in 10 N NaOH for 1 hr, and sterilized in an autoclave before use [5].

#### *Cells*

Rat aortic smooth muscle cells and rat aortic endothelial cells were purchased from VEC Technologies and used without further characterization. Smooth muscle cells were cultured in Dulbecco's Modified Eagle's Medium (DMEM, Hyclone) supplemented with 10% Fetal Bovine Serum (FBS, Hyclone) and 1% Penicillin/Streptomycin (P/S, Hyclone), while endothelial cells were cultured in MCDB-131 Complete Medium (VEC Technologies). All cells were maintained under standard cell culture conditions (that is, a sterile, humidified, 95% air, 5% CO<sub>2</sub>, 37 °C environment). Population numbers (for both cell lines) used in experiments were between 6 and 10.

### Experiments

#### *Adhesion on Polymer Substrates*

Endothelial and smooth muscle cells were seeded separately (3500 cells/cm<sup>2</sup> in either MCDB-131 Complete Medium or DMEM supplemented with 10% FBS and 1% P/S, respectively) onto various PLGA films and were allowed to adhere for 4 hours under standard cell culture conditions. Non-degraded (untreated) polymer substrates were used as controls.

#### *Proliferation on Polymer Substrates*

Endothelial and smooth muscle cells were seeded separately (3500 cells/cm<sup>2</sup> in either MCDB-131 Complete Medium or DMEM supplemented with 10% FBS and 1% P/S, respectively) onto various PLGA films and were allowed to proliferate for 1, 3, and 5 days under standard cell culture conditions. Non-degraded (untreated) polymer substrates were used as controls.

### **Staining and Counting**

At the end of the prescribed time periods, all substrates were rinsed in phosphate buffered saline to remove non-adherent cells, fixed in 10% formalin, and stained with 0.1% Coomassie Brilliant Blue. The number of cells in each of five random fields per substrate were counted using a light microscope, averaged, and recorded as cell density (cells/cm<sup>2</sup>). Experiments were run in triplicate and repeated at least three separate times.

## **RESULTS**

### *Adhesion on PLGA*

Compared to non-degraded (untreated) PLGA, vascular endothelial cell adhesion decreased significantly ( $p < 0.05$ ) on the extensively degraded PLGA formulations after 4 hours (Figure 1). Specifically, endothelial cell density was two times less on the extensively degraded, compared to non-degraded, PLGA. In contrast, smooth muscle cell adhesion was significantly ( $p < 0.05$ ) enhanced on extensively degraded PLGA compared to non-degraded PLGA after 4 hours (Figure 1). Cell density ranged from 1,036 cells/cm<sup>2</sup> for the non-degraded PLGA to 1,433 cells/cm<sup>2</sup> for extensively degraded PLGA.

### *Proliferation on PLGA*

Compared to non-degraded (untreated) PLGA, results provided evidence that endothelial cell proliferation decreased ( $p < 0.05$ ) on extensively degraded PLGA compared to non-degraded PLGA at every time point tested in the present study (Figure 2). For example, after 5 days of culture, the number of endothelial cells decreased by approximately one half on extensively degraded compared to non-degraded PLGA. In contrast, smooth muscle cell proliferation increased ( $p < 0.01$ ) on extensively degraded PLGA formulations after 3 and 5 days of culture (Figure 3). Specifically, the number of smooth muscle cells was two and four times greater on extensively degraded compared to non-degraded PLGA after 3 and 5 days, respectively.

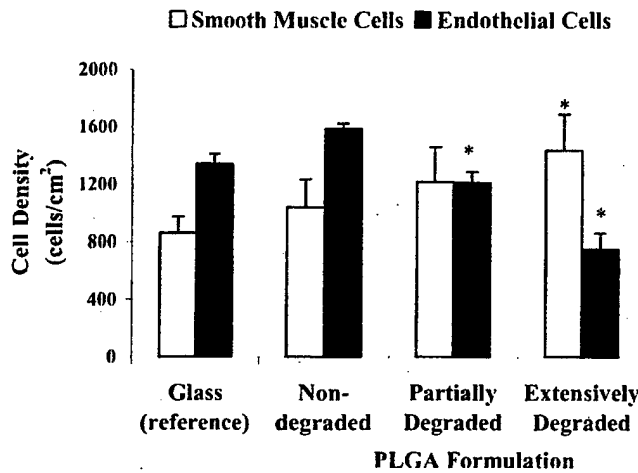


**Figure 1.** Enhanced Smooth Muscle Cell and Decreased Endothelial Cell Adhesion on Extensively Degraded PLGA. Data are mean  $\pm$  SEM;  $n = 3$ ; \*  $p < 0.05$  (compared to respective adhesion on non-degraded, or untreated, PLGA).

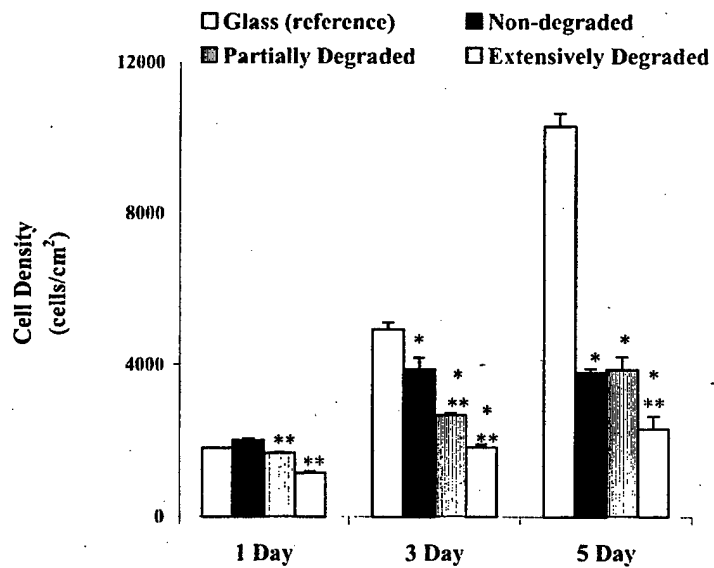


**Figure 2.** Decreased Endothelial Cell Proliferation on Extensively Degraded PLGA. Data are mean  $\pm$  SEM;  $n = 3$ ; \*  $p < 0.01$  (compared to proliferation on respective PLGA after 1 day); \*\*  $p < 0.05$  (compared to proliferation on non-degraded, or untreated, PLGA at respective day).

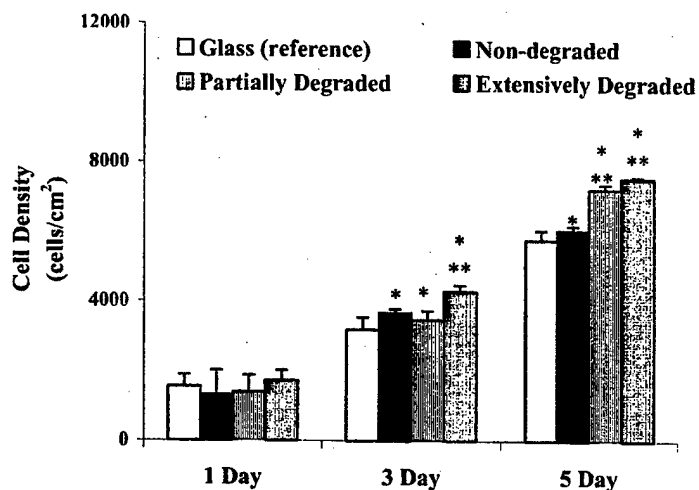


**Figure 3.** Enhanced Smooth Muscle Cell Proliferation on Extensively Degraded PLGA. Data are mean +/- SEM; n = 3; \*  $p < 0.01$  (compared to proliferation on respective PLGA after 1 day); \*\*  $p < 0.05$  (compared to proliferation on non-degraded, or untreated, PLGA at respective day).

#### DISCUSSION AND CONCLUSIONS

The present study sought to model alkaline degradation of PLGA as would be experienced by this polymer when exposed to blood in arteries [6]. This was accomplished by soaking PLGA in select concentrations of NaOH for specific periods of time, thereby developing a partially degraded and extensively degraded PLGA film. Gao et al. [4] previously described the hydrolysis procedure by which poly(glycolic) acid (PGA) meshes degrade in an alkaline environment. Briefly, hydroxide anions from NaOH hydrolyze the ester bond on the surface of the PGA mesh, thereby exposing carboxylic acid and hydroxyl groups by breaking the polymer chain. This process happens at various locations in the polymer leading to multiple-chain hydrolysis depending upon access of hydroxide ions to the polymer chains. Such hydrolysis may result in degradation of the polymer into oligomeric or monomeric forms whereby NaOH is able to further dissolve portions of the polymer fibers.

Since PLGA is also a poly (ester), we expected to observe similar interactions between the hydroxide ions of NaOH and the ester bonds of this polymer during the alkaline degradation events used in the present study. Results of endothelial cell experiments demonstrated, for the first time, that these cells adhere and proliferate better on non-degraded, compared to degraded, PLGA. In contrast, smooth muscle cells adhere and proliferate to a greater extent on degraded rather than non-degraded PLGA. Increased spreading of vascular smooth muscle cells have been

---

previously observed on PGA treated with NaOH [4]. However, this is the first study to report increased vascular smooth muscle cell adhesion and proliferation, as well as decreased functions of endothelial cells, on PLGA polymers treated with increasing concentrations of and exposure to NaOH. This information suggests that as PLGA degrades under alkaline blood conditions in the artery, smooth muscle cell functions will be enhanced while endothelial cell functions will be inhibited. Although it is not clear at the time whether altered vascular cell function is due to topographical or chemical changes in PLGA as alkaline degradation occurs, it is clear that successful endothelialization of degrading PLGA will require use of different polymer formulations.

#### ACKNOWLEDGEMENTS

The authors of the present study would like to thank the Whitaker Foundation and the Purdue Research Foundation Minority Engineering Program for financial support.

#### REFERENCES

- 1) C.F.L. Chu, A. Lu, M. Liszkowski, and R. Sipchia. *Biochimica et Biophysica Acta*. **1472**, 479 (1999).
- 2) K.A. Hooper, N.D. Macon, and J. Kohn. *J. Biomed. Mater. Res.* **41**, 443 (1998).
- 3) H. Suh, B. Jeong, R. Rathi, S.W. Kim. *J. Biomed. Mater. Res.* **42**, 331 (1998)
- 4) J. Gao, L. Nikalson, R. Langer. *J. Biomed. Mater. Res.* **42**, 417 (1998).
- 5) T.J. Webster, C. Ergun, R.H. Doremus, and R. Bizios, *J. Biomed. Mater. Res.* **59**, 312 (2002).
- 6) L. Sherwood, *Human Physiology From Cells to Systems*, 2<sup>nd</sup> ed. (West Publishing Company, NY, 1993), p. 349.

### Nanoscale Patterning of Antigen on Silicon Substrate to Examine Mast Cell Activation

Reid N. Orth<sup>1\*</sup>, Min Wu<sup>2\*</sup>, Theodore G. Clark<sup>3</sup>, David A. Holowka<sup>2</sup>, Barbara A. Baird<sup>2</sup>, and Harold G. Craighead<sup>1</sup>

<sup>1</sup>School of Applied and Engineering Physics, <sup>2</sup>Department of Chemistry and Chemical Biology, Cornell University, <sup>3</sup>Department of Microbiology and Immunology Ithaca, NY 14853

#### ABSTRACT

Rat Basophilic Leukemia (RBL) cells are immobilized and stimulated on micro- and nanometer scale patterns of supported lipid bilayers. The patterns are realized as the photolithographically patterned polymer is mechanically peeled away in one contiguous piece in solution. The  $0.36 \mu\text{m}^2$  to  $4.489 \mu\text{m}^2$  patches can contain both fluorescent lipids and lipid-linked antigen and provide a synthetic biological substrate for analysis of cell surface receptor-mediated events. 100-nm unilamellar lipid vesicles spread to form a supported lipid bilayer on a thermally oxidized silicon surface as confirmed by fluorescence recovery after photobleaching (FRAP). Aggregation of fluorescently labeled receptors is observed as their coincidence with the patterned antigen. Cell morphology is analyzed with scanning electron microscopy (SEM). Thus, a novel method has been developed for patterning antigen, capturing and immobilizing cells via specific receptors, and spatially controlling antigenic stimulus on the nanoscale.

#### INTRODUCTION

Dinitrophenyl-conjugated lipids have been patterned on the micro- and nanometer scale to spatially control the stimulation of specific immunoreceptors on RBL mast cells. This work was motivated by previous research to elucidate the cascade of events from the initial receptor ligand interaction through cellular activation. Typically, many membrane-bound molecules work collectively to achieve specific cell-cell and cell-substrate recognition. The immunological synapse formation between antigen receptors on T cells (TCR) and antigen presenting cells is an example of the complex interaction initiating T cell activation in many immune responses [1].

IgE receptors (IgE-Fc $\epsilon$ RI) on mast cells are structurally and functionally similar to TCR and they are mainly involved in the allergic immune response and related inflammatory diseases. IgE are soluble, Y-shaped antibodies with binding sites for antigen in each of two segments. The third segment binds tightly to Fc $\epsilon$ RI on the mast cell surface, thereby becoming part of the receptor and effectively sensitizing the cell to the specific antigen. Cross-linking of IgE-Fc $\epsilon$ RI by bi- or multivalent antigens initiates transmembrane signaling which leads to exocytosis of secretory granules containing histamine and other inflammatory mediators. Mast cells are long-term residents of vascularized tissues and have specific roles in acute, 'late phase' and chronic aspects of adaptive or pathological IgE-associated acquired immune responses [2].

Recent research on immunoreceptor signaling has begun to focus on the initial stages involving specialized membrane domains, commonly called lipid rafts. In the mast cell system, for example, coalesced lipid rafts facilitate functional coupling of antigen-crosslinked IgE-Fc $\epsilon$ RI with the first signaling component on the cytoplasmic side of the membrane, the Lyn tyrosine kinase. Similar observations have been made for T cells and B cells operating in other immune responses [3]. Assembly of the signaling complex of enzymes and scaffolding proteins occurs with localization provided by the plasma membrane that is organized around the cross-linked

\* Co first authors

receptors. Interplay between these domains and the actin-cytoskeleton affects the localization and thereby the manner in which signaling proceeds. Such structural localization allows the cell to respond rapidly to a variety of stimuli with a limited number of targeted signaling components. Although this view is supported with a large accumulation of data, important details of the localized assembly remain to be elucidated. Systematic examination requires spatial and ultimately temporal control over the initial stimuli that can be exerted with appropriately engineered molecules and surfaces.

Microfabrication advances have enabled subcellular biomaterials patterning. These methods have enabled enzymes, antibodies, and nucleic acids to be spatially distributed on silicon, glass, and plastic substrates [4]. Recent lipid patterning techniques using microfabrication offer new methods for analyzing lipid characteristics including the formation, stability, and sensitivity of lipid bilayers on solid substrates [5-7]. Microcontact printing [8,9] has been used to study supported lipid bilayer lateral diffusion [10], mobility within confined barriers [11], and formation of concentration gradients during electrophoresis [12]. Barriers to lipid bilayers were formed on silicon with 10-nm thick gold corrals [13] and mechanical scratches [14]. Cell studies involving micropatterned biomaterials on solid substrates include microcontact printing anti-*E. coli* O157:H7 IgG to capture *E. coli* O157:H7 cells from solution [15], patterning neuronal cells using light-assisted functionalized photoresists [16], and culturing differentiated B104 neuroblastoma cells on four substrates to determine the preferred support substrate [17].

This paper presents a method for spatially patterning an antigenized (haptenated), supported lipid bilayer at sub-micron resolution for mast cell immobilization and activation leading to degranulation. This provides a system to study localized initiation of signal transduction that occurs in mast cells and is a model for the immunological synapse that occurs between T cells and antigen presenting cells. By these means cell surface receptors can be clustered by mobile, specific antigen at natural length scales in the micron and submicron range. Moreover, the size of the patch and the density of the antigen can be systematically tested for functional effects. The patterned, antigen rich surface is created using a polymer lift-off method [18,19]. In this method, the Parylene C, di-para-xylylene, dimer is conformally vapor polymer deposited and photoresist is spun over the thermally oxidized silicon substrate (Figure 1A). Conventional photolithography and reactive ion etching (RIE) pattern the polymer (Figure 1B). Lipid vesicles are applied (Figure 1C). Parylene is removed with a one-step mechanical lift-off (Figure 1D) leaving patterned supported lipid bilayers. RBL cells are sensitized with Alexa-488 labeled IgE

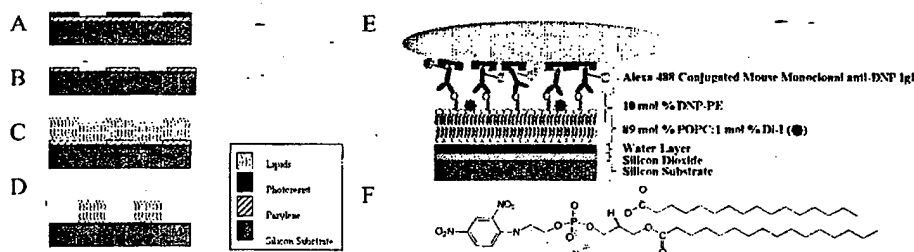


**Figure 1.** Fabrication process flow schematic [19]. (A) Photolithography. (B) Reactive ion etching. (C) POPC lipid immobilization. (D) Peeling of Parylene. (E) Schematic of the lipid pattern illustrated in figures 2A and 2B. (F) Dinitrophenyl-phosphocholamine structure [20].

and subsequently applied to the hapten-patterned substrate. Confocal and epifluorescence microscopy allow the cell morphology and surface aggregation of IgE-Fc $\epsilon$ RI with respect to the pattern features to be visualized. SEM imaging provides high-resolution morphological images.

## EXPERIMENTAL DETAILS

**Reagents.** Milli-Q water (18.2 Mohm-cm) was used for rinsing. The OCG\_OiR 897-121 photoresist was developed in Microposit MIF 300 (Shipley, Marlboro, MA). N-[2-Hydroxyethyl]piperazine-N'-[2-ethanesulfonic acid] (HEPES), sodium chloride (NaCl), and phosphate buffered saline (PBS) (Aldrich, Milwaukee, WI) formed the buffer solution.

**Silicon Wafer Preparation and Parylene Deposition.** 3-inch <1-0-0> N/phos type wafers (Silicon Qwest, Int'l, Santa Clara, CA) were cleaned in base and acid baths to remove surface contaminants and baked at 1100°C for 50 minutes in a wet oxide furnace to grow a 500-nm thermal oxide layer. A pinhole-free conformal layer of Parylene C was deposited using the PDS-2010 Labcoater 2 Parylene deposition system (Specialty Coating Systems, Indianapolis, IN). 1.5 g of Parylene dimer was used to deposit a 1- $\mu$ m thick Parylene film on 3-inch silicon wafers.

**Photolithography.** 1.5  $\mu$ m of photoresist was applied to the Parylene-coated silicon wafers and patterned using standard photolithographic techniques. The samples were subjected to an oxygen-based RIE etch, rinsed with acetone and isopropyl alcohol, and dried with a nitrogen gas.

**Lipid Preparation.** The lipids used include Dinitrophenyl-Phosphoethanolamine (DNP-PE), Di-I-conjugated Dioleoylphosphatidylethanolamine (Di-I-DPPC), and Di-I-conjugated 1-Palmitoyl-2-SN-Glycero-3-Phosphocholine ((Di-I-POPC) (Avanti Polar Lipids, Alabaster, Alabama). The POPC:Di-I:DNP (99:1 molar ratio) solution was prepared in chloroform. 5  $\mu$ moles of total lipid was transferred to 13x100 mm glass test tubes, dried with nitrogen gas and placed under a 10<sup>-5</sup> torr vacuum. The solution was rehydrated to a final lipid content of 2 mM using 150 mM NaCl, 10 mM HEPES, pH 7.4. The solutions were vortexed and subjected to 10 freeze-thaw cycles (liquid nitrogen/room temperature water). The vesicle solution was extruded 10 times with a high pressure 10 mL Thermobarrel Extruder (Northern Lipids, Vancouver, British Columbia) as described by Mayer [21] using two stacked 0.1  $\mu$ m Nucleopore polycarbonate filters (Whatman, Inc., Clifton, NJ) to create 100 nm unilamellar lipid vesicles.

**Lipid Application.** 10  $\mu$ l of a 2 mM lipid solution were bath-applied onto the Parylene-patterned polymer substrate. After a 5-minute lipid application, the sample was immersed in water (18-M $\Omega$ -cm). The Parylene was mechanically peeled from the surface and rinsed.

**Mast Cell Preparation and Application.** The monoclonal IgE specific for DNP was labeled with Alexa 488 (Molecular Probes, Eugene, OR) according to standard procedures. RBL-2H3 cells were maintained in monolayer cultures and harvested with trypsin-EDTA (Life Technologies, Rockville, MD) 3–5 days after passage, as described previously [22] and preincubated with this anti-DNP IgE and washed as previously reported [23]. The sensitized cells were incubated with the lipid-patterned surface at 37°C for 1 hour in TYRODES buffer (in mM: 140 NaCl, 6 KCl, 1 MgCl<sub>2</sub>, 2 CaCl<sub>2</sub>, 10 glucose, 2 pyruvate, Aldrich, Milwaukee, WI).

**Microscopy.** Epifluorescence microscopy was performed with an Olympus AX 70 upright microscope, water immersion objectives, Omega Optical filter sets, and Spot CCD camera. Rhodamine and Di-I fluorescent dyes were observed with a 510-590-nm excitation/590-nm emission filter set and an Alexa 488 fluorescent dye was observed with a 450-490-nm excitation/520-nm emission filter set. SEM imaging was performed with a LEO SEM. A BioRad confocal head stage and an Olympus AX 70 inverted microscope were used for confocal

microscopy and FRAP photobleaching, the latter with a 100X objective and 10X digital zoom (100% power) for 1-minute exposures. Time series images were taken with 10-second intervals.

## RESULTS

In this investigation, the aim was to create a micro- and nanometer scale array of patterned hapten-conjugated lipids for sub-cellular stimulation, test specific binding of IgE-Fc $\epsilon$ RI on sensitized RBL cells, confirm the presence of a supported lipid bilayer, investigate cell surface aggregation of IgE-Fc $\epsilon$ RI, and examine morphological changes following cellular encounter with the patterned features of squares or stripes.

An array of Di-I-POPC conjugated IgE patterns were created with sub 600-nm to 67- $\mu$ m square edge widths and 0.36  $\mu$ m $^2$  to 4,489  $\mu$ m $^2$  surface area, respectively. The sub 600nm pattern is approximately the 500 nm threshold attainable with the 10X stepper used in this experiment. Pattern uniformity relies upon an optimized photoresist thickness of 1.5  $\mu$ m and a Parylene thickness 1.0  $\mu$ m, photolithography precision, optimized RIE duration to prevent underetching, and sufficient biomaterial incubation time. Application of 1  $\mu$ m of Parylene and 1.5  $\mu$ m of photoresist provide optimal conditions for polymer removal and patterning resolution.

Anti-DNP IgE are labeled with an Alexa-488 to monitor their binding to the DNP-conjugated lipid patterns. This binding to the DNP-conjugated lipid patterns confirms the specificity attainable with the patterned antigen target. Non-DNP-conjugated lipid bilayer surfaces demonstrate negligible fluorescence over the background fluorescence intensity. Figure 1E illustrates layering of the molecules in this patterning process. Figure 1F illustrates the structure of the DNP-conjugated POPC. The surface area of each pattern ranges from 0.283  $\mu$ m $^2$  for the 600 nm circles to 4,489  $\mu$ m $^2$  for the 67  $\mu$ m squares. By comparison, these cells are commonly tested for 96 well plates with each well having a surface area of 44.78  $\text{mm}^2$ !

The continuity of the supported lipid bilayer is examined with a FRAP experiment. The POPC-Di-I lipids formed a uniform supported lipid bilayer after the five-minute incubation. A 5  $\mu$ m x 5  $\mu$ m patch was photobleached for one minute. The photobleaching recovers within 30-120 seconds. Supported lipid bilayer formation offers a method for creating a model cell membrane template for immobilization and stimulation. A thin film of water exists between the membrane and the substrate, as demonstrated by NMR [24] on glass beads. 100-nm vesicles appear to fuse onto silicon surfaces and form supported bilayer membranes.

RBL cells are fully immobilized on the patterned surface after one-hour incubation. The fluorescent IgE bound to Fc $\epsilon$ RI on the cell surface show the cells flattening and spreading response to stimulation. When a cell approaches a pattern edge, the cells preferentially remain in contact with the silicon substrate while still aggregating their IgE-Fc $\epsilon$ RI toward the haptenated contact interface (Figures 2A-B). When the pattern spacing is too small for a cell to squeeze between patterns, the cell rests on top of the pattern (Figure 2C). In this case, the aggregation can be observed in discrete circles around the underlying pattern. This result demonstrates that cells bind to multiple spatially separated regions on the patterned surface. In contrast, cells off the pattern remain unstimulated, rounded and not stably attached such that the majority could easily be removed in a wash step. Because the aggregated IgE-Fc $\epsilon$ RI cause coalescence of lipid rafts, there appears to be lipid raft mobility in RBL cells toward the patterned antigen.

SEM images are taken of cells immobilized and stimulated by the micro- and nanometer scale pattern. These images complement the fluorescent antibody staining images and provide clear images of the antigen stimulated, cytoskeleton-directed morphological changes. The cells extend

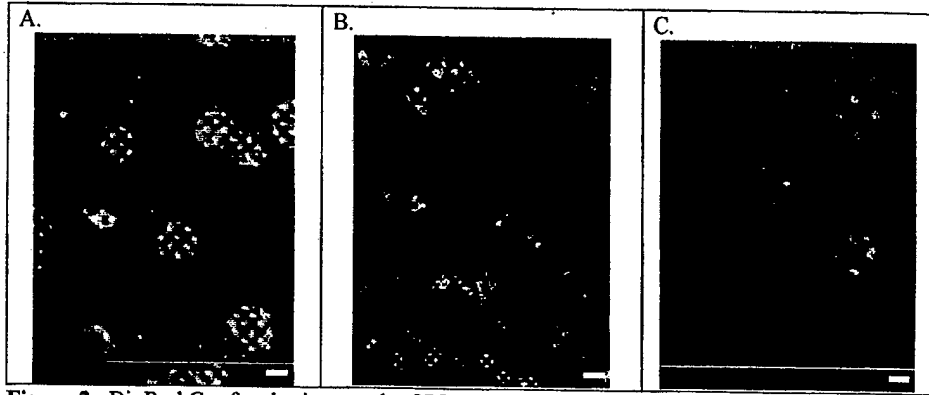


**Figure 2.** BioRad Confocal micrograph of RBL cells sensitized with Alexa-488 labeled IgE (green) on DNP-conjugated Di-I-DPPC patterns (red). (A) 2  $\mu$ m pattern, 8  $\mu$ m period, 15  $\mu$ m scalebar. (B) 3-8  $\mu$ m pattern, 30  $\mu$ m scalebar. (C) 5  $\mu$ m pattern, 15  $\mu$ m period, 15  $\mu$ m scalebar.

their pseudopodia along the patterned antigen forming finger-like patterns to maximize contact area (Figures 3A and 3B). Cells attempt to surround small square features (Figure 3C).

### CONCLUSIONS

This procedure provides a method for analyzing cellular responses to different spatially isolated patterned antigen and controlling the antigenic surface density, the surface area covered by antigen, the spacing between features, and the actual feature dimensions. The Parylene lift-off technique offers a rapid and precise way to create supported micro- and nanometer-scale patterns of biologically active compounds. The haptenated lipid surface serves as a model of interaction of immune cells and their surroundings. The purpose of studying mast cell response is to understand localized signal transduction components, to develop a novel model system for studying cell-cell interactions such as those occurring in the immunological synapse, and to lay the groundwork for more general studies of cellular receptors and responses at interfaces.

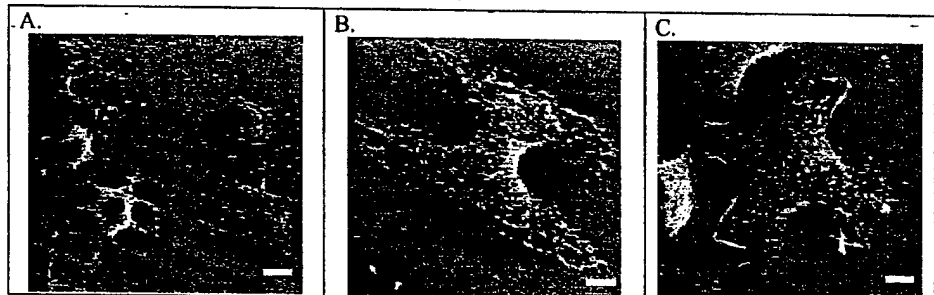


**Figure 3.** SEM images of stimulated RBL cells over DNP-conjugated Di-I-DPPC. (A) ~2  $\mu$ m antigen lines, ~13  $\mu$ m scalebar. (B) ~4  $\mu$ m antigen lines, ~4  $\mu$ m scalebar. (C) 4 adjacent ~4  $\mu$ m antigen squares, ~4  $\mu$ m scalebar.

## ACKNOWLEDGEMENTS

We acknowledge the NSF support through the Nanobiotechnology Center (NBTC), an STC Program of the NSF under Agreement No. ECS-9876771, and the Cornell Nanofabrication Facility resources. We thank Mathieu Foquet for his imaging assistance, Dr. Ismail Hafez for his assistance preparing lipids, and Marisol Barrero for her manuscript review. The views expressed in this article are those of the authors and do not reflect the official policy or position of the United States Air Force, Department of Defense, or the U.S. Government.

## REFERENCES

1. S. K. Bromley, W. R. Burack, K. G. Johnson, K. Somersalo, T. N. Sims, C. Sumen, M. M. Davis, A. S. Shaw, P. M. Allen, and M. L. Dustin, *Annu Rev Immunol* **19**, 375 (2001).
2. J. Medemeyer and S. J. Galli, *Br Med Bull* **56**, 936 (2000).
3. D. Holowka and B. Baird, *Sem. Immunol.* **13**, 1 (2001).
4. N. Dontha, W. B. Nowall, and W. G. Kuhr, *Anal. Chem.* **69**, 2619 (1997).
5. H. T. Tien and Z. Salamon, *Biotechnology and Applied Biochemistry* **12**, 478 (1990).
6. M. Zviman and H. T. Tien, *Biosensors & Bioelectronics* **6**, 37 (1991).
7. E. Sackman, *Science* **271**, 43 (1996).
8. R. J. Jackman, J. L. Wilbur, and G. M. Whitesides, *Science* **269**, 664 (1995).
9. C. D. James, R. C. Davis, L. Kam, H. G. Craighead, M. Isaacson, J. N. Turner, and W. Shain, *Langmuir* **14**, 741 (1998).
10. J. S. Hovis and S. G. Boxer, *Langmuir* **16**, 894 (2000).
11. L. A. Kung, L. Kam, J. S. Hovis, and S. G. Boxer, *Langmuir* **16**, 6773 (2000).
12. J. T. Groves and S. G. Boxer, *Biophysical Journal* **69**, 1972 (1995).
13. J. T. Groves, H. Ulman, and S. G. Boxer, *Science* **275**, 651 (1997).
14. P. S. Cremer, J. T. Groves, L. A. Kung, and S. G. Boxer, *Langmuir* **15**, 3893 (1999).
15. P. M. St. John, R. Davis, N. Cady, J. Czajka, C. A. Batt, and H. G. Craighead, *Anal Chem.* **70**, 1108 (1998).
16. D. V. Nicolau, T. Taguchi, H. Taniguchi, H. Tanigawa, and S. Yoshikawa, *Biosens Bioelectron* **14**, 317 (1999).
17. J. M. Corey, A. L. Brunette, M. S. Chen, J. A. Weyhenmeyer, G. J. Brewer, and B. C. Wheeler, *J Neurosci Methods* **75**, 91 (1997).
18. B. Ilic and H. G. Craighead, *Biomedical Microdevices* **2**, 317 (2000).
19. R. Orth, I. Hafez, M. Wu, B. Ilic, B. Baird, T. G. Clark and H. G. Craighead, *MRS Fall 2001 Conference Proceedings*, Section Y.7.18 (2001).
20. Avanti Polar Lipid Catalogue, Avanti Polar Lipids, Inc., Alabaster (2001).
21. L. D. Mayer, M. J. Hope, and P. R. Cullis, *Biochim Biophys. Acta* **858**, 161 (1986).
22. L. Pierini, D. Holowka, and B. Baird, *J. Cell Biol.* **134**:1427-1439 (1996).
23. D. Holowka, E. D. Sheets, and B. Baird, *J. Cell Sci.* **113**, 1009 (2000).
24. S. G. Johnson, T. M. Bayerl, D. C. McDermott, G. W. Adam, A. R. Rennie, R. K. Thomas, and E. Sachmann, *Biophys J.* **59**, 289 (1991).

### Formation, Characterization, Protein Resistance, and Reactivity of $\text{Cl}_3\text{Si}(\text{CH}_2)_{11}(\text{OCH}_2\text{CH}_2)_3\text{OH}$ Self-Assembled Monolayers

Jiehyun Seong, Seok-Won Lee, and Paul E. Laibinis  
Department of Chemical Engineering, Massachusetts Institute of Technology,  
Cambridge, MA 02139-4307, U.S.A.

#### ABSTRACT

We report a method for generating tri(ethylene glycol)-terminated-*n*-alkyltrichlorosiloxane monolayers on  $\text{SiO}_2$  surfaces. These chemisorbed films, with a thickness of ~2-3 nm, provide an oligo(ethylene glycol) surface that reduces the nonspecific adsorption of proteins and hydroxyl attachment sites for covalently immobilizing biomolecules to the substrate. These monomolecular films were formed by adsorbing an acetoxy-tri(ethylene glycol)-terminated *n*-alkyltrichlorosilane,  $\text{CH}_3(\text{C}=\text{O})\text{O}(\text{CH}_2\text{CH}_2\text{O})_3(\text{CH}_2)_{11}\text{SiCl}_3$ , onto glass and  $\text{Si}/\text{SiO}_2$  substrates, where the terminal acetate provided a protecting group for the hydroxyl functionality during self-assembly of the film. After formation of the monolayer, the acetate functionality was reduced chemically to form films exposing a covalently attached  $-(\text{OCH}_2\text{CH}_2)_3\text{OH}$  terminus at a density of  $\sim 3 \times 10^{14}$  molecules/cm<sup>2</sup>. Protein adsorption studies verified that the films exhibited notable resistances against the non-specific adsorption of various proteins. Chemical modification of the  $-(\text{OCH}_2\text{CH}_2)_3\text{OH}$  surface with protein A provided a non-adsorbing surface for selective immobilization of immunoglobulins.

#### INTRODUCTION

The construction of a variety of solid-state devices that interface fabricated systems with biological components or systems requires methods for assembling biomolecules on their surface in controlled ways. Examples include biosensors, chip-based diagnostic assays, and biomaterials used for implants and tissue engineering.<sup>1-4</sup> A key issue in the design of analytical devices that contact biomolecules is that the non-specific adsorption of biological species, particularly proteins, can hinder their performance. For example, the unwanted adsorption of proteins and other species can hinder or alter the selective adsorption of agents to be analyzed, disturb the binding characteristics of immobilized receptor agents used in sensing, and introduce defects in patterned surfaces used in array-based assays. The structural integrity of immobilized biological species are greatly affected by their interactions with the underlying surface, where effects that cause non-specific adsorption can alter their activity and binding abilities as a result of structural changes effected by surface effects. A key need is the ability to have "inert" surfaces that minimize unwanted adsorption events and allow the immobilization of biomolecules.

In a previous paper, we detailed the preparation of self-assembled monolayer coatings by the adsorption of  $\text{CH}_3\text{O}(\text{CH}_2\text{CH}_2\text{O})_{2,3}(\text{CH}_2)_{11}\text{SiCl}_3$  onto glass and  $\text{Si}/\text{SiO}_2$  substrates.<sup>5</sup> The resulting chemisorbed films, approximately 2-3 nm in thickness, expressed a densely packed methoxy-capped oligo(ethylene glycol) surface that dramatically retards the non-specific adsorption of various proteins. The methoxy cap provides a chemically inert surface that does not allow subsequent chemical modification as may be wanted for immobilizing a receptor agent onto the surface of a transducer for generation of a biosensor. A target would be a monolayer film that

expressed a terminus that replaced the methoxy cap with a hydroxyl functionality that could be used as a reactive site for subsequent chemical modification.

In this paper, we generate self-assembled monolayers on  $\text{SiO}_2$  surfaces that provide the following: (1) a terminal hydroxyl group for possible subsequent on-surface modification, (2) a tri(ethylene glycol) surface for non-fouling characteristics, and (3) an underlying alkyl domain for dense packing within the film. We detail their preparation and characteristics through use as a support for immobilization, here using a binding protein and an immunoglobulin.

## EXPERIMENTAL

### Formation of self-assembled monolayers

Acetyl[[(11-trichlorosilyl)-undecyl]tri(ethylene glycol) (EG<sub>3</sub>OAc) (3) was prepared by the three-step synthesis shown in Figure 1. Silicon wafers were cleaned in 2:8 mixture (v/v) of

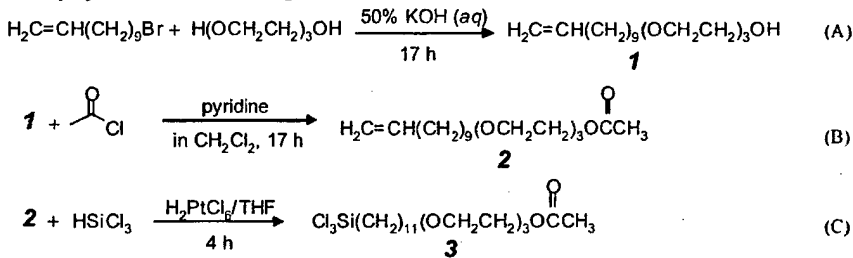


**Figure 1.** Synthesis of acetyl[[(11-trichlorosilyl)-undecyl]tri(ethylene glycol) (3).

30%  $\text{H}_2\text{O}_2$ (aq)/98%  $\text{H}_2\text{SO}_4$ (aq) for 10 min, rinsed with distilled water, and blown dried by a  $\text{N}_2$  stream. The wafers were immersed into 2-5 mM solution of 3 in anhydrous toluene for 24-48 h, rinsed with toluene, and dried under  $\text{N}_2$ . HO-terminated EG<sub>3</sub>(CH<sub>2</sub>)<sub>11</sub> films were formed by immersion of the EG<sub>3</sub>OAc films in LiAlH<sub>4</sub>/ether solutions (see text).

### Protein resistance of EG<sub>3</sub>OH surfaces

Proteins were obtained from Sigma and dissolved in phosphate buffer saline (PBS) solution (10 mM phosphate buffer at pH 7.4, 2.7 mM KCl, and 137 mM NaCl) at 0.25 mg/mL. Samples were immersed in the protein solutions for 24 h, rinsed with deionized water, and dried under  $\text{N}_2$ . Amounts of adsorbed protein were determined by ellipsometry using a refractive index of 1.45.

### Subsequent immobilization of biomolecules onto EG<sub>3</sub>OH surfaces

EG<sub>3</sub>OH coated surfaces were immersed in a 0.5 M 1,1-carbonyldiimidazole (CDI) (Aldrich) solution in anhydrous acetonitrile for 1 h, rinsed with acetonitrile, and dried under  $\text{N}_2$ . The CDI-reacted surfaces were contacted with a Protein A (Sigma) solution (0.5 mg/mL) in 50 mM carbonate buffer at pH 9.0 at 4 °C for 24 h. The activity of the resulting protein A surfaces were

examined by contacting the surface with a PBS solution containing a model IgG for 30 min and measuring the nitrogen signals from the sample by x-ray photoelectron spectroscopy.

## RESULTS AND DISCUSSION

### Synthesis of the silanating reagent (3)

Acetyl[(11-trichlorosilyl)-undecyl]tri(ethylene glycol) (EG<sub>3</sub>OAc) was prepared by the three-step synthesis shown in Figure 1. Each step was a direct modification of previously reported procedures. The reaction of 11-bromo-undecene and an excess of triethylene glycol and KOH produced **1** in a yield of ~70% as reported previously.<sup>6,7</sup> The hydroxyl group in **1** was protected from reaction with the target -SiCl<sub>3</sub> functionality in the final product by conversion to the acetate **2** (step B). Conversion of **2** to the final silanating product **3** used an excess of HSiCl<sub>3</sub> and H<sub>2</sub>PtCl<sub>6</sub> as a catalyst. Purification of **3** was performed by vacuum distillation.

### Formation of self-assembled monolayers from 3

Figure 2 shows thickness data for the formation of EG<sub>3</sub>OAc films onto Si/SiO<sub>2</sub> surfaces at room temperature and 60 °C. At room temperature, the maximum film thickness, as determined ex situ by ellipsometry, was achieved after ~2 days of reaction. At the higher temperature, the reaction achieved its final thickness after only ~8 h, with these conditions generating thicker films than possible by extended reactions at room temperature. The thicker films exhibited lower water contact angles and contact angle hysteresis than the thinner films. The thickest films in Figure 2 (and those presumably the most densely packed) exhibited water contact angles of 70-75° and contact angle hysteresis of ~20°.

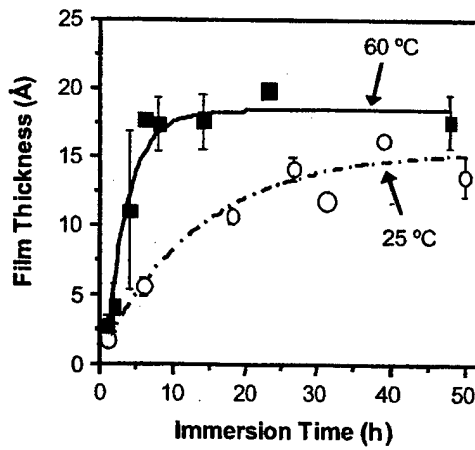


**Figure 2.** Kinetics of monolayer formation for reaction of ~4 mM solutions of Cl<sub>3</sub>Si(CH<sub>2</sub>)<sub>11</sub>(OCH<sub>2</sub>CH<sub>2</sub>)<sub>3</sub>OC(=O)CH<sub>3</sub> (3) in anhydrous toluene onto Si/SiO<sub>2</sub> surfaces.

The terminal acetate groups in monolayer films prepared from **3** were converted to hydroxyl variants by reduction of these surface acetates with LiAlH<sub>4</sub>. An optimization of reaction conditions determined that the exposure of the acetate-terminated film to 1.0 M LiAlH<sub>4</sub> in ether for ~10 min at room temperature produced the best results. Under these reaction conditions, the reduction of the acetate caused a decrease in the ellipsometric thickness of the film by ~4 Å, a decrease in the advancing contact angle of water from 70–75° to 62–65°, and evidence for the quantitative conversion of the terminal acetate groups to hydroxyl groups.

Figure 3 shows representative infrared spectra for the film obtained by attenuated total reflection (ATR) for films prepared from **3** before and after reaction with LiAlH<sub>4</sub>. The spectra were taken on an ATR silicon crystal that had been derivatized with **3**. In Figure 3a, the absorption peak at ~1745 cm<sup>-1</sup> corresponds to the stretching band for the ester functionality comprising the terminal acetate group of the EG<sub>3</sub>OAc SAM on the ATR crystal. Figure 3(b) shows the same spectral region after reacting the SAM with LiAlH<sub>4</sub>, and shows a complete loss of the ester peak. Complementary experiments using trifluoroacetic anhydride were performed to confirm the conversion of the terminal acetates to reactive hydroxyl groups by quantification of fluorine signals from the film by x-ray photoelectron spectroscopy (XPS). This analysis determined a site density of ~3x10<sup>14</sup> molecules/cm<sup>2</sup> for the EG<sub>3</sub>OH surface.

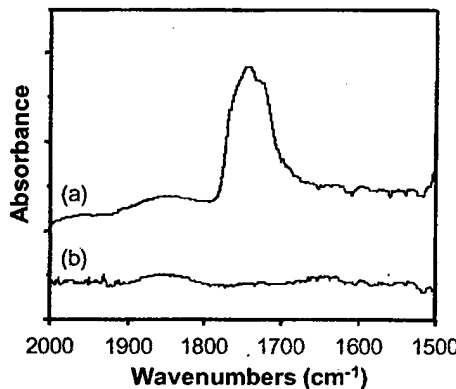


**Figure 3.** ATR/FT-IR spectra of  $\text{Cl}_3\text{Si}(\text{CH}_2)_{11}(\text{OCH}_2\text{CH}_2)_3\text{OC}(=\text{O})\text{CH}_3$  (**3**) SAM on Si/SiO<sub>2</sub>. (a) before deprotection and (b) after deprotection.

#### Protein resistance of EG<sub>3</sub>OH SAM

Protein adsorption experiments on the EG<sub>3</sub>OH-modified SiO<sub>2</sub> wafers showed that the coating resulted in significant reductions in the non-specific protein adsorption compared to silanating procedures that hydrophobize the surface by reaction with *n*-octadecyltrichlorosilane [CH<sub>3</sub>(CH<sub>2</sub>)<sub>17</sub>SiCl<sub>3</sub>]. The EG<sub>3</sub>OH-terminated films showed no change in film thickness after contact with a 0.25 mg/mL lysozyme solution for 24 h. Similar results were obtained with other proteins, including albumin and insulin. As an example of when the films were not fully able to suppress the non-specific adsorption of a protein, Figure 4 shows data for fibrinogen, where the

prevention of adsorption was not possible. We note, however, that the adsorbed amount of fibrinogen was reduced by ~70% as compared to the characteristics of hydrophobized octadecyltrichlorosilane (OTS)-treatments (Figure 4).

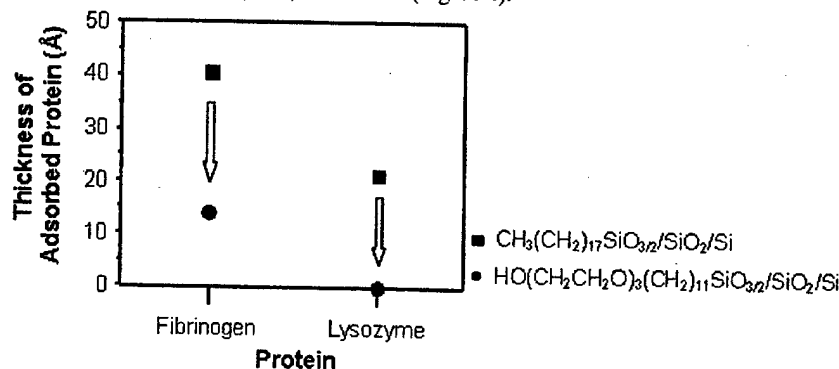


**Figure 4.** Ellipsometric thicknesses of adsorbed fibrinogen and lysozyme onto EG<sub>3</sub>OH and CH<sub>3</sub> surfaces after contact with 0.25 mg/mL protein solutions for 24 h.

#### Subsequent modification of EG<sub>3</sub>OH SAM surface for immobilization of biomolecules

We used the EG<sub>3</sub>OH surface as a platform for attaching agents to these thin films. Figure 5 shows N(1s) peak intensities taken from XPS spectra of the EG<sub>3</sub>OH surface through its exposure to various agents to develop covalent attachments. We used carbonyl diimidazole (CDI) chemistry to derivatize and activate the hydroxyl-surface for the immobilization of Protein A. In

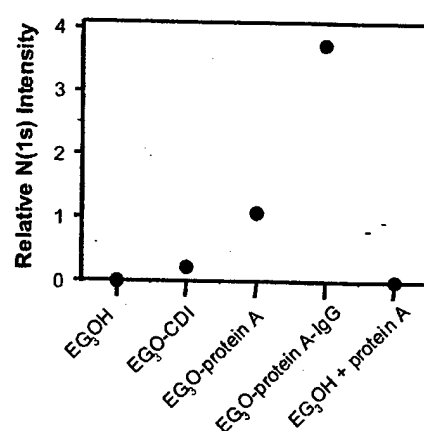


**Figure 5.** N(1s) peak intensities of the XPS spectra of EG<sub>3</sub>OH surfaces after subsequent sequential modification steps to immobilize Protein A and an IgG. The rightmost data point illustrates the lack of attachment and adsorption of Protein A onto the native EG<sub>3</sub>OH surface.

Figure 5, the initial EG<sub>3</sub>OH surface displayed no N(1s) intensity. Treatment with CDI resulted in a N(1s) signal that increased in intensity when this surface was further treated with Protein A and then a model IgG that becomes bound by the immobilized Protein A. Figure 5 shows that treatment of the EG<sub>3</sub>OH surface with Protein A for 24 h in the absence of activation by CDI results in essentially no attachment of adsorption of Protein A to the surface, in contrast to the results when CDI is employed previously. The suggestion from the data is that the EG<sub>3</sub>OH film presents an "inert" surface towards unwanted non-specific protein adsorption; however, its hydroxyl-termination provides a means for immobilizing proteins and other species to this surface. Together, the EG<sub>3</sub>OH system provides characteristics that offer possibilities as a flexible platform for biosensor construction particularly those such as waveguide technologies that required immobilization and binding events extremely close (a few nanometers) from the transducer surface.

## CONCLUSIONS

The self-assembly of CH<sub>3</sub>C(=O)O(CH<sub>2</sub>CH<sub>2</sub>O)<sub>3</sub>(CH<sub>2</sub>)<sub>11</sub>SiCl<sub>3</sub> (3) onto Si/SiO<sub>2</sub> substrates (and presumably onto related oxide surfaces) provides an ability to generate densely packed, hydroxyl-terminated, oligo(ethylene glycol) surfaces. These chemisorbed molecular films exhibit low levels of non-specific protein adsorption and allow subsequent chemical modification for attaching biomolecules onto these hydroxyl-terminated "inert" surfaces. The attachment of Protein A onto this surface and its binding to an immunoglobulin provides new possibilities for immobilizing such species useful in the generation of biosensors and other diagnostic devices.

## ACKNOWLEDGMENTS

We gratefully acknowledge the financial support of the Office of Naval Research and SatCon Technologies (Cambridge, MA).

## REFERENCES

1. P. Singh, B.P. Sharma and P. Tyle, *Diagnostics in the Year 2000: Antibody, Biosensor, and Nucleic Acid Technologies* (Van Nostrand Reinhold, 1993).
2. G.L. Kenausis, J. Vörös, D.L. Elbert, N. Huang, R. Hofer, L. Ruiz-Taylor, M. Textor, J.A. Hubbell and N.D. Spencer, *J. Phys. Chem. B* **104**, 3298 (2000).
3. L.A. Ruiz-Taylor, T.L. Martin, F.G. Zaugg, K. Witte, P. Indermuhle, S. Nock and P. Wagner, *Proc. Natl. Acad. Sci., USA* **98**, 852 (2001).
4. N.P. Huang, J. Vörös, S.M. DePaul, M. Textor and N.D. Spencer, *Langmuir* **18**, 220 (2002).
5. S.-W. Lee and P.E. Laibinis, *Biomaterials* **19**, 1669 (1998).
6. C. Pale-Grosdemange, E.S. Simon, K.L. Prime and G.M. Whitesides, *J. Am. Chem. Soc.* **113**, 12 (1991).
7. K.L. Prime and G.M. Whitesides, *J. Am. Chem. Soc.* **115**, 10714 (1993).

### Helical, Disordered, and What that Means: Structural Characterization of a New Series of Methyl 1-Thiaoligo(ethylene Oxide) Self-Assembled Monolayers

David J. Vanderah, Jennifer Arsenault, Hongly La, Vitalii Silin, Curtis W. Meuse, Richard S. Gates

Biotechnology Division, Chemical Science and Technology Laboratory, National Institute of Standards and Technology, Gaithersburg, MD 20899-8313

#### ABSTRACT

Self-assembled monolayers (SAMs) of a series of linear thiols containing a 1-thiaoligo(ethylene oxide) [TOEO] moiety, i.e.,  $\text{HS}(\text{CH}_2\text{CH}_2\text{O})_x\text{CH}_3$ , where  $x = 3 - 6$ , were prepared on polycrystalline gold (Au) and characterized by reflection absorption infrared spectroscopy (RAIRS) and spectroscopic ellipsometry (SE). For  $x = 5$  and 6, the RAIRS data show that the TOEO segment, oriented normal to the substrate, adopts the highly ordered 7/2 helical structure of the folded-chain crystal polymorph of poly(ethylene oxide). For  $x = 3$  and 4, the RAIRS and SE data indicate disordered, "amorphous" SAMs with essentially no evidence of the helical conformation in the TOEO segment. These data suggest that, for SAMs with TOEO segments, a minimum of five ethylene oxide units is required to adopt a helical conformation.

#### INTRODUCTION

Biocompatible materials for biomedical devices and diagnostic technologies continue to be an area of intense interest.<sup>1</sup> A central issue for much of this activity is surfaces that are resistant to the adsorption of proteins.<sup>2</sup> Protein resistant surfaces are desirable for implants (prostheses, pacemaker electrodes<sup>3</sup>, etc.), contact lenses<sup>4</sup> and inert matrices for chemical and biosensors.<sup>5</sup> Self-assembled monolayers (SAMs) of  $\omega$ -oligo(ethylene oxide) [ $\omega$ -OEO] alkylthiols or alkylsilanes, where OEO =  $(\text{CH}_2\text{CH}_2\text{O})_x\text{R}$ ,  $x = 3 - 6$ ,  $\sim 17$ , or  $\sim 144$ , and  $\text{R} = \text{H}$  or  $\text{CH}_3$ , assembled on  $\text{Au}^{6-11}$  or  $\text{SiO}_2^{12,13}$ , respectively, have been found to be highly protein resistant. For the SAMs on Au with short OEO segments ( $x = 3$  or 6), protein resistance was attributed to a film of water on helical OEO conformations.<sup>7</sup> However, RAIRS data for these SAMs, is most consistent with the OEO segments as mixtures of helical and non-helical conformations.

In contrast to the above  $\omega$ -OEO SAMs of mixed conformations, essentially all helical, near single phase OEO segments have been reported for the SAMs of  $\text{HS}(\text{CH}_2\text{CH}_2\text{O})_6\text{R}$ , where  $\text{R} = \text{CH}_3$ ,  $\text{C}_{10}\text{H}_{21}$  and  $\text{C}_{18}\text{H}_{37}$ .<sup>14,15</sup> The RAIRS spectra of these alkylated 1-thiahexa(ethylene oxide) [THEO] SAMs, which position the OEO segments closer to the Au, nearly exactly match the spectral characteristics of the 7/2 helix of the folded-chain crystal polymorph of crystalline poly(ethylene oxide).<sup>16</sup> In addition, the RAIRS spectra of these SAMs do not show bands at  $\sim 1130 \text{ cm}^{-1}$  and  $\sim 1145 \text{ cm}^{-1}$  indicative of OEO segments in amorphous<sup>17</sup> and/or all-*trans* conformations<sup>7</sup>, respectively. The THEO segments in these SAMs likely adopt the highly ordered, helical conformation because of a nearly perfect match between the cross-sectional area of the helix,  $21.38 \text{ \AA}^2$ , and the packing density,  $21.4 \text{ \AA}^2/\text{thiolate}^{18}$ , of a  $(\sqrt{3} \times \sqrt{3})R30^\circ$  adlayer on Au [assuming predominantly (1 1 1) Au with  $\text{S-S} \approx 0.50 \text{ nm}$ ].

This paper compares the structures for the SAMs of  $\text{HS}(\text{CH}_2\text{CH}_2\text{O})_x\text{CH}_3$ , where  $x = 3 - 6$ . Our interest in this homologous series is based on two very different ideas. On the one hand, SAMs with  $x < 6$  that have the TOEO segments identical with  $x = 6$  (ordered, helical) would be potential standard ultrathin films in the 1 - 2 nm range. As discussed previously, SAMs of increasing OEO length that have the OEO segments in the 7/2 helix would be isostructural and film thickness would increase in a predictable manner.<sup>19,20</sup> Alternatively, if the SAMs with  $x < 6$  do not have helical TOEO segments, then these surfaces would be candidates for protein resistant surfaces because ordered, helical SAMs were found not to be protein resistant.<sup>14</sup>

## EXPERIMENTAL DETAILS<sup>21</sup>

**Synthesis.** The compounds  $\text{HS}(\text{CH}_2\text{CH}_2\text{O})_x\text{CH}_3$  [hereafter referred to as  $(\text{EO})_x\text{CH}_3$ ], where  $x = 3 - 6$ , were prepared by conversion of the corresponding oligo(ethylene oxide) monomethyl ether (TCI America, Inc., Portland, OR) to the bromide [trifluoroacetic anhydride/tetrahydrofuran (THF)] followed by reaction with LiBr/THF-[hexamethylphosphoramide (HMPA)]. The thiols were then prepared by first converting the bromides to the thiol acetates ( $\text{CH}_3\text{COSNa}/\text{MeOH}$ ), followed by hydrolysis ( $\text{H}_3\text{O}^+/\text{MeOH}$ ). Structural assignments were made from proton nuclear magnetic resonance and high resolution mass spectrometry data.<sup>22</sup> Sample purity (>98%) was determined from thin-layer chromatography (TLC) analysis (one spot by TLC). All chemicals, except THF, were purchased from Aldrich Chemical Co., (Milwaukee, WI). THF (Mallinckrodt AR) was purchased from North Strong Scientific (Phillipsburg, NJ). THF and HMPA were distilled from calcium hydride. The THF was distilled under  $\text{N}_2$  immediately before use; whereas the HMPA was distilled and stored under  $\text{N}_2$  over 0.3 nm molecular sieves.

**Sample Preparation.** Silicon (1 0 0) wafers (Virginia Semiconductor, Fredricksburg, VA) were initially coated with chromium (~ 2 nm) and then with gold (~ 200 nm) by magnetron sputtering (Edwards Auto 306, UK) at a base pressure of  $\sim 1.3 \times 10^{-6}$  mbar as described previously.<sup>15</sup> The monolayers were prepared by immediately immersing the gold substrates in  $\sim 0.5 \times 10^{-3}$  mol/L solutions of the corresponding thiol in distilled 95% ethanol for at least 18 h, unless otherwise stated.

**Visible Spectroscopic Ellipsometry (SE).** Multiple wavelength ellipsometric measurements were performed on a J. A. Woollam Co., Inc. (Lincoln, NE) M-44 spectroscopic ellipsometer aligned at a nominal incidence angle of  $\sim 70^\circ$  as described elsewhere.<sup>20</sup>

**Reflection-Absorption Infrared Spectroscopy (RAIRS).** The RAIRS data were obtained using a Nicolet Magna-IR model 570 Series II spectrometer (Thermo Nicolet, Madison, WI) with a model FT-85 (85° grazing angle) Spectra-Tech external reflection accessory (Thermo Spectra-Tech, Shelton CT) as described elsewhere.<sup>19</sup>

## RESULTS AND DISCUSSION

The SAMs of  $(\text{EO})_6\text{CH}_3$  were described previously.<sup>14</sup> For direct comparison, SAMs of  $x = 6$  were prepared along with the  $x < 6$  SAMs. Some of the data presented here, for  $x = 6$ , are new observations not in the previous report. Figures 1 and 2 show the RAIRS data between 1440 - 920  $\text{cm}^{-1}$  and from 3120 - 2640  $\text{cm}^{-1}$ , respectively, for the  $(\text{EO})_3\text{CH}_3$  -  $(\text{EO})_6\text{CH}_3$  SAMs. The bands at 1347, 1243, 1119, and 965  $\text{cm}^{-1}$  (Figure 1), assigned as the symmetry designated  $A_2$  (4)

to  $A_2$  (7) bands, respectively, of the 7/2 helix of the folded-chain crystal polymorph of crystalline PEO, are found in the spectra of both the  $(EO)_5CH_3$  and  $(EO)_6CH_3$  SAMs. The absence of additional spectral bands in this region, other than the expected  $OCH_3$  rocking mode<sup>7</sup> at 1202  $cm^{-1}$ , indicates other OEO conformations are not present. In Figure 2, the prominent  $CH_2$  symmetric stretch at  $\sim 2894 cm^{-1}$ , characteristic of a helical OEO segment<sup>15,20,23</sup>, is also found in the spectra of both the  $(EO)_5CH_3$  and  $(EO)_6CH_3$  SAMs. Thus, within the limits of the RAIRS measurements, the TOEO segments of these SAMs are identical and essentially all in the helical conformation.

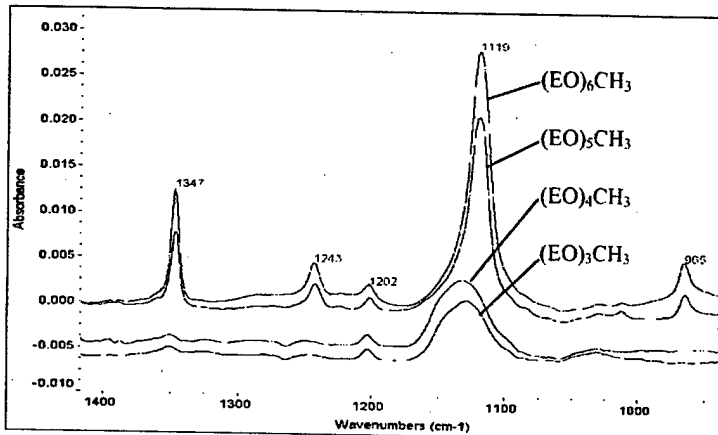


Figure 1: RAIRS spectra of  $(EO)_{3-6}CH_3$  from  $1420 cm^{-1}$  -  $920 cm^{-1}$

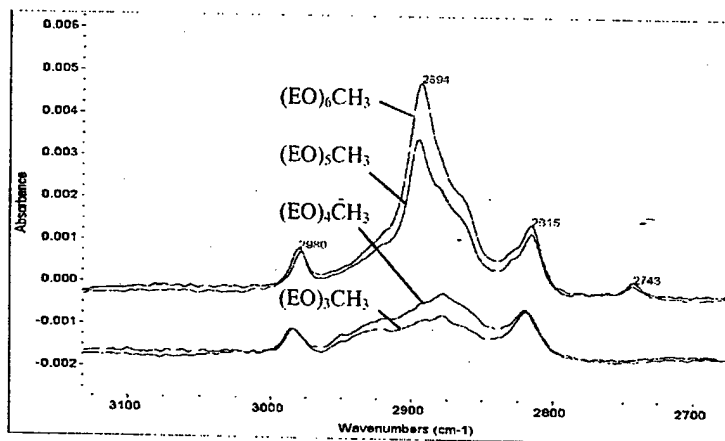


Figure 2: RAIRS spectra of  $(EO)_{3-6}CH_3$  from  $3120 cm^{-1}$  -  $2680 cm^{-1}$

In contrast, the RAIRS spectra of the  $(EO)_5CH_3$  and  $(EO)_4CH_3$  SAMs (Figures 1 and 2) are significantly different from those of  $(EO)_5CH_3$  and  $(EO)_6CH_3$  SAMs. The  $A_2$  bands found in RAIRS spectra of the  $(EO)_5CH_3$  and  $(EO)_6CH_3$  SAMs are absent (Figure 1). The broad C-O absorption band at  $\sim 1328\text{ cm}^{-1}$  is similar to that obtained for the  $HS(CH_2)_{11}O(EO)_3CH_3$  SAMs<sup>7</sup> and corresponds more closely to the C-O stretch of amorphous PEO.<sup>17</sup> In Figure 2 the spectra for the  $(EO)_5CH_3$  and  $(EO)_4CH_3$  SAMs show a broad ensemble of bands with two maxima in the C-H stretching region at  $\sim 2923\text{ cm}^{-1}$  and  $\sim 2878\text{ cm}^{-1}$ . These maxima more closely resemble the CH<sub>2</sub> asymmetric and symmetric stretch at  $2930$  and  $2865\text{ cm}^{-1}$ , respectively, of molten PEO.<sup>24</sup> Thus, the RAIRS data indicate that these SAMs consist of disordered OEO segments.

The  $(EO)_5CH_3$  SAMs showed variability. Figure 3 shows a comparison of the ordered, helical  $(EO)_5CH_3$  SAM (top spectrum) with spectra from other samples which, in all cases, exhibited attenuation of the four  $A_2$  bands accompanied with the appearance of a higher wavenumber shoulder on the  $A_2(6)$  [ $1118\text{ cm}^{-1}$ ] band. Similar asymmetry in the  $A_2(6)$  band was observed for  $HS(EO)_xR$  SAMs, where  $x = 5$  and  $7$  and  $R = C_{10}H_{21}$ <sup>20</sup>, as well as in the  $(EO)_6CH_3$  SAMs after exposure to protein<sup>14</sup>. The position of this shoulder at  $\sim 1130\text{ cm}^{-1}$  is evidence of less ordered SAMs with the TOEO segments containing non-helical conformations.<sup>17</sup>

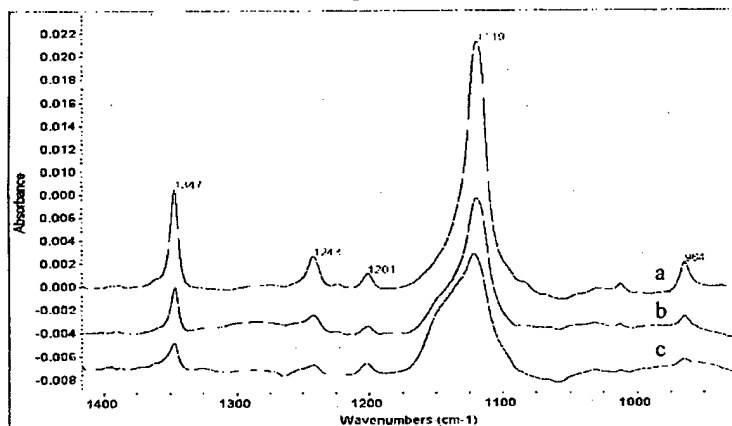


Figure 3: RAIRS spectra of three different  $(EO)_5CH_3$  samples on Au. Spectrum (a) shows helical SAM. Spectra (b) and (c) show samples with small and larger amounts of non-helical OEO segments, respectively.

The cause for the variability of the  $(EO)_5CH_3$  SAMs is unclear and is currently being investigated. Variability in SAMs with  $\omega$ -OEO segments has been previously reported.<sup>7</sup> SAM assembly parameters were varied but none afforded helical  $(EO)_5CH_3$  SAMs with any increased consistency. In addition, the kinetics of formation of helical  $(EO)_5CH_3$  and  $(EO)_6CH_3$  SAMs were different (Table 1). Whereas SE data indicates that the  $(EO)_6CH_3$  SAMs reached the expected thickness for a helical SAM after  $\sim 17$  h, the  $(EO)_5CH_3$  SAMs required significantly longer time.

**Table 1.** Calculated Thicknesses and SE Data for the  $\text{HS}(\text{EO})_{3-6}\text{CH}_3$  SAMs

Compound	Thickness, Calculated <sup>a</sup> (nm)			Thickness, Measured (nm $\pm$ 0.2 nm)				
	All-trans Extended	Helical	Disordered	17 h	28 h	2 d	6 d	8 d
$\text{HS}(\text{EO})_3\text{CH}_3$	1.44	1.15	< 1.15	-	0.81	0.88	0.86	0.89
$\text{HS}(\text{EO})_4\text{CH}_3$	1.79	1.43	< 1.43	-	1.13	1.26	1.26	1.29
$\text{HS}(\text{EO})_5\text{CH}_3$	2.14	1.71	< 1.71	-	1.44	1.52	1.51	1.70
$\text{HS}(\text{EO})_6\text{CH}_3$	2.49	1.99	< 1.99	1.97	-	1.94	-	-

<sup>a</sup>Film thickness calculations.  $(\text{EO})_x\text{CH}_3$  SAMs: helical = 1.99 nm; all-trans extended conformation = 2.49 nm.<sup>14</sup> Thickness decrease/EO unit: helical = 0.28 nm<sup>25</sup>; all-trans extended = 0.35 nm<sup>7</sup>.

## CONCLUSIONS

Highly ordered  $(\text{EO})_x\text{CH}_3$  SAMs, with the TOEO segments in the helical conformation, are obtained and, within the limits of the RAIRS measurements, appear to be isostructural with the  $(\text{EO})_x\text{CH}_3$  SAMs, reported earlier.<sup>14</sup> The highly ordered  $(\text{EO})_x\text{CH}_3$  SAMs take longer to form and showed variation in their molecular conformation. Many of the  $(\text{EO})_x\text{CH}_3$  SAMs remained less ordered, with the TOEO segments consisting of mixtures of helical and non-helical conformations. For the shorter  $(\text{EO})_3\text{CH}_3$  and  $(\text{EO})_4\text{CH}_3$  SAMs, the RAIRS spectra show bands consistent with a much more disordered, "amorphous" structure with no indication of the helical conformation. We conclude that there is no isostructural series for  $x = 3 - 6$ , due to the variability of the  $(\text{EO})_x\text{CH}_3$  SAMs. Also, the significant change in the TOEO conformation that occurs from  $x = 5$  to 4 suggesting a minimum of five ethylene oxide units are necessary for a TOEO segment to adopt a helical conformation.

## REFERENCES

1. Ratner, B.D.; Hoffman, F.J.; Schoen, J.E.; Lemons, F. *Biomaterials Science. An Introduction to Materials in Medicine*; Academic Press: New York, 1996.
2. Hench, L.L. *Biomaterials: An Interfacial Approach*; Academic Press, New York, 1982.
3. Stelzle, M.; Wagner, R.; Nisch, W.; Jägermann, W.; Fröhlich, R.; Schaldach, M. *Biosensors & Bioelectronics* 1997, 12, 853.
4. Wedler, F.C.; Riedhammer, T.M. *Biocompatibility in Clinical Practice* 1982, 11, 1.
5. Vadgama, P. *Chemistry in Britain* 1992, 249.
6. Benesch, J.; Svedhem, S.; Svensson, S.C.T.; Valiokas, R.; Liedberg, B.; Tengvall, P. *J. Biomat. Sci. - Polym. E.* 2001, 12, 581-597.

---

7. Harder, P.; Grunze, M.; Dahint, R.; Whitesides, G.M.; Laibinis, P.E. *J. Phys. Chem. B* **1998**, *102*, 426.
8. Silin, V.; Wetall, H.; Vanderah, D.J. *J. of Coll. and Interface Sci.* **1997**, *185*, 94.
9. Prime, K.L.; Whitesides, G.M. *J. Am. Chem. Soc.* **1993**, *115*, 10714.
10. Prime, K.L.; Whitesides, G.M. *Science* **1991**, *252*, 1164.
11. Pale-Grosdemange, C.; Simon, E.S.; Prime, K.L.; Whitesides, G.M. *J. Am. Chem. Soc* **1991**, *113*, 12.
12. Papra, A.; Gadegaard, N.; Larsen, N.B. *Langmuir* **2001**, *17*, 1457.
13. Yang, Z.; Galloway, J.A.; Yu, H. *Langmuir* **1999**, *15*, 8405.
14. Vanderah, D.J.; Valincius, G.; Meuse, C.W. *Langmuir*, submitted.
15. Vanderah, D.J.; Meuse, C.W.; Silin, V.; Plant, A.L. *Langmuir* **1998**, *14*, 6916 - 6923.
16. Kobayashi, M.; Sakashita, M. *J. Chem. Phys.* **1992**, *96*, 748-760.
17. Dissanayake, M.A.K.L.; Frech, R. *Macromolecules* **1995**, *28*, 5312-5319.
18. Laibinis, P.; Bain, C.D.; Nuzzo, R.G.; Whitesides, G.M. *J. Phys. Chem.* **1995**, *99*, 7663.
19. Vanderah, D.J.; Gates, R.S.; Silin, V.; Meuse, C.W.; Zeiger, D.N.; Valincius, G. *Langmuir*, submitted.
20. Vanderah, D.J.; Pham, C.P.; Springer, S.K.; Silin, V.; Meuse, C.W. *Langmuir* **2000**, *16*, 6527.
21. The specification of commercial products is for clarity only and does not constitute endorsement by NIST.
22. HRMS:  $(EO)_6CH_3$  characterized by HRMS as reported earlier.<sup>14</sup>  $(EO)_5CH_3$ : HR FAB [M + 1]<sup>+</sup> calcd for  $C_{11}H_{25}O_5S$  269.14227; found 269.14309.  $(EO)_4CH_3$ : HR FAB [M + 1]<sup>+</sup> calcd for  $C_9H_{21}O_4S$  225.11606; found 225.11533.  $(EO)_3CH_3$ : HR FAB no mass found for  $C_7H_{14}O_3S$ ; [M + 1]<sup>+</sup> found for disulfide, calcd for  $C_{14}H_{31}O_6S_2$  359.15622; found 359.15418. 270 MHz <sup>1</sup>H NMR for x = 3 - 5; δ 2.70 (relative to tetramethylsilane). 2H, dt, J ≈ 6.5 Hz and 6.2 Hz; HSCH<sub>2</sub>CH<sub>2</sub>O<sub>x</sub>CH<sub>3</sub>; 3.38, 3H, s, HSCH<sub>2</sub>CH<sub>2</sub>O<sub>x</sub>CH<sub>3</sub>.
23. Miyazawa, T.; Fukushima, K.; Ideguchi, Y. *J. Chem. Phys.* **1962**, *37*, 2764.
24. Bailey, F.E., Jr.; Koleske, J.Y. *Poly(ethylene oxide)*, Academic Press: New York, **1976**, p 115.
25. Takahashi, Y.; Tadokoro, H. *Macromolecules* **1973**, *23*, 672-675.

### Selectivity of Polypeptide Binding to Nanoscale Substrates

Steven R. Lustig and Anand Jagota  
Central Research & Development, E.I. du Pont de Nemours & Co., Inc.  
Experimental Station, Route 141  
Wilmington, DE 19880-0356, U.S.A.

#### ABSTRACT

We present new computational methodology for designing polymers, such as polypeptides and polyelectrolytes, which can selectively recognize nanostructured substrates. The methodology applies to polymers which might be used to: control placement and assembly for electronic devices, template structure during materials synthesis, as well as add new biological and chemical functionality to surfaces. Optimization of the polymer configurational sequence permits enhancement of both binding energy on and binding selectivity between one or more atomistic surfaces. A novel Continuous Rotational Isomeric State (CRIS) method permits continuous backbone torsion sampling and is seen to be critical in binding optimization problems where chain flexibility is important. We illustrate selective polypeptide binding between either analytic, uniformly charged surfaces or atomistic GaAs(100), GaAs(110) and GaAs(111) surfaces. Computational results compare very favorably with prior experimental phage display observations [S.R. Whaley *et al.*, *Nature*, **405**, 665 (2000)] for GaAs substrates. Further investigation indicates that chain flexibility is important to exhibit selective binding between surfaces of similar charge density. Such chains begin with sequences which repel the surfaces, continue with sequences that attract the surface and end with sequences that neither attract nor repel strongly.

#### INTRODUCTION

We present new computational methodology for designing polymers, such as polypeptides and polyelectrolytes, which can selectively recognize nanostructured substrates. The methodology applies to polymers which might be used to: control placement and assembly for electronic devices, template structure during materials synthesis, as well as add new biological and chemical functionality to surfaces. Optimization of the polymer configurational sequence permits enhancement of both binding energy on and binding selectivity between one or more atomistic surfaces. This optimization is enabled by combining highly-efficient, atomistic modeling of the polymer and surfaces with genetic mutation of the polymer configuration. The atomistic modeling permits the calculation of macromolecular statistics and thermodynamics of substrate binding, while genetic sequence mutation enables the search and enhancement of the desired polymer-surface interactions.

Previous experimental works have demonstrated polypeptides with selectivity for binding to surfaces of metals and metal oxides [1-8] as well as a range of semiconductor surfaces [9]. Polypeptides which can recognize desired surfaces are typically selected from a library of several million candidates using either bare proteins or phages, often in the presence of surfactants or salts. These methods are often both practical and useful. There still exist several issues. First, it is not always clear whether the selected polypeptides will retain their binding and selectivity once

removed from the parent protein or phage body. Second, practical experimental libraries of even  $10^8$  candidates might not well represent the complete range of functionalities present in the  $>10^{15}$  possibilities from natural residues. Third, experimental screening does not typically teach why particular consensus sequences emerge. Hence we might not always be able to predict new and better binding sequences. Finally, we ask if it is possible to design better polymer sequences and compositions than those available from natural sources and residues.

If theoretical and computational methods are to be as practical and useful, they will surely need to contain the salient physics and chemistries of polymers and surfaces while remaining both accurate and quickly solvable. Toward this end, we illustrate methodology for selective polypeptide binding between either analytic, uniformly-charged surfaces or atomistic model surfaces. Here we compare our preliminary findings to recent pioneering, experimental results [9]. Further, we ask how to find optimal sequences which selective a target surface over closely similar surfaces.

## COMPUTATIONAL METHODS

Polypeptides are described as rotational isomeric state chains in which bond lengths and bond angles are frozen at equilibrium values while torsional rotations remain degrees of freedom. In applying discrete Rotational Isomeric State, RIS, theory [see e.g. 10-12], we select discrete energy states at the minima in a potential energy surface from mapping pairwise-conditional, rotational angles around neighboring N-C<sub>α</sub> and C<sub>α</sub>-C' bonds for each natural amino acid residue. In applying our new Continuous Rotational Isomeric State, CRIS, method, the torsional angles may be selected within a continuous range from rectangular tiles around minima in the potential energy surface. The tiles are defined from energy minima bounded by a preset, maximum well height, typically 1 kcal/mol. If a local potential energy surface exhibits a relative maximum before reaching the preset height, then the tile boundary is defined at the relative maximum. Tile boundaries are combined by overall union if the tile definitions create overlapping regions from multiple energy minima. A chain backbone conformation is completely defined from the fixed bond lengths, fixed bond angles and selected torsions. Non-backbone atom positions are described as "pendtors", i.e. pendant vectors. Amide hydrogens and oxygens are placed on the backbone from constant vectorial components using a basis set generated from the [C'-N], [N-C<sub>α</sub>] bond vectors and their cross-product. Likewise each residue's pendant atoms are placed from constant vectorial components using a basis set generated from the [N-C<sub>α</sub>], [C<sub>α</sub>-C'] bond vectors and their cross-product. The various rotational states within each residue's pendant group can be represented by sets of their atomic pendtors. A rotational potential energy surface and the aforementioned fixed geometrical parameters for each amino acid residue with amide terminations was created using the PCFF forcefield [13,14]. When implementing RIS, a table of discrete rotational states (each state comprising the conditional pair of torsion angles and the associated energy value) for each residue is stored in memory during a simulation to look-up the rotational energy. When implementing CRIS the entire pairwise-conditional torsional energy surface for each residue is simply stored in memory during a simulation to look-up and interpolate the rotational energy.

The polypeptide potential energy includes additional interatomic contributions. Self-avoidance is ensured by assigning hard-sphere radius, typically 0.5 Å, for each atom. The hydrophobic effect is approximated by contributing a fixed energy decrement, typically -0.25

kcal/mol, when two hydrophobic groups reach a minimum separation, typically 5 Å. Electrostatic potential energy between atoms arises from partial charges for each atom assigned by the COMPASS forcefield [15]. Since the polypeptide is ensconced in an effective solvent medium, atoms experience diminished electrostatic potentials,  $V$ , through the Debye-Hückel potential,

$$V = \left( \frac{L e^2}{4 \pi \epsilon_0} \right) \left( \frac{q_i q_j}{\epsilon r_{ij}} \right) \exp(-\kappa r_{ij}) \quad (1)$$

where the first enclosed term is the thermal Bjerrum length,  $q_i$  is the partial charge on the  $i$ th atom,  $\epsilon$  is the solvent dielectric constant,  $\kappa$  is the inverse electrostatic screening or Debye length which is dictated in actual experiments by the concentration of dissolved ions and  $r_{ij}$  is the distance between the  $i$ th and  $j$ th atoms. Equation (1) applies also between polymer and surface atoms. For infinite analytic surfaces with uniform charge, we compute the potential between atoms and the analytic surface using the integrated form of Equation (1) below:

$$V = \left( \frac{L e^2}{2 \epsilon_0} \right) \left( \frac{\sigma q_i}{\epsilon \kappa} \right) \exp(-\kappa z_i) \quad (2)$$

where  $\sigma$  is the surface charge density and  $z_i$  is the height above the surface of the  $i$ th atom.

Our simulations utilize an unusual methodology to sample the polymer degrees of freedom (sometimes referred as “simple sampling Monte Carlo” [16] or direct phase-space integration) for computing molecular statistics and thermodynamics. The degrees of freedom consist of: the internal torsion states along the polymer backbone, the position of an end bond vector relative to the surface origin and a rigid-body rotation of the chain around the end bond vector. Torsional states are selected randomly such that each discrete state (for RIS) or position in a torsional tile state (for CRIS) is selectable with equal and uniform probability. Phage display and tumble chain sampling methods are used to integrate over the remaining spatial degrees of freedom. Phage display sampling always assigns the C'-terminus bond vector normal to the surface (with the penultimate bond vector toward the surface) and chooses a random, rigid-body rotation about the end bond vector. Note that the polypeptide C'-terminus is fixed so that the N-terminus can be displayed to the surface to emulate a phage peptide display. Tumble sampling comprises selecting a random spatial orientation of an end bond vector and selecting a random rigid-body rotation about the end bond vector. For both sampling methods the absolute distance between the lowest atom in the polymer and the highest component of the surface is varied to sample a profile of important statistical quantities as a function of height above the surface. Since all Monte Carlo trials are always “accepted”, statistical quantities are computed with each configuration being weighted by its appropriate thermal Boltzmann factor,  $\exp[-(E-E_{\text{form}})/kT]$ . Here  $E$  is the total potential energy of a Monte Carlo trial and  $E_{\text{form}}$  is the energy of formation. Statistical quantities of interest include the well known polymer-surface binding free energy,  $A$ , internal energy,  $U$ , entropy,  $S$ , binding constant,  $K$ , as well as geometrical shape changes, e.g. strain,  $\epsilon$ , and squash,  $\xi$ .

$$\epsilon = \frac{1}{2} \frac{\langle R^2 \rangle_{\text{surface}}}{\langle R^2 \rangle_{\text{solvent}}} - 1, \quad \xi = \left[ \frac{\langle R_{\perp}^2 \rangle_{\text{surface}} - \langle R_{\parallel}^2 \rangle_{\text{surface}}}{\langle R^2 \rangle_{\text{solvent}}} \right] \quad (3a,b)$$

Here we define a strain in terms of the mean-squared end-to-end chain distance on the surface,  $\langle R^2 \rangle_{\text{surface}}$ , relative to free solvent,  $\langle R^2 \rangle_{\text{solvent}}$ . The chain squash is defined in terms of the mean-squared, chain end-to-end vector components parallel to the surface (designated by horizontal arrows) and normal to the surface (designated by vertical arrows).

## RESULTS

Figure 1 illustrates the typical convergence of a polypeptide-surface binding free energy as a function of the number of Monte Carlo samples. This example polypeptide has over  $10^7$

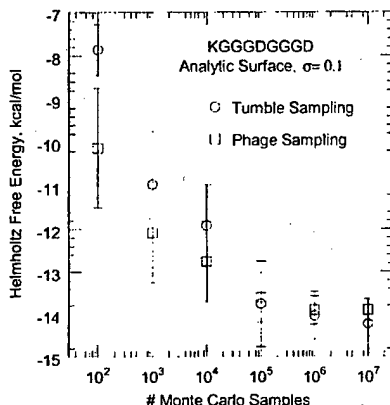


**Figure 1.** Polypeptide-surface binding free energy as a function of Monte Carlo samples using CRIS chain model. The test polypeptide is presented a flat surface with uniform charge density  $0.1 \text{ e}/\text{\AA}^2$ . Error bars indicate the standard deviation from 10 independent, replicated simulations.

discrete torsional degrees of freedom yet the free energy has less than 1.5 kcal/mol uncertainty after  $10^5$  phage samples and  $10^6$  tumble samples. Note that this particular chain is a very strong binder. Metropolis Monte Carlo methods typically do not converge as quickly [17] and require extensive equilibration to surmount chain conformation trapping in deep potential energy wells which is intrinsic to these systems [18].

Our computational results compare favorably with previously-published, experimental phage display observations. We subjected model RIS chains to phage sampling over an atomistic GaAs(100) surface model. The residue sequences match the pIII coat proteins of M13 coliphages reported in Figure 1 of reference [9] which were found to bind to GaAs(100) substrates. While these preliminary computations predict 8 of the 11 polypeptides have very favorable binding free energies ( $\Delta A < 0$ ), all chains are predicted to bind significantly to the surface. The statistical binding constant, K, takes a value of unity for permanent surface binding and zero for no surface binding. Our computed values of K range from 0.4 to 0.9, which is consistent with elutable surface binding. Typically, we find that those chains with the lowest binding free energies also show the greatest tendency to spread across the surface (high values of  $\epsilon$  and  $\xi$ ). Most significantly, our computations do reproduce experimental observations that clone G1-3 exhibits preferential binding to GaAs(100), over both gallium and arsenic terminated GaAs(111) faces.

**TABLE I.** Binding results for RIS chain models of phage display polypeptides (see Figure 1 of reference [9]) tested by phage sampling over atomic GaAs(100) model.

Phage [9]	$\Delta A$	$\Delta U$	$\Delta S \times 10^3$	$K$	$\epsilon$	$\xi$
G1-3	-1.6	-1.9	-0.9	0.9	2.19	0.45
G1-4	-0.6	0.5	3.8	0.7	1.64	-1.80
G7-4	0.3	-0.6	-3.1	0.4	-0.19	-0.10
G11-3	0.2	1.0	2.6	0.4	-0.16	-0.17
G12-3	-0.9	1.3	7.3	0.8	0.26	0.94
G12-4	-0.5	-1.2	-5.6	0.7	-0.18	0.10
G12-5	0.3	-0.6	-2.8	0.4	-0.27	-0.06
G13-5	-1.0	1.1	7.0	0.8	0.58	1.66
G14-3	-1.0	0.8	6.0	0.9	1.62	0.93
G14-4	-0.4	-0.2	0.9	0.7	0.28	1.41
G15-5	-0.8	0.2	3.5	0.8	0.20	-0.14

In a separate set of computational experiments, we explore how to construct chains to bind selectively to only modestly, Lewis acidic surfaces. Sequences were limited to the residue-pair combinations of: KP (stiff base), KG (flexible base), DP (stiff acid), DG (flexible acid), GG (flexible neutral) and PP (stiff neutral). Furthermore we compare fully atomistic chain models to united-atom chain models (where each backbone entity possesses the net charge from all of its pendant atoms while preserving RIS properties for each residue). Not surprisingly, we find chains with high base residue content bind strongly to surfaces with increasing surface charge density, but this is only trivial selectivity. More interestingly, we found only chains with flexible residue pairs exhibit non-monotonic binding to surfaces with increasing surface charge density. Table II illustrates sequences with optimized binding constants for intermediate-valued surface charge densities. Such chains begin with base sequences which repel the surfaces, continue with acid sequences that attract the surface and end with neutral sequences that neither attract nor repel strongly. This suggest that several types of star polymers could exhibit interesting selective binding properties.

**TABLE II.** Surface binding constant,  $K$ , for RIS united atom chain models on analytic surfaces.

Sequence	Surface Charge Density ( $e/\text{\AA}^2$ )				
	0.20	0.16	0.12	0.08	0.04
(KP) <sub>2</sub> (DP) <sub>2</sub> (G) <sub>12</sub>	0.90	0.98	0.82	0.48	0.51
(KG) <sub>2</sub> (DG) <sub>2</sub> (G) <sub>12</sub>	0.92	1.00	0.69	0.51	0.52
(KG) <sub>2</sub> (DP) <sub>2</sub> (G) <sub>12</sub>	0.96	0.96	0.46	0.55	0.51
(KG) <sub>2</sub> (DG) <sub>2</sub> (P) <sub>12</sub>	0.98	0.74	0.86	0.63	0.56

#### ACKNOWLEDGEMENTS

The authors would like to acknowledge and thank Angela Belcher (Massachusetts Institute of Technology) and Siqun Wang (E.I. du Pont de Nemours & Co., Inc.) for very helpful discussion.

---

Correspondence should be addressed to S.R.L. (Email at the time or writing this manuscript: steve.r.lustig@usa.dupont.com)

## REFERENCES

1. W.D. Huse, L. Sastry, S.A. Iverson, A.S. Kang, M. Alting-Meers, D.R. Burton, S.J. Benkovic and R.A. Lerner, *Science*, **246**, 1275-1281 (1989).
2. J.D. Marks, H.R. Hoogboom, T.P. Bonner, J. McCafferty, A.D. Griffiths and G. Winter, *J. Mol. Biol.* **222**, 581-597 (1991).
3. J.K. Scott and G.P. Smith, *Science*, **249**, 386-390 (1990).
4. S.E. Cwirla, E.A. Peters, R.W. Barrett and W.J. Dower, *Proc. Natl. Acad. Sci. USA*, **87**, 6378-6382 (1990).
5. J.J. Devlin, L.C. Panganiban, P.E. Devlin, *Science*, **249**, 404-406 (1990).
6. K.S. Lam, S.E. Salmon, E.M. Hersh, V.J. Hruby, W.M. Kazmierski and R.J. Knapp, *Nature (London)*, **354**, 82-84 (1991).
7. S. Brown, *Proc. Natl. Acad. Sci. USA*, **89**, 8651-8655 (1992).
8. S. Brown, *Nature Biotechnol.* **15**, 269-272 (1997).
9. S.R. Whaley, D.S. English, E.L. Hu, P.F. Barbara and A.M. Belcher, *Nature*, **405**, 665-668 (2000).
10. P.J. Flory, *Statistical Mechanics of Chain Molecules* (Interscience, New York, 1969).
11. W.L. Mattice and U.W. Suter, *Conformational Theory of Large Molecules; The Rotational Isomeric State Model in Macromolecular Systems* (Wiley, New York, 1994).
12. M. Rehahn, W.L. Mattice and U.W. Suter, "Rotational Isomeric State Models in Macromolecular Systems," *Advances in Polymer Science*, **131/132**, (Springer, New York, 1997).
13. J. R. Maple, M.-J. Hwang, T. P. Stockfisch, U. Dinur, M. Waldman, C. S. Ewig, and A. T. Hagler, *J. Comput. Chem.* **15**, 162-182 (1994)
14. H. Sun, *J. Comput. Chem.* **15**, 752-757 (1994)
15. At the time of writing this manuscript, the COMPASS force field is a licensed product of Accelrys Inc., 9685 Scranton Road, San Diego, CA 92121 (<http://www.accelrys.com>). See for example: H. Sun and D. Rigby, *Spectrochim. Acta*, **53A**, 1301 (1997); H. Sun, *J. Phys. Chem. B*, **102**, 7338-7364 (1998); H. Sun, P. Ren and J. R. Fried, *Comput. Theor. Polym. Sci.* **8**, 229. (1998).
16. K. Binder and D.W. Heermann, "Monte Carlo Simulation in Statistical Physics", 2nd corrected ed., *Solid-State Sciences*, **80**, (Springer-Verlag, New York, 1992).
17. See for example: C.Y. Kong and M. Muthukumar, *J. Chem. Phys.* **109**, 1552-1527 (1998); -Y.-H. Lee and B.J. Berne, *J. Phys. Chem.*, **104**, 86-95 (2000); S. Santos, U.W. Suter, M. Muller and J. Nievergelt, *J. Chem. Phys.* **114**, 9772-9779 (2001); P. Chodanowski and S. Stoll, *Macromolecules*, **34**, 2320-2328 (2001).
18. M Muthukumar, *Proc. Nat. Acad. Sci. USA*, **96**, 11690-11692 (1999).

---

**Composite Biomaterials—  
Bones and Teeth I**

## DEVELOPING BIO-STABLE AND BIODEGRADABLE COMPOSITES FOR TISSUE REPLACEMENT AND TISSUE REGENERATION

Min Wang

Rehabilitation Engineering Centre, Hong Kong Polytechnic University  
Hung Hom, Kowloon, Hong Kong

### ABSTRACT

Bone is the substantial unit of human skeletal system, which supports the body and its movement. At the ultra-structure level, the bone matrix is a composite material consisting of bone mineral particles, which are mainly substituted, calcium-deficient hydroxyapatite, and collagen, which is a natural polymer. Bone serves as the template for developing bone replacement materials. Research on biomaterials analogous to bone was started in the early 1980s by incorporating bioactive particles into biocompatible polymers so as to produce bone substitutes. Over the last two decades, a variety of bioactive polymer matrix composites have been developed for tissue substitution and tissue regeneration. The bioactive phases in these composites are normally one of the calcium phosphates, especially synthetic hydroxyapatite ( $\text{HA, Ca}_{10}(\text{PO}_4)_{6}(\text{OH})_2$ ) which closely resembles bone apatite and exhibits osteoconductivity. If enhanced bioactivity is required, bioceramics having higher bioactivity such as Bioglass® and A-W glass-ceramic can be used as the bioactive phase in the composites. For tissue replacement, bio-stable polymers such as polyethylene (PE) and polysulfone (PSU) are used as the matrix polymer. For tissue regeneration, natural, biodegradable polymers such as polyhydroxybutyrate (PHB) and chitin are used as matrices. Furthermore, mechanical as well as biological performance of a particular composite can be controlled by varying the amount of the bioactive phase in the composite, thus meeting specific clinical requirements. For bioactive ceramic-polymer composites, major influencing factors such as shape, size and size distribution of bioactive particles, mechanical properties and volume percentage of the bioactive phase, properties of the matrix polymer, distribution of bioactive particles in the matrix and the particle-matrix interfacial state should be controlled in order to obtain materials of desirable properties. Various techniques are used to evaluate the composites.

### INTRODUCTION

Numerous materials have been used for bone substitution since the 19th century. In modern day orthopaedic surgery, metals such as stainless steel and titanium alloy and ceramics such as alumina and toughened zirconia are common in a variety of implants and devices. However, these materials, having been developed originally for other purposes rather than medical applications, are considerably stiffer than human bone. The modulus mismatch between an implant material and the host tissue can cause bone to resorb at the bone-implant interface, which leads to implant instability and hence eventual failure [1]. A long lasting bone replacement requires the establishment of a stable bone-implant interface, which necessitates the careful matching of the mechanical behaviour as well as properties of synthetic implant materials with the tissue [2]. Furthermore, bone replacement materials must withstand any anticipated physical

loads imposed by body actions without substantial dimensional changes, catastrophic fracture, or failure due to impact, creep, or fatigue within their expected lifetime in the body.

It is now generally recognised that the best material for replacing a body tissue is the one that is similar, if not identical, to that tissue [2]. The advances in composite technology have led to the production of new composites that mimic the structure and match properties of human tissues [3]. These novel materials may overcome problems that have been encountered with the use of conventional implant materials.

### STRUCTURE AND PROPERTIES OF BONE

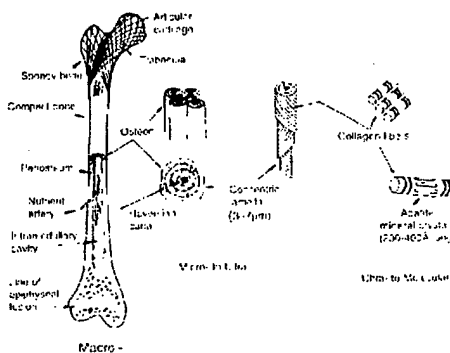


Figure 1 Structural organisation in a human long bone [4]

Bone is the substantial unit of human skeletal system, which supports the body and its movement. Bone, as a natural tissue, has a complex structure in which several levels of organization, from macro- to micro-scale, can be identified [4]. Take a human long bone such as femur for an example (Figure 1). It consists of an outer load-bearing shell of cortical bone with a medullary cavity containing cancellous bone towards the bone ends. Cortical (or compact) bone as a material is anisotropic with osteons (also known as "Haversian systems") being oriented parallel to the long axis of the bone and interspersed in regions of non-oriented bone. Each osteon (about 100 to 300µm in diameter) has a central Haversian canal (20 to 40µm in diameter) containing a blood vessel, which supplies the elements required for bone remodeling. The Haversian canal is surrounded by 4 to 20 concentrically arranged lamellae with each lamella being 3 to 7µm thick. Each adjacent lamellar layer has a different orientation of collagen fibres. Circumscribing the outermost concentric lamella of the osteon is a narrow zone known as cement line, which contains calcified mucopolysaccharides and is devoid of collagen. The cement line is 1 to 2µm thick and is the weakest part of bone. The densely packed concentric lamellae in osteons are composed of two major components: fibrous collagen, which is a natural polymer, and bone mineral. The mineral crystallites that human bone contains are structurally calcium-deficient, carbonate-substituted hydroxyapatite (HA). They are usually referred to as bone apatite, which normally has dimensions of 5nmx5nmx50nm with a rod-like (or sometimes plate-like) habit and is embedded in collagen fibres. In mature bone, bone apatite occupies about 50% of the total volume. The precise microstructural organization of bone is a function of age and varies between different bones and between different locations of the same bone. Two levels of composite structure are considered when developing bone substitutes: first, the bone apatite

reinforced collagen forming individual lamella (on the nm to  $\mu\text{m}$  scale) and, second, osteon reinforced interstitial bone (on the  $\mu\text{m}$  to mm scale). It is the apatite-collagen composite at the microscopic level that provides the basis for producing bioceramic-polymer composites for bone replacement.

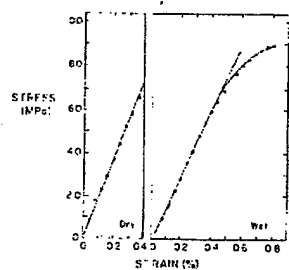


Figure 2 Effect of drying on the behaviour of human cortical bone [5]

Table 1 Mechanical properties of bone and current implant materials [2]

Material	E (GPa)	$\sigma$ (MPa)	$\epsilon$ (%)	$K_{IC}$ (MN m $^{-3/2}$ )
Cortical bone	7-30	50-150	1-3	2-12
Cancellous bone	0.05-0.5	10-20	5-7	
Co-Cr alloys	230	900-1540	10-30	~100
Austenitic stainless steel	200	540-1000	6-70	~100
Ti-6Al-4V alloy	106	900	12.5	~80
Alumina	400	450	~0.5	~3
Hydroxyapatite	30-100	60-190		~1
Polyethylene	1	30	>300	

E : Young's modulus

$\epsilon$ : elongation at fracture

$\sigma$  : tensile strength (in the case of alumina: flexural strength)

$K_{IC}$  : fracture toughness

The mechanical behaviour of bone may be assessed on whole bones *in vivo*. But the results obtained are difficult to interpret due to irregular shapes of bones and the organizational hierarchy in bones. Normally, mechanical properties of bone (cortical or cancellous) are determined *in vitro* using standard or miniature specimens that conform to various standards originally designed for engineering materials such as metals and plastics. The conditions required to prepare and test dead bone specimens so as to give meaningful results representative of living bone have been well established. It is very important to maintain water content of bone for mechanical assessment as the behaviour of bone in the "wet" condition significantly differs from that of bone in a dry state (Figure 2). In the quasi-static testing condition, a tensile test of "wet" cortical bone at ambient temperature gives a stress-strain curve exhibiting a small viscoelastic component and culminating in brittle fracture at a total strain of 0.5-3.0%. As a result of orientation, location and age, cortical bone has a range of associated properties rather than a unique set of values (Table 1). Young's modulus of bone ranges between 7 and 30 GPa. It can also be seen from Table 1 that bone is significantly less stiff than the various alloys and ceramics currently utilized as prosthetic materials, but is stiffer than biomedical polymers. Cortical bone fractures in a brittle fashion, with the ultimate tensile strength being 50 to 150 MPa.

It has been shown that fracture toughness, an important parameter for brittle solids, of bone is considerably lower than those of metallic implant materials. The structure and properties of cancellous (or spongy) bone are also well understood and documented [6].

A good understanding of the structure and properties of bone gives structural features and provides the range for approximating mechanical compatibility that is required of a bone analogue material for an exact structural replacement of bone with a stabilized bone-implant interface. It is important to bear in mind, however, that bone is unlike any engineering material in that it can alter its properties and configuration in response to changes in mechanical demand.

### BIO-STABLE COMPOSITES

As bone is an apatite-collagen composite material at the ultra-structural level, a polymer matrix composite containing a particulate, bioactive component appears a natural choice for substituting cortical bone. Bonfield *et al* pioneered the use of hydroxyapatite (HA) particles as the bioactive and strengthening phase in polymers to produce bone analogues [7].

Hydroxyapatite (HA,  $\text{Ca}_{10}(\text{PO}_4)_6(\text{OH})_2$ ) closely resembles bone apatite and exhibits excellent bioactivity. Polyethylene (PE) is a proven biocompatible polymer and hence widely used in orthopaedics. It is therefore natural to combine the two materials to produce a composite that mimics the structure and matches mechanical properties of cortical bone. The ductile polyethylene allows the incorporation of relatively high volume percentages of HA particles in the polymer matrix, which is essential for obtaining bioactivity of the composite. As no other materials are used, all components of the composites are biocompatible.

HA/HDPE composites containing up to 45 vol% (i.e. 73 wt%) of HA can be routinely made through standardised procedures [8, 9]. The process for manufacturing HA/HDPE composites consists of compounding, powdering (or pelletising) and compression moulding (or injection moulding). Both commercially available HA powders and particulate HA produced in-house have been used to produce HA/HDPE composites. Either a twin screw extruder [8] or an internal mixer [9] was used for compounding the materials efficiently. Powdering of compounded materials usually took place in a centrifugal mill at below -100°C. Compression or injection moulding could produce bulk materials for prostheses or some small medical devices. Composites plates as thick as 20mm could be made by compression moulding. These plates were voids-free, as was revealed by X-ray radiographs.

Rheological studies revealed that the incorporation of particulate HA into HDPE resulted in an increase in the viscosity of composites at their processing temperatures [9]. The presence of the HA particles restricted molecular mobility of HDPE under shear and hence resulted in higher viscosity. This increase in viscosity was more pronounced at low shear rates. With an increase in shear rate, the viscosity of HA/HDPE composites approached that of the unfilled HDPE. Both HDPE and HA/HDPE composites showed pronounced shear thinning behaviour. HA/HDPE composites at their processing temperatures exhibited discontinuity with a varying shear rate. As the HA content in the composites increased, the shear rates at which discontinuity occurred were reduced. The die swell ratio of HA/HDPE composites was reduced as the HA content was increased. It is possible that the presence of HA particles in the polymer matrix reduced the degree of recoil of the HDPE molecular chains and hence led to the reduction in swelling of composites. Analysis of rheological behaviour of HA/HDPE composites is important for optimising composite processing conditions and for producing high quality net-shape (or near near-shape) devices.

SEM examinations of polished HA/HDPE surfaces showed that after the compounding process, HA particles were well dispersed, exhibiting a homogeneous distribution in the polymer matrix (Figure 3). Subsequent composite processing by compression moulding or injection moulding preserved these characteristics. This uniform distribution of HA particles in composites is essential for mechanical as well as biological performance of implants. Using the image analysis technique and stereology, it was possible to calculate the average volume diameter of HA particles in composites from SEM micrographs (i.e., from two-dimensional images to three-dimensional projections). The calculations indicated that the high shear forces generated during the compounding process broke up HA particle agglomerates into unit particles in the polymer matrix [10]. The average volume diameter of HA particles in compounded HA/HDPE was nearly the same as the mean particle size of HA powder used for producing the composites. SEM examinations of tensile fracture surfaces suggested that in the composites there was only mechanical bond between HA particles and HDPE matrix resulting from the shrinkage of HDPE around individual HA particles during thermal processing [8,11].

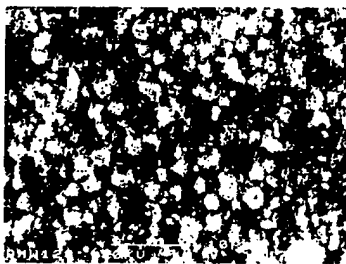


Figure 3 Uniform distribution of HA particles in HA/HDPE composite containing 40vol% of HA [8]

It was found that compounding caused slight decreases in the weight average molecular mass ( $M_w$ ) of HDPE, with the decrease being dependent on the HA volume percentage [11]. Further thermal processing by compression or injection moulding also reduced  $M_w$ . Differential scanning calorimetry (DSC) results indicated that the addition of HA particles caused decreases in the degree of crystallinity of HDPE, with composites of higher HA contents having lower degrees of crystallinity for the polymer matrix [12].

Thermogravimetric analysis (TGA) was used to determine the real HA content in HA/HDPE composites. Calculations made from TGA curves showed that the difference between the actual mass percentages of HA in the composites produced and the "Rule of Mixtures (ROM)" values was negligible and hence the intended compositions had been achieved [9, 12].

By varying the amount of HA in the composites, a range of mechanical properties of the composites could be obtained. An increase in the HA volume percentage led to increases in the Young's modulus, shear modulus and tensile strength of HA/HDPE, with a corresponding decrease in the strain to fracture [8, 13]. The particle morphology and average particle size of HA were found to affect mechanical properties of HA/HDPE composites [13]. HA/HDPE with 45vol% of HA possessed a Young's modulus value of 5.54GPa, which approaches the lower bound for cortical bone (Table 2). HA/HDPE composites containing 40vol% or more of HA appeared to be suitable for bone substitution, with the actual composite to be used being dependent on the nature of bone being replaced and the applied physiological load.

Table 2 Mechanical properties of HA/HDPE composites and cortical bone

HA Volume (%)	E (GPa)	G (GPa)	$\sigma$ (MPa)	$\epsilon$ (%)
0	0.65 $\pm$ 0.02	0.28 $\pm$ 0.10	17.89 $\pm$ 0.29	>360
10	0.98 $\pm$ 0.02	0.39 $\pm$ 0.16	17.30 $\pm$ 0.27	>200
20	1.60 $\pm$ 0.02	0.48 $\pm$ 0.07	17.77 $\pm$ 0.09	34.0 $\pm$ 9.5
30	2.73 $\pm$ 0.10	0.71 $\pm$ 0.17	19.55 $\pm$ 0.20	6.4 $\pm$ 0.5
40	4.29 $\pm$ 0.17	1.18 $\pm$ 0.07	20.67 $\pm$ 1.56	2.6 $\pm$ 0.4
45	5.54 $\pm$ 0.62	1.46 $\pm$ 0.26	18.98 $\pm$ 2.11	1.9 $\pm$ 0.2
Cortical bone*	7-30	$\sim$ 3.2	50-150	1-3

E : Young's modulus    G : shear modulus     $\sigma$  : tensile strength     $\epsilon$  : elongation at fracture

\* E,  $\sigma$  and  $\epsilon$  values from Ref.2; G value from Ref.14.

The creep behaviour of HA/HDPE composites was investigated using a three-station tensile creep machine [15, 16]. The inclusion of HA particles in HDPE improved the short-term creep resistance when specimens were subjected to similar stresses, and an increase in the HA volume percentage increased creep resistance. However, creep failure of composites could occur at long times due to debonding at the HA-HDPE interface. The immersion in Ringer's solution reduced the creep resistance of HA/HDPE composites. The decrease in creep resistance was found to be a function of HA volume percentage [16]. This effect was due to the penetration of fluid into the composites.

Biaxial (i.e., axial and torsional) fatigue tests were conducted for HA/HDPE composites [17]. A fixed axial component of 50% of ultimate tensile strength (UTS) with the torsional component varying from 0% to 50% of ultimate shear strength (USS) was used for fatigue tests. Generally, the fatigue life of HDPE and the composites was reduced with an increasing shear stress in the biaxial stress condition. The addition of particulate HA in HDPE led to shorter fatigue life in low shear stress conditions. In high shear stress conditions, the effects of shear stress became dominant and the fatigue life of both HDPE and HA/HDPE was about the same.

Tribological properties of HA/HDPE composites were evaluated against duplex stainless steel under dry and lubricated conditions [18]. Lubricants used were distilled water and aqueous solutions of proteins (egg albumen or glucose). HA/HDPE composites appeared unsuitable for implants with articulating surfaces due to the formation of an abrasive slurry of HA in the lubricants.

The biological performance of implant materials can be evaluated by *in vitro* tests, using simulated body fluid or cell cultures, or by *in vivo* assessments. In *in vitro* experiments using human osteoblast cell primary cultures, it was observed that the osteoblast cells attached to "islands" of HA in the composites and subsequently proliferated, which clearly showed the biocompatibility and bioactivity of HA/HDPE composites [19].

For *in vivo* experiments, following sterilization by  $\gamma$  irradiation, machined pins ( $\Phi$ 2.4mm $\times$ 5mm) of HA/HDPE composites were implanted in the lateral femoral condyle of adult New Zealand white rabbits [20]. It was demonstrated that cortical and cancellous bones responded positively to the presence of HA/HDPE implants by localized apposition adjacent to the implant surface. After six month implantation, the areas of direct bone apposition, as measured from histological sections, had reached 40% of the implant surface. The mechanical compatibility of the HA/HDPE composite with natural bone had resulted in the absence of significant relative movement at the bone-implant interface, thus encouraging bone growth

around the implant. Ultra-microtomed specimens were prepared for the TEM examination of the bone-implant interface [21]. At one month, the new bone was mainly seen adjacent to the interface where HA particles were present. At six months, the bone tissue was seen growing along the whole length of composite implant including exposed HA particles and polyethylene matrix. The image of lattice planes at the bone-implant interface after three months implantation is shown in Figure 4, exhibiting continuity across the interface and thus indicating epitaxial growth of apatite crystals from the implant.



Figure 4 High resolution TEM image of the bone-implant interface for a HA/HDPE implant (The interface between the bone region B and composite C is marked with arrows.) [21]

Since the late 1980s, subperiosteal orbital floor implants made from HA/HDPE composites have been used in the correction of volume deficient sockets and in orbital floor reconstruction following trauma [22, 23]. All the implants remained in position and no infection or extrusion occurred. Clinical examinations found the implants to feel stable. After six months implantation, computer tomography (CT) was unable to detect any gap between the implant and the bone, implying at least partial integration of the implant with the orbital floor, which accounted for the marked implant stability. More recently, middle ear implants were made from HA/HDPE composites and satisfactory clinical results have been obtained [24].

To improve mechanical properties of HA/HDPE composites for load bearing implant applications, hydrostatic extrusion of the composites was investigated [25]. It was found that higher extrusion ratios led to higher Young's modulus and tensile strength of HA/HDPE composites which are inside the bounds for mechanical properties of cortical bone. The fracture strain of HA/HDPE was also substantially increased by hydrostatic extrusion. Hydrostatically extruded HA/HDPE containing 40vol% of HA possessed a strain to fracture which was far greater than that of human cortical bone (9.4% vs. 1-3%). Furthermore, the bioactivity of the composites was retained after extrusion. Therefore, HA/HDPE further processed via hydrostatic extrusion exhibits great potential for major load bearing applications. An alternative method to enhance mechanical properties of the composites, i.e., using coupling agents for the composites, was also investigated [26]. However, only marginal improvements were achieved.

Apart from polyethylene, there are a few other biomedical polymers that could be used for producing bone analogue materials. Polysulfone (PSU) is an amorphous polymer which possesses high specific strength and modulus. To develop bioactive composites for load bearing prostheses, PSU may be a better choice for the matrix of a composite than HDPE as its strength and modulus are significantly higher [27], which can provide a higher baseline for composite properties. Other favourable properties of PSU are low creep rate, resistance to oxidation, excellent resistance to hydrolysis or reduction of molecular weight, stability in aqueous inorganic acids, alkalies and salt solutions, and bioinertness. Furthermore, PSU has high resistance to  $\beta$ -,  $\gamma$ -, X- and IR-radiation and can be steam-sterilised. Therefore, HA/PSU composite has been

developed as a new tissue replacement material [28]. The production of HA/PSU composite followed the same procedure as that for manufacturing HA/HDPE composites [9]. HA/PSU composite containing up to 40vol% of HA was produced. HA particles were also well dispersed in the PSU matrix. Thermogravimetric analysis (TGA) verified the amount of HA in the composite. Density close to the theoretical value was achieved for the composite, indicating a void-free structure. Rheological analysis revealed that PSU and the composite exhibited pseudoplastic flow behaviour at processing temperatures. With an increase in HA content, stiffness of HA/PSU composite also increased. Mechanical properties of HA/PSU composite are within the lower bound for bone. Just as for the HA/HDPE composites, in biaxial fatigue testing, the torsional stress significantly reduced the fatigue life of HA/PSU composite [17].

In order to establish a stronger implant-bone bond within a shorter period of time, glass or ceramics that are more bioactive than HA, such as Bioglass® and A-W glass-ceramic, could be used as the bioactive phase in composites. Bioglass® is a family of bioactive glasses that elicit specific physiological responses, including the provision of surface-reactive silica, calcium and phosphate groups, and alkaline pH levels, at interfaces with tissues. A particular advantage of Bioglass® is its ability to bond to both hard and soft tissues. A-W glass-ceramic has excellent mechanical properties while possessing good bioactivity. Using the technology for HA/HDPE composites, Bioglass® or A-W glass-ceramic reinforced polyethylene composites were produced [29, 30]. It was found that Bioglass® particles were well dispersed and a reasonably homogeneous distribution of the particles in the polymer matrix was achieved. Composite with up to 30vol% of Bioglass® exhibited levels of elastic compliance, tensile strength and fracture strain comparable to those of soft connective tissues. Composite with Bioglass® volumes in excess of 30vol% possessed mechanical properties comparable to cancellous bone. In *in vitro* experiments, osteoblast cells were found to attach to Bioglass® particles in the composite (Figure 5), indicating excellent biocompatibility and bioactivity of the composite.



Figure 5 Osteoblast cells attaching to Bioglass® particles in the Bioglass®/HDPE composite [19]

## BIODEGRADABLE COMPOSITES

In recent years, emphasis in biomaterials engineering has moved from materials that remain stable in the biological environment to materials that can alter their properties (i.e., "biodegrade") in response to the cellular environment. Biodegradable materials are designed to degrade gradually in the body and will be replaced eventually by newly formed tissues. After implantation in the body, a biodegradable bone substituting material will have gradual decreases in strength and stiffness over a clinically determined optimal period. As bone repairs itself, the

external load will be transferred from the biodegrading implant to bone. This approach provides the best biomaterials solution to tissue replacement and regeneration, if requirements for the initial stiffness and strength and other short-term properties can be met. Polyhydroxybutyrate (PHB) is a natural polymer and is degradable in the body. Therefore, biodegradable composites based on PHB and its co-polymers were produced [31, 32] for potential clinical applications using the technology for making composites such as HA/HDPE and HA/PSU.

With the established processing technology, particulate bioceramics (HA or TCP) could be homogeneously distributed in the PHB matrix for both HA/PHB and TCP/PHB composites containing up to 30vol% of the bioceramic. The stiffness of the composites increased with an increase in bioceramic content. In *in vitro* experiments using a simulated body fluid (SBF), bone-like apatite formed on HA/PHB and TCP/PHB composites (Figure 6), which was indicative of bioactivity of these materials *in vivo*. The height of bone-like apatite peaks in thin-film XRD (TF-XRD) patterns increased with the increase in immersion time in SBF (Figure 7), indicating the growth of apatite *in vitro*. Dynamic mechanical analysis (DMA) results showed that the storage modulus of HA/PHB and TCP/PHB composites increased initially with an increase in immersion time, which was due to the formation of the dense apatite layer on composite surfaces. However, with prolonged immersion in SBF (i.e., beyond 2 months), both HA/PHB and TCP/PHB composites exhibited decreases in storage modulus. These decreases indicated the degradation of composites in the simulated body environment. Both HA/PHB and TCP/PHB composites have the potential for tissue regeneration applications.

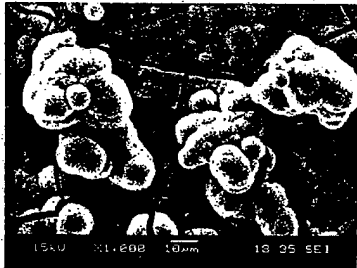


Figure 6 Bone-like apatite layer formed *in vitro* on 30vol% HA/PHB composite after immersion in SBF for 3 days

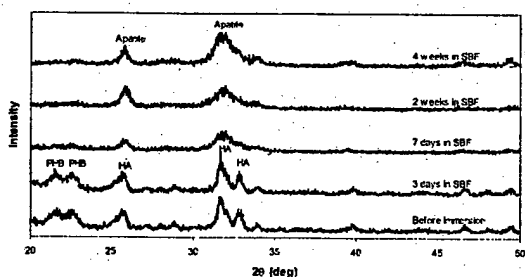


Figure 7 TF-XRD patterns of 30vol% HA/PHB composite before and after immersion in SBF

Chitin is another naturally occurring polymer that can be used for degradable composites. It is an important constituent of the exoskeleton of crustacea, molluscs and insects. Chitin as a

natural polymer is biodegradable due to its  $\beta$ -1,4 glycosidic linkages being susceptible to the lysozyme present in the human body. HA/chitin composite could be produced using the solution casting technique, with a homogeneous distribution of HA particles in the composites being achieved [33]. The solution casting process did not change the crystalline structure of chitin. TGA results indicated that intended compositions were achieved for the composite. Tensile testing results revealed that the strength and modulus of HA/chitin composite decreased with an increase in the amount of particulate HA in the composite. SEM examination of fracture surfaces showed that HA particles were separated from the chitin matrix completely after tensile tests. These results suggested that there was no chemical bond between the two constituents of the composite. *In vitro* mineralisation experiments showed that HA particles rendered the composite bioactive and significantly improved the ability of composites to induce the formation of bone-like apatite on their surfaces. Degradation of chitin in the simulated body environment was observed.

### SUMMARY

Using body tissues as templates, various bioactive ceramic-polymer composites have been developed over the last two decades for tissue replacement and tissue regeneration. Each of these composites has its distinctive characteristics and may be used in specific clinical situations. Biostable composites have gained success for tissue replacement. Biodegradable composites appear to provide the best biomaterials solution for tissue substitution and there is still a large scope for developing this type of composites. The advances in materials science and technology certainly aid in further research into bioactive composites for medical applications.

### ACKNOWLEDGEMENTS

The author would like to thank his colleagues and students in the University of London, UK, and Nanyang Technological University, Singapore, for their assistance and discussions. Funding for the research in bioactive composites from various sources (research councils and industrial partners) is gratefully acknowledged.

### REFERENCES

1. W.Bonfield, *Metals and Materials*, Vol.3 (1987), 712-716
2. W.Bonfield, M.Wang, K.E.Tanner, *Acta Materialia*, Vol.46 (1998), 2509-2518
3. W.Bonfield, *Bioceramics*, Vol.8, (1995), 375-380
4. J.B.Park, *Biomaterials: An Introduction*, Plenum Press, New York, (1979)
5. F.G.Evans, M.Lebow, *American Journal of Surgery*, Vol.83 (1952), 326-331
6. L.J.Gibson, M.F.Ashby, *Cellular Solids: Structure and Properties*, 2<sup>nd</sup> Edition, Cambridge University Press, Cambridge, (1997)
7. W.Bonfield, M.D.Grynpas, A.E.Tully, J.Bowman, J.Abram, *Biomaterials*, Vol.2 (1981), 185-186
8. M.Wang, D.Porter, W.Bonfield, *British Ceramic Transactions*, Vol.93 (1994), 91-95
9. F.Tang, M.Wang, *Proceedings of the 8<sup>th</sup> International Conference on Processing and Fabrication of Advanced Materials*, Singapore, (1999), 299-306
10. M.Wang, W.Bonfield, *Polymer Processing Towards AD2000*, Singapore, (1996), 203-204

11. M.Wang, R.Joseph, W.Bonfield, *Biomaterials*, Vol.19 (1998), 2357-2366
12. F.Tang, C.H.Ng, M.Wang, *Proceedings of the International Conference on Thermophysical Properties of Materials*, Singapore, (1999), 502-508
13. M.Wang, C.Berry, M.Braden, W.Bonfield, *Journal of Materials Science: Materials in Medicine*, Vol.9 (1998), 621-624
14. Y.C.Fung, *Biomechanics: Mechanical Properties of Living Tissues*, 2<sup>nd</sup> Edition, Springer-Verlag, New York, (1993)
15. J.Suwanprateeb, K.E.Tanner, S.Turner, W.Bonfield, *Journal of Materials Science: Materials in Medicine*, Vol.6 (1995), 804-807
16. J.Suwanprateeb, K.E.Tanner, S.Turner, W.Bonfield, *Journal of Materials Science: Materials in Medicine*, Vol.8 (1997), 469-472
17. M.Wang, B.Chua, F.Tang, *Proceedings of the 10<sup>th</sup> International Conference on Biomedical Engineering*, Singapore, (2000), 219-220
18. M.C.Neo, M.Chandrasekaran, M.Wang, N.L.Loh, W.Bonfield, *Bioceramics*, Vol.12, (1999), 449-452
19. J.Huang, L.Di Silvio, M.Wang, K.E.Tanner, W.Bonfield, *Journal of Materials Science: Materials in Medicine*, Vol.8 (1997), 775-779
20. W.Bonfield, J.C.Behiri, C.Doyle, J.Bowman, J.Abram, in *Biomaterials and Biomechanics*, Edited by P.Ducheyne, G.Van der Perre and A.E.Aubert, Elsevier Science Publishers, Amsterdam, (1984), 421-426
21. W.Bonfield, Z.B.Luklinska, in *The Bone-Biomaterial Interface*, Edited by J.E.Davies, University of Toronto Press, Toronto, (1991), 89-93
22. R.N.Downs, S.Vardy, K.E.Tanner, W.Bonfield, *Bioceramics*, Vol.4, (1991), 239-246
23. K.E.Tanner, R.N.Downs, W.Bonfield, *British Ceramic Transactions*, Vol.93 (1994), 104-107
24. R.E.Swain, M.Wang, B.Beale, W.Bonfield, *Biomedical Engineering: Applications, Basis & Communications*, Vol.11 (1999), 315-320
25. M.Wang, I.M.Ward, W.Bonfield, *Proceedings of the 11<sup>th</sup> International Conference on Composite Materials*, Gold Coast, Australia, (1997), Vol.1, 488-495
26. M.Wang, S.Deb, K.E.Tanner, W.Bonfield, *Proceedings of the 7<sup>th</sup> European Conference on Composite Materials*, London, U.K., (1996), Vol.2, 455-460
27. J.Black, G.Hastings, (eds.), *Handbook of Biomaterial Properties*, Chapman & Hall, London, (1998)
28. B.Chua, M.Wang, *MRS Symposium Proceedings*, Vol.599, (1999), 45-50
29. M.Wang, W.Bonfield, L.L.Hench, *Bioceramics*, Vol.8, (1995), 383-388
30. M.Wang, T.Kokubo, W.Bonfield, *Bioceramics*, Vol.9, (1996), 387-390
31. M.Wang, C.X.Wang, J.Weng, J.Ni, *Transactions of the 6<sup>th</sup> World Biomaterials Congress*, Hawaii, USA, (2000), 81
32. M.Wang, J.Weng, C.H.Goh, J.Ni, C.X.Wang, *Bioceramics*, Vol.13, (2000), 741-744
33. J.Weng, M.Wang, *Bioceramics*, Vol.13, (2000), 657-660

**Effects of Counterface Roughness and Conformity on the Tribological Performance of Crosslinked and Non-crosslinked Medical-Grade Ultra-High Molecular Weight Polyethylene**

**A. D. Chawan,<sup>1</sup> A. M. Chakravartula,<sup>1</sup> J. Zhou,<sup>1</sup> L. A. Pruitt,<sup>1,3</sup> M. Ries,<sup>2</sup> and K. Komvopoulos<sup>1</sup>**

<sup>1</sup>Department of Mechanical Engineering, University of California, Berkeley, CA 94720

<sup>2</sup>Department of Orthopaedics, University of California, San Francisco, CA 94131

<sup>3</sup>Department of Bioengineering, University of California, Berkeley, CA 94720

**ABSTRACT**

The tribological behavior of crosslinked ultra-high molecular weight polyethylene (UHMWPE) was compared to that of non-crosslinked UHMWPE, used as control sample. A reciprocating pin-on-disk tribometer was used to determine the effects of countersurface roughness and conformity on wear mechanisms occurring during the initial stage of sliding. Pin samples of two different radii of curvature were slid against medical-grade Co-Cr alloy disks with surface roughness ranging from 0.005 to 0.04  $\mu\text{m}$  in a lubricant of bovine serum. Normal loads were chosen to provide physiological contact stresses. The focus of this study was on the dependence of early wear mechanisms on surface roughness and conformity. Although a correlation between coefficient of friction data and dominant wear mechanisms was not observed, different wear mechanisms were found between control and crosslinked UHMWPE. The results of this study provide insight into the differences of the initial wear behavior of non-crosslinked and crosslinked UHMWPE used in total joint replacements.

**INTRODUCTION**

Ultra-high molecular weight polyethylene (UHMWPE), articulating against a ceramic or metal counterpart, is the prime load-bearing material system in most total joint replacements. While the intrinsic mechanical properties of UHMWPE make this polymer well suited for this purpose, methods to further improve the *in vivo* mechanical behavior of UHMWPE are still under development, the principal objective being to reduce the amount of submicron-sized polymer wear particles generated through joint motion. Accumulation of such fine wear debris elicits a foreign body response leading to osteolysis, and eventually to loosening of the prosthesis necessitating revision surgery. Increasing the wear resistance of the polymer surface is thus a high priority in the area of orthopaedics research, as it can be correlated to an increase of the expected life of total joint replacements.

UHMWPE is a semicrystalline polymer. In its non-crosslinked form it is about 50% crystalline. The amorphous phase is well above its glass transition temperature, rendering the polymer susceptible to chain orientation or texture development under contact sliding conditions. Polymer chains in bulk UHMWPE exhibit random orientation. Chain crosslinking through chemical means or radiation results in decreased crystallinity (~20%) and inhibits polymer chain reorientation near the surface in a direction parallel to the direction of sliding. Since such chain re-arrangement is the precursor to wear in non-crosslinked polyethylene [1,2], restricting polymer chain movement should increase the wear resistance of the polymer surface. Although the surface wear resistance of polyethylene can be improved by treatments inducing crosslinking,

studies have shown that other bulk mechanical properties may be degraded, such as fracture toughness [3].

Variations in the wear behavior of crosslinked and non-crosslinked polyethylene may be encountered due to significant microstructural differences. Insight into the micromechanics of crosslinked polyethylene may enhance more accurate prediction of *in vivo* behavior and perhaps also lead to improved treatments of the polymer. While several studies have been devoted to characterizing and comparing the wear rates of UHMWPE in both crosslinked and non-crosslinked conditions, very little is known about the effect of roughness and conformity on the early stage of the wear process. Slight increases in surface roughness of the material articulating against the UHMWPE surface have been found to significantly increase the wear rate [4]. Therefore, the main objective of this study was to investigate the initial wear mechanisms of medical-grade UHMWPE sliding against polished Co-Cr alloy disks in bovine serum under contact pressures typical of knee joints.

## EXPERIMENTAL METHODS

### Specimens

Two types of UHMWPE microstructures were examined in this study: non-crosslinked UHMWPE obtained from tibial inserts (Smith & Nephew, Memphis, TN) and crosslinked UHMWPE obtained from Durasul™ tibial components (Sulzer Orthopedics, Austin, TX). Crosslinking was performed at  $\sim 100$  kGy of electron beam radiation at a temperature below melt, followed by melt annealing at  $150$  °C. Ethylene oxide (EtO) gas was used to sterilize both polymer materials used in this study. A total of 15 pins of length 19.1 mm were machined from the tibial components of each material. To study the role of surface conformity in total joint replacements, the ends of seven pins from each group were machined to hemispherical shapes of radius equal to 3.2 mm, and those of the remaining eight pins to radius equal to 7.9 mm. The ends of each pin were then polished with fine polishing cloth to remove gross machining marks.

Flat disks of diameter 63.5 mm and thickness equal to 7.9 mm, machined from F77 Co-Cr alloy (Depuy Orthopaedics, Warsaw, IN), were used as the counterpart material. Tests were performed using two surface conditions. The first corresponded to an orthopaedic-grade surface finish, and the second represented a roughened surface, similar to those seen in retrieved Co-Cr femoral components [5]. Four of the seven disks were roughened using 600-grit SiC abrasive paper. This procedure created sharp surface features on the counterpart that have been shown to be an important factor contributing to the increase of the wear rate of UHMWPE [6].

For each disk, the average surface roughness with respect to the mean profile line,  $R_a$ , and peak surface height above the mean line,  $R_{peak}$ , were measured using a Dektak IID mechanical stylus profilometer (Sloan Technology Co., Santa Barbara, CA), equipped with a 12.5- $\mu\text{m}$  radius tip, having a vertical resolution of 0.5 nm.  $R_{peak}$  gives statistical information about asperity heights above the zero-height plane. Measurements were obtained over 4 mm scan lengths at ten different locations of each disk surface, where reciprocating sliding with the pins occurred during subsequent wear testing. Mean and standard deviation values of the surface roughness parameters of each disk used in this study are given in Table I. The calculations were based on the assumption that the roughness data followed normal distributions.

### Experimental Apparatus and Microscopy

A reciprocating pin-on-disk tribometer was used for wear testing. Previous studies have demonstrated that unidirectional sliding does not yield wear rates for UHMWPE relevant to those expected *in vivo* [7]. In the tribometer used in this study, the direction of sliding was reversed after 90° rotation. The friction force between the pin and disk surfaces was continuously recorded by strain gauges that measured the horizontal deflection of the arm holding the pin. The rotational speed was chosen to produce a maximum linear velocity of 35 mm/s for all specimens. In order to keep the rotational speed constant throughout the study, the stroke length of different tests was varied from 15.7 to 37.68 mm. One sliding cycle corresponded to a total distance of sliding equal to 35 mm. The pin was held stationary above the rotating disk under a constant normal load of 10.29 N. The lubricant used in this study was Hyclone Alpha Calf Fraction serum diluted 1:1 with distilled water and 0.1 wt% sodium azide, resulting in a protein concentration of 23 mg/mL. Sodium azide was added to prevent degradation of the bovine serum. The protein concentration corresponds to levels found in healthy synovial joints [8]. All tests were conducted at room temperature and relative humidity typically in the range of 40%-50%.

**Table I.** Surface roughness of Co-Cr disk specimens

Disk #	$R_a$ ( $\mu\text{m}$ )	$R_{peak}$ ( $\mu\text{m}$ )
1	0.028 $\pm$ 0.004	0.167 $\pm$ 0.099
2	0.029 $\pm$ 0.003	0.108 $\pm$ 0.028
3	0.042 $\pm$ 0.007	0.518 $\pm$ 0.128
4	0.031 $\pm$ 0.002	0.377 $\pm$ 0.079
5	0.005 $\pm$ 0.001	0.066 $\pm$ 0.027
6	0.031 $\pm$ 0.003	0.372 $\pm$ 0.044
7	0.007 $\pm$ 0.002	0.082 $\pm$ 0.042

The apparent mean contact pressure  $\bar{p}$  between the pin and the disk surfaces was approximately determined using classical Hertz theory. For hemispherical pin and flat disk specimens,  $\bar{p}$  is given by

$$\bar{p} = \frac{1}{\pi} \left( \frac{4E^*}{3R} \right)^{2/3} P^{1/3} \quad (1)$$

where  $P$  is the normal load,  $R$  is the radius of curvature of the hemispherical end of the pin, and  $E^*$  is the effective elastic modulus, given by  $E^* = [(1 - \nu_1^2)/E_1 + (1 - \nu_2^2)/E_2]^{1/2}$ , where  $E$  and  $\nu$  denote elastic modulus and Poisson's ratio and subscripts 1 and 2 refer to UHMWPE and Co-Cr materials, respectively. Assuming  $E_1 = 1$  GPa,  $\nu_1 = 0.45$ ,  $E_2 = 210$  GPa, and  $\nu_2 = 0.3$ , the effective elastic modulus is found to be  $E^* = 1.25$  GPa. Based on these values, the apparent mean contact pressure obtained from Eq. (1) for pin radii of 3.2 and 7.9 mm is 44.98 and 24.42 MPa, respectively, which is within the contact stress range of healthy synovial joints [9]. Since the polymer is expected to plastically deform under such pressure values, Eq. (1) yields only an approximate estimate of the apparent mean pressure.

After 2, 6, and 8 h of testing, worn polymer surfaces were observed in an Electroscan E3 environmental scanning electron microscope (ESEM) (FEI Company, Hillsboro, OR) in order to study the evolution of wear. The ESEM is an ideal instrument because UHMWPE can be

observed at electron microscope magnification levels without the need to coat the sample surfaces with a conductive layer that may alter the topography during observation.

## RESULTS AND DISCUSSION

### Coefficient of Friction

Figures 1 and 2 show typical friction coefficient responses for four representative material cases. In all experiments, the coefficient of friction evolved to a steady-state value after a relatively short sliding distance (run-in period), thus allowing for the calculation of an average steady-state value after testing for  $\sim 2$  h. Mean and standard deviation values for the steady-state coefficient of friction (obtained assuming the data followed normal distributions) are given in Table II for different pin radius (conformity) and counterface roughness. The data do not reveal a conformity effect on friction behavior. However, both polymer materials exhibit lower average steady-state friction coefficients when articulated against a smooth counterface than a rough counterface. Higher friction is expected with rough surfaces due to the greater contributions of asperity deformation and plowing friction mechanisms, although adhesion may decrease due to the reduced real contact area in the presence of a rough surface. However, if the dominant process is surface fatigue, resulting from the differential plastic flow and toughness of crystalline and amorphous phases or non-crosslinked and crosslinked microdomains, then the roughness controls the intensity and number of secondary load (asperity) cycles accumulating in each passage of the pin (primary load cycle). Fewer secondary load cycles are produced with the rougher counterface, though the stress intensity at asperity microcontacts is higher. Thus, cycle-dependent mechanisms, such as surface pitting, could be impeded during articulation against a rougher surface. This may provide explanation for the less surface damage of both crosslinked and control pins articulated against the rougher Co-Cr disk surfaces.

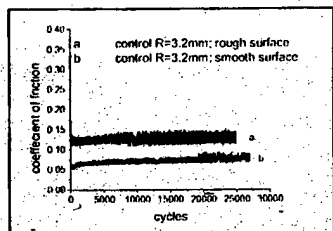


Figure 1. Coefficient of friction vs. sliding cycles for control UHMWPE.

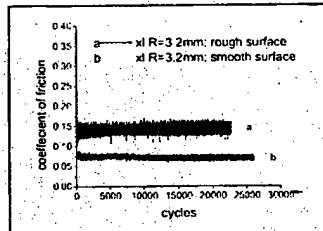


Figure 2. Coefficient of friction vs. sliding cycles for crosslinked UHMWPE.

Table II. Steady-state coefficient of friction vs. Co-Cr counterface roughness

Polymer material	Pin radius (mm)	Smooth counterface	Rough counterface
Control	3.2	$0.09 \pm 0.02$	$0.14 \pm 0.02$
Control	7.9	$0.10 \pm 0.05$	$0.16 \pm 0.06$
Crosslinked	3.2	$0.09 \pm 0.05$	$0.19 \pm 0.07$
Crosslinked	7.9	$0.11 \pm 0.07$	$0.17 \pm 0.05$

### **Wear Mechanisms**

To study the evolution of wear during the initial stage of sliding, the pin surfaces were examined after 2, 6, and 8 h of testing, corresponding to approximately 6,200, 18,500 and 24,700 sliding cycles. After 2 and 6 h of continuous sliding, the original machining and polishing marks (e.g., see Figs. 3(a) and 4(a)) were still visible, regardless of the counterface against which the pin was tested, for both crosslinked and control materials. After 8 h of testing, the surfaces of the control and crosslinked pins with radius of curvature equal to 7.9 mm did not reveal any discernible changes; however, the surface topographies of the pins with the lower conformity exhibited noticeable differences. Control pins tested against the smooth counterface revealed surface features similar to those observed by Rostoker et al. [2]. That study showed regions of plastic deformation with a striated topography, similar to those shown in Figs. 3(b)-3(d). Surface features observed in the present study, such as folding and rippling, could contribute to adhesive wear by creating regions more susceptible to rupture than the bulk material. The produced particles could then lead to third-body abrasive wear, thereby accelerating surface deterioration.

Crosslinked pins tested against the same smooth counterface showed pitting similar to that observed in crosslinked retrievals [10]. Surface pitting can be considered to be a manifestation of adhesion and surface rupture due to excessive localized plastic shearing. As discussed above, the roughness of the counterface may promote this wear mechanism. It is hypothesized that wear of the amorphous phase of UHMWPE occurs at a rate higher than that of the crystalline phase, leading to a surface consisting of protruding harder microdomains. These low-toughness surface features presumably undergo microfracture during repeated asperity sliding, leading to the surface topographies shown in Figs. 4(b)-4(d).

Neither material showed significant surface evolution against the rougher counterface. It is thought that the rougher counterface actually enhanced lubrication by providing serum paths at the contact region, thereby resulting in less wear in the early stages of sliding.

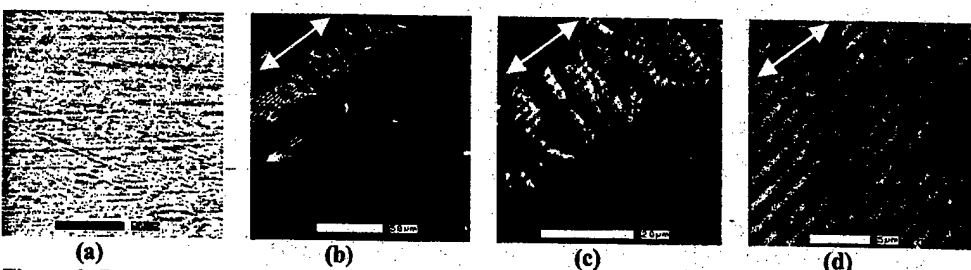


**Figure 3.** Representative ESEM micrographs of control UHMWPE surfaces obtained (a) before and (b)-(d) (representing three different magnifications) after testing for 21,300 sliding cycles against a smooth Co-Cr counterface. (Arrows denote direction of sliding.)

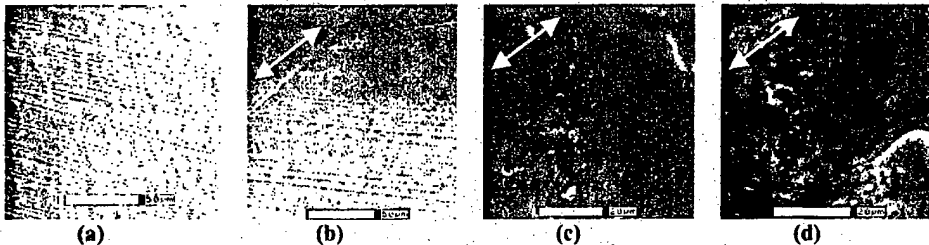


Figure 4. Representative ESEM micrographs of crosslinked UHMWPE surfaces obtained (a) before and after testing for (b) 27,000 (c) 26,200 and (d) 18,400 sliding cycles. (Sliding occurred against (b) smooth and (c); (d) rough Co-Cr counterfaces. Arrows denote direction of sliding.)

## CONCLUSIONS

Surface damage of non-crosslinked and crosslinked UHMWPE was investigated in this study. Distinct differences in surface damage modes were observed between crosslinked and non-crosslinked polymers after continuous reciprocating sliding against orthopaedic-grade Co-Cr alloy surfaces immersed in alpha calf fraction serum. Surface rippling and folding were the dominant surface deformation features on the non-crosslinked material, while crosslinked UHMWPE showed evidence of pitting and cracking. The latter behavior may be attributed to the reduced modes of plasticity of the crosslinked material. Despite the lower wear rate of the crosslinked material (afforded by the resistance to orientation softening), crosslinking may yield damage modes not possible with untreated polyethylene. Differences in plasticity between adjacent crosslinked and non-crosslinked regions may promote localized excessive shearing, leading to micropitting due to the high shear strain gradients at the boundaries of different microdomains. This highlights the need for further investigation of wear mechanisms commencing at the micro- and nano-scale. Therefore, in addition to the wear rates of different types of UHMWPE used in total joint replacements, it is essential to obtain insight into the different modes of plasticity and wear micromechanisms encountered during the early stage of sliding, and to further examine the precursors of the steady-state wear process.

## REFERENCES

- [1] C. Klapperich, K. Komvopoulos, L. Pruitt, *J. Tribology* **121**, 394-402 (1999).
- [2] W. Rostoker, E. Y. S. Chao, J. O. Galante, *J. Biomed. Mater. Res.* **3**, 317-335 (1978).
- [3] D. A. Baker, R. S. Hastings, L. A. Pruitt, *J. Biomed. Mater. Res.* **4**, 573-81 (1999).
- [4] P. S. Barbour, M. H. Stone, J. Fisher, *Proc. Inst. Mech. Eng., Part H*, **6**, 569-76 (2000).
- [5] A. P. Elfick, S. L. Smith, A. Unsworth, *J. Arthroplasty* **7**, 901-8 (2000).
- [6] P. S. Barbour, M. H. Stone, J. Fisher, *Proc. Inst. Mech. Eng., Part H*, **6**, 569-76 (2000).
- [7] C. R. Bragdon, D. O. O'Connor, J. D. Lowenstein, M. Jasty, W. D. Snyuta, *Proc. Inst. Mech. Eng., Part H*, **3**, 157-65 (1996).
- [8] H. Saari, S. Santavirta, D. Nordstrom, P. Paavolainen, Y. T. Konttinen, *J. Rheumatol.* **1**, 87-90 (1993).
- [9] D. L. Bartel, V. L. Bicknell, T. M. Wright, *J. Bone Joint Surg. (Amer.)* **7**, 1041-51 (1986).
- [10] S. Greenwald, *Annual Meeting Amer. Assoc. Orthop. Surg.*, 13-17 Feb. 2002, Dallas, TX.

**Composite Biomaterials—  
Bones and Teeth II**

**Effects of Ionic Flow and Amelogenins on the Lengthwise Growth of Octacalcium Phosphate Crystals in a Model System of Tooth Enamel Formation.**

M. Iijima<sup>1</sup>, Y. Moriwaki<sup>1</sup>, H.B. Wen<sup>2#</sup>, T. Takagi<sup>3</sup>, A.G. Fincham<sup>2</sup> and J. Moradian-Oldak<sup>2</sup>

<sup>1</sup> Asahi University School of Dentistry, Dental Materials and Technology, 1851-1 Hozumi, Hozumi-cho, Motosugi, Gifu 501-0296, Japan. <sup>2</sup> University of Southern California, School of Dentistry, Center for Craniofacial Molecular Biology, USA. <sup>#</sup> Present Affiliation : DePuy, a Johnson & Johnson company. <sup>3</sup> Tokyo Medical and Dental University, School of Dentistry, Oral Biology, Japan.

**ABSTRACT**

This paper briefly reviews our recent studies, which aimed to investigate the effects of 1) the  $\text{Ca}^{2+}$  and  $\text{PO}_4^{3-}$  ions flow and 2) amelogenins on the lengthwise growth of octacalcium phosphate (OCP), which is a potent precursor of enamel apatite crystal. OCP crystals were grown at 37°C in a dual membrane system under various amount of ionic inflow into a reaction space, using 1) 5-30mM  $\text{Ca}$  and  $\text{PO}_4$  solutions as ionic sources and 2) extracted bovine amelogenin and recombinant murine amelogenins (rM179, rM166). With an increase in the amount of  $\text{Ca}^{2+}$  and/or  $\text{PO}_4^{3-}$  ions flow, the length of OCP crystal increased, while the width decreased. As a result, the length to width (L/W) ratio of crystal changed from 3 to 95, while the width to thickness (W/T) ratio from 32 to 9. The effect of amelogenins was unique, regardless of the type of amelogenins : Rod-like and prism-like OCP crystals with large L/W (61-107) and small W/T (1.3~2.2) ratios were formed in 10% amelogenin gels. In contrast, characteristic ribbon-like OCP crystals grew without protein and with gelatin, albumin, polyacrylamide gel and agarose gel. Specific interaction of amelogenins with OCP crystal was ascribed to the self-assembly property of amelogenin molecules and their hydrophobic nature. It was suggested that ionic flow and amelogenins play some critical roles in the elongated growth of enamel crystals.

**INTRODUCTION**

Enamel crystals of mammalian tooth are formed in an enamel matrix, which is abundant in amelogenins, under regulated  $\text{Ca}^{2+}$  and  $\text{PO}_4^{3-}$  ion supply from the layer of ameloblasts. In the early stage of the enamel crystal formation, very long and thin crystallites deposit in an enamel matrix with their long axis parallel to each other. In the later stage, crystals mainly increase their width and thickness, and grow into flat-hexagonal prisms [1,2]. The morphology is quite different from the irregular shaped plate-like morphology of bone and dentin crystals. We speculate that the uniqueness of enamel crystals relates to their growth condition : 1) lattice ions of enamel crystals,  $\text{Ca}^{2+}$  and  $\text{PO}_4^{3-}$  ions, are transported from the layer of ameloblasts into the enamel matrix, which might cause ionic flow, and the mode of the ionic flow changes during the tooth enamel formation [3,4] ; 2) molecules of amelogenin, which is major component of enamel proteins [5,6] and highly hydrophobic [7], assemble into nanospheres and form gel [8-10] with unique property [11].

We have been studying the mechanism of the lengthwise and oriented growth of enamel crystals based on a hypothesis that 1) octacalcium phosphate (OCP)-like phase is initiated as a precursor of enamel apatite; 2) one directional supply of the lattice ions contribute to the lengthwise growth in the c-axis direction ; 3) amelogenin nanospheres play roles as a scaffolding matrix in the highly organized growth of enamel crystals [reviewed in 12,13]. To evaluate the hypothesis, OCP crystals were grown in a model system of tooth enamel formation, where  $\text{Ca}^{2+}$  and  $\text{PO}_4^{3-}$  ions were supplied through membranes into amelogenin gels (a dual membrane system [14-16]). The present paper shows how ionic flow and amelogenins affected the growth of OCP crystals.

**EXPERIMENTAL**

**A dual membrane system**

Reactions were carried out at 37 °C and pH6.5 for 3days in a dual membrane system [14], where a cation selective membrane (CMV<sup>TM</sup>) (Asahi Glass Co.) and a dialysis membrane (Visking Cellulose Tubing ; Union Carbide Co.) were used to control diffusion of  $\text{Ca}^{2+}$  and  $\text{PO}_4^{3-}$  ions. Membranes (about 8mm in diameter) were

attached to a Ca solution ( $\text{Ca}(\text{CH}_3\text{COO})_2 \cdot \text{H}_2\text{O}$ , 1.8ml) container. The Ca solution container was put into a  $\text{PO}_4$  solution ( $\text{NH}_4\text{H}_2\text{PO}_4 + (\text{NH}_4)_2\text{HPO}_4$ ; 1:1 molar ratio, 100ml).  $\text{Ca}^{2+}$  and  $\text{PO}_4^{3-}$  ions diffuse into the reaction space between the membranes (about 15 $\mu\text{l}$  of volume) from mutually opposite sides respectively through the CMV and the dialysis membrane. Crystals deposited on the CMV or on the both membranes depending on the solution concentration.

#### Effect of ionic flow

To evaluate the effect of ionic flow on the growth mode, crystal growth was carried out under different amount of  $\text{PO}_4^{3-}$  and  $\text{Ca}^{2+}$  ions' flux [15]. One of factors that determine the driving force of diffusion of ions through a membrane is the potential difference across it. Therefore, amount of  $\text{PO}_4^{3-}$  and  $\text{Ca}^{2+}$  ions' influx across the membrane was changed by changing concentration of phosphate solution and Ca solution used as  $\text{PO}_4^{3-}$  and  $\text{Ca}^{2+}$  ionic sources. 5, 10, or 30mM of  $\text{PO}_4$  and Ca solutions were used in different combinations.

#### Effects of amelogenins

To evaluate the effect of amelogenins, crystal growth was carried out in 10% amelogenin gels, using 10mM Ca and  $\text{PO}_4$  solutions. Three types of amelogenins were used: 1) extracted bovine amelogenin and 2) recombinant murine amelogenins, rM179 (M=20kDa) and rM166 (M=16.8kDa). About 40% of the bovine amelogenin was 20.7kDa fraction, which lack the hydrophilic C-terminal residues of the full length amelogenin [17,18], and the rest was degraded fractions with the molecular weight of about 3-8, 13, 16kDa [14]. rM179 has the hydrophilic C-terminal residues and lacks an N-terminal methionine and a phosphorylated serine residue; rM166 lacks the hydrophilic C-terminal residues present in rM179 [19]. Their purity was higher than 95% [16]. 10% amelogenin solution was put in the reaction space and 10mM of Ca and  $\text{PO}_4$  solutions were used as ionic sources. Some parallel reactions were carried out in 10% bovine serum albumin, gelatin, polyacrylamide (PAA) gel and 1% agarose gel for a comparison.

After a reaction, the precipitates still fixed on the membrane were rinsed superficially with distilled water and air dried or lyophilized when organic materials were used. Crystals were identified by an X-ray diffractometer (XRD) (Rigaku, RINT 2500). Morphology of crystals was observed by a scanning electron microscope (SEM) (Hitachi, S4500). Crystal size was measured on the SEM photographs, and their averages and standard deviations were calculated.

## RESULTS

#### Effect of ionic flow

Morphology of OCP crystal changed, depending on the concentration of Ca and  $\text{PO}_4$  solutions used as ionic sources (figure 1). Plate-like crystals grew, when 5mM solutions, which were minimum concentration to form crystals in the present condition, were used. Length of OCP crystal increased from about 13 $\pm$ 4  $\mu\text{m}$  to 91 $\pm$ 7  $\mu\text{m}$  with an increase in concentration of Ca and/or  $\text{PO}_4$  solutions. Increase in length was smaller than expected, when the solution concentration was higher than 10mM, because crystal grew on both CMV and dialysis membrane, while they grew only on the CMV when the concentrations were lower than 10mM. The width decreased under a large amount of ionic flow. The drastic change of morphology from rectangle to long ribbon is figured by the length to width (L/W) and width to thickness (W/T) ratios (figure 2): The L/W ratio changed from 3 to 95, whereas the W/T ratio changed between 32 and 8, as the concentration of Ca and/or  $\text{PO}_4$  solutions increased. Thus, longer and narrower ribbon-like crystals grew, when the amount of flux across the membranes was large.

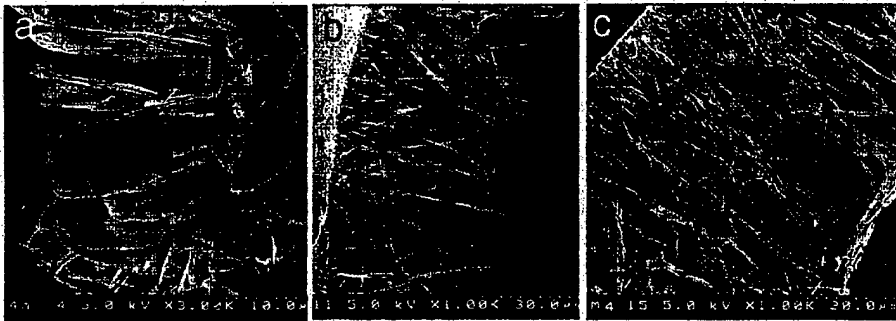


**Figure 1.** Morphology of OCP crystals grown under various amount of  $\text{PO}_4^{3-}$  and  $\text{Ca}^{2+}$  ions' influx.  
Concentration of Ca and  $\text{PO}_4$  solutions used as ionic sources are (a) Ca 5mM,  $\text{PO}_4$  5mM ; (b) Ca 5mM,  $\text{PO}_4$  30mM ; (c) Ca 10mM,  $\text{PO}_4$  30mM.

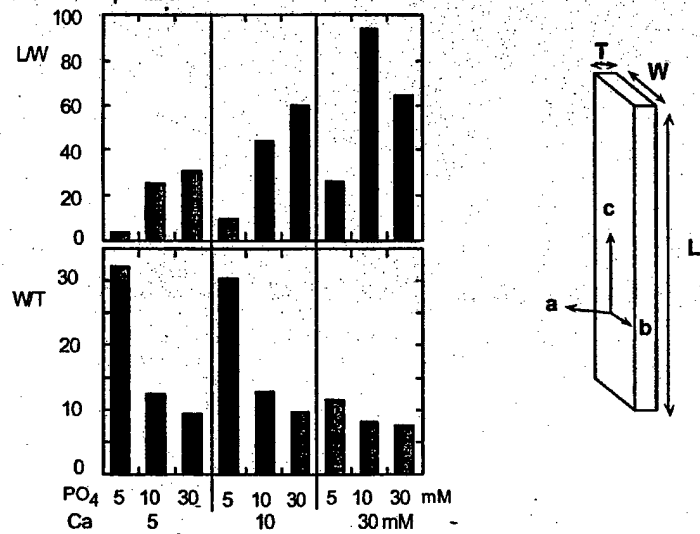


**Figure 2.** Length to width (L/W) ratio and width to thickness (W/T) ratio of OCP crystals grown under various ion flows [15]. The scheme shows morphology and crystallographic axes of OCP crystal.

#### Effects of amelogenins

The effect of amelogenins on the crystal morphology was unique (figure 3) : Ribbon-like crystals grew in the absence of organic materials (control) and in gelatin, albumin, PAA gel and agarose gel : In contrast, prism-like and rod-like crystals grew in 10% amelogenins, regardless the type of amelogenins. The XRD indicated these products are OCP with good crystallinity.

Drastic reduction in length and width of OCP crystal was caused by organic materials with different efficiency (figure 3, 4). The length decreased from  $90 \pm 8 \mu\text{m}$  (control) to  $6 \pm 2 \mu\text{m}$  (bovine amelogenins) and  $3.6 \pm 1 \mu\text{m}$  (albumin), and the width from  $2 \pm 0.5 \mu\text{m}$  (control) to  $94 \pm 35 \text{ nm}$  (bovine amelogenins) and  $83 \pm 17 \text{ nm}$  (albumin). The inhibitory activity of the bovine amelogenins in length was larger than that of rM179 and rM166. Both rM166 and

rM179 had similar effect on the growth of OCP. The inhibitory activity of amelogenins gels in length and width were larger than that of PAA gel. Whereas, the decrease in thickness caused by amelogenins gels was smaller than that caused by other materials. The inhibitory effect of albumin was the largest.

The degree of crystal size reduction in 10% amelogenins gels was in the order of width, length and thickness. This means that amelogenins suppressed the growth of OCP in the order, b-axis > c-axis > a-axis direction and that the interaction of amelogenins with the crystal face of OCP was in the order of (010) > (001) > (100).

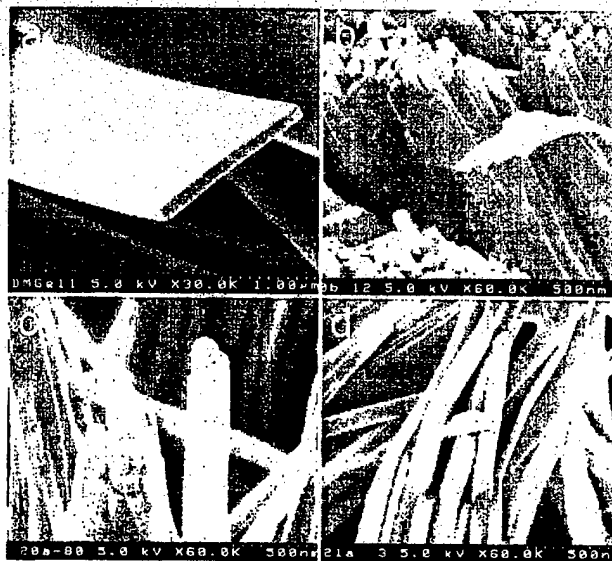


**Figure 3.** Morphology of crystals grown (a) without additives, in (b) 10% albumin, (c) 10% rM179, and (d) 10% rM166. Note that both rod-like and prism-like crystals were obtained in three types of amelogenins, i.e., bovine amelogenin, rM179 and rM166.

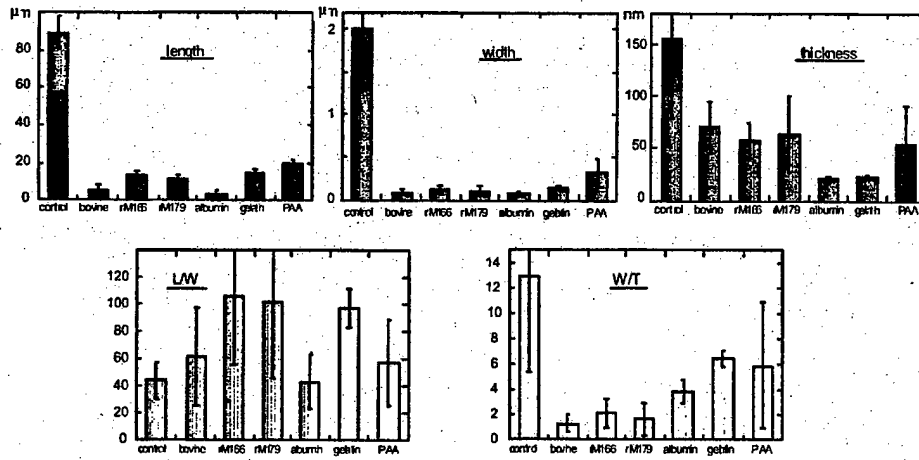


Figure 4. Length (L), width (W), thickness (T), L/W ratio and W/T ratios of OCP crystals grown without proteins and in 10% bovine amelogenins, rM179, rM166, albumin and gelatin.

The L/W and W/T ratios of the crystals (figure 4) show the unique effect of amelogenins on morphology. Bovine amelogenin, rM179 and rM166 resulted crystals with the L/W ratio larger than that of control crystals and with the smallest W/T ratio. In case of rM166 and rM179, the L/W ratio was about 2.5 times larger than and the W/T ratio was about 1/6 times smaller than those of control crystals. Gelatin also caused the elongation as well as rM166 and rM179, but the W/T ratio was 1/2 of the control crystal.

## DISCUSSION

The results of our in vitro experiments demonstrate that both ionic flow and amelogenin contributed to form OCP crystals with elongated morphology. Under a larger amount of ionic flow, the lengthwise growth was enhanced, while the growth in the width direction was reduced. OCP crystal grew preferentially in the c-axis direction, while grew less actively in the b-axis direction. The (001) face of OCP crystal was, presumably, the most active face on which ions and molecules of the lattice components were attached and subsequently OCP structure was quickly constructed in the c-axis direction. As a result, the maximum L/W ratio of crystals was about 25 times larger than that of crystal grown under the smallest ionic flow (figure 2). In the absence of organic materials, even when the ionic flow changed, crystal length and width were not reduced less than 13 and 4 μm, respectively. When the ionic flow was further decreased, i.e., when the concentration of the ionic sources were less than 5mM, there was no precipitation on the membrane. Drastic reduction in crystal size was caused by organic materials with different efficiency (figure 4).

Amelogenin gels caused a large decrease in width and small decrease in thickness of OCP crystal. As a result, decrease in W/T ratio caused by 10% amelogenin gels was larger than those caused by other organic materials used (figure 4). The W/T ratio, 1.3, was much smaller than that caused by the change in the amount of ion flow in the absence of amelogenins (figure 2). The effect of amelogenins on crystal morphology was common among bovine amelogenins, rM166 and rM179, regardless of the homogeneity of molecular weight and the existence of the hydrophilic C-terminal. This indicates that the specific interaction of amelogenins with the crystal faces of OCP related to some common factors among these amelogenins. That is hydrophobicity [14,16], because most part of amelogenin molecules are composed with hydrophobic amino acids, except the C-terminal of rM179 [20]. According to the crystal structure analysis [21], OCP has ten H<sub>2</sub>O molecules per one unit cell. Amount of H<sub>2</sub>O molecules exposed in its crystal face is in the order of (100) > (001) >> (010). Therefore, it is expected that the (100) and (001) faces are hydrophilic, while the (010) face is rather hydrophobic. The ionic arrangement in its crystal face suggests that the (100) and (010) faces are positive, while the (001) face is slightly negative. The amount of the positive charge of the (100) is higher than that of the (001). Amelogenin molecules are hydrophobic and positive at pH6.5, and they assemble into nanospheres with hydrophobic property [8-10]. AFM imaging of the

10%, 30% and 35% amelogenin gels revealed that those nanospheres were basic building block of the amelogenin gels [16,22,23]. On the other hand, PAA gel has the closed-cellular structure with the pore size of a few micron [24]. Due to the cell walls, the mechanical interference of the PAA gel was supposed to be larger than that of the amelogenin gels. Nevertheless, the decrease in length by amelogenin gels was larger than that by PAA gel. This also supports the interaction with amelogenin nanospheres with the (001) face of OCP crystal. The hydrophobic and positive nanospheres would react with the hydrophobic (010) and negative (001) faces rather than with the hydrophilic and positive (100) face. This coincides with the result that the degree of the interaction was in the order of (010) > (001) > (100).

During tooth enamel formation,  $\text{Ca}^{2+}$  and  $\text{PO}_4^{3-}$  ions are transported from the layer of ameloblasts into the enamel matrix and the mode of ionic transports change during enamel formation, accompanied with the changes in activity of these ions and the  $\text{Ca}/\text{PO}_4$  ratio [3,4]. Recent studies have postulated that amelogenin nanospheres play active roles in the elongation of enamel crystals [9,13]. In the dual membrane system, it was demonstrated that the L/W ratio was increased about 2.5 times by increasing the amount of the ionic flow and it was increased in 10% amelogenin gels 1.5-2.5 times larger than that of control crystals [14-16], thereby, indicating that the ionic flow and amelogenin gels played a key role in the lengthwise growth of OCP crystal. In a gelatin gel system, 1-2% amelogenins effectively elongated OCP crystals, which have the L/W ratio 3-5 times larger than that of control crystals [25]. The width and thickness of human enamel crystals in the early stage are 15nm and 1.5nm, respectively, and those in maturation stage are 68nm and 26nm, respectively [2]. Since enamel crystals are long, not straight and fragile, it is difficult to measure the length. It is reported that enamel crystals extend over an entire layer from the dentino-enamel junction to Tomes' processes of ameloblasts [26] and they are at least 100 $\mu\text{m}$  [27], which maybe the longest reported value. When the length and the width were 100 $\mu\text{m}$  and 15nm, respectively, the L/W is 6667. When the length and width were 100 $\mu\text{m}$  and 68nm, respectively, the L/W is 1470. The extremely large L/W ratio of enamel crystals might still require other factors/mechanism to be involved, which work to reduce the width (i.e., the growth in the b-axis direction) and to increase the length (i.e., the growth in the c-axis direction) in combination with amelogenins and ionic flow.

## CONCLUSIONS

The increase in the amount of calcium and phosphate ionic flow enhanced OCP crystal to grow longer and narrower. Organic materials reduced crystal size. The effect of amelogenins on the morphology of OCP was unique, when it was compared with albumin, gelatin, PAA, and agarose. Only 10% amelogenin gels changed the morphology from ribbon-like to prism-like with large L/W ratio and small W/T ratio. Amount of water molecules and electric charge of the (100), (010) and (001) face of OCP crystal reflected the degree of interaction with amelogenins. The present study supported the view that the ionic flow and amelogenin nanospheres play key roles in controlling the lengthwise and oriented growth of enamel crystal.

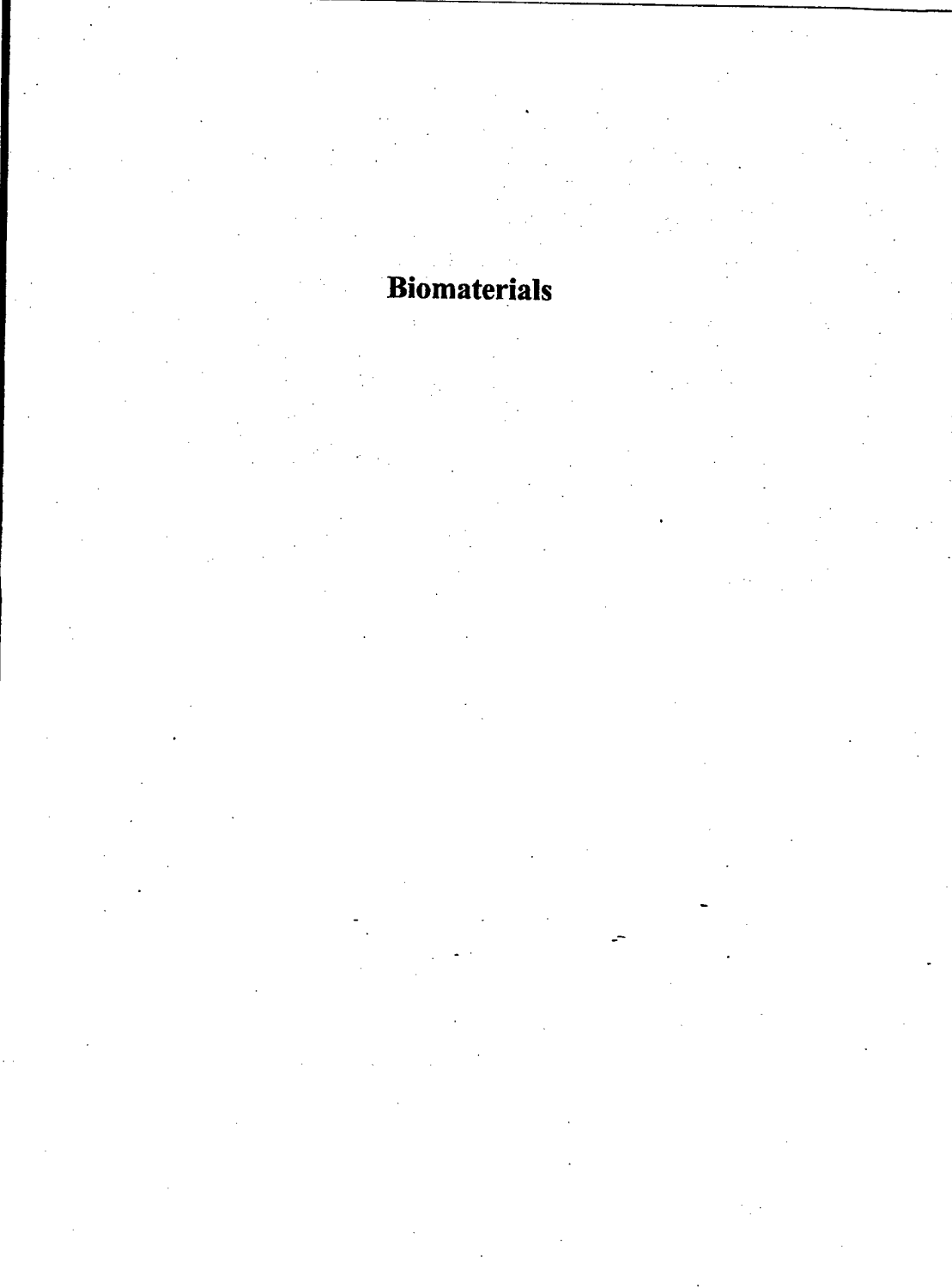
## ACKNOWLEDGMENTS

The authors acknowledge the technical assistance of Mr. Narbeh Gharakhain in protein expression and purification. This work was supported by NIH-NIDCR research grant DE12350 and DE13414 (J.M.O.) and by the Miyata Grant from Asahi University (M.I.).

## REFERENCES

1. M.U. Nylen, E.D. Eanes and K.A. Oinnel, *J. Cell Biol.* **18**, 109 (1963).
2. B. Kerebel, G. Daculsi and L.M. Kerebel, *J. Dent. Res.* **58B**, 844 (1979).
3. T. Kawamoto and M. Shimizu, *Calcif. Tissue Int.* **46**, 406 (1990).
4. T. Kawamoto and M. Shimizu, *Jpn. J. Oral Biol.* **36**, 365 (1994).
5. J.E. Eastoe, *J. Dent. Res.* **58B**, 753 (1979).
6. J.D. Termine, A.B. Belcourt, P.J. Christener, M.K. Conn and M.U. Nylen, *J. Biol. Chem.* **255**, 9760 (1980).
7. T.P. Hopp and K.R. Woods, *Proc. Natl. Acad. Sci. USA* **78**, 3824 (1981).
8. J. Moradian-Oldak, J.P. Simmer, E.C. Lau, P.E. Sarte, H.C. Slavkin and A.G. Fincham, *Biopolymers* **34**, 1339 (1994).
9. A.G. Fincham, J. Moradian-Oldak, T.G.H. Diekwiisch, D.M. Layaruu, J.T. Wright, P. Bringas and H.C. Slavkin, *J. Struct. Biol.* **115**, 50 (1995).

10. J. Moradian-Oldak, W. Leung and A.G. Fincham, *J Struct Biol.* **122**, 320 (1998).
11. G. Nikifolk and N.S. Simmons, *J. Dent. Res.* **44**, 1119 (1965).
12. M. Iijima, "Formation of Octacalcium Phosphate in vitro", *Monographs in Oral Sci Vol.18. / Octacalcium Phosphate*, ed. L.C. Chow and E.D. Eanes (Karger AG, 2001) pp17-49.
13. J. Moradian-Oldak, *Matrix Biology* **20**, 293 (2001).
14. M. Iijima, Y. Moriwaki, T. Takagi and J. Moradian-Oldak, *J. Crystal Growth* **222**, 615 (2001).
15. M. Iijima, K. Hayashi and Y. Moriwaki, *J. Crystal Growth* **234**, 539 (2002).
16. M. Iijima, Y. Moriwaki, H.B. Wen, A.G. Fincham and J. Moradian-Oldak, *J. Dent. Res.* **81**, 69 (2002).
17. T. Takagi, M. Suzuki, T. Baba, K. Minegishi and S. Sasaki, *Biochem. Biophysics. Res. Comm.* **121**, 592 (1984).
18. H. Shimokawa, Y. Ogata, S. Sasaki, M.E. Sobel, C.I. McQuillan, J.D. Termine and M.F. Young, *Adv. Dent. Res.* **1**, 293 (1987).
19. J.P. Simmer, E.C. Lau, C.C. Hu, P. Bringas, V. Santos, T. Aoba, M. Lacey, D. Nelson, M. Zeichner-David, M.L. Snead, H.C. Slavkin and A.G. Fincham *Calcif. Tissue Int.* **54**, 312 (1994).
20. T.P. Hopp and K.R. Woods, *Proc. Natl. Acad. Sci. USA* **78**, 3824 (1981).
21. W.E. Brown, J.P. Smith, J.R. Lehr and A.W. Frazier, *Nature* **196**, 1048 (1962).
22. H.B. Wen, J. Moradian-Oldak, W. Leung, P.Jr. Bringas and A.G. Fincham, *J. Struct. Biol.* **126**, 42 (1999).
23. H.B. Wen, A.G. Fincham and J. Moradian-Oldak, *Matrix. Biol.* **20**, 387 (2001).
24. R. Ruchel and M.D. Brager, *Anal. Biochem.* **68**, 415 (1975).
25. H.B. Wen, J. Moradian-Oldak and A.G. Fincham, *J. Dent. Res.* **79**, 1902 (2000).
26. T.G.H. Diekhwisch, B.J. Berman, S. Gentner and H.C. Clavkin, *Cell Tissue Res.* **279**, 149 (1995).
27. G. Daculsi, L.M. Kerebel and D. Mitre, "Enamel crystals : size, shape, and length and growing process ; high resolution TEM and biochemical study." *Tooth Enamel IV*, ed. R.W. Fearnhead and S. Suga, (Elsevier, 1984) pp.14-18.



## **Biomaterials**

### Magnetic Material Arrangement In *Apis Mellifera* Abdomens

Darci M. S. Esquivel, Eliane Wajnberg, Geraldo R. Cemicchiaro, Daniel Acosta-Avalos<sup>1</sup> and B.E. Garcia

Centro Brasileiro de Pesquisas Físicas, R. Xavier Sigaud 150, 22290-180, Rio de Janeiro, Brazil.

<sup>1</sup> Pontifícia Universidade Católica do Rio de Janeiro, R. Marques de S Vicente 225, 22453-970, Rio de Janeiro, Brazil.

#### ABSTRACT

Honeybees are the most studied insects in the magnetic orientation research field. Experiments on the magnetic remanence of honeybees have shown the presence of magnetite nanoparticles, aligned transversely to the body axis on the anterodorsal abdomen horizontal plane. These results support the hypothesis of ferromagnetic sensors for the magnetoreception mechanism. An Electron Paramagnetic Resonance (EPR) study identified isolated magnetite nanoparticles and aggregates of these particles with a low temperature transition (52 K – 91 K). Hysteresis curves of *Apis mellifera* abdomens organized parallel and perpendicular to the applied magnetic field were obtained from 5K to 310K. At low temperatures, the hysteresis curves indicate a preferential orientation of the magnetic easy axis parallel to the body axis. The saturation ( $J_s$ ) and remanent ( $J_r$ ) magnetizations, coercive field ( $H_c$ ) and initial susceptibility ( $\chi$ ) were obtained. Results were interpreted based on the presence of magnetite nanoparticles with 50 K and 120 K mean blocking temperatures.

#### INTRODUCTION

The honeybee, *Apis mellifera*, is the most studied insect in the magnetic orientation research field. Different experiments aiming the localisation of sensory magnetic particles in honeybees were reviewed [1]. Studies of the magnetic properties of honeybee have shown the presence of magnetite superparamagnetic or single domain nanoparticles in the anterodorsal abdomen region. Remanence measurements demonstrate that adult honeybees and older pupae possess magnetic material aligned transversely to the body axis on their horizontal plane while dead bees induced remanence tends to be aligned with the magnetic applied field. The transverse horizontal orientation could be the result of crystals that are forced to grow aligned north-south in the geomagnetic field, the most common comb natural orientation. Moreover, each honeybee showed different natural remanence [2-5].

Based on the ferromagnetic hypothesis for magnetoreception, Electron Paramagnetic Resonance (EPR) studies have contributed to the identification of magnetic material [6,7]. The presence of isolated magnetite nanoparticles of about  $3 \times 10^2 \text{ nm}^3$  and  $10^3 \text{ nm}^3$  depending on the hydration degree of the sample, and aggregates of these particles was proposed. A low temperature transition in the 52 K – 91 K region was reported [6].

A lack of hysteresis data yield us to focus on the analysis of the temperature dependence of hysteresis curves of *Apis mellifera* abdomens oriented parallel and perpendicular to the applied magnetic field of the magnetometer.

## EXPERIMENTAL DETAILS

Natural dead bees found at the entrance of a hive in Itaborai, Southeast of Brazil were collected and kept in 80% (v/v) ethanol. Bees were extensively washed with this solution. The three first segments of 16 bee abdomens were separated with stainless steel scalpel blades to avoid contamination. Two samples with eight abdomen segments each were oriented one with the axis body parallel and the other perpendicular to the magnetic field.

Hysteresis curves were obtained using a SQUID magnetometer (Quantum Design) from 5 K to 310 K for fields up to 30 kOe in the first positive branch, and up to 500 Oe in the negative branch. A straight line dominates the curves with a negative or positive slope depending on the temperature range and orientation of the sample. Linear fits from 10 kOe to 30 kOe were performed using Origin<sup>R</sup> software. The angular coefficient was taken as an effective dia-paramagnetic susceptibility and used to subtract the dia-paramagnetic contribution from the hysteresis curves.

## RESULTS

The hysteresis loop obtained at 50 K for the two sample orientations in the low field region are shown in Figure 1. One branch of each curve including the saturation region is presented in the insert. The saturation ( $J_s$ ) and the remanent ( $J_r$ ) magnetizations, the coercive field ( $H_c$ ) and initial susceptibility ( $\chi$ ) are obtained from these curves.

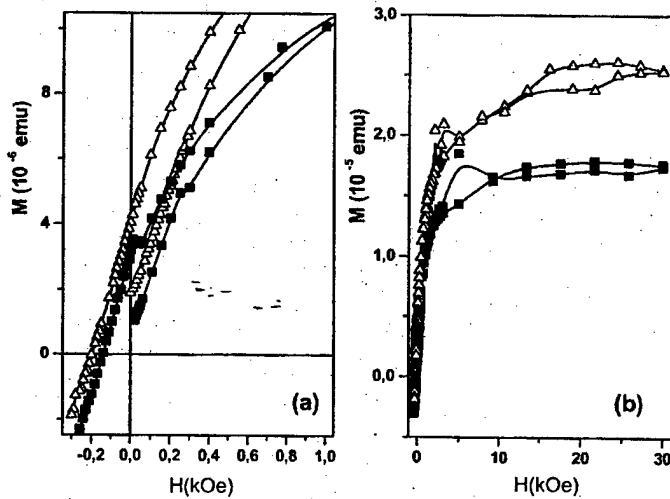
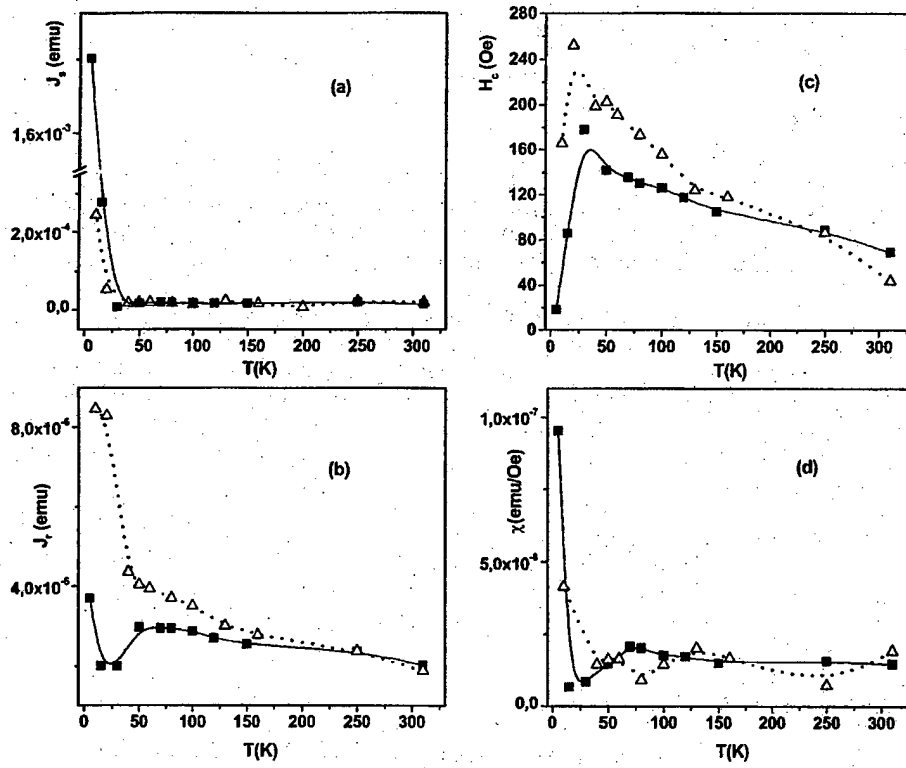


Figure 1. (a) Low Field region of hysteresis curves at 50 K. (b) First branch of hysteresis curves. Abdomen segments of eight bees oriented perpendicular (full square) and parallel (open triangle). Lines are guides to the eyes.



**Figure 2.** Temperature dependence of magnetic parameters. (a) Saturation magnetization,  $J_s$ , (b) Remanent magnetization,  $J_r$ , (c) Coercive field,  $H_c$  and (d) Initial susceptibility,  $\chi$ . Abdomen segments of eight bees oriented perpendicular (full square) and parallel (open triangle). Lines are guides to the eyes.

The temperature dependence of these parameters from 5 K to 310 K is plotted in figure 2 for both orientations. From these data it is evident that the magnetic parameters depend on the orientation of the magnetic field. This suggests that the magnetic particles in bee abdomens are preferentially aligned in specific directions rather than being arranged isotropically. The parallel and perpendicular  $J_s$  values are in the same magnitude range for temperatures above 50 K, but with weak oscillations (not visible in the scale of figure 2a) not observed in the perpendicular direction. Below 50 K there is a splitting of the curves, and at 10 K  $J_s$  in the perpendicular orientation is eight times larger than  $J_s$  in the parallel direction. Similar oscillations are also observed for  $\chi$  (Figure 2d) in the same temperature range with a 2.5 ratio between the two orientations at 10 K (even considering this parameter uncertainty). In contrast,  $H_c$  and  $J_r$  values are anisotropic for a wide range of temperatures (lower than about 200 K) shown in Figures 2b,c. The slope changes (obtained from derivative curves) appear at around 120 K and 50 K for

$H_c$  and  $J_r$ . At 20-30K  $H_c$  curves present a maximum while  $J_r$  curve behaviors are opposite with a minimum for the perpendicular orientation.

## CONCLUSIONS

The almost indistinguishable  $J_s$  values observed above 50 K are consistent with the previous results of dead bcc magnetization tracking the applied magnetic field. At lower temperatures, the higher values for  $J_s$  when the magnetic field is applied perpendicular to the body axis suggests that magnetic moments are aligned perpendicular to the body axis as found for live bees [2].

The anomalous increase of  $J_s$  and  $J_r$  could be associated with superparamagnetic particles that stabilize with a low blocking temperature. This is supported by smooth changes on the  $J_r$  and  $H_c$  curves indicating mean blocking temperatures of about 50K and 120 K related to 20 nm and 26 nm particle diameters [8]. Low temperature transitions in smashed bcc abdomens were also observed by EPR, 60-91 K for natural samples and 52-72 K for lyophilised ones. At temperatures lower than 25 K the background EPR component changes to an unexpected asymmetric line shape [6]. This result can be related to the peak at around 25 K shown in  $H_c$  curve which is possibly influenced by oxidized surface as observed in nanostructured Fe grains [9]. These magnetic properties presenting several temperature range behaviors could be due to different magnetic nanoparticle system arrangements. This paper present original results on the magnetic material in bee abdomens it points to the complexity of this system that requires complementary experiments and theoretical developments, especially with respect to 310 K, the bcc body temperature.

## ACKNOWLEDGMENTS

The authors would like to thank M. G. Malheiros for providing specimens. Research and authors partially supported by FAPERJ, CNPq and CAPES.

## REFERENCES

1. M. Vacha, *Biologia Bratislava* **52**, 629 (1997).
2. J. L. Gould, J. L. Kirschvink and K. S. Deffeyes, *Science* **201**, 1026 (1978).
3. J. L. Kirschvink, *Bioelectromagnetics* **10**, 239 (1989).
4. J. L. Gould, J. L. Kirschvink, K. S. Deffeyes and M. L. Brines, *J. Exp. Biol.* **80**, 1 (1980).
5. J. L. Kirschvink, T. Kuwajima, S. Ueno, S. J. Kirschvink, J. Diaz-Ricci, A. Morales, S. Barwig and K. J. Quinn, in *Sensory Transduction* (The Rockefeller University Press, N. Y., 1992) chap.14, 227.
6. L. J. El-Jaick, D. Acosta-Avalos, D. M. S. Esquivel, E. Wajnberg and M. P. Linhares, *Eur. Biophys. J.* **29**, 579, (2001).
7. S. Takagi, *J. Phys. Soc. Japan* **64**, 4378, (1995)
8. W. F. Towne and J. L. Gould, in *Magnetite Biominerilization and Magnetoreception in Organisms* (Plenum Press, N.York, 1985) chap. 18, 385.
9. J. F. Loffler, J. P. Meier, B. Doudin, J. P. Ansermet and W. Wagner, *Phys. Rev. B* **57**, 2915, (1998).

### Microstructure and Thermal Expansion Properties of Ostrich Eggshell

A. Heredia, L. Lózano, C.A. Martínez-Matías, M.A. Peña-Rico, A. Rodríguez-Hernández, E. Villarreal<sup>1</sup>, A. Martínez, M.V. García-Garduño<sup>1,2</sup>, V.A. Basiuk<sup>3,5</sup>, L. Bucio and E. Orozco

Instituto de Física UNAM, Apdo. Postal 20-364, 01000 México D.F., México

<sup>1</sup>Facultad de Ciencias UNAM, 04510 México D.F. México

<sup>2</sup>Div. de Posgr. e Invest., Facultad de Odontología UNAM, 04510 México D.F. México

<sup>3</sup>Instituto de Ciencias Nucleares UNAM, 04510 México D.F. México

<sup>5</sup>Faculty of Engineering, Yokohama National University, Japan. Hodogaya-Ku, Yokohama 240-8501.

<sup>4</sup>Instituto de Investigaciones en Materiales, UNAM, 04510 México D.F. México

### ABSTRACT

Textures of calcite crystals from ostrich (*Struthio camelus*) eggshells were examined with X ray diffractometry (XRD), transmission and scanning electron microscopy (TEM, SEM), and the thermal stability by thermal expansion analysis (TEA). Results showed that textures vary through the thickness of the eggshell and that expansion properties and thermal behaviour are unusual. Crystals from ostrich eggshell are arranged in two main configurations or layers; the outer layer with the *c*-axis of crystals oriented perpendicular to the eggshell surface and the inner layer with the *c*-axes of the crystals arranged almost parallel to eggshell surface; thermal expansion analysis show high stability through a wide range of temperatures until a steep growth near 450-460 °C. These results show that the manipulation of crystal texture and properties is under biological control and a better understanding of this biological phenomenon will provide more and better data for improving new synthetic composite materials.

### INTRODUCTION

Biominerals (or biocrystals) has long been the object of biomimetic study because of its characteristic structural arrangements and interesting mechanical properties [1, 2]. Determining the structures of biological materials is the most important challenge to understand all this properties and mechanisms to design a new generation of biomimetic materials. The avian eggshell is an unusual kind of natural biomaterial because its formation process is extremely rapid ( $\approx$  5.0 g of  $\text{CaCO}_3$  deposited in 24 h [4]) and the structure features arrangement of calcium carbonate crystals (calcite) in different layers relative to a biological macromolecule. In turn among avian eggshells, ostrich is of particular interest because of its fine assembly and therefore excellent structural and mechanical properties [4]. However, information on the crystal distribution is not enough. Some authors have done microstructural analysis to determine qualitatively the crystal orientation relationship between the neighbouring crystals in ostrich eggshell, obtaining randomly distribution of crystals in inner layer. This information should be especially valuable for a complete understanding of biominerization and particularly in controlling the organic framework role of crystal nucleation and orientation, assembly as well as preferred crystal growth [3]. As we know it is not the first description of crystals orientation and their physico-chemical processes in biological nature [1, 3-8] and in order to extend the understanding of biominerals properties and biominerization as well, here we present the

---

microstructural characterization concerning to morphology, texture and structures of the two surfaces (inner and outer) by scanning and transmission electron microscopy and X-ray diffraction and inner membrane by XRD. To our knowledge, it is the first report of a property (thermal expansion) related to crystal orientation and the first description of the organic amorphous related to a crystalline phase.

### EXPERIMENTAL DETAILS

Ostrich eggshell samples (OE), obtained from Veterinary and Zootechnical Faculty, National Autonomous University of Mexico, were analyzed by powder X-ray diffraction method. Samples were prepared by cutting pieces of  $1.0 \text{ cm}^2$  area. Both inner and outer surfaces were analysed putting the piece in the sample holder like a specimen having flat geometry and powdered eggshell was analysed as well. X-ray powder diffraction pattern was recorded with a step size of  $0.02^\circ$  over  $22-90^\circ$  2 $\theta$ -range. The diffraction data were collected with a counting time of 10s each step using a Siemens D5000 Diffractometer  $\text{CuK}\alpha$  radiation ( $35 \text{ kV}$ ,  $25 \text{ mA}$ ), vertical goniometer, fixed diffracted beam graphite monochromator and scintillation counter. The slits configuration was an aperture slit of 2 mm, a scattered radiation slit of 2 mm, a monochromator slit of 0.6 mm and detector slit of 0.6 mm. For SEM and TEM studies OE samples were sliced with a diamond wheel producing  $0.3 \times 0.3 \text{ cm}$  slices 250 to 500  $\mu\text{m}$  thick. The slices were subsequently polished down to a thickness of approximately 100  $\mu\text{m}$  with a No. 1000 silicon carbide paper and water. Afterwards they were ground to the thickness of 10  $\mu\text{m}$  using a Fischione dimpler, with periodical reversals to make both surfaces as homogeneous as possible. The specimen was thinned in a Dual 600 Gatan Ion Mill machine until a small hole was observed at its center with edges thin enough for TEM observation. Finally, the specimens were covered with a carbon film 20 nm thick in order to minimize electron beam damage and electrical charging resulting from ion bombardment. For thermal expansion analysis, OE were cut in pieces of  $8 \times 3 \text{ mm}$  parallel to longitudinal axis of eggshell and  $8 \times 3 \text{ mm}$  for the perpendicular to longitudinal axis of eggshell, other sample was cut to expand in the thickness of eggshell and the data corresponding to thickness of samples is the thickness of ostrich eggshell (2 mm). These samples were analysed in a home-made thermal expansion device in accord with the international standard ASTM E 228-95 [10]; heating them from room temperature to  $1000^\circ\text{C}$ .

### DISCUSSION

The outer layer of ostrich eggshell is the most crystalline and preferred orientation region comparing with inner layer, which is oriented in *a*, *b*- axis (see figure 1) what seems in some areas a monocrystalline layer (outer layer) by SEM (see figure 2).

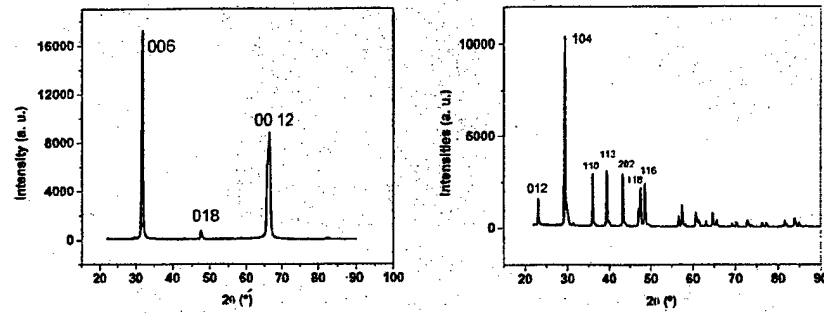


**Figure 1.** Powder XRD pattern of outer (left) and inner (right) layer of the ostrich eggshell. Due to the peaks and its intensities we have determined a preferred orientation of crystallites. This orientation regards  $c$ -axis perpendicular to ostrich eggshell surface (left) and crystals oriented parallel to surface (inner). The figure shows the only mineral phase is calcite.

Although some authors [4, 11] identified minerals of apatite group in the outer eggshell's layer, we did not find them in our samples. The results shown by other authors agree with ours and we include the crystallite average size in preferred orientation as well (See table I).

**Table I.** Average size of crystallites related to ostrich eggshell surface.

	Outer	Inner	membrane
Crystallite average size	558.77 Å* <sub>(006)</sub>	1000-3000 Å**	
Preferential orientation vector	001	Perpendicular to 001	None

By Sherrer's equation and \*\*By SEM

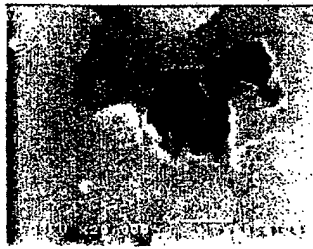


**Figure 2.** SEM image of outer layer of ostrich eggshell showing a region of a gaseous interchange pore. The smooth surface is due to compact arrangement of calcite nanocrystals. We regard this arrangement is a biological design directed by biopolymeric phase. Scale bar = 1.0  $\mu$ m



**Figure 3.** SEM (left) and dark field TEM (right) microphotographs of inner layer of ostrich eggshell showing biopolymer fibres bound to a grains of calcite crystals. This unidentified biopolymer we consider is the responsible for the thermal properties. Scale bar in SEM= 1.0  $\mu$ m. Bigger grain measure in TEM is = 0.13  $\mu$ m diameter.

Calcite crystals orientation resemble results obtained by other authors [4] but with some differences: those authors describe a non-preferred orientation in the inner crystal layer, whereas we found a preferred orientation with respect to the  $a$ -crystal axis (see XRD pattern shown in figure 1) and a large amount of unidentified fibrous biopolymer (Seen in figure 3).

This biopolymer cluster is associated with calcite crystals (Figure 3 and 4) to biominerilizate and although it is not well known some authors have found signs of type I, V and X collagen [11]. The biopolymer-crystal interaction is not well understood as well. In this work the crystals are regarded as needles due to the XRD spectra where only some peaks are seen. In other words, the  $c$ -axis of needle-like crystals is preferentially arranged in parallel to the eggshell surface, and through the equivalence in  $a$  an  $b$ -axes in calcite we distinguish a longitudinal arrangement to eggshell surface of  $c$ -axis in inner layer.

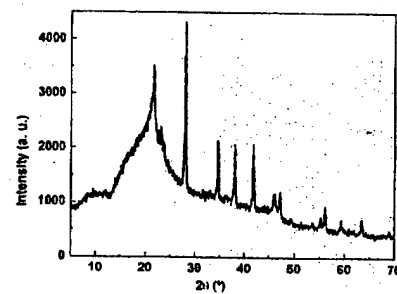


**Figure 4.** Powder XRD pattern of inner membrane of the ostrich eggshell. The peaks are more diverse than the presented in figure 1 what seems randomly oriented crystals and by its intensities we have determined a biggest size of crystallites than figure 1 cases. This figure is an approach to crystal-biopolymer interaction.

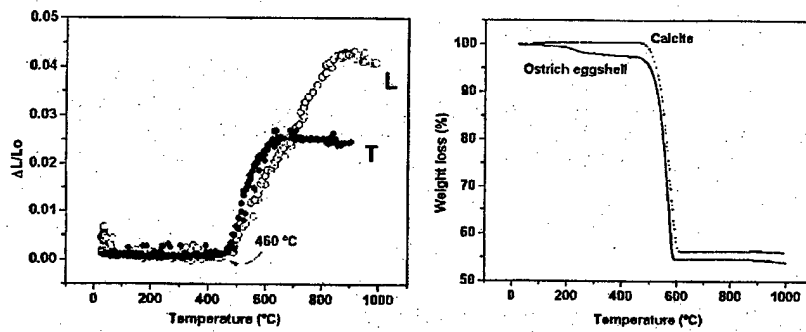


**Figure 5.** Anisotropic thermal expansion of OE (left) and OE TG (right) where mass loss initiate near 460 °C what is related to chemical reactions in TG. In left graph L means a slice parallel to longitudinal OE axis while T is transversal direction (or side view) to longitudinal axis of OE.

The average size of crystallite was measured through Scherrer's equation with full width at half maximum FWHM of a distinctive peak (006) and obtaining values presented in table I. Scherrer's equation was useful only for outer layer because are colloidal crystals.

On the basis of the experimental data the ostrich eggshell has an evident quantitative expansion starting at high temperatures near 450-460 °C (As presented in figure 5). Preferred expansion is in longitudinal axis of OE. This temperature is related by a TGA with a reaction of mass loss of calcite phase in OE.

We think the anisotropic thermal expansion of OE is due to amorphous biopolymer-calcite interactions producing a phenomenon that resemble monocrystallization and is possible the rearrangement from  $a$  to  $c$ -axis by heating samples on OE samples. The rearrangement of crystals can be inferred by anisotropic thermal expansion of calcite [11], changing the orientations it would change the expansion behaviour as well. Any way a detailed analysis is required to elucidate this behaviour.

## CONCLUSIONS

The results reported here directly show a complex structure on OE which is related to anisotropic physical properties (*i.e.* thermal expansion) independent of calcite properties what seems is related to biopolymer-crystal relationship.

How the biopolymeric matrix is forming calcite crystals is until now an unresolved problem. However, it is tempting to speculate that the multiple interactions of amorphous biopolymer and calcite is the responsible of nucleation, growth control and orientation assembly, and preferred crystal growth performing ion-ion reactions that withdraw properties of biomimetic from mineral structure. The knowledge of interactions and properties of biological structures will provide the opportunity to mimic these highly complex structures by the manipulation of the molecules to synthesize nanostructural materials or composites with special anisotropic physical properties.

## ACKNOWLEDGMENTS

We thank J. Puente, P. Mexía, R. Hernández, A. Pulido, R. Salazar and J. Reyes for their help in our MET and SEM experiments. The authors also acknowledge the financial support of UNAM DGAPA-PAPIIT IN113199, IN120801 and IN103700; and A. Heredia to Dirección General de Estudios de Posgrado (DGEP-UNAM) and National Council of Science and Technology (CONACyT) funding.

## REFERENCES

1. Q. L. Feng, F. Z. Cui, G. Pu, R.Z. Wang and H.D. Li, *Materials Science and Engineering C* **11**, 19-25 (2000)
2. L. Addadi and S. Weiner, *Nature* **389**, 912-915 (1997)
3. L.T. Kuhn, D.J. Fink and A.H. Heuer, "Biomimetic Strategies and Materials Processing", *Biomimetic Materials Chemistry*, edited by S. Mann. (John Wiley & Sons Publish, 1996) pp. 41-68
4. Q. L. Feng, X. Zhu, H.D. Li and T.N. Kim, *Journal of Crystal Growth* **233**, 548-554 (2001)
5. B.R. Heywood, "Template-Directed Nucleation and Growth of Inorganic Materials" *Biomimetic Materials Chemistry*, edited by S. Mann, (John Wiley & Sons Publish, 1996) pp. 143-173
6. S. Brown, M. Sarikaya and E. Johnson, *J. Mol. Biol.* **299**, 725-735 (2000)
7. A.P. Wheeler, J.W. George and C.A. Evans, *Science* **212**, 1397-1398 (1981)
8. A. Berman, J. Hanson, L. Leiserowitz, T.F. Koetzle, S. Weiner and L. Addadi, *Science* **259**, 776-779 (1993)
9. C.A. Martínez Matías. Licentiáte in Mechanic Electrician Engineering Thesis. "Design, building and instrumentation of a dilatometer to study the thermal properties of materials" Assessor Dr. E. A. Orozco Mendoza. National University of Mexico. 2001 (In spanish)
10. M.S. Fernández, A. Moya, L. Lopez and J.L. Arias. *Matrix Biology* **19** 793-803 (2001)
11. K.V. Krishna Rao, S.V. Nagender Naidu and K. Satyanarayana Murthy. *J. Phys. Chem. Solids*. **29** pp 245-248 (1968)

### Thermal Properties of Mineralized and Non Mineralized Type I Collagen in Bone

L. F. Lozano<sup>1</sup>, M. A. Peña-Rico<sup>1</sup>, H. Jang-Cho<sup>4</sup>, A. Heredia<sup>1</sup>, E. Villarreal<sup>3</sup>, J. Ocotlán-Flores<sup>2</sup>, A. L. Gómez-Cortes<sup>1</sup>, F. J. Aranda-Manteca<sup>5</sup>, E. Orozco<sup>1</sup> and L. Bucio<sup>1</sup>.

<sup>1</sup>Instituto de Física, UNAM, Ciudad Universitaria, Coyoacan. C.P. 01000, Mexico. D.F.

<sup>2</sup>Centro de Instrumentos, UNAM, Ciudad Universitaria, Coyoacan. C.P. 04510. Mexico. D.F.

<sup>3</sup>Instituto de Investigaciones en Materiales, UNAM, Ciudad Universitaria, Coyoacan. C.P. 04510. Mexico. D.F.

<sup>4</sup>Instituto de Investigaciones Antropológicas, UNAM, Ciudad Universitaria, Coyoacan. C.P. 04510. Mexico. D.F.

<sup>5</sup>Facultad de Ciencias Marinas, UABC, Km 103 carret. Tijuana Ensenada. C.P. 453. Ensenada, Baja California, Mexico.

#### ABSTRACT

The research about the structural stability of bone, as a composite material, compromises a complete understanding of the interaction between the mineral and organic phases. The thermal stability of human bone and type I collagen extracted from human bone by different methods was studied in order to understand the interactions between the mineral and organic phases when is affected by a degradation/combustion process. The experimental techniques employed were calorimetry and infrared spectroscopy (FTIR) techniques. The extracted type I collagens result to have a bigger thermal stability with a Tmax at 500 and 530 Celsius degrees compared with the collagen present in bone with Tmax at 350 Celsius degrees. The enthalpy value for the complete degradation/combustion process were similar for all the samples, being  $8.4 \pm 0.11$  kJ/g for recent bones diminishing with the antiquity, while for extracted collagens were  $8.9 \pm 0.07$  and  $7.9 \pm 1.01$  kJ/g. These findings demonstrate that the stability loss of type I collagen is due to its interactions with the mineral phase, namely carbonate hydroxyapatite. This cause a change in the molecular properties of the collagen during mineralization, specifically in its cross-links and other chemical interactions, which have a global effect over the fibers elasticity, but gaining tensile strength in bone as a whole tissue. We are applying this characterization to analyze the diagenetic process of bones with archaeological interest in order to identify how the environmental factors affect the molecular structure of type I collagen. In bone samples that proceed from an specific region with the same environmental conditions, the enthalpy value per unit mass was found to diminish exponentially with respect to the bone antiquity.

#### INTRODUCTION

Bone is one of the biological structures that has been analyzed in different areas, as medicine, biology, archaeology, science materials, etc. by means of different techniques. It is composed of a mineral and an organic phase, which are hydroxyapatite and collagen respectively. This biomaterial properties are of main importance for developing new materials that mimics its structure and for other applications in which it plays a specific and transcending role. To understand its structural characteristics, as the collagen-hydroxyapatite relationship, the collagen thermal stability, the collagen degradation process, we have, in a recent work, address these problems by the use of different calorimetric, gas chromatography and FTIR techniques (6). These findings demonstrate that the stability loss of type I collagen is due to its interactions with

the mineral phase, namely carbonate hydroxyapatite, since its enthalpy value for the complete degradation/combustion process of mineralized collagen and bone extracted collagen are similar,  $8.4 \pm 0.11$  and  $8.9 \pm 0.07$  kJ/g respectively, but their  $T_{max}$  values differ, being bigger for the extracted collagen. This cause a change in the molecular properties of the collagen during mineralization, specifically in its cross-links and other chemical interactions, possibly provoked by the hydroxyapatite crystals which acts as degradation centers accelerating the protein combustion. The changes in this biomaterial structure properties, have a global effect over the fibers elasticity, but gaining tensile strength in bone as a whole tissue. We pretend to apply these findings to the characterization of the collagen loss process (diagenetic process) in archaeological bone, to develop a calorimetric approach to the dating of bone remains, that can be found in specific environmental conditions.

Type I collagen of archaeological bone has been a matter of several investigations mainly because it is a source of valuable information for understanding the diagenetic process [1,2,4,5,7,8,], which is variable from one environment to another, and depends on different physical, chemical and biological factors. It is well known that both, the inorganic and organic phases of bone, are altered during the time this material expends buried. Differential scanning calorimetry has been used for investigating the deterioration of archaeological and actual bone collagen by analysing the denaturation of the extracted protein [7]. Our approach consists in obtaining the  $\Delta H$  of combustion of the collagen molecule present in the bone structure and comparing it with remains of different antiquity, assuming that older bones will have less protein than younger ones because of the degradation provoked by various factors [9]. Studying the combustion process implies the use of a larger temperature range of analysis than with the protein denaturation process, and it also has the outstanding benefit of obtaining satisfactory signals and reproducible results for all the archaeological bones, which has been a difficulty in other studies [7].

Understanding the diagenetic process may provide a better conceptual framework to obtain a possible relationship between the antiquity and the collagen loss in archaeological bones. Due to the fact that the diagenetic process is provoked by multiple factors and that there is no very clear consensus for the particular chemistry involved in any given diagenetic process [4], it turns very difficult to describe it meticulously. Then, the collagen mass of antique bones must be analized in a way that allows the obtainment of a realistic collagen loss and bone antiquity relationship. For achieving this, an initial prerequisite is to work with bone samples from the same region to assure that the environmental conditions are nearly equal for all the remains.

#### EXPERIMENTAL DETAILS

Archaeological bone samples were supplied from the Anthropological Research Institute at National Autonomous University of Mexico and Autonomous University of Baja California, all were from the Mexico Valley, except Xcambo and Bonampak from Yucatan and Chiapas respectively. The samples were suitable to perform the different experiments. The archaeological bones were powdered in an agate mill and sieved through a 325 mesh. The paleontological bone sample was analyzed using a fragments of 10 mg. DSC measurements were carried out in a Thermal Analysis System 9900, Du Pont 910 (DSC module). For DSC measurements the heating rate was constant and equal to  $10^{\circ}\text{C}/\text{min}$  in air atmosphere. The sample amount used was 2.0 mg for all archaeological samples. The FT-IR analysis were carried out using a Nicolet 680. The bone samples were mixed with KBr powder (1:100 ratio) and then compressed into pellets. IR spectra were obtained for different samples.

Table 1. Antiquity and enthalpy values of archaeological samples (femur bone).

SAMPLE (origin)	ENTHALPY (J/g)	ANTIQUITY (years)	BONE
Tlatilco Ent. 27	-688.1 $\pm$ 27.11	3150 $\pm$ 150	Femur
Tlatilco Ent. 197	-1202.27 $\pm$ 86.64	3150 $\pm$ 150	Femur
Cuicuilco A.	-422.06 $\pm$ 70.60	2250 $\pm$ 350	Femur
Cuicuilco I.	-313.33 $\pm$ 35.84	2250 $\pm$ 350	Femur
Oztoyohualco Ent. 14	-1586.86 $\pm$ 27.90	1450 $\pm$ 100	Femur
Xcambo	-688.34 $\pm$ 31.29	1350 $\pm$ 150	unknown
Bonampak	-315.06 $\pm$ 37.29	1350 $\pm$ 150	unknown
Tlalocan Ent. 2	-471.61 $\pm$ 124.91	1300 $\pm$ 100	Femur
Xochimilco Ent. 17	-1613.16	1250 $\pm$ 150	Femur
Tlatelolco C6 T8	-1431.14 $\pm$ 197.70	614.5 $\pm$ 135.5	Humerus
Xochimilco Ent. 14-A	-1476.43 $\pm$ 93041	614.5 $\pm$ 135.5	Femur
San Jerónimo 1	-2224.56 $\pm$ 82.51	274.5 $\pm$ 99.5	Femur
San Jerónimo 3	-2522.86 $\pm$ 14.11	274.5 $\pm$ 99.5	Femur
San Pedro San Pablo U1 Ent. 1	-2153.66 $\pm$ 159.91	185 $\pm$ 25	Femur
San Pedro San Pablo U7 Ent. 5	-814.96 $\pm$ 90.03	185 $\pm$ 25	Femur
San Pedro San Pablo U7 Ent. 16	-1860.98 $\pm$ 115.64	185 $\pm$ 25	Femur
San Pedro San Pablo U7 Ent. 18	-1596.79 $\pm$ 27.14	185 $\pm$ 25	Femur

## DISCUSSION

The calorimetric curves of the archaeological bone samples (fig 1, left graphic; table 1), show that all of them have a similar thermal stability, defined by the  $T_{max}$  between 330 and 345°C of the combustion process, which represents the temperature where the maximum value of heat flow intensity the process reach. In a previous work we found that the right shoulder in the calorimetric curve of the actual bones, changes if the sample experimental conditions are varied.

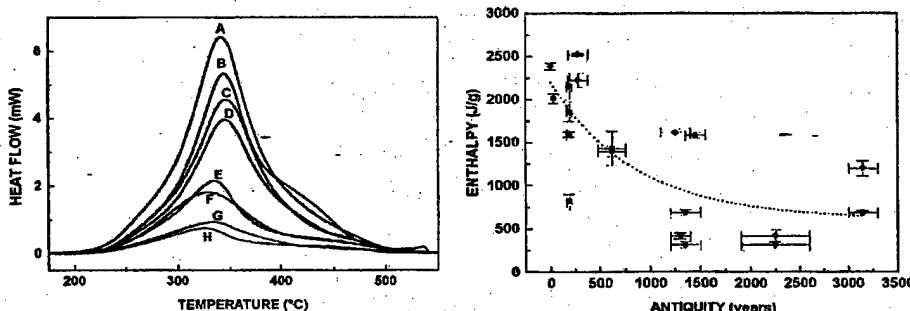


Figure 1. Left graphic shows the archaeological bone samples calorimetric curves. The different curves represent samples with distinct antiquities (A=274, B=185, C=1450, D=614, E=3150, F=1300, G=2250 and H=1350, all in years). Right graphic shows the relationship between the enthalpy and the antiquity of all the bone samples studied, the exponential decay curves shows the general tendency for the collagen loss.

i.e. the use of small bone fragments rather than powdered bone; this is explained by the fact that the DSC analysis is very sensible to the sample conditions, taking this in account all samples were analyzed with the same conditions. The fact that the archaeological bones calorimetric curves gradually diminish is because the thermograms heat flow intensity variation depends on the collagen mass of the bone remains, and the overall process is then represented by smaller calorimetric curves when the collagen loss of the structure is bigger.

The DSC curves shape is not very useful for a good comparison between the samples and their antiquity. This is best represented by the enthalpy values obtained for each bone. When these values varies in modern bones, the organic/mineral phase ratio may be altered, and so the structure properties. In this study, we employ a different approach for interpreting these values, which, as shown in table 1, are not in concordance with the respective antiquity of the bones under study, since we expected to found that the older samples will have lower enthalpy values and vice versa.

In fig. 1 (right graphic) the enthalpy values for all the bone samples are placed against their antiquity and represents the global behavior of the analyzed bones, it also shows that a larger group of samples is needed to fulfill the complete range of antiquities. The enthalpy values for all the bone samples are placed against their antiquity, and an exponential decay curve is obtained which represents the collagen loss rate. The archaeological bones came from the same region to assure that the environmental conditions that act over the collagen molecules degradation is similar, this is not well represented, since some sample of the same antiquity have different enthalpy values, so that the protein degradation process carry out by the soil characteristics (pH, humidity, temperature, etc.) may not be equal for all the bone remains. It is expected that some bone samples may not have the same collagen loss, but a general tendency of such loss rate must be represented by the exponential decay curve in the range of antiquity analyzed.

FTIR analysis also shows that archaeological bones have different collagen loss (fig.2). By comparing the amide I band ( $1650\text{ cm}^{-1}$ ), which is assigned to the C=O stretch, is observed that there are different organic content for the samples. A collagen and a hydroxyapatite spectra are compared with the archaeological bones; the mineralization of the later samples differs

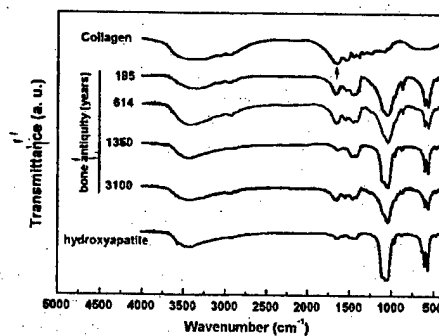


Figure 2. FTIR spectra of bone extracted collagen, hydroxyapatite and archaeological bone samples of different antiquity. The arrow shows the amide I band at  $1650\text{ cm}^{-1}$  that is assigned to the C=O stretching.

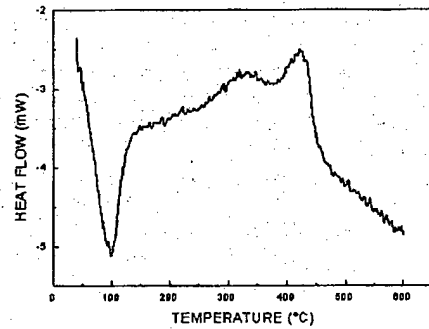


Figure 3. Calorimetric curve of a 73 millions old paleontological bone. Two exothermic processes are evident at 330 and 420 °C.

with their respective antiquity, this may be a consequence of the burial conditions in which the remains were found. The 1350 years old sample (Bonampak) is very similar to the hydroxyapatite spectra, suggesting that the degree of collagen loss is bigger and that the mineral phase does not suffer any kind of modification.

We found that the calorimetric analysis have a greater sensibility for detecting the organic presence in the bone material. To illustrate the sensitivity of the DSC module, let just notice that it was able to detect the presence of the organic phase in some paleontological bones of even 73 million years old (fig.3). This fact confirms that the calorimetry approach is suitable for fossil samples.

The present results may be considered as a first approach to the study of bone changes by the combustion process of the organic phase. It must be taken in consideration that collagen is the principal constituent of bone, so by analyzing the organic phase we are primarily characterizing this specific protein which by the way, is expected to be the unique organic remain in the older bones structure, when external contamination is negligible, because of his great stability. The improvement of the present research may be achieved by the use of a bigger set of bone samples with different antiquities, so that the exponential decay curves may represent in a more precise way the collagen loss rate. It is also very important to characterize this collagen loss rate in different burial conditions that may provoke an accelerated degradation process and loss of the organic content.

## CONCLUSION

We have applied our recent findings on the thermal stability and degradation process of collagen, and its relationship with the hydroxyapatite phase in the bone structure, to the analysis of archaeological bone. By the use of DSC analysis, we obtain the collagen loss rate from the enthalpy values of the combustion process of the organic phase present in bones. The enthalpy of the combustion process from the archaeological samples has in some cases, no direct concordance with their respective antiquities. By studying a bigger set of bone sample of different antiquities, this calorimetric approach could be employed, as an alternative technique, for the analysis of bone remains of archaeological and paleontological interest.

Material science research may have different applications in areas where structural knowledge and the relationship between different phases in a material exist, and can give useful information to develop a more robust conceptual framework about specific processes. Paleontology and archaeology, are two scientific areas where the characterization of the properties of an important biomaterial are of trascendence to achieve a better understanding of the changes produced in bone by external factors.

Calorimetry is, as shown by the present results, a very useful technique for biomaterials study. The organic content in bone tissues of millions years old, can be detected and correlated to their antiquity, these must be carefully interpreted with the burial context where the remains are found. The use of calorimetry with other commonly used techniques may help in this aspect.

#### ACKNOWLEDGEMENTS

The authors acknowledge the financial support of UNAM DGAPA-PAPIIT IN113199 and UNAM DGAPA-PAPIIT IN120801; and A Heredia to General Direction of Postgrade Studies (DGEP-UNAM) and National Council of Science and Technology (CONACyT) funding.

#### REFERENCES

1. Collins, M., Riley, M., Child, A. and G. Turner-Walker. 1995. A basic mathematical simulation of the chemical degradation of ancient collagen. *J. Archaeol. Sci.* 22, 175-183.
2. Grupe, G. 1995. Preservation of collagen in bone from dry, sandy soil. *J. Archaeol. Sci.* 22, 193-199.
3. Hedges, E. M. and A. Millard. 1995. Bones and groundwater: Towards the modelling of diagenetic processes. *J. Archaeol. Sci.* 22, 155-164.
4. Hedges, E. M. and A. Millard. 1995. Measurements and relationships of diagenetic alteration of bone from three archaeological sites. *J. Archaeol. Sci.* 22, 201-209.
5. Katzenberg, M. and R. Harrison. 1997. What's in a bone? Recent advances in archaeological bone chemistry. *J. Archaeol. Res.* Vol. 5, No. 3, pp. 265-293.
6. Lozano L. F., Peña-Rico, M.A., Heredia, A., Ocotlán-Flores, J., Gómez-Cortés, A.L., Velazquez, R. and Bucio, L. Thermal Analysis Study of Human Bone. 2002. Submitted.
7. Nielsen-Marsh, C., Hedges, R., Mann, T. and M. Collins. 2000. A preliminary investigation of the application of differential scanning calorimetry to the study of collagen degradation in archaeological bone. *Thermochim. Acta.* 365, 129-139.
8. Schoeninger, M., Moore, K., Murray, M. and J. Kingston. 1989. Detection of bone preservation in archaeological and fossil samples. *Applied Geochemistry*, Vol. 4, pp. 281-292.
9. Vento, C.E. Rodríguez, SR & Franco, M.L. 1981. La datación Absoluta por el método de colágeno residual en Cuba. Koblé (Bilbao), Grupo espeleológico Vizcaíno. Diputación Federal de Vizcaya. Vol. 11.

### Tissue Engineering of Fibroblast Constructs and Anisotropic Collagen Gels

Sarah Calve<sup>1,3</sup>, Ellen Arruda<sup>2</sup>, Robert Denis<sup>2,3</sup>, Karl Grosh<sup>2</sup> and Krystyna Pasyk<sup>3</sup>

<sup>1</sup>Macromolecular Science and Engineering Center, <sup>2</sup>Department of Mechanical Engineering, <sup>3</sup>Institute of Gerontology, University of Michigan, Ann Arbor, MI 48109

#### ABSTRACT

The creation of an *in vitro* functional tendon construct will enable testing of the influence of mechanics and nutrients on the development and remodeling of tendon under known controlled stimuli which is difficult to achieve *in vivo*. Tendon constructs were engineered *in vitro* via stress-mediated self organization of fibroblasts and ECM on a laminin coated elastomer substrate. Varying the laminin density and the amount of fetal bovine serum on the substrate affected the ability of tendon fibroblasts to form a confluent cell layer and the time to layer delamination. Understanding the factors that promote self-assembly of tendon constructs will enable their combination with already developed *in vitro* muscle constructs.

#### INTRODUCTION

Self-assembled muscle constructs, termed myooids, have been formed without a synthetic scaffold via stress-mediated self-organization [1]. Myooids can transmit force spontaneously and upon the application of an electrical stimulus. They display an immature phenotype both morphologically and mechanically however, which hinders their use as a model of *in vivo* muscle function. Mechanical stress is one of the mechanisms that has been shown to facilitate muscle maturation [2], but the interface between the anchor, medical silk suture, and the myooid is not strong enough to withstand stress on the physiological scale. This problem may be ameliorated by creating, *in vitro*, the natural interface muscle uses to transmit generated force. (Figure 1) The myotendinous junction is highly infolded increasing the interfacial area between the



**Figure 1.** TEM of a neonatal myotendinous junction from a 2 day old Fischer 344 rat (x10,140). The muscle cell is coming out of the lower right hand corner and is outlined by dark, electron rich areas which demarcate areas of adhesion between the fibroblasts and collagen of the tendon and the muscle cell. Note the involuting membrane. These will become more pronounced during development as the unit is put under more stress. The wavy lines in the central portion of the picture represent collagen fibrils of the tendon. Photo: Krystyna Pasyk

tendon and muscle, allowing for the tension to be transmitted primarily via shear. A critical step towards myotendinous junction formation *in vitro* is the development of an independent tendon construct. After understanding the factors that facilitate tendon formation, myooids and tendon constructs can be combined by co-culturing tenoblasts and myoblasts or by growing the constructs independently of each other and inducing the two constructs to combine.

## EXPERIMENTAL DETAILS

### Acquisition of tendon fibroblasts

Primary rat tendon fibroblasts were obtained by surgically removing the Achilles tendon from a Fischer 344 rat and dissociated by placing in a 0.25% trypsin-EDTA solution (GIBCO BRL, Rockville, MD 25200-027) containing 100 units/mL type I collagenase (Worthington Biochemical Corporation, Lakewood, NJ 4196) at 37°C for several hours. After tissue was dissociated, the solution was centrifuged and the supernatant was suctioned off. The cells were reconstituted with growth medium (GM): 400 mL Ham F-12 (GIBCO BRL 11765-054), 100 mL fetal bovine serum (FBS) (GIBCO BRL 10437-036), 100 units/mL antibiotic-antimycotic (Sigma, St. Louis, MO A9909) and expanded in 100 mm diameter tissue culture dishes (Falcon, Becton Dickinson Labware, Franklin Lakes, NJ 353003). Cells were passaged at 60% confluence and kept in LN<sub>2</sub> until needed for experimentation.

### Preparation of culture dishes

1.5 mL SYLGARD (Dow Chemical Corporation, Midland, MI type 184 silicone elastomer) was poured into each 35 mm diameter culture dish (Falcon 351008). After curing for at least 2 weeks, the dishes were rinsed with Dulbecco's Phosphate-Buffered Saline (DPBS) (pH = 7.2 GIBCO BRL 14190-136) and coated with varying densities of natural mouse laminin (GIBCO BRL 23017-015) by diluting the laminin in ~3 mL DPBS and allowing the DPBS to evaporate overnight. The dishes were rinsed with DPBS and the anchors, 6 mm segments of size-0 silk suture (Ethicon, metric size 3.5), were dipped into 50 µg/mL solution of natural mouse laminin, then pinned 12 mm apart with 0.10 mm diameter stainless steel minuten pins (Fine Science Tools, Foster City, CA, 26002-10). The sutures were allowed to dry and the plates were filled with ~2 mL GM, enough to cover the top of the sutures, and the plates were sterilized with ultraviolet irradiation (253.7 nm, bulb G30T8) in a biological safety hood for 90 minutes. The sterilized plates were placed in an incubator (5% CO<sub>2</sub>, 37°C) for 5-8 days.

When the plates were ready, 1x10<sup>5</sup> cells were added to each plate and grown in 2mL GM. After two days, 100 µg/mL of ascorbic acid (GIBCO BRL 13080-023) was added to each dish. Fresh ascorbic acid was added to the dishes when the media was changed, every 2-3 days. After 2 or 5 days, the media was changed from GM to differentiation media (DM): 465 mL DMEM (GIBCO BRL 11995-065), 35 mL FBS, 100 units/mL A9909.

### **Preparation of anisotropic collagen constructs**

6 mL of 2 mg/mL collagen solution was made by combining 0.6 mL 10x MEM (GIBCO BRL 11430-030), 0.06 mL NaOH (1.0 N), 2.56 mL DI water and 2.78 mL type I rat tail collagen solution (BD Biosciences, Bedford, MA 354236 4.31 mg/mL) in that order. The pH was adjusted to 7.4 by the addition of 0.1 N acetic acid or NaOH. A cell solution was made by suspending tendon fibroblasts in GM at a concentration of  $1 \times 10^5$  cells/mL. Gels were formed by mixing 1.0 mL cell solution with 1.0 mL collagen solution and poured into a UV treated 35 mm diameter plate with anchors but without laminin coating.

### **DISCUSSION**

#### **Self assembling tendon constructs**

Cells that have reached confluence before plating on prepared substrates do not form confluent layers. (Figure 2b) This is likely a result of contact inhibition in which the cells become quiescent, losing their ability to proliferate when dissociated and re-plated. Cells should not be allowed to become more than 60% confluent when expanding.

Ascorbic acid is utilized during the synthesis of collagen [3], and it is necessary for the formation of confluent cell layers on the laminin coated substrates used in these studies. The extra collagen synthesized in cultures supplemented with ascorbic acid probably acts as scaffold, maintaining the integrity of the cell layer. Without the addition of ascorbic acid, the cells dissociate from the substrate in a spatially sporadic manner. (Figure 2c)

When the fibroblasts are grown in 20% FBS, they will only delaminate when the substrate is coated with 2.0 mg/cm<sup>2</sup> laminin. At lower laminin concentrations, the fibroblasts will not form a confluent monolayer and at concentrations higher than 2.0 mg/cm<sup>2</sup>, the cell layer will not delaminate. But, when the cells are initially grown in GM (20% FBS) then changed to DM (7% FBS), the cell layer delaminates for all laminin densities studied, 2.0-20.0 mg/cm<sup>2</sup>.

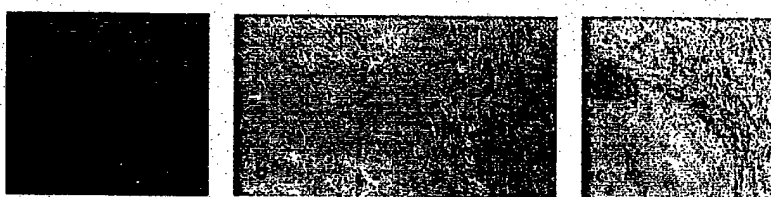


**Figure 2.** Rat tendon fibroblasts grown under various conditions. **A:** Confluent fibroblast layer which was plated with cells less than 60% confluent and supplemented with 100  $\mu$ g/mL ascorbic acid. **B:** Cells that reached confluence before plated on laminin coated substrates could not form a confluent cell layer. **C:** Inability of cells to form confluent layer without addition of ascorbic acid. (100x magnification)

When the media was changed from GM to DM on day 3, the layer began to delaminate after 9 days. It formed a cylinder bounded by the anchors after 10-11 days, but the construct was too fragile and fractured. The extracellular matrix (ECM) secreted by the cells was not strong enough to maintain the integrity of the layer as the cells contracted or tried to adhere to one another. If the culture medium was changed to DM after 5 days instead, the cell layer started detaching after ~2.5 weeks and was much more stable. The higher percentage of FBS in GM, 20%, is hypothesized to facilitate the production of ECM significantly more than the 7% FBS in DM due to an increase in nutrients, creating a stronger cell layer.

Fibroblasts are believed to preferentially adhere to each other rather than the artificial substrate since there is only one adhesion ligand on the substrate and there are multiple adhesion proteins present on the cell membranes as well as the secreted ECM. When delamination starts, the fibroblast layer rolls up on itself and the fibroblasts preference for the cell layer acts as a catalyst for self assembly into a cylinder bounded by the anchors.

#### Cell-collagen constructs

The combination of cells and collagen as described in the experimental section is a simple and repeatable way to create fibroblast constructs. This construct more closely mimics the physiology of adult tendons than pure tendon cell constructs since there is a larger initial ratio of collagen to cells, and the fibroblast density can be easily controlled by varying the seeding density. Alternate anchor materials are being investigated for use with these collagen constructs since they do not adhere well to the silk suture (as seen in the top suture in figure 4). Porous polyethylene (PE) is an inert polymer currently used in



**Figure 3:** A: 19 days after plating. The cell layer has started to detach from the substrate. B: 19 days after plating. This picture was taken 3 hours after the media was changed and there is considerably more detachment evident. Whether or not this is a result of a fresh supply of FBS, which has been implicated in promoting fibroblast contraction [4], or a response to the mechanical stimulus of the addition of fluid to the plate is still unknown and an investigation of this phenomenon is planned. C: 21 days after plating. The increase in ECM allows for the contracted cell layer to maintain the connection between the anchors.

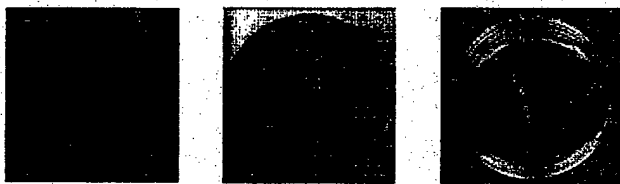


**Figure 4.** Anisotropic collagen-fibroblast constructs are easily formed over the course of a week. **A:** 12 hours after plating. **B:** 3 days after plating. **C:** 8 days after plating. The force of contraction is causing the gel to pull up from the anchor at the top of **C**.

medical applications. The inherent hydrophobic nature of PE can be overcome by introducing functional peroxide groups to the surface. These peroxides can then be reacted with chemicals that bind to collagen [5]. The use of plasma discharge treatment to create the desired interface that will bind with collagen is currently under investigation.

## CONCLUSION

Self-assembled and collagen-based fibroblast constructs have been created. The knowledge gained from varying certain parameters (laminin density, % FBS, state of cell before plating, ascorbic acid concentration) will allow for control of the length of time it takes for delamination, as well as the collagen composition of the construct, to more closely mimic tendon physiology. One future direction is the combination of the self-assembled tendons with the collagen constructs in which the collagen construct will form a relatively acellular core that the cell layer wraps around.

It is anticipated that these constructs will be able to combine with previously developed myooids. It has been shown that when myoblasts are cultured adjacent to a type I collagen gel, the developing myotubes invaginate the collagen creating a structure similar to that seen in a myotendinous junction [6]. Myooids are expected to form this type of interface with the three-dimensional tendon constructs described above since tendon cells predominantly secrete type I collagen [7]. Further support comes from developmental studies showing that tendon and muscle initially grow independent of each other and only in later development combine in a non-site specific way [8].

## REFERENCES

- [1] Dennis, R. G. and Kosnik, P. E., "Excitability and Isometric Contractile Properties of Mammalian Skeletal Muscle Constructs Engineered *In Vitro*," *In Vitro Cellular Developmental Biology - Animal*, vol. 36 pp. 327-335, 2000.
- [2] Russell, J. E. and Manske, P. R., "Ascorbic Acid Requirement for Optimal Flexor Tendon Repair *In Vitro*," *Journal of Orthopaedic Research*, vol. 9 pp. 714-719, 1991.

---

- [3] Stewart, D. M., "The Role of Tension in Muscle Growth," in Goss, R. J. (ed.) *Regulation of Organ and Tissue Growth* 1972, pp. 77-100.
- [4] Danowski, B. A., "Microtubule Dynamics in Serum-Starved and Serum-Stimulated Swiss 3T3 Mouse Fibroblasts: Implications for the Relationship Between Serum-Induced Contractility and Microtubules," *Cell Motility and the Cytoskeleton*, vol. 40 pp. 1-12, 1998.
- [5] Kinoshita, Y. and Kuzuhara, T., "Soft tissue reaction to collagen-immobilized porous polyethylene: subcutaneous implantatation in rats for 20 wk," *Biomaterials*, vol. 14, no. 3, pp. 209-215, 1992.
- [6] Swasdison, S. and Maync, R., "In Vitro Attachment of Skeletal Muscle Fibers to a Collagen Gel Duplicates the Structure of the Myotendinous Junction," *Experimental Cell Research*, vol. 193 pp. 227-231, 1991.
- [7] Doane, K. J. and Birk, D. E., "Fibroblasts Retain Their Tissue Phenotype When Grown in Three-Dimensional Collagen Gels," *Experimental Cell Research*, vol. 195 pp. 432-442, 1991.
- [8] Kardon, G., "Muscle and Tendon Morphogenesis in the Avian Hind Limb," *Development*, vol. 125 pp. 4019-4032, 1998.

## The investigation on preparation & physicochemical process of nanosized hydroxyapatite powder

Yunjing Song<sup>1,2,a)</sup> Shulin Wen<sup>1</sup> Musen Li<sup>1</sup>

<sup>1</sup>College Of Materials Science and Engineering, Shandong University, Jinan 250062, People's Republic of China

<sup>2</sup>Shandong Electricity Power Institute, Jinan, 250002, People's Republic of China

### Abstract

The investigations of the preparation and physicochemical process of the HA nanostructured powder with high performance have been performed at present study. The HA preparation starts from the ethanol solution of calcium nitrate tetra-hydrate and phosphorous pentoxide as raw materials. The characterization of the effects of reacting temperatures on preparation, the crystalline degrees (some amorphous HA formed at certain condition) of the reacting products are carried out in the meanwhile. The physicochemical processes and the conditions for different reactions stages of the HA preparation have been traced and characterized by the TG-DTA (thermogravimetric and differential thermal analysis), the FTIR (Fourier-transformed infrared spectroscopy) and other methods. The investigations of the chemical reactions for the HA preparation show that the synthesis of HA is completely finished at the temperature of 500 °C for hours. The grain sizes and shapes of the HA reacting products are observed and characterized by the TEM and the XRD. The results show that the mean diameters of these product grains are as fine as 30-40nm at the temperature of 500 °C. The XRD pattern of the present HA powders sintered at 500 °C for 2h coincided very well with the JCPDS standards showing its superior purity and therefore, with really high performance for later applications.

### 1. Introduction

Hydroxyapatite,  $\text{Ca}_{10}(\text{PO}_4)_6(\text{OH})_2$ , commonly referred to as HA or Hap, has attracted widespread interest because of its excellent biocompatibility and bioactivity. Being the major inorganic constituent of bone HA can provide a chemical bond to the bone and gradually replaced by bone. Hence, HA has become an attractive materials for hard tissue implants<sup>1</sup>.

Conventionally, HA powers can be prepared by several methods such as wet precipitation method<sup>2</sup>, dry method<sup>3</sup>, hydrothermal method<sup>4</sup>, sol-gel method<sup>5-12</sup>, etc.

The advantages of sol-gel technique include: increase of the homogeneity due to mixing the reagents on the molecular scale; decrease of the heating temperature due to small particle size with high surface areas; ability to produce uniform fine-grained structures.

Various processes and reagents have been used to prepare the HA powder and coating. Pierre<sup>5-6</sup> et al. use calcium diethoxide( $\text{Ca}(\text{OEt})_2$ ) and orthophosphoric acid( $\text{H}_3\text{PO}_4$ )as the reagents. Masuda<sup>7</sup> et al. and Chai CS et al.<sup>8</sup> have prepared HA coating using Calcium diethoxide ( $\text{Ca}(\text{OEt})_2$ ) and triethyl phosphate ( $\text{PO}(\text{OEt})_3$ ). CM.Lopatin<sup>9</sup> et al. form the sol with a hydrated solution of N-butyl acid phosphate and calcium nitrate tetrahydrate dissolved in 2-methoxyethanol. The reagents such as calcium diethoxide and triethyl phosphate are expensive. It is necessary to find the cheaper reagents in order to produce nanosized HA powder in large quantities. Wenjian Weng<sup>10-11</sup> has ever used the ethanol solution of calcium nitrate tetrahydrate and phosphorus pentoxide to prepare the HA coating on the different substrate. The reagents are cheap but the process is complex because the mixed ethanol

<sup>a)</sup> corresponding author. Tel: +86-531-8395693  
e-mail: yj\_song@163.com

solution of calcium nitrate tetrahydrate and phosphorus pentoxide need to be refluxed for 24h.

The aim of this paper is to prepare the nanosized HA powders with the cheap reactant and simple process. The results would try to illustrate the physicochemical process of HA preparation with ethanol solution of calcium nitrate tetrahydrate and phosphorous pentoxide.

## 2. Experimental procedures

Reagent grade  $\text{Ca}(\text{NO}_3)_2 \cdot 4\text{H}_2\text{O}$  and  $\text{P}_2\text{O}_5$  are dissolved in ethanol solution according to  $\text{Ca}/\text{P}=1.67$  respectively. The ethanol solution of  $\text{P}_2\text{O}_5$  is slowly dropped into the stirred  $\text{Ca}(\text{NO}_3)_2 \cdot 4\text{H}_2\text{O}$  ethanol solution and then the mixture turn into transparent sol after being continuously stirred for 10min. The mixture is dried at 80°C for 24h and turns yellow powder. Afterwards, it is ground into powder with a mortar and pestle. The powder is divided into three groups. The first group is used to perform the TG-DTA test with the heating rate of 10°C/min from room temperature to 1300°C. The second group is used to perform the FTIR test. After getting the results of TG-DTA, the exothermic and endothermic peaks and their corresponding temperatures are obtained. In order to investigate the components of the powder, the second group is sintered on Nicolet Magna 750 spectrometer with the heating rate of 10°C/min. The FTIR spectra are obtained in situ at temperature to which the main exothermic and endothermic peaks respond. The last group is sintered at different temperature and cooled to room temperature to be characterized by XRD patterns(Model: D/max, Japan). Data are collected over 20° range from 20° to 60°. Identification of phases is carried out by comparing the diffraction data with JCPDS standards. The morphology and size are obtained by TEM(Model: H800, Japan). The sample is dispersed by ultrasound in ethanol for 5min and then deposit on a copper grid for transmission electron microscopic observation. The crystal size is estimated from micrograph.

## 3. Results and discussion

### 3.1. TG-DTA results

Fig.1 is the TG-DTA curves of the mixture. The TG curve includes two stages: in the first stage (0—600°C), the weight decrease quickly and about total 64.92% weight loss is observed. weight loss is possibly due to evaporation of water and ethanol and burn of the residual solvent. In the second stage(600-1400°C), the weight decreases slowly and a total weight loss of is just only 3.83%.

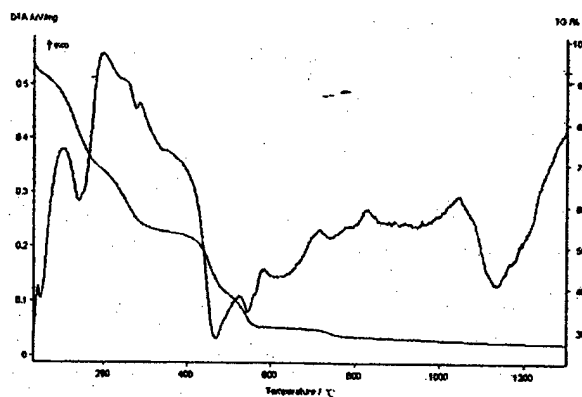


Figure 1 TG-DTA curve of the HA powders

The results of DTA are consistent with those of TG. The DTA curve shows that there are about four exothermic peaks situated at 102.1, 195.3, 825.8, 1047.8°C. The exothermic peaks at 102.1, 195.3°C are

due to burn of organic. The exothermic peaks at 825.8, 1047.8°C indicate the onset of crystallization. There are also six endothermic peaks situated at 49, 151, 273.9, 463.3, 545, 741.7, 1138.9°C. The endothermic peaks at about 49, 151, 273.9, 463.3, 545°C are attributed to the evaporation of free water and ethanol or loss of structural water. The endothermic peak at 1138.9°C possibly shows that the HA decompose into  $\beta$ -TCP and CaO. The HA prepared by wet precipitation method began to decompose at about 1300-1400°C the temperature of decomposition of HA prepared by sol-gel method is only 1138.9°C due to the small size and big surface area of grains<sup>10</sup>.

### 3.2 IR results

In order to investigate the composition of the mixture at 80, 102, 151, 195, 273, 350, 463°C (the main several exothermic and endothermic peaks are present at these temperature in TG-DTA curves), the IR spectra of the mixture sintered at different temperature are obtained in situ. The results are shown in Figure 2 (a),(b),(c),(d),(e),(f),(g), respectively.

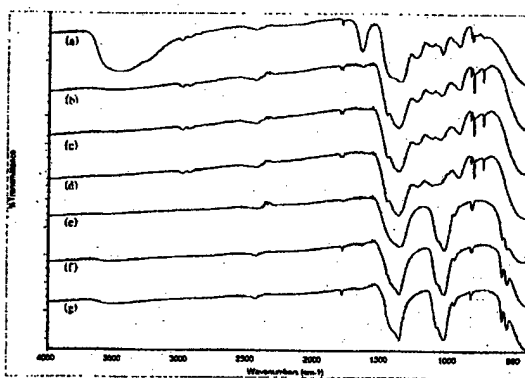


Figure 2 FTIR curve of HA samples heated at different temperatures

In Figure 2, the bands at about 1363 and 835  $\text{cm}^{-1}$  are attributed to the  $\text{NO}_3^-$  ions. In Figure 2 (a), the strong peaks at 3458 and 1637  $\text{cm}^{-1}$  are attributed to water from ethanol or  $\text{Ca}(\text{NO}_3)_2 \cdot 4\text{H}_2\text{O}$ . In Figure 2 (a),(b),(c),(d), the peaks at about 1236, 1064, 920, 813, 742  $\text{cm}^{-1}$  assigned to  $\text{PO}(\text{OH})_{3-x}(\text{OR})_x$ <sup>12</sup> are present, suggesting that the mixture is mainly composed of  $\text{Ca}(\text{NO}_3)_2$  and  $\text{PO}(\text{OH})_{3-x}(\text{OR})_x$  from 80 to 195°C. In Figure 2 (e),(f),(g), the bands at about 1031, 1060, 603, 563  $\text{cm}^{-1}$  are assigned to  $\text{PO}_4^{3-}$ , indicating the mixture maybe mainly consists of HA,  $\text{Ca}(\text{NO}_3)_2$  and  $\beta\text{-Ca}_2\text{P}_2\text{O}_7$ .

It can be seen from Figure 2 that the shapes of (a),(b),(c),(d) are similar and the shapes of (e),(f),(g) are also similar. But the shapes of the two groups are obviously different. On one hand, the peaks at about 1236, 1064, 920, 813, 742  $\text{cm}^{-1}$ , present in Figure 2 (a),(b),(c),(d), disappear from Figure 2 (e),(f),(g), indicating that  $\text{PO}(\text{OH})_{3-x}(\text{OR})_x$  decomposes before 273°C. On the other hand, the intensity of peaks at about 1031  $\text{cm}^{-1}$  turn stronger in Figure 2 from (a) to (b), suggesting that the amount of HA increases with the elevated temperature. These results are consistent with the following results of XRD patterns.

### 3.3 XRD results

Fig.3(a),(b),(c),(d),(e),(f),(g) are the XRD patterns of mixture sintered at 200, 300, 400, 500, 800 and 1200°C.

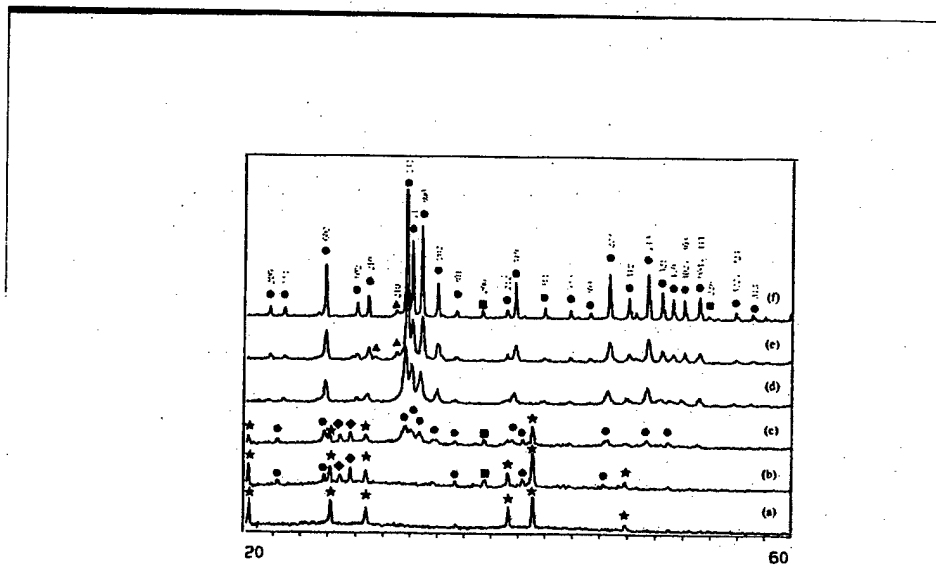


Figure 3 The as-prepared powders heated at different temperature for 2h

(a) 200°C (b) 300°C (c) 400°C (a) 500°C (b) 800°C (c) 1200°C

● — HA, ★ —  $\text{Ca}(\text{NO}_3)_2$ , ◆ —  $\alpha\text{-Ca}_3\text{P}_2\text{O}_7$ , ▲ —  $\beta\text{-TCP}$ , ■ —  $\text{CaO}$

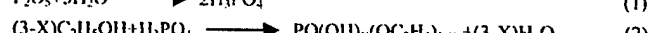
At 200°C, the mixture consists of  $\text{Ca}(\text{NO}_3)_2$  and a small amount of amorphous matter (according to IR analysis, this kind of organic matter is  $\text{PO}(\text{OH})_{3-x}(\text{OR})_x$ ). At 300°C and 400°C, the peaks of HA and  $\text{CaO}$  is present. This shows that the mixture is composed of  $\text{Ca}(\text{NO}_3)_2$ ,  $\alpha\text{-Ca}_3\text{P}_2\text{O}_7$ , HA and  $\text{CaO}$ . In addition, it can be seen that the amount of HA increase while the amount of  $\text{Ca}(\text{NO}_3)_2$  decrease with the increase of temperature. At 500°C, the peaks attributed to  $\text{Ca}(\text{NO}_3)_2$  and  $\alpha\text{-Ca}_3\text{P}_2\text{O}_7$  disappear completely. The XRD patterns are identical to HA. The results in table 1 also showed that sample sintered at 500°C for 2h is pure HA compared with the JCPDS standards (JCPDS#9-432). The XRD patterns at 800°C and 1200°C are similar with the pattern at 500°C. The slight differences are that XRD pattern of HA powders sintered at 500°C exhibit broad peaks and turned sharper at 800°C and 1200°C, proving that HA crystallize gradually with the increase of temperature. Additionally, a trace amount of  $\beta\text{-TCP}$  ( $\beta\text{-Ca}_3(\text{PO}_4)_2$ ) and  $\text{CaO}$  are detected in the pattern at 800 and 1200°C.

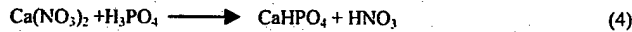
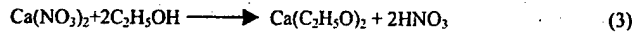
Table 1. Comparison of HA samples values heated

at 500°C for 2h with the JCPDS standards (#9-432)

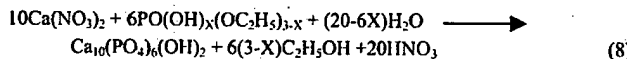
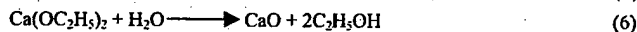
number	Observed		JSPDS (#9-432)		hkl
	D(Å)	intensity	D(Å)	intensity	
1	2.815	100	2.814	100	211
2	2.719	66	2.720	60	300
3	2.778	59	2.778	60	112
4	3.443	39	3.44	40	002
5	1.839	39	1.841	40	213
6	1.943	37	1.943	30	222
7	2.627	26	2.631	25	202
8	2.263	27	2.262	20	310
9	3.081	16	3.08	18	210
10	1.890	17	1.890	16	212

When the ethanol solution of calcium nitrate tetrahydrate and phosphorus pentoxide are mixed together. The reactions are as follows<sup>13</sup>:





From 200 to 500, The process can be described as Eq. (5),(6),(7),(8)<sup>6</sup>:



The results of Figure 3 have proved that the mixture are composed of  $\text{Ca}_2\text{P}_2\text{O}_7$ ,  $\text{CaO}$ , HA. The amount of HA increases with the increase of temperature. The reactions to prepare HA in Eq. (7),(8) are finished at 500

A amount of HA begins to decompose over 800 as described in Eq. (9)<sup>10</sup>



In short, the results from XRD patterns are consistent with the results of IR analyses and TG-DTA results. The mixture consists of  $\text{Ca}(\text{NO}_3)_2$ , HA,  $\text{PO}(\text{OH})_{3-x}(\text{OR})_x$ ,  $\alpha\text{-Ca}_2\text{P}_2\text{O}_7$  and  $\text{CaO}$  from 200 to 500°C. At 500°C, mixture is mainly composed of HA. The morphology of the HA powder sintered at 500°C for 2h is shown in Figure 4. The individual particles are uniform. The size is about as big as 30-40nm. At 800°C, 1200°C, the mixture is composed of HA, a trace amount of  $\beta\text{-TCP}$  and  $\text{CaO}$ .

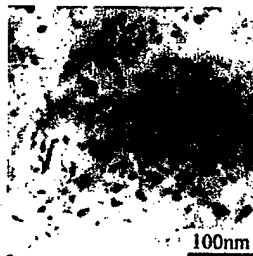


Figure 4 Transmission electron micrograph of HA grains heated at 500°C for 2h

#### 4. Conclusion

Nanosized HA powders can be prepared from ethanol solution of  $\text{Ca}(\text{NO}_3)_2 \cdot 4\text{H}_2\text{O}$  and  $\text{P}_2\text{O}_5$  by sol-gel method. The reactants are cheap and the process is simple without refluxing. The results are encouraging because the advantages offered by this process can make it possible to produce the nanosized HA powder at low cost in large quantities. The size of hydroxyapatite crystal sintered at 500°C for 2h is as fine as about 30-40nm. The synthesis of HA is finished until about 500°C. From 200 to 500°C, The mixture is composed of amorphous HA,  $\text{Ca}(\text{NO}_3)_2$ ,  $\text{PO}(\text{OH})_{3-x}(\text{OR})_x$ ,  $\alpha\text{-Ca}_2\text{P}_2\text{O}_7$ . A trace amount of  $\beta\text{-TCP}$  and  $\text{CaO}$  are present due to the decomposition of HA after 800°C.

#### Acknowledgements

The authors thank the Mr. Liu Futian, Mr. Liu Yuxian and Mrs. Shi Wenhua for their assistance with the experiments. They are also grateful to the commission of the support from the Science Council of Shandong Province

#### References

1. Wojciech Suchanek, Masahiro Yoshimura. Processing and properties of hydroxyapatite-based biomaterials for use as hard tissue replacement implants. *J. Mater. Res.* 13, 94 (1998)

2.A. Osaka, Y. Miura, K. Takeuchi, M. Asada, K. Takahashi. Calcium apatite prepared from calcium hydroxide and orthophosphoric acid. *J. Mater. Sci.: Mater. Med.* 2,51(1991)

3.R. Ramachandra Rao. Solid State Synthesis And Thermal Stability Of Hap And HAP- $\beta$  -TCP Composite Ceramic Powders. *J. Mater. Sci.: Mater. Med.* 8,51(1997)

4.Li Yubao, K. De Groot, J. De Wijn, C. P. A. T. Klein, S. V. D. Meer. Morphology and composition of nanograde calcium phosphate needle-like crystals formed by simple hydrothermal treatment. *J. Mater. Sci.: Mater. Med.* 5,326(1994)

5.Pierre Layrolle, Atsuo Ito, Tetsuya Tateishi. Sol-gel synthesis of amorphous calcium phosphate and sintering into microporous hydroxyapatite bioceramics. *J. Am. Ceram. Soc.* 81,1421(1998)

6.Pierre Layrolle, Albert Lebugle. Characterization and reactivity of nanosized calcium phosphates prepared in anhydrous ethanol. *Chem. Mater.* 6,1996(1994)

7.Masuda Y, Matubara K, Sakka S. Synthesis of hydroxyapatite from metal alkoxides through sol-gel technique. *J. Ceram. Soc. Japán.* 98,1266(1990)

8. Chai C.S., Gross K.A., Ben-Nissan B.. Critical ageing of hydroxyapatite sol-gel solutions *Biomaterials*, 19,2291(1998)

9. C.M. Lopatin, V. Pizziconi, T.L..Alford, T. Laursen. Hydroxyapatite powders and thin films prepared by a sol-gel technique. *Thin solid films*, 326,227(1998)

10. Wenjian Weng, Joao Lopes Baptista. Preparation and characterization of hydroxyapatite coatings on Ti6Al4V alloy by a sol-gel method. *J. Am. Ceram. Soc.* 82,27(1998)

11. Wenjian Weng, JL. Baptista Sol-gel derived porous hydroxyapatite coating. *J. Mater. Sci.: Mater. Med.* 9,159( 1998)

12.Kyuseog Ilwang, Jongeun song, Boan Kang, Yeongjoo Park. Sol-gel derived hydroxyapatite films on alumina substrates. *Surface and Coatings Technology*, 123,252(2000)

13. J. Livage, P. Barboux, M.T. Vandeborre, Sichmutz C., Taulelle F.. Sol-gel synthesis of phosphates. *J.Non-Cryst Solids*, 147-148,18(1992)

### Spatio-Temporal Patterns in Ferritin Crystal Growth

Olga Gliko and Peter G. Vekilov

Department of Chemical Engineering, University of Houston, Houston, TX 77204-4004

#### ABSTRACT

We investigate the unsteady kinetics and the formation of spatio-temporal patterns during the ferritin crystal growth, which is controlled by the rate of supply of material. For this, we apply a novel phase-shifting interferometry technique. We find that the growth rate and local slope fluctuate by up to 100% of their average values as a result of step bunching. The fluctuation amplitudes decrease with higher supersaturation and larger crystal size, as well as with increasing distance from the step sources. Since these are parameters that govern the protein supply field, we conclude that fluctuations are rooted in the coupling of the interfacial processes of growth to the bulk transport in the solution. Analysis of the step velocity dependence on local slope indicates a very weak interaction between the steps. Hence, in transport-controlled systems with non-interacting or weakly interacting steps the step bunches decay and step train tends towards its stable, equidistant state.

#### INTRODUCTION

The loss of stability of equidistant step trains leads to bunches of steps spreading along the crystal face, interspersed with bands of lower step density. The step bunches leave trails of higher defects density in the crystal lattice, and in this way lower the perfection and the utility of the grown crystals [1-3].

The kinetics instabilities and step bunching during the crystallization of the protein lysozyme were studied using a high-resolution interferometry technique [4]. It was concluded that fluctuations are intrinsic and result from the coupled bulk transport and interfacial kinetics processes [3]. According to this mechanism, the strongest instabilities occur when the growth proceeds under equal weights of the transport and kinetics in the overall rate control. Hence, shifts towards purely kinetic, or, conversely, purely diffusive regimes should lead to higher stability. Developed numerical model of coupled bulk transport and nonlinear interfacial kinetics quantitatively reproduces the experimentally observed unsteadiness [5]. If the rationale developed based on lysozyme data holds, in crystallization systems with dominant transport control, such as ferritin, a shift of the working point toward slower transport should dampen the fluctuations. Thus, the aim of this work is to experimentally study the origin of kinetics unsteadiness in ferritin growth. We investigate the dependencies of the amplitude of local slope fluctuations on the parameters affecting transport to the interface: supersaturation, crystal size and location on the crystal faces.

#### EXPERIMENTAL PROCEDURES

The crystallizing solution contains between 2–2.5 mg/mL horse spleen ferritin purchased from Sigma and purified to reduce the level of the most common impurity, the covalent dimer of ferritin, to below 5% [6]. We use 2.0% (w/v)  $\text{CdSO}_4$  as a precipitant, and 0.2 M sodium acetate

buffer ( $\text{NaCH}_3\text{COO}$ ) to fix pH at 5.05. The temperature of the solution in the growth cell is stabilized to  $23 \pm 0.01^\circ\text{C}$  by a thermoelectric (Peltier) cooler [7]. The supersaturation is calculated as  $\sigma = \ln(C/C_c)$ , where  $C$  is concentration of the solution,  $C_c = 35 \mu\text{g/mL}$  [8] is solubility.

We used a phase-shifting interferometry technique specifically developed for this study [7]. The phase-shifting algorithm chosen by us employs five-image sequences captured with a phase shift of  $\pi/2$ ; digital processing of the sequence allows reconstruction of the surface morphology with a depth resolution of 5 nm across a field of view of  $1 \times 1 \text{ mm}^2$ , for details see ref [7]. The time traces of the normal growth rate  $R$ , local slope proportional to step density  $p$ , and step velocity  $v$  are recorded at select locations on the crystal surface with time resolution of 1 s [4].

Figure 1 shows the morphology of (111) faces of two ferritin crystals with sizes  $200 \mu\text{m}$  and  $470 \mu\text{m}$ . Figure 1a–c presents five interference images of the growing crystal surface recorded during 1 s with a phase shift of  $\pi/2$  between them; the underlying assumption is that the surface does not change within this time period. Five images are combined to give one “phase-wrapped” image (Figure 1f, g) using, for each pixel

$$h = \frac{\lambda_{\text{laser}}}{2\pi n} \tan^{-1} \left[ \frac{2(I_2 - I_4)}{2I_3 - I_5 - I_1} \right] \quad (1)$$

where  $I_1, \dots, I_5$  are the intensity of a pixel in each of five images,  $h$  is the height on the respective point of crystal surface,  $\lambda_{\text{laser}} = 0.6328 \mu\text{m}$  is the laser wavelength and  $n = 1.3320$  is the refractive index of the solution.

## RESULTS AND DISCUSSION

### Phenomenology of the time-dependent kinetics

During the growth of ferritin crystals the growth layers are always generated by 2D-nucleation. For small crystal sizes and  $\sigma < 3$ , the distribution of 2D-nuclei is uniform across the whole face and, on a macroscopic scale, the face remains flat as the crystal grows. For higher supersaturations and crystals larger than  $100 \mu\text{m}$ , 2D-nucleation localizes at the facet edges and

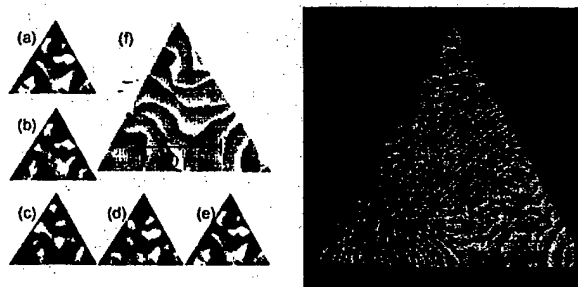


**Figure 1.** Typical morphology of a (111) face of a ferritin crystal. (a–e) A sequence of five interferometric images recorded with a phase shift of  $\pi/2$ . (f, g) The phase-wrapped images. The difference in height between the brightest and darkest pixels is  $\lambda/4n = 0.119 \mu\text{m}$ . (f)  $\sigma = 4.0$ , (g)  $\sigma = 4.3$ . +, locations of layer generation;  $\times$ , locations of growth kinetics monitoring.

corners. Numerical modeling of diffusive-convective transport of crystallizing proteins has linked this localization to higher interfacial supersaturation at the edges [9].

Figures 2a-c show the time traces of the normal growth rate  $R$ , local slope  $p$ , and step velocity  $v$  recorded at the marked location near the facet center in Figure 1g at  $\sigma = 4.3$ . The  $R$ ,  $p$ ,  $v$  fluctuate by up to 100% of their respective average values. The fluctuations of local slope indicate that the unsteadiness occurs through the formation of step bunches. In order to analyze the fluctuations dependencies on different factors such as supersaturation, crystal size, location on the facet, we use Fourier decomposition of the three time traces. Earlier work has shown that the Fourier frequencies, characterizing the fluctuation time scales, and the Fourier amplitudes, corresponding to the deviations from average values of the respective kinetic variables, are reproducible characteristics of the unsteady behavior and only depend on the external conditions [10]. Figures 2d-f present the normalized Fourier spectra  $A(f_m)/A_0$  of  $R(t)$ ,  $p(t)$  and  $v(t)$ .

### Step-step interactions

Figures 2d-f show that the Fourier spectra for  $R$ ,  $p$ , and  $v$  are similar. Since the Fourier spectra of  $p$  directly reflect the step bunching, we will use only these spectra in further considerations.

As shown in Figures 3a-c, the fluctuations are rather periodic. However, there appears to be no correlation between the fluctuations of the slope and the step velocity. The dependence of step velocity on local slope and the reduced concentration  $(C - C_e)C_e^{-1}$  can be expressed as [10]

$$v = \frac{b_{\text{step}}(C - C_e)/C_e}{1 + kp} \quad (2)$$

where  $b_{\text{step}}$  is an effective step kinetic coefficient and  $k$  is a parameter characterizing the step-step interactions. For non-interacting steps,  $k = 0$ ; for strongly interacting steps such as those in lysozyme growth, where incorporation into steps is preceded by slow diffusion through the solution bulk and the terraces between the steps,  $k$  is in the range 1000–2000 [10]; for the growth of inorganic phosphates with a similar growth mechanism, values of  $k$  are ~1000 [11].

Prompted by the form of the  $v(p)$  dependence in (2), we plot the reciprocal step velocity  $1/v$  as a function of the local slope  $p$  for a trace recorded over several hours at the location near the center of facet in Figure 1g. To extract the deterministic link between  $v$  and  $p$ , we calculate the least square fit of the data to a straight line. From extrapolated intercept of this line with the

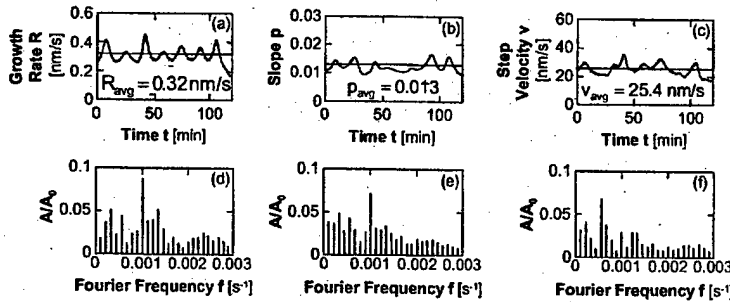


Figure 2. (a)–(c) Time traces of the normal growth rate  $R$ , the local slope  $p$  and the step velocity  $v$  recorded during growth of ferritin crystal at supersaturation  $\sigma = 4.3$ . (d)–(f) corresponding normalized Fourier spectra; in (d)–(f)  $A/A_0 = 1$  at  $f = 0$  is omitted.

ordinate axis and known value of  $(C - C_c)/C_c = 71$ , we obtain the value of  $b_{\text{step}} = 4.8 \times 10^{-8} \text{ cm/s}$ . The step kinetic coefficient  $\beta = b_{\text{step}}/\Omega C_c = 11 \times 10^{-4} \text{ cm/s}$  ( $\Omega$  is the crystal volume per molecule,  $\Omega C_c = 4.2 \times 10^{-3}$ ) is somewhat higher than the value of  $\beta = 6 \times 10^{-4} \text{ cm/s}$  obtained using AFM [8]. From the slope of the fit we calculate  $k = 32$  and  $k p_{\text{avg}} \approx 0.35$ . This low value of  $k$  indicates a very weak interaction between steps, i.e. the diffusion supply fields around the steps do not overlap. This makes the ferritin system quite different from lysozyme, which is characterized by strong interaction between steps, which results in dependence of step velocity on slope [10].

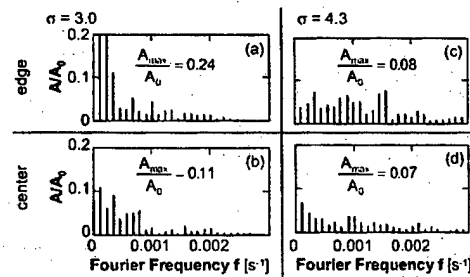
#### Variations of the fluctuation patterns with the external conditions

Figure 3 presents the Fourier spectra of slope traces recorded at two locations on the facet shown in Figure 1g. Comparison of the spectra shows that the fluctuation amplitudes decrease as supersaturation increases and are greater near the facet edges than at the facet center. Note that the lower fluctuations at the facet center and at the higher supersaturations occur despite being accompanied by higher average vicinal slope. This is a remarkable observation, because the average vicinal slope has been identified as a major *destabilizing* factor for equidistant step trains [12]. We conclude that the mechanism leading to decay of the fluctuations is sufficiently strong to overpower the average slope effects.

We calculated the Fourier spectra of slope traces recorded at the center of two facets with different size (Figures 1f and 1g) at the same supersaturation. The maximum amplitude value is significantly higher for the smaller crystal, while the averaged slope is lower in this case.

We also compared the Fourier spectra of slope traces recorded simultaneously at two different locations of the facet shown in Figure 1f. The first location is close to the location of layer generation near the facet corner, while the second is further removed from the layer source. The amplitude of the slope fluctuations increases with the distance from layer source, while, as above, the averaged value of the slope decreases.

To understand these observations, we use that the crystal size, the location on the facet and the supersaturation are parameters that strongly affect the solute supply to the interface. Hence, the observed dependencies of the fluctuation amplitudes with these parameters indicate that, similar to lysozyme [3], the growth instability is due to the coupling of the nonlinear interfacial processes of growth to the bulk transport in the solution.



**Figure 3.** Fourier spectra of traces of the local slope  $p$  for the crystal of a  $470 \mu\text{m}$  size shown in Figure 1g. (a)  $\sigma = 3.0$ , monitoring location at the facet edge,  $p_{\text{avg}} = 0.006$ ; (b)  $\sigma = 3.0$ , monitoring location near the facet center,  $p_{\text{avg}} = 0.008$ ; (c)  $\sigma = 4.3$ , edge,  $p_{\text{avg}} = 0.012$ ; (d)  $\sigma = 4.3$ , center,  $p_{\text{avg}} = 0.014$ .

However, in all of the cases, the dependence of the fluctuation amplitudes on the respective parameter is opposite to that for lysozyme, and may appear counterintuitive. Thus, we would expect the faster growth at higher supersaturations to be more instable and with stronger fluctuations, we would expect the instabilities to evolve as the steps propagate down their pathway, and so on. This last controversy provides the key to understanding the unsteady behavior of the step trains in ferritin growth. Indeed, if the fluctuation amplitudes are damped as the steps move on, it follows that the stable state, towards which the step train is converging, is the equidistant step train. Along this line of thought, we must conclude that the step bunches are generated at the location of step generation, i.e., the 2D nucleation process is highly unsteady, and consist of spurts of nucleated layers, leading to stacks of steps, followed by lower activity. The dependence of the fluctuation amplitudes on the supersaturation in the solution bulk suggests that the unsteady layer generation is caused by its coupling to the solute supply to the location of step generation.

The non-uniform step generation at the facet edges produces the step bunches. As the steps move away from their sources towards the facet center, the step bunches decay. An important factor for this decay is the lack of step-step interactions—such interactions are known to strongly destabilize the uniform step trains, and lead to increasing fluctuations [10].

The motion of steps and the evolution of the step bunches formed at the stage of layer generation is only affected by the coupled bulk transport and surface kinetics. The estimation of the kinetic Peclet number  $Pe_t = \beta p \delta D$  ( $\delta$  is the characteristic diffusion layer thickness, typically of the order of  $200 \mu\text{m}$ , and  $D = 3.2 \times 10^{-7} \text{ cm}^2/\text{s}$  is diffusivity) gives value  $\sim 1.0$ . Hence, ferritin growth is predominantly controlled by the transport in the solution. For such systems, the rationale predicts higher stability at *even higher* relative weight of transport. Thus, we should expect lower kinetic fluctuations at higher supersaturations, at larger crystals sizes, and at the facet centers.

#### Spatial-temporal characteristics of the step patterns

The phase-shifting technique allows reconstruction of the surface morphology. Figure 4a shows the height profile along the line depicted in Figure 1g. The height decreases as the distance from layer sources increases. The corresponding slope profile and its spatial Fourier spectrum are shown in Figure 4b and c, respectively. The wave numbers in Figure 4c are reciprocal to the corresponding step bunch wavelengths  $\lambda$ . The maximum amplitude occurs at a wave number of  $0.045 \mu\text{m}^{-1}$  corresponding to fluctuations with  $\lambda_{\text{max}} \sim 21 \mu\text{m}$ . From the time

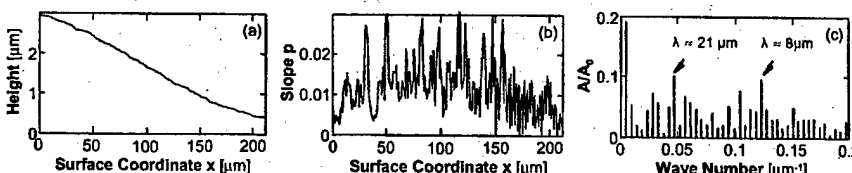


Figure 4. (a) Height and (b) local slope profiles along the line shown in Figure 1g. (c) Corresponding Fourier spectrum of p. The characteristic step bunch wavelengths  $\lambda$  are indicated in the plot. The first amplitude in (c) corresponds to the overall bending of the surface seen in (b)

traces measured at the location on profile line at the same  $\sigma = 4.3$ , see Figure 3c, we determine the characteristic step bunch frequency  $f_{\max} = 0.0016 \text{ s}^{-1}$  ( $\Delta t \sim 10.7 \text{ min}$ ). From these two values, we can evaluate the step bunch velocity as  $v_{\text{bunch}} = \lambda_{\max} f_{\max} \sim 33 \text{ nm/s}$ . The value of  $v_{\text{bunch}}$  is close to mean step velocity under those conditions,  $v \approx 35 \text{ nm/s}$ . Thus, in the case of non-interacting steps, the step bunches move with the same velocity as elementary steps.

## CONCLUSIONS

Under steady growth conditions, ferritin growth kinetics fluctuate up to 100% of the average. The fluctuations reflect the dynamics of formation and evolution of step patterns. The lack of correlation of the step velocity and local slope indicates very weak step-step interactions. Correspondingly, the propagation rate of step bunches is same as elementary step velocity.

The unsteady growth is the result of the coupling between solute transport towards the interface and the nonlinear interfacial kinetics. The main factor introducing non-linearity onto the interfacial kinetics is the generation of layers via a 2D nucleation mechanism. The fluctuation amplitude decreases with increasing distance from the layer sources. Hence, for non-interacting steps growing under diffusion control the randomly arising step bunches decay and the stable growth mode is that via equidistant step trains.

These findings in a transport-controlled system provide a strong support to the rationale for the control of the step bunching instabilities in layer growth system that was previously based on observation with a kinetically controlled system.

## ACKNOWLEDGMENTS

We thank Bill Thomas for the analysis and purification of the protein solutions and Kai Chen for supplementary AFM determinations. Research support was generously provided by the Office of Biological and Physical Sciences, NASA under Grants NAG8-1857 and NAG8-1354.

## REFERENCES

1. A. A. Chernov, "Modern Crystallography III, Crystal Growth," Springer, Berlin, 1984.
2. E. Bauser, in "Handbook of Crystal Growth" (D. T. J. Hurle, ed.), Vol. 3b, p. 879. North Holland, Amsterdam, 1994.
3. P. G. Vekilov, J. I. D. Alexander, and F. Rosenberger, *Phys. Rev. E* **54**, 6650 (1996).
4. P. G. Vekilov, L. A. Monaco, and F. Rosenberger, *J. Cryst. Growth* **148**, 289 (1995).
5. H. Lin, P. G. Vekilov, and F. Rosenberger, *J. Cryst. Growth* **158**, 552 (1996).
6. B. R. Thomas, D. Carter, and F. Rosenberger, *J. Cryst. Growth* **187**, 499 (1998).
7. O. Gliko, N. A. Booth, and P. G. Vekilov, *Crystal Growth and Design*, in press (2002).
8. K. Chen, unpublished.
9. H. Lin, F. Rosenberger, J. I. D. Alexander, and A. Nadarajah, *J. Cryst. Growth* **151**, 153 (1995).
10. P. G. Vekilov, B. R. Thomas, and F. Rosenberger, *J. Phys. Chem.* **102**, 5208 (1998).
11. N. A. Booth, A. A. Chernov, and P. G. Vekilov, *J. Cryst. Growth*, in print (2002).
12. A. A. Chernov, S. R. Coriell, and B. T. Murray, *J. Cryst. Growth* **132**, 405 (1993).

### Influence of DNA, Alginate, Lysozyme and Bovine Serum Albumin on Sodium Silicate Condensation

Thibaud Coradin, Aurélie Coupé and Jacques Livage  
Laboratoire de Chimie de la Matière Condensée, CNRS-UMR 7574, UPMC,  
F-75252 Paris cedex 05, France.

#### ABSTRACT

The interaction of DNA, alginate, Lysozyme and Bovine Serum Albumin with diluted solutions of sodium silicate was studied using the molybdosilicate method. DNA and alginate showed very weak interactions with silica precursors whereas both proteins were able to form silica gels. Both electrostatic interactions and hydrogen bonds are suggested to arise between peptide chain and polysilicates, bringing new informations on the nature of inorganic and bio-organic species involved in the natural biosilicification processes.

#### INTRODUCTION

Biomineralization processes often occur at the interface between inorganic precursors and biological macromolecules [1]. For instance, bone formation involves hydroxyapatite deposition in a collagen proteinaceous matrix whereas the  $\beta$ -chitin polysaccharide and calcium carbonate are associated within crab cuticles. The formation of the silica skeleton of diatoms was shown to take place mainly at the interface with proteins, even though the presence of sugars in the cell wall was reported [2-3].

Aiming at understanding the interactions that may arise between the naturally-occurring form of silica precursors, i.e. silicic acids, and proteins, we have undertaken the study of the effect of various biopolymers on the behaviour of sodium silicate diluted solutions. We have first focused on amino acids and poly-amino acids and shown that poly-lysine and poly-arginine were able to induce silica formation, the catalytic effect increasing with polymer chain length [4-5]. These results correlate well with the fact that the silaffin proteins that were extracted from diatom cells are characterized by lysine and arginine patches along the peptide chain [6].

In order to get a better understanding of the possible silica-biopolymers interactions, we have selected two proteins that bear an important number of lysine and arginine groups, as well as a polysaccharide macromolecule and DNA. The evolution of the silicic acid content of a diluted sodium silicate solution in the presence of these polymers was monitored using the molybdosilicate method [7]. Depending on the solution pH, only the two proteins were able to induce silica formation. These results are discussed in terms of electrostatic interactions and hydrogen bonds.

## EXPERIMENTAL

Waterglass (27%  $\text{SiO}_2$ , 10 % NaOH) from Riedel-de Haen was chosen as the source of silicic acid. Aqueous silicate solutions were preferred to silicon alkoxide precursors because they correspond to the usual form of soluble silica in nature. For similar reasons, diluted solutions (10 mM) of  $\text{SiO}_2$  were used. Lysozyme grade I from Chicken Egg White and Bovine Serum Albumin (BSA) were purchased from Sigma. Deoxyribonucleic acid (DNA) from fish sperm was obtained from Amersham and alginic acid sodium salt from brown algae from Fluka. Molybdate studies were performed in a 0.05 M Tris-HCl buffer (pH = 7.2) and 0.05 M acetate buffer (pH = 4.9).

In a typical experiment, 65 mg of the sodium silicate solution were diluted in 30 mL of the appropriate buffer in order to obtain a  $10^{-2}$  M silica solution. The mixture was stirred for ten minutes before adding a solution containing the appropriate quantity of polymer so that the monomer (i.e amino acid, sugar or DNA unit)-to-Si ratio was kept equal to 0.1 dissolved in 3 mL of the buffer solution. At regular intervals of time, 400  $\mu\text{l}$  of the reacting solution were taken and added to 5 mL of deionized water, 200  $\mu\text{l}$  of  $\text{H}_2\text{SO}_4$  (1.5 M) and 200  $\mu\text{l}$  of ammonium molybdate (0.08 M) were then added [8]. The mixture was left to stand for 10 minutes in order to allow monomeric silicic acid and small silica oligomers to react with the heptamolybdate to form the yellow silicomolybdate acid  $\text{H}_8\text{Si}(\text{Mo}_2\text{O}_7)_6$ . The optical density (OD) of the final solution was measured at 400 nm using a double beam Uvikon XS spectrophotometer. Data were reproducible within a 5 % error range.

When silica formation occurred, solids were centrifuged and freeze dried at  $-30^\circ\text{C}$ . Thermogravimetric analysis were performed on a Netzsch STA409 apparatus under  $\text{O}_2$  flow with a heating rate of  $5^\circ\text{C}/\text{min}$ .

BSA and Lysozyme titration curves were calculated using ExPASY softwares from the Swiss Institute of Bioinformatics (SIB) [9].

## RESULTS

Silicic acid is obtained upon acidification and dilution of sodium silicate solutions. A clear solution (10 mM in silica) is obtained. In a Tris-HCl buffer (pH = 7.2), the initial amount of silicic acid decreases slowly but no gelation is observed within the first 3 hours (Figure 1). This amount decreases slightly faster in the presence of DNA, alginic acid and BSA but the solutions remain optically clear and gelation is not observed either. Addition of Lysozyme induces a first increase in silicic acid content followed by a slow decrease and solutions become turbid, leading to the formation of a loose gel.

In contrast, in acetate buffer (pH = 4.9), a slow increase of initial silicic acid content is observed that is only slightly modified by biopolymers addition (Figure 2). No gel is formed except in the presence of BSA.

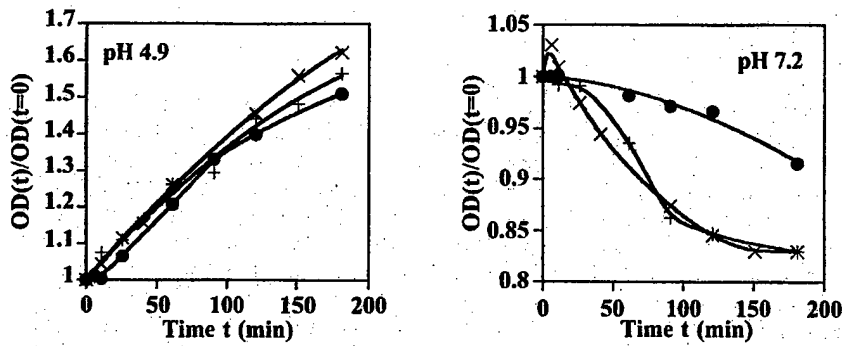


Figure 1 Condensation of silicic acid in the absence (●) and in the presence of DNA (+) and alginic acid (X) in acetate (left) and Tris.HCl (right) buffer. Evolution with time of the silicic acid content as measured by the optical density ratio  $OD(t)/OD(t=0)$  at 400 nm using the molybdosilicate method.

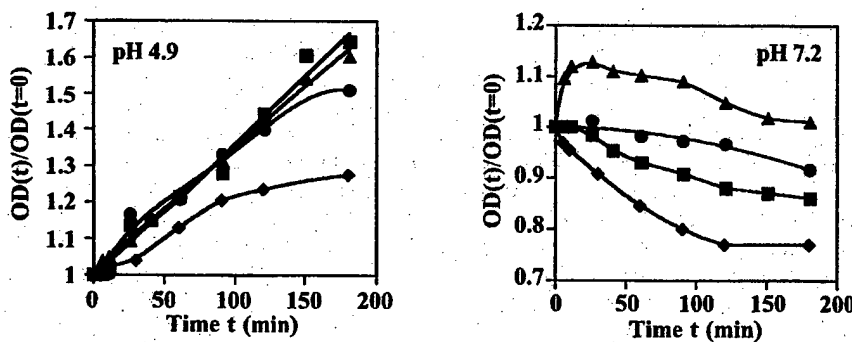


Figure 2 Condensation of silicic acid in the absence (●) and in the presence of Lysozyme (▲), BSA (■) and poly-Lysine (◆) in acetate (left) and Tris.HCl (right) buffer. Evolution with time of the silicic acid content as measured by the optical density ratio  $OD(t)/OD(t=0)$  at 400 nm using the molybdosilicate method.

After freeze drying, the two obtained solids, hereafter named Lys07 and BSA4, contain *c.a.* 50 w% of silica. Corresponding yields, calculated on the basis of the initial solution molar Si content, are 20% for Lys07 and 10 % for BSA4.

## DISCUSSION

Concentrated sodium silicate solutions are known to contain a mixture of oligomeric silicate anions, ranging from chain trimers to cage octamers [10]. Upon dilution, decondensation occurs leading to monomolecular  $[\text{SiO}_4\text{H}_{4-x}]^x$  species, where  $x$  increases with pH above the point of zero charge (pH  $\approx$  3).  $\text{Si}(\text{OH})_4$  is the predominant species in the pH range 4-9 and  $[\text{SiO}(\text{OH})_3]^-$  above pH  $\approx$  10 [11]. However, monomeric silicic acid exists only in very dilute solutions. At higher concentration, polymerization occurs by condensation of silanol Si-OH groups between neutral silicic acid and negatively charged species. The rate of condensation goes through a minimum around the point of zero charge and increases with pH. It is for instance two orders of magnitude faster at pH 6 than at pH 4 [12]. Therefore, two opposite processes, decondensation and polymerization, compete when concentrated sodium silicate solutions are diluted. At pH 7.2, the condensation process is faster so that a small decrease in silicic acid content is observed whereas the decondensation process mainly predominate at pH 4.9.

In the 4.5-7.5, pH domain, both DNA and alginic acid are negatively charged so that only repulsive interactions are expected to occur with negatively charged silica oligomers. However, the slight decrease in the silicic acid content when compared to sodium silicate alone at both pH suggest that monomeric species may weakly interact through hydrogen bonding with the polymers.

In contrast, the observed formation of Lyso7 and BSA4 is rather surprising when compared to previous studies on p-Lysine [5]. In the same experimental conditions, addition of this peptide led to rapid silica polymerization at pH 7 and not at pH 4, close to Lysozyme behaviour. However, as shown on Fig. 1 and Fig. 2, silica precipitation was correlated to an important decrease in silicic acid content at pH 7. This was attributed to the possibility for monomeric silica to interact electrostatically with lysine amine group and through hydrogen bonds with peptide backbone carbonyls. Because lysine groups are present all along the peptide chain, precursors are brought close enough to promote condensation [5]. In the case of the two proteins used in this work however, lysine and arginine groups are distributed along the peptide chain so that silica monomers may be too far from one another to interact. This argument, combined with the absence of important decrease in silicic acid content, suggests that the silica species responsible for gel formation are not, in this case, monomers but correspond to the oligomeric anions present in the starting solution. This hypothesis is strengthened by the fact that only a small part (10-20 %) of the initial silica is present in the final solids, indicating that participation of monomers through condensation is limited.

The difference in behaviour of Lysozyme and BSA in acidic and neutral media can be correlated to both silica species and proteins charges. Calculated titration curves for both proteins are given in Fig. 3. BSA is a large protein (MW  $\approx$  66 kDa) containing 582 amino acid residues. Basic lysine and arginine groups account for *c.a.* 14 % of the total sequence whereas acidic aspartic acid and glutamic acid account for *c.a.* 16 %. As a consequence, its point of zero charge is close to pH 5. In contrast, Lysozyme is a small chain peptide (MW  $\approx$  16 kDa, 147 amino acids) with 12 % basic and 6% acidic groups with a point of zero charge close to 11. Lysozyme bears a small nearly constant (*c.a.* 10-12) positive charge in the 4.5-7.5 pH range. In contrast, BSA is slightly negatively charged at pH 7.2 and positively charged at pH 4.9.

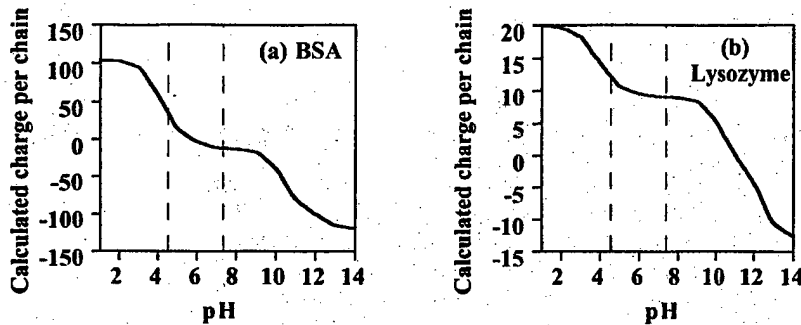


Figure 3 Evolution of calculated charge per chain with pH for (a) BSA and (b) Lysozyme.

Therefore, at neutral pH, BSA and silicate bear charges of same sign and no interaction is expected whereas electrostatic interactions may arise between positively charged Lysozyme and anionic silicates, thus explaining the observed silica gelation. Accordingly, at pH 4.9, BSA becomes positively charged leading to BSA4 formation. However, at this pH, it should be expected that Lysozyme also induces silica formation, in contradiction with experimental results. Since Lysozyme charge is only slightly modified by the pH decrease, the explanation should lie in the silicate reactivity. Even though it is difficult, at this time, to conclude, it may be attributed to the decrease of polysilicates negative charges as pH comes closer to silica point of zero charge around pH 3.

## CONCLUSION

These studies aimed at identifying the nature of inorganic and bio-organic species, which are likely to be involved in biosilicification processes. Considering activation of silica polymerisation, this work suggests that proteins are the most likely to interact with mineral precursors. However, it should be noticed that polymers like polysaccharides might be involved in other aspects of silica biomineralization such as morphology control, as previously suggested [3, 13]. As far as silica precursors are concerned, our results suggest that oligomeric polysilicates may be involved in the silicification process. These species therefore add to monomeric silica and silica nanoparticles which were previously shown to form silica gels in the presence of poly-amino acids [5]. Such diversity reflects the complexity of natural processes that is the main challenge of the biomimetic design of new materials.

---

## REFERENCES

1. S. Mann, *Nature* **332**, 119 (1988).
2. B. E. Volcani in *Silicon and Siliceous Structures in Biological Systems*, edited by T. L. Simpson and B. E. Volcani (Springer, 1981) pp. 157-200.
3. C. C. Perry and T. Keeling-Tucker, *J. Biol. Inorg. Chem.* **5**, 537 (2000).
4. T. Coradin and J. Livage, *Colloids Surf. B : Biointerfaces* **21**, 329 (2001).
5. T. Coradin, O. Durupthy and J. Livage, *Langmuir* (in press).
6. N. Kröger, R. Deutzmann and M. Sumper, *Science* **286**, 1229 (1999).
7. B. G. Alexander, *J. Am. Chem. Soc.* **75**, 2887 (1953).
8. T. Mizutani, H. Nagase, N. Fujiwara and H. Ogoshi, *Bull. Chem. Soc. Jpn.* **71**, 2017 (1998).
9. R. D. Appel, A. Bairoch and D. F. Hochstrasser, *Trends Biochem. Sci.* **19**, 258 (1994).
10. C. T. G. Knight, *J. Chem. Soc. Dalton Trans.* 1457 (1988).
11. C. F. Baes, Jr. and R. E. Mesmer, *The Hydrolysis of Cations* (Wiley, 1974) pp. 337-342.
12. R. K. Iler, *The Chemistry of Silica* (Wiley, 1979) pp. 172-311.
13. T. Coradin and J. Livage, *J. Sol-Gel Sci. Technol.* (in press).

### Colorimetric Biosensor Vesicles for Biotechnological Applications.

Revital Halevy<sup>1</sup>, Sofiya Kolusheva<sup>1</sup>, Robert E.W. Hancock<sup>2</sup> Raz Jelinck<sup>1</sup>.

<sup>1</sup> Department of chemistry, Ben-Gurion University of the Negev,  
Beersheva, 84105 Israel.

<sup>2</sup> Department of Microbiology and Immunology, University of British Columbia, Vancouver,  
British Columbia, Canada.

### ABSTRACT

Supramolecular assemblies of vesicles composed of natural lipids embedded in a matrix of polydiacetylene are shown to undergo blue-to-red color changes related to specific interactions between the lipids or recognition elements and biomolecules. The colorimetric transitions observed in the vesicles are due to structural modifications within the conjugated PDA polymer backbone. This colorimetric assay could serve as a membrane-mimicking environment for detection of interfacial processes, such as peptide-membrane interactions, antibody-antigen binding, enzymatic catalysis, and detection of physiological ions. The lipid/PDA mixed vesicles are robust and can be readily applied to diagnosis of physiological molecules and rapid screening of biological and chemical libraries.

### INTRODUCTION

PDA-based vesicles have been previously shown to undergo blue-to-red color transitions induced by a variety of interfacial processes. The color transitions observed in the vesicles are believed to originate from structural changes at the conjugate PDA polymer backbone [1]. Previous studies have shown that biological processes leading to structural perturbations at the PDA vesicle interface, including enzymatic catalysis [2], pH- changes [3], or ligand-receptor recognition [4], also induce blue-to-red transitions occurring in the vesicle assemblies.

We have recently demonstrated that PDA vesicles incorporating a high percentage of lipid molecules [Figure 1] similarly undergo colorimetric transitions and could be used for studying biological and chemical processes [5-8]. In the following we demonstrate some applications of the system.

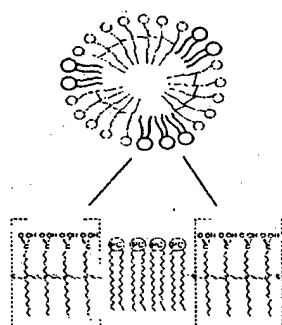


Figure 1 Schematic representation of the lipid/PDA vesicles, indicating a part of the assembly of lipids and polydiacetylene. PC denotes the phosphatidylcholine headgroup.

## EXPERIMENTAL DETAIL

Mixed vesicles composed of physiological lipids and PDA were prepared using approximately 40% (mole ratio) lipids, such as dimyristoylphosphatidylcholine (DMPC) and dimyristoylphosphatidylglycerol (DMPG), and 60% polydiacetylene (PDA) lipids. Following sonication and polymerization, the lipids form organized assemblies that exhibit an intense blue color due to the conjugated backbone of the PDA polymer. The macrocyclic receptor homooxacalixarene triether [9] was inserted into the lipid moieties within DMPC/PDA following the polymerization step without disruption of the liposome organization or chromatic properties.

UV-vis measurements: samples were prepared by adding peptides to 0.4 mL vesicle solutions at 1 mM total lipid and 2 mM Tris. The pH in the solutions was 8.0 in all experiments. Examined peptides were dissolved in water, and the peptide-vesicle solutions were diluted to 1 mL prior to spectral acquisition. All measurements were carried out at 27 °C on a Hewlett-Packard 8452A diode-array spectrophotometer, using a 1cm optical path length cell.

Indolicidin ILPKWPWWPWRR (CP10), and indolicidin analogue

ILKKWPWWPWRRK (CP11) have been chemically synthesised at the University of British Columbia.

A quantitative value for the extent of blue-to-red color transition is given by the *colorimetric response* (%CR), which is calculated from the visible absorbance spectra acquired for the vesicle solutions. The colorimetric response is defined:

$$\%CR = [(PB_0 - Pb_1)/PB_0] * 100$$

where  $PB = \Lambda_{blue}/(\Lambda_{blue} + \Lambda_{red})$ ,

$\Lambda$  is the absorbance at either the "blue" component in the UV-vis spectrum (640nm) or "red" component (500nm),  $PB_0$  is the red/blue ratio of the control sample (before induction of color change), and  $Pb_1$  is the value obtained for the vesicle solution after addition of the tested compound.

Fluorescence measurements: changes in tryptophan intrinsic emission were measured for 10 μM peptide solution titrated with DMPG/DMPC/PDA vesicles incorporating the radical spin-probes 12-doxyloctanoic acid [12-DS] and 16-doxyloctanoic acid [16-DS] (Sigma).

## RESULTS AND DISCUSSION

### Peptide-membrane interactions

Interactions between peptides and lipid membrane play major roles in numerous physiological processes and the activities of antibacterial drugs. A variety of structural models describing interactions between short peptides and membranes and membrane permeation have emerged in recent years, such as the transmembrane channel aggregates, the "barrel-stave" model and the "carpet" mechanism [10]. The new colorimetric assay provides information upon peptide-membrane interactions between and could contribute to the elucidation of structural and

functional properties of membrane-associated peptides, and their organization in membrane environments.

The relationships between the observed colorimetric transitions in the vesicle solutions and the mechanisms of peptide-membrane interactions could be obtained from comparison between native membrane-peptides and their analogs. We have previously studied native melittin (L-melittin) and a melittin analogue in which certain L-amino acids have been replaced with the corresponding D-amino acids (D-melittin) [8]. D-melittin is bound on the surface of the lipid assemblies and induces greater interfacial perturbations, and thus a more pronounced color change, compared to transmembrane insertion of a helical peptide such as native melittin [10].

We have applied the lipid/PDA colorimetric assay for studying indolicidin and its analogues. Figure 2 shows the colorimetric response of indolicidin (CP10) and its analogue CP11. According to our hypothesis, CP11, which clearly induces a greater blue-red color change compared to native indolicidin, causes more significant interfacial membrane perturbations compared with indolicidin, which inserts deeper to the membrane.

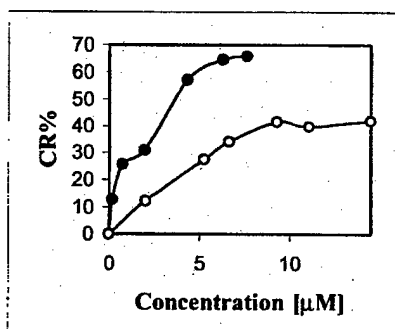
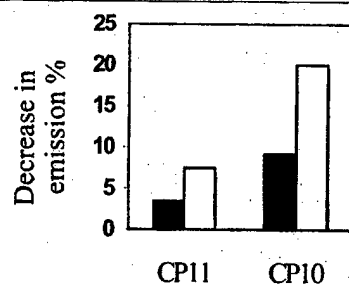


Figure 2: Tiration curves depicting the change of CR% in DMPG/DMPC/PDA vesicles as a function of peptide concentration: (•) CP11 and (○) CP10.

In order to corroborate that conclusion we have examined liposomes incorporating the spin-labeled lipids 12-DS and 16-DS in order to estimate the average position of the tryptophan residues in the liposome, as spin-labels will cause a decrease in tryptophan fluorescence when in close proximity. Figure 3 shows that the decrease in the fluorescence emission of tryptophan in indolicidin (CP10) is greater than the corresponding decrease in CP11. This result confirms that indolicidin (CP10) penetrates deeper into the lipid core while CP11 bind to the surface of the lipids.



**Figure 3:** Decrease in tryptophan emission data of indolicidin (CP10) and indolicidin analogic (CP11) added to 1 mM DMPC/DMPC/PDA vesicles incorporated the spin-labeled lipids: (■)12-DS, (□) 16-DS.

#### Ligand-receptor binding

The lipid/PDA system can also be chemically modified to allow for detection of selective guest-host or ligand-receptor binding events. We have examined the colorimetric properties of lipid/PDA vesicles incorporating the synthetic macrocyclic receptor homooxacalixarene triether, which exhibits selectivity among various neurotransmitters and ions [9,11]. The data presented in Figure 4 indicate that the receptor/lipid/PDA vesicle assembly exhibits distinct ligand selectivity. Specifically, the highest colorimetric response of the assay is observed when dopamine or sodium ions are added to the vesicle solution. Adrenaline or  $K^+$  ions, on the other hand, give rise to significantly smaller blue-red color transitions. These results are similar to the complexation selectivity of homooxacalixarene triether in two phase system ( $CH_2Cl_2/H_2O$ ) [9] and in PVC liquid membranes [11].

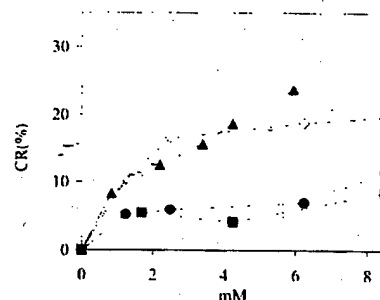


**Figure 4:** Colorimetric response for ligands added to DMPC/PDA vesicles incorporating homooxacalix arene triether:  $Na^+$  (○),  $K^+$  (●), dopamine (▲), adrenaline (■).

## CONCLUSIONS

Experiments carried out in our laboratory demonstrate that incorporation of natural lipids into the PDA matrix enables the vesicles to successfully mimic environments of cellular membranes, thus opening the way to a variety of biochemical applications. The lipid/PDA vesicle assembly exhibits rapid colorimetric transitions upon specific interactions with a variety of biological analytes in aqueous solutions, including membrane peptides, ions, and neurotransmitter ligands. The assay can be readily applied to diagnosis of physiological molecules and for rapid screening of chemical and biological libraries.

## REFERENCES

1. Tanaka, H., Gomez, M.A., Tonelli, A.E., Thakur, M. Thermochromic phase transition of a polydiacetylene, studied by high resolution solid-state  $^{13}\text{C}$  NMR. *Polymer* 22, 1208-1215(1991).
2. Jelinek, R., Okada, S., Norvez, S., Charych, D.H. Interfacial catalysis by phospholipases at conjugated lipid vesicles: colorimetric detection and NMR spectroscopy, *Chem. Biol.* 5, 619-629(1998).
3. Cheng, Q., and Stevens, R. C. Charge-Induced Chromatic Transition of Amino Acid-Derivatized Polydiacetylene Liposomes. *Langmuir* 14, 1974-1976(1998).
4. Charych, D.H., Nagy, J. O., Specvak, W., Bednarski, M. D. Direct colorimetric detection of a receptor-ligand interaction by a polymerized bilayer assembly. *Science* 261, 585-588(1993).
5. Kolusheva, S., Boyer, L., Jelinek, R. A colorimetric assay for rapid screening of antimicrobial peptides, *Nature Biotechnology* 18, 225-227 (2000).
6. Kolusheva, S., Kafri, R., Katz, M., Jelinek, R. Rapid Colorimetric Detection of Antibody-Epitope Recognition at a Biomimetic Membrane Interface, *J. Am. Chem. Soc.* 123(3) 417-422 (2001).
7. Kolusheva, S., Shahal, T., Jelinek, R. Cation - Selective Color Sensors Composed of Ionophore-Phospholipid- Polydiacetylene Mixed Vesicles, *J. Am. Chem. Soc.* 122, 776-780 (2000).
8. Kolusheva, S., Shahal, T., Jelinek, R. Peptide-Membrane Interactions Studied by a New Phospholipid/Polydiacetylene Colorimetric Vesicle Assay. *Biochemistry* 39(51), 15851-15859 (2000).
9. Araki, K.; Inada, K.; Otsuka, H.; Shinkai, S. Conformational isomerism in and binding properties to alkali-metals and an ammonium salt of *O*-alkylated homooxacalix[3]arenes *Tetrahedron* 49, 9465-9478(1993).

---

10. Oren, Ziv; Shai, Yechiel. Molecular mechanism of cell selectivity by linear amphipathic  $\alpha$ -helical and diastereomeric antimicrobial peptides. Development of Novel Antimicrobial Agents: Emerging Strategies 183-204. (2001).

11. Odashima, K.; Yagi, K.; Tohda, K.; Umezawa, Y. *Bioorg. and Med.* Dopamine-selective response in membrane potential by homooxacalix[3]arene triether host incorporated in PVC liquid membrane. *Chem. Let.* 1999, 9, 2375-2378.

## **Tissue Engineering I**

### Self-Assembly of Hydrogels From Elastin-Mimetic Block Copolymers

Elizabeth R. Wright<sup>1</sup>, R. Andrew McMillan<sup>1</sup>, Alan Cooper<sup>2</sup>, Robert P. Apkarian<sup>3</sup>, and Vincent P. Conticello<sup>1</sup>

<sup>1</sup>Department of Chemistry, Emory University,  
Atlanta, GA 30322

<sup>2</sup>Chemistry Department, University of Glasgow,  
Glasgow, Scotland, UK

<sup>3</sup>Integrated Microscopy & Microanalytical Facility, Department of Chemistry, Emory  
University, Atlanta, GA 30322

#### ABSTRACT

Triblock copolymers have traditionally been synthesized with conventional organic components. However, triblock copolymers could be synthesized by the incorporation of two incompatible protein-based polymers. The polypeptides would differ in their hydrophobicity and confer unique physiochemical properties to the resultant materials. One protein-based polymer, based on a sequence of native elastin, that has been utilized in the synthesis of biomaterials is poly (Valine-Proline-Glycine-Valine-Glycine) or poly(VPGVG) [1]. This polypeptide has been shown to have an inverse temperature transition that can be adjusted by non-conservative amino acid substitutions in the fourth position [2]. By combining polypeptide blocks with different inverse temperature transition values due to hydrophobicity differences, we expect to produce amphiphilic polypeptides capable of self-assembly into hydrogels. Our research examines the design, synthesis and characterization of elastin-mimetic block copolymers as functional biomaterials. The methods that are used for the characterization include variable temperature 1D and 2D High-Resolution-NMR, cryo-High Resolution Scanning Electron Microscopy and Differential Scanning Calorimetry.

#### INTRODUCTION

Biomaterials have become increasingly important in medical research and applied medicine. They are used in many roles, from drug delivery systems to implantation devices. Biomaterials are varied in their composition; they can be composed of synthetic organic polymers, ceramics, metals and protein-based polymers. Protein-based polymers are of interest because they do not have some of the biocompatibility issues of some other materials; this is attributable to their similarity to native protein materials [3]. The focus of this research is the synthesis of amphiphilic block copolymers based on elastin-mimetic peptide sequences. These amphiphilic block copolymers undergo heat-induced micellization and form complex fluids in aqueous solution [4]. Elastin-mimetics are of special interest in medical applications because they do not adhere to cells and are non-immunogenic. We have designed blocks that, when combined, would provide different physiochemical properties to the copolymers. The peptides are modifications of the naturally occurring vertebrate elastin sequence, Valine-Proline-Glycine-Valine-Glycine (VPGVG). The peptide sequences will be joined together sequentially to form diblock and triblock copolymers. The block copolymers are being produced to afford unique

micelle- and gel-forming proteins. The resulting proteins could be used as the basis of drug delivery systems, coatings for implantation devices, or other medical roles.

## EXPERIMENTAL DETAILS

All reagents were obtained from Fisher Scientific (Pittsburgh, PA) or Sigma Chemical Corporation (St. Louis, MO). Enzymes were purchased from New England Biolabs, Inc. (Beverly, MA). Plasmids pZErO 1.1, pZErO 2.0 and *E. coli* strain Top10F' were from Invitrogen Corporation (Carlsbad, CA). *E. coli* strains SCS110 and BL21Gold(DE3) were obtained from Stratagene (La Jolla, CA). Plasmid purification kits were purchased from Qiagen Inc. (Chatsworth, CA). Genosys Biotechnologies, Inc. (The Woodlands, TX) synthesized all single-stranded DNA oligonucleotides. Reagents were sterilized by either autoclave or passage through a 0.22  $\mu$ m filter.

Procedures for DNA manipulations, transformation of competent cells, and the growth of bacterial cultures were adapted from literature [5] or the instructions supplied by manufacturers. Enzymatic reactions were performed in the buffers supplied by the manufacturers. An Applied Biosystems Voyager-DE<sup>TM</sup> STR Biospectrometry<sup>TM</sup> matrix-assisted laser desorption ionization time-of-flight mass spectrometer (MALDI-TOF MS) was utilized to determine mass of the proteins. All the proteins, which have been expressed and purified, were run on 10-15 % gradient SDS-PAGE (Pharmacia Biotech PHAST System) with a negative zinc-staining technique in order to determine molecular weight and purity.

All solution NMR experiments were carried out with samples consisting of 43 mg of protein and 1 mg of sodium 2,2-dimethyl-2-silapentane-5-sulfonate (DSS) as internal standard (0.0 ppm), dissolved in 50:50 sterile ddH<sub>2</sub>O and D<sub>2</sub>O. Spectra were recorded on a Varian INOVA 600 (600 MHz, <sup>1</sup>H; 150 MHz <sup>13</sup>C) instrument. Samples were run at 4 °C and 25 °C to follow the changes in the copolymers' structure due to hydrophobic collapse of the plastin end-blocks. Standard solvent suppression techniques were employed to reduce signal due to the residual protons of water in the <sup>1</sup>H NMR of aqueous solutions. The JMQC NMR experiments were acquired at 4 °C and 25 °C with a 90° pulse of 8  $\mu$ s on the proton (sweep width 5500.2 Hz) and a 90° pulse of 12  $\mu$ s on the carbon. The data matrix contained 256  $t_1$  increments (sweep width in  $F_1$  (carbon), 33 999.2 Hz) at 96 scans per increment. The NMR data were processed using the program NutsPro from Acorn NMR, Inc. (Livermore, CA).

Differential scanning Calorimetry (DSC) was performed by Dr. Alan Cooper, Chemistry Dept., University of Glasgow, Scotland, UK using a Microcal VP-DSC instrument, as detailed previously [6, 7]. The temperature range was 5 ° to 60 °C at a scan rate of 1 °C/min. The sample concentrations were approximately 1 mg/ml. Sample pH was varied between high and low pH.

Approximately 5 to 10  $\mu$ L of the solutions were pipetted into 3 mm gold planchets (Balzers BU 012 130T), which had been pre-equilibrated to 4 °C in an isothermal environmental cooler (Torrey Pines Scientific). The temperature of the cooler was raised to 20 to 25 °C and allowed to stabilize for 10 minutes. The solidified samples were plunge frozen in liquid ethane at its melting point (-183°C); the samples were stored in liquid nitrogen (LN<sub>2</sub>). A sample was transferred to and mounted on the precooled (~-170 °C) Oxford CT-3500 cryo-stage held in the cryo-preparation chamber. The specimen

was fractured with a prechilled blade and washed with LN<sub>2</sub>. The shutters on the stage were closed to minimize frost contamination and the cryo-stage was transferred to the Denton DV-602 Cr coater. At this point, if the samples were to be etched in order to remove excess water (vitreous ice), the stage was allowed to equilibrate in a vacuum of  $\sim 10^{-7}$  torr. Once this occurred, the shutters were opened and the stage was brought to a temperature between  $-105^{\circ}\text{C}$  and  $-99^{\circ}\text{C}$  for varying time intervals. The stage shutters were closed and the stage was returned to  $\sim -170^{\circ}\text{C}$ . A 1 nm film was sputter coated onto the specimen, the stage shutters were closed and the stage was transferred to the upper stage of the DS-130F field emission scanning electron microscope operated at 25 kV. During the imaging process, specimen temperature was maintained at  $-115^{\circ}\text{C}$ . Images were digitally collected (5 Mbytes) in 16 s in order to reduce radiation damage.

## DISCUSSION

### Synthetic gene construction

The methods used to produce the DNA inserts which encode the various elastin block copolymers has been described elsewhere [8]. The basic scheme follows. Single-stranded DNA was annealed together to form double-stranded DNA with cohesive ends. The double-stranded DNA 'monomers' were inserted into plasmids engineered for DNA modifications (pZErO 1.1 and pZErO 2). Once monomers were found which had the correct sequence, the plasmid was purified on a large scale and the monomers were removed via restriction enzyme digestion. The resulting monomers were concatemerized to produce large repetitive genes (1200 to 3000 base pairs), which were enzymatically ligated into a modified expression plasmid (pET 24a) to afford the block copolymers.

### Protein expression and purification

Expression plasmids containing the DNA sequences encoding proteins of suitable size and correct sequence were transformed into *E. coli* strain BL21(Gold)DE3. The proteins were expressed and purified following a hyperexpression protocol defined by Daniell et. al. [9]. This method allowed the production of gram quantities of the proteins of interest. Depending on the characteristics of each polymer, modifications to the purification protocol were made in order to afford the greatest quantity of pure protein.

The amino acid sequences for two of the resulting polypeptides are defined in Table I. Protein 1 is a diblock consisting of two equivalent polypeptides. Protein 2 is a triblock of two equivalent end-blocks and a unique internal block. From SDS-PAGE analysis, the estimated size of protein 1 is 80 kDaltons and protein 2 is 150 kDaltons. Amino acid compositional analysis, 1; Calc. [mol-%]: Ala, 19.8; Gly, 20.2; Ile, 15.7; Pro, 17.66; Val, 24.3; Obs. [mol-%]: Ala, 19.7; Gly, 20.1; Ile, 14.9; Pro, 21.6; Val, 24.3; 2; Calc. [mol-%]: Ala, 10.4; Glx, 1.9; Gly, 29.6; Ile, 8.2; Pro, 20.0; Val, 29.9; Obs. [mol-%]: Ala, 11.14; Glx, 2.9; Gly, 29.62; Ile, 9.64; Pro, 17.66; Val, 29.51 and MALD-TOF MS, Obs. (Calc): 1, 72 016 (72 116); 2, 134 097 (134 438), confirmed the identity of the recombinant polypeptides.

**Table I.** Amino acid sequences for the two elastin-mimetic block copolymers.

{VPAVG[(IPAVG)<sub>4</sub>(VPAVG)]<sub>16</sub>IPAVG}-[X]-{VPAVG[(IPAVG)<sub>4</sub>(VPAVG)]<sub>16</sub>IPAVG}  
1; [X] = VPGVGVPVG  
2; [X] = VPGVG[(VPGVG)<sub>2</sub>VPGEG(VPGVG)<sub>2</sub>]<sub>10</sub>VPGVG

(A, Alanine; G, Glycine; I, Isoleucine; P, Proline; V, Valine)

#### Copolymer characterization

On analysis of the <sup>1</sup>H, <sup>13</sup>C, and HMQC spectra, we determined that the resonances associated with the plastin end-blocks disappear at 25 °C due to their hydrophobic collapse above the inverse temperature transition. Resonances that noticeably disappear when comparing the (CH) $\alpha$  region of the <sup>1</sup>H, <sup>13</sup>C HMQC NMR spectra of protein 2 (Figure 1) are those associated with alanine and isoleucine contained in the end-blocks of the polypeptide. Individual resonances were assigned from known chemical shifts of elastin-mimetic polymer sequences [10]. The remaining resonances were assigned to the end-blocks and are commensurate with literature values [11, 12].

The DSC data obtained for the block copolymers shows a single transition between 21 °C and 23 °C. The transitions were reversible and minutely dependent on sample pH. Representative data for protein 2 is presented in Figure 2.

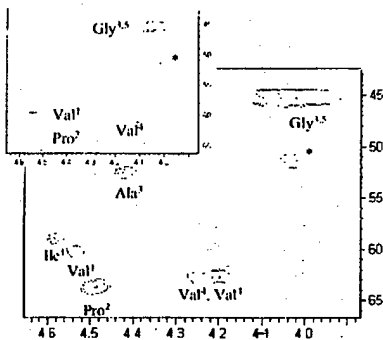


**Figure 1.** HMQC NMR data for triblock protein 2 at 4 °C and 25 °C (inset). Note the absence of resonances, which are assigned to the endblocks at 25 °C (inset).

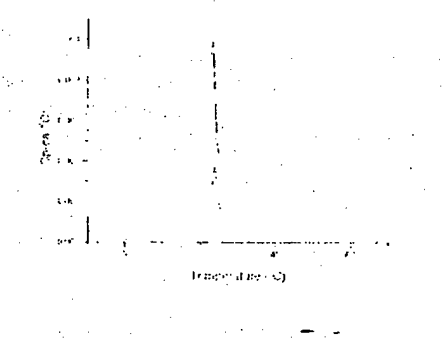


**Figure 2.** DSC data for the triblock protein 2; demonstrating the inverse temperature transition lies at approximately 23 °C and is independent of pH

Analysis of the data from the cryo-HRSEM studies reveals strong correlations to elastin-mimetic hydrogels produced by chemical crosslinking [13]. Electron micrographs of protein 2 are in Figure 3. The average size of the micelles for protein 2 ranged from 15

to 20 nm (A). After etching (B), protein 2 displayed micelles of 15 to 20 nm in diameter connected by fibrils of less than 10 nm in diameter. The micelles are evenly spaced along the lengths of the fibrils. This feature was attributed to the size of the midblock of protein 2 limiting the aggregation behavior of the endblock domains.

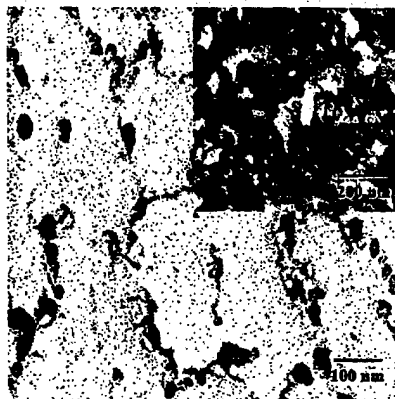


**Figure 3.** Cryo-HRSEM images of vitrified specimens of a concentrated aqueous solution of protein 2 prepared via rapid cryo-immobilization from gel specimen equilibrated at 25 C. Inset, specimen etched prior to image collection by controlled sublimation of vitreous ice to expose protein at interface.

## CONCLUSIONS

The data presented demonstrates our ability to design and synthesize elastin-mimetic triblock copolymers that are capable of thermoreversible self-assembly into hydrogels. The characterization of the copolymers supports the hypothesis that the copolymer systems consist of a network of interconnected micelles of the end-blocks at increased concentrations (20 to 30 % w/v) when raised above the inverse transition temperature of the polypeptide.

## ACKNOWLEDGEMENTS

This research was supported through a grant from the NASA Office of Life and Microgravity Sciences and Applications (NAG8-1579). E.R.W. acknowledges a Department of Education Assistance in Areas of National Need (G.A.A.N.N.) fellowship. The UK Biotechnology and Biological Sciences (BBSRC) and Engineering and Physical Sciences (EPSRC) Research Councils jointly fund the Biological Microcalorimetry Facility at Glasgow University. We thank Dr. Sarla Goel of Paar Physica for assistance with the dynamic rheology measurements. We thank Dr. Shaoxiong Wu for assistance with the High Resolution 2D-NMR experiments.

## REFERENCES

1. Urry, D.W., Luan, C.H., Harris, C.M., Parker, T.M. (1997) Protein-based materials with a profound range of properties and applications: The elastin  $\Delta T_g$  hydrophobic paradigm, *Protein-Based Materials*, 133-177.
2. Urry, D.W. (1988) Entropic elastic processes in protein mechanisms. I. Elastic structure due to an inverse temperature transition and elasticity due to internal chain dynamics, *J. Protein Chem.*, 7, 1-34.
3. Urry, D.W. (1991) Protein folding controlled by chemically shifting the temperatures of inverse temperature transitions, *Proteins: Structure, dynamics and design*, 352-360.
4. Kleppinger, R., Mischenko, N., Theunissen, E., Reynaers, H.L., Koch, M.H.J., Almdal, K., and Mortensen, K. (1997) Shear-induced single crystalline mesophases in physical networks of gel-forming triblock copolymer solutions, *Macromolecules*, 30, 7012-7014.
5. Sambrook, J., Fritsch, E. F., Maniatis, T., *Molecular Cloning: A Laboratory Manual*, 2<sup>nd</sup> ed., Cold Spring Harbor Laboratory Press: Cold Spring Harbor: NY, 1989.
6. Lee, T.A.T., Cooper, A., Apkarian, R. P., Conticello, V.P. (2000) Thermo-reversible self-assembly of nanoparticles derived from elastin-mimetic polypeptides, *Advanced Materials*, 12, 1105-1110.
7. E. R. Wright, R. A. McMillan, A. Cooper, R. P. Apkarian, and V. P. Conticello. Thermoplastic Elastomer Hydrogels via Self-Assembly of an Elastin-Mimetic Triblock Polypeptide. *Advanced Functional Materials*, 12 (2), 149-154 (2002).
8. McMillan, R.A., Lee, T.A.T., Conticello, V.P. (1999) Rapid assembly of synthetic genes encoding protein polymers, *Macromolecules*, 32, 3643-3648.
9. Daniell, H., Guda, C., McPherson, D., Zhang, X., Urry, D.W. (1996) Hyperexpression of a synthetic protein-based polymer gene, *Methods in Molecular Biology*, 63, 359-371.
10. McMillan, R.A., Conticello, V.P. (2000) Synthesis and characterization of elastin-mimetic protein gels derived from a well-defined polypeptide precursor, *Macromolecules*, 33, 4809-4821.
11. Wishart, D.S., Sykes, B.D (1994) The  $^{13}\text{C}$ -chemical shift index: A simple method for the identification of protein secondary structure using  $^{13}\text{C}$  chemical-shift data, *J. Bio NMR*, 171-180.
12. Wishart, D.S., Bigam, C.G., Holm, A., Hodges, R.S., Sykes, B.D. (1995)  $^1\text{H}$ ,  $^{13}\text{C}$ ,  $^{15}\text{N}$  random coil NMR chemical shifts of the common amino acids. I. Investigations of near-neighbor effects, *J. Bio NMR*, 67-81.
13. McMillan, R.A., Caran, K., Apkarian, R.P., Conticello, V.P. (1999) High-Resolution topographic imaging of environmentally responsive, elastin-mimetic hydrogels, *Macromolecules*, 32, 9067-9070.

### Lipid Exchange Rates of Conventional and Polymer Stabilized Liposomes

Awad Ahmed, Nicole Heldt, Gregory Slack, and Yuzhuo Li

Department of Chemistry and Center for Advanced Materials Processing,  
Clarkson University, Potsdam, New York, 13699-5810, USA

#### ABSTRACT

Polymer-stabilized liposome systems consisting of polyethylene glycol bound lipids (PEG-lipids) and conventional (nonpolymer stabilized) liposomes were compared in terms of their inter-membrane lipid migration rates. In order to monitor the exchange of lipids between the membranes, 1-hexadecanoyl-2-(1-pyrenedecanoyl)-sn-glycero-3-phosphocholine (PY-PC), a phospholipid with pyrene attached to the hydrophobic tail, was used to label the liposome. Labeled and unlabeled liposome systems were mixed and fluorescence spectroscopy was used to examine the lipid transfer. More specifically, the relative employed to deduce the exchange kinetics. After labeled and unlabeled liposome systems were mixed, the E/M ratio for PY-PC in a polymer stabilized liposome system decreased by 66% over a period of 80 minutes, while the E/M for PY-PC in a conventional liposome system decreased 70% in less than 2 minutes. This suggests that the exchange rate for lipids in polymer stabilized liposome systems is much slower than that of conventional liposome systems. In addition, the exchange rates for both conventional and polymer stabilized liposome systems are accelerated at an elevated temperature.

#### INTRODUCTION

Liposome is a very important supermolecular structure because of its similarity to biological membranes and its therapeutic value as delivery agent for enzymes, drugs, genetic manipulation, and diagnostic imaging applications [1]. Recently, liposomes with polyethylene glycol chains attached to the polar head group (polymer stabilized or Stealth liposomes) have been implemented in pharmaceutical applications due to their increased lifetime in the blood stream [1,2].

In the field of liposome studies, fluorescence has emerged as a useful analytical technique, as it provides a large amount of diversified information concerning the biophysics of lipid vesicles and biomembranes [3]. Artificial and biological membranes can be considered as two-dimensional fluids, characterized by a high lateral mobility of lipid components. Almgran was the first to use a fluorescence stopped-flow technique to investigate the migration of pyrene between unilamellar vesicles [4]. The results indicated that the migration of pyrene from one vesicle to another occurs mainly via a desolubilizations-diffusion-resolubilization mechanism [4]. Doody et al. also provided evidence that the transfer of a fluorescent fatty acid probe is through the aqueous phase [5]. Sengupa et al. measured pyrenyl-decanoic acid transfer rates between DPPC vesicles using a stop-flow technique and found that multilamellar vesicles had much slower exchange rates than that of unilamellar vesicles. In addition, charging the surface of the vesicles also reduces the exchange rate [6]. Wolkowicz and collaborators found that an increase in the vesicle size reduces the transfer rate of a probe. Furthermore, natural membranes, such as cardiac and mitochondrial membranes, exhibit a marked decrease in transfer rates [7]. In a study by Ollmann et al., the lateral lipid diffusion rate in a phosphatidylcholine membrane was determined by using pyrene-labeled gangliosides as probes [8]. It was found that the lateral diffusion rate is significantly higher than the inter-membrane transfer rate.

---

In addition to conventional liposome systems, inter-membrane lipid transfer between polymer-stabilized liposomes has also been studied. In one investigation, the transfer of PEG-lipids was monitored using biotinylated (acceptor) liposomes [9]. When PEG-liposomes were mixed with biotinylated liposomes, the inhibition of the biotinylated liposomes to bind to streptavidin was used to measure the transfer of the PEG-lipids [10]. It was found that transfer of PEG-lipids is dependent upon temperature and acyl chain length of the lipid anchor. Lipid transfer is decreased when the acyl chain length is increased and increased with increases in temperature [9].

A systematic study and comparison between the properties of conventional and polymer-stabilized liposomes are fundamentally important to the application of vesicles in drug delivery. The information is critical for a structural design that balances the need for polymer stabilization or "stealth effect" and the specificity possessed by the original membrane surface. It is desirable to develop a liposome system that has an adequate stealth effect without compromising the surface activity that is critical in targeting other membranes for drug delivery. The use of polymer stabilized liposomes as ligand targeting agents is still somewhat limited because the protective polymer border prevents most molecules from being attached [10]. The focus of this paper is the investigation of lipid exchange rate difference between conventional and polymer stabilized liposome systems. The lipid transfer rates were monitored using a fluorescent labeled phospholipid, 1-hexadecanoyl-2- [1-pyrenedecanoyl]-sn-glycero-3-phosphocholine (PY-PC). The temperature effect on lipid exchange rates was also investigated

## EXPERIMENTAL DETAILS

### Materials

The lipids used were 1,2-dipalmitoyl-sn-glycero-3-phosphate monosodium (DPPA) (Avanti Polar Lipids, Inc. Alabaster, AL), 1,2-dipalmitoyl-sn-glycero-3-phosphocholine (DPPC) (Lipoid GmbH, Ludwigshafen, Germany), 1,2-Dipalmitoyl-sn-glycero-3-phosphoethanolamine-N-[methoxypolyethyleneglycol 5000] (DPPE-MPEG 5000) (Shearwater Polymers, Inc. Huntsville, AL), 1,2-dipalmitoyl-sn-glycero-3-phosphoethanolamine (DPPE) (Sygena, Inc. Cambridge, MA), and the pyrene labeled phospholipid, 1-hexadecanoyl-2- (1-pyrenedecanoyl)-sn-glycero-3-phosphocholine (PY-PC) (Molecular Probes, Inc. Eugene, OR). Extrusion was accomplished by the Mini-Extruder® (Avanti Polar Lipids, Inc. Alabaster, AL).

### Liposome Preparation

Polymer stabilized liposome systems were prepared by adding a 9:1:1 molar blend of DPPC, DPPA, and DPPE MPEG-5000 to polyethylene glycol and bath sonicating at 69°C until clear. A mixture of 1 part glycerol to 8 parts 0.9% aqueous NaCl was then added to the sonicated blend. The conventional liposomes were prepared in the same manner as the polymer stabilized liposome systems except that the DPPE-MPEG 5000 was replaced by DPPE. In addition, the conventional liposome samples were extruded through 0.1 polycarbonate filters. Pyrene-labeled liposome systems of polymer stabilized and conventional liposomes were prepared by adding 1 mg of PY-PC (dissolved in 1ml ethanol) to 75 mg of dry lipid blends.

### Fluorescence Emission Spectra

All samples were purged with and sealed under nitrogen gas to prevent oxygen quenching. All monomer and excimer intensity measurements were performed on a Perkin Elmer LS 50 spectrophotometer. The excitation wavelength was set at 340nm (2.5nm slit width). Monomer and excimer emission peaks were observed at 395nm and 476nm, respectively. Mixtures of 1:1 pyrene-labeled and unlabeled liposome systems for both polymer stabilized and conventional liposomes were examined at various temperatures (12°C, 24°C, 37°C, and 50°C). PY-PC transfer between liposome membranes was determined by the decrease in E/M after labeled and unlabeled liposome systems were mixed.

### Particle Size

Particle size and size distribution were measured using a dynamic light scattering (DLS) method, which was performed on a Brookhaven Instruments System, equipped with a water-cooled argon-ion laser light source (Model 85, Lexel Laser). The device was operated at the wavelength of 514.5nm and a 90 degree of scattering angle.

### RESULTS AND DISCUSSION

Conventional and polymer stabilized liposome systems were prepared and characterized as described in the experimental section. Dynamic Light Scattering (DLS) measurements show that conventional and polymer stabilized liposome systems have average particle sizes ranging from 100 to 200nm. Although both systems give a similar particle size range, it is understood that the PEG chains attached to the lipid bilayer of polymer-stabilized liposomes contribute to a significant share of the particle size.

Conventional and polymer stabilized liposome systems containing a fluorescence probe were prepared according to the procedures described in the experimental section. Pyrene labeled 1-hexadecanoyl-2-(1-pyrenedecanoyl)-sn-glycero-3-phosphocholine (PY-PC) has the pyrene molecule attached to the fatty acid tail end, which is located in the lipid bilayer region. Fluorescence emission spectra were obtained for both systems as well. The emission at 395 nm is assigned to one of the monomer peaks (M) and 476 nm to the excimer peak (E). Peak ratios E/M were then calculated and used to study the migration of pyrene-labeled lipids from one liposome (labeled) to another (unlabeled) [11]. There are two possible modes for the migration of the probe from vesicle to vesicle. PY-PC may either migrate via the aqueous phase, or move from one vesicle to another during vesicle collision [3,9].

Excimers may form upon collision between an excited pyrene derivative and a ground state pyrene derivative [12]. The E/M ratio is thus proportional to the collision frequency of pyrene derivatives, which in turn depends on the local concentration and lateral diffusion rate of pyrene derivatives [11]. A greater E/M ratio indicates a greater local concentration of PY-PC. L'Hereux and Fraga studied the localization of pyrene and pyrenyl-hexadecanoyl acid in PC small unilamellar vesicles [13]. It was found that below 4 molar percent of probe molecules the excimer formation is essentially diffusion controlled, while above 4% excimers are obtained in aggregated form. In our study, the molar percent of the fluorescent probe is significantly lower than 4%. The excimer formation is, therefore, likely to be a diffusion controlled process. Interestingly, the conventional liposomes yielded E/M values nearly two times greater than

polymer stabilized liposome systems. (Figures 1, 2 and Table 1) The larger E/M value for conventional liposome systems is a strong indication that the lateral diffusion rate is significantly higher than that in a polymer stabilized system.

The effect of temperature on excimer formation in both conventional and polymer-stabilized liposomes was also examined. As seen in Figure 1 and Table 1, the higher the temperature smaller the initial excimer peak intensity. As temperature increases, the mobility of the lipid molecules increases and the excimer lifetime decreases. Conventional liposome systems appeared to be more sensitive to temperature changes than polymer stabilized liposome systems, as indicated by a larger drop in excimer emission from 24 to 50°C (Table 1). This is again consistent with the notion that the PEG chains reduce the mobility of the lipids in the polymer-stabilized liposome bilayers [14]. In addition, PEG produces a shielding effect that not only prevents molecules from binding the lipid surface, but also restricts the molecules within the lipid bilayer from leaving.

Roseman and Thompson used a pyrene labeled phosphatidylcholine to study the kinetics of spontaneous phospholipid transfer between unilamellar (conventional) liposomes [15]. It was found that there is a significant rate decrease for phospholipid transfer when the flip-flop rate exceeds the lipid migration at certain temperature. It was also concluded that pyrene-PC transfer takes place through the aqueous medium than collision of membranes, and is independent of acceptor vesicle concentration [15].

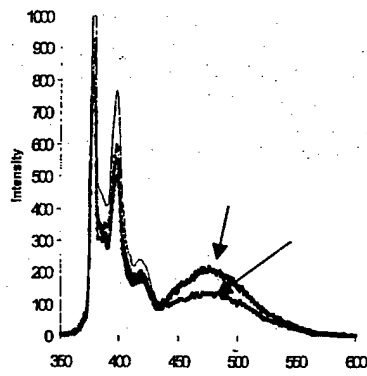


**Figure 1.** Effect of temperature on excimer formation in polymer stabilized liposome systems.

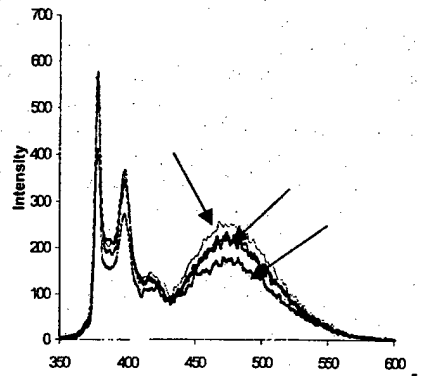


**Figure 2.** Effect of temperature on excimer peak formation in conventional liposome systems.

**Table 1:** Effect of temperature on excimer formation in conventional and polymer-stabilized liposomes (monomer peaks measured at 395 nm and excimer peaks measured at 476 nm)

Temperature °C	Conventional Liposomes			Polymer Stabilized Liposomes		
	Monomer (M)	Excimer (E)	E/M	Monomer (M)	Excimer (E)	E/M
12	358.8	251.6	0.70	764.4	210.0	0.27
24	302.8	221.5	0.73	580.2	210.0	0.36
37	266.9	224.4	0.84	495.1	210.0	0.42
50	360.2	177.0	0.49	563.2	131.7	0.23

In our study, as shown in Figures 1 and 2, there is a gradual change in initial E/M ratios for conventional liposome systems and a sharp change above 37 °C for polymer stabilized liposome systems. It is possible that the temperature at which the flip-flop rate is greater than inter-membrane transfer for polymer stabilized liposome systems is somewhat greater than that for a conventional liposome. This is a direct result of the rigidity introduced by the PEG chains.

The impact of PEG chains on inter-membrane lipid transfer was further examined and illustrated in Figure 3. As an inter-membrane lipid exchange should result in a decrease in E/M ratios, a plot of E/M vs time represents the exchange kinetics. When a labeled conventional liposome sample was mixed with an unlabeled conventional liposome sample, the E/M ratio decreased ca. 70% in less than two minutes (not shown), followed by a very slow exchange process in agreement with Galla et al [16]. When a labeled polymer stabilized system was mixed with another polymer stabilized system, the E/M ratio decreased ca. 60% in 80 minutes. When a labeled conventional liposome sample was mixed with an unlabeled polymer stabilized liposome sample, the initial exchange behavior is similar to the conventional-conventional case, followed by an E/M decrease that is parallel to the polymer-polymer case.

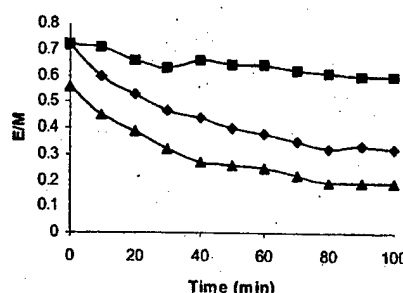


**Figure 3.** Lipid exchange (E/M) for mixtures of labeled conventional and unlabeled polymer stabilized liposomes (-■-) labeled and unlabeled polymer stabilized liposomes (-▲-) and labeled and unlabeled conventional liposomes (-○-).

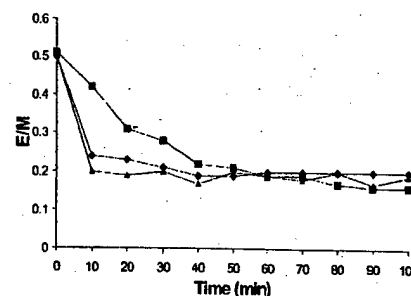


**Figure 4.** Lipid exchange (E/M) for mixtures of PY-PC labeled and unlabeled polymer stabilized at different temperatures (24°C -■-, 37°C -○-, and 50°C -▲-).

The remarkable difference between polymer stabilized and conventional liposome systems in lipid exchange rate can be traced to the shielding effect of the PEG border and the rigidity of the lipid bilayer due to the presence of PEG-lipids. The temperature dependence of the exchange rate in polymer-stabilized liposome is shown in Figure 4. As expected, an increase in temperature directly corresponded to an increase in lipid exchange rate. Temperature effect found in this study for polymer stabilized liposome system is consistent with findings reported for conventional liposome systems [17].

## CONCLUSIONS

Changes in E/M values can be used to monitor the exchange rate of lipids in conventional liposome systems and polymer stabilized liposome systems. Polymer stabilized liposome systems were observed to have slower lipid exchange rates than conventional liposome systems. In addition, polymer stabilized liposome systems had a lower sensitivity to temperature changes. It is believed that the PEG chains that form the outer portion of the lipid bilayer for these polymer-stabilized liposomes provides restricted mobility of the lipids within the lipid bilayer and the interliposomal phospholipid transfer.

## REFERENCES

1. D.D. Lasic, *Liposomes: from Physics to Applications*, Elsevier, New York, 1993.
2. M.C. Woodle, D.D. Lasic, *Biochim. Biophys. Acta.*, **1113**, 171 (1992)
3. A. Nakajima, *Bull. Chem. Soc. Japan*, **44**, 3272 (1971)
4. M. Almagren, *Chem. Phys. Lett.*, **71**, 539 (1980)
5. M.C. Doody, H.J. Pownall, Y.J. Kao, and L.C. Smith, *Biochemistry*, **19**, 108 (1980)
6. P. Sengupta, E. Sackmann, W. Kuhnle, and H.P. Scholz, *Biochim. Biophys. Acta* **436**, no. 4, 869 (1976)
7. P.E. Wolkowicz, J.H. Pownall, D.F. Pauly, and J.B. McMillin-Wood, *Biochemistry*, **23**, 6426 (1984)
8. M. Ollman, G. Schwarzmann, K. Sandhoff, and H. Galla, *Biochemistry*, **26**, 5943 (1987)
9. W. Li, L. Xue, L.D. Mayer, and M.B. Bally, *Biochim. Biophys. Acta.*, **1513**, 193 (2001)
10. P. Corley, and H.C. Loughrey, *Biochim. Biophys. Acta.*, **1195**, 149 (1994)
11. T. Forster, *Agnew. Chem.*, **8**, 333 (1969)
12. P.J. Samerharju, J.A. Virtanen, K.K. Eklund, P. Vainio, and P.K.J Kinnunen, *Biochemistry*, **24**, 2773 (1985)
13. G.P. L'Heurux and M. Fragata, *J. Photochem. Photobio. B*, **3**, 53 (1989)
14. N. Heldt, M. Gauger, J. Zhao, G. Slack, J. Pietryka, Y. Li, *Reactive and Functional Polymers*, **48**, 181 (2001)
15. M.A. Roseman, and T.E. Thompson, *Biochemistry*, **19**, 439 (1980)
16. H. Galla, and W. Hartman, *Chem. Phys. Lipids.*, **27**, 199 (1980)
17. G. Duportail, and P. Lianos, "Fluorescent probing of vesicles using pyrene and pyrene derivatives derivatives," in M. Rosoff (Ed.), *Vesicles*, Marcel Dekker, New York. 1996, pp. 295-372.

### Synthesis of biocompatible surfaces by different techniques

E. Garreta, T. Fernández, S. Borrós\*, J. Esteve<sup>1</sup>, C. Colominas, L. Kempf  
Materials Science Laboratory, Institut Químic de Sarrià (IQS), Universitat Ramón Llull,  
Barcelona, Spain.

<sup>1</sup> Applied Physics Department, Universitat de Barcelona, Barcelona (Spain)

#### ABSTRACT

In the present work, a sol-gel method of HA synthesis has been developed using different calcium and phosphorous precursors. In order to make a porous scaffold, HA aerogel formation and HA liofilization processes have been studied. The liofilized HA and the HA aerogels have been characterized by SEM-EDX and X-Ray diffraction. Finally, so as to improve the biocompatibility and the bioadhesion of the HA scaffolds, different plasma polymerization techniques have been studied. Acrylic acid has been polymerized using plasma polymerization with a radiofrequency source. Different radiofrequency source powers and reactor designs have been tried. The kinetics of the thin film growth have been studied and the optimal polymerization conditions have been established. Polymeric layers have been characterized by IR and XPS.

#### INTRODUCTION

Regeneration or replacement of damaged tissues remains one of the most important challenges in both medicine and bioengineering. Specifically, methods of bone/cartilage reconstruction in orthopaedic surgery are not completely successful yet. In addition, they are among the most costly therapies available. Materials science can help in finding new suitable materials for bone/cartilage regeneration, and this is why it represents a major area of study in tissue engineering [1].

Green [2] postulated correctly that the advent of new biocompatible materials might enable cells to be seeded onto a synthetic scaffolding and implanted into animals to generate new functional tissue. Scaffold or three-dimensional construct initially provides mechanical stability as well as cell anchorage sites and structural cues. Furthermore, the scaffold must also provide an appropriate environment to enhance cells reorganization and the correct extracellular matrix generation by these cells [3]. Several scaffold materials have been investigated for tissue engineering bone and cartilage, and several reviews have been published on the general properties and design features of biodegradable and bioresorbable polymers and scaffolds [4-9]. Natural materials are advantageous in that they contain information that facilitates cell adhesion or maintenance of differentiated function. Synthetic polymers, on the other hand, allow precise control over molecular weight degradation time, hydrophobicity and other attributes [1]. The advantages of both have been tried to combine in different strategies [7].

This work is a part of a global project that wants to create a biomaterials program for bone and cartilage regeneration. The main goal is to develop biocompatible and bioresorbable scaffolds that restore, maintain or improve bone and cartilage function. It is important that these scaffolds give mechanical resistance in the reconstructed area, but also they must be osteoconductive in order to promote the area reconstruction by a new bone or cartilage.

Hydroxyapatite,  $\text{Ca}_{10}(\text{PO}_4)_6(\text{OH})_2$ , is a crystalline form of calcium phosphate, very similar to the mineral component of bones. It has been studied for bone and cartilage regeneration because of its biocompatible, bioactive and osteoconductive properties, which make it a good biomaterial for bone/cartilage repair [10-12]. Thus, HA has been chosen in this work and it has been synthesized by an optimized sol-gel method. Sol-gel synthesis of HA ceramics has recently attracted much attention [13-14]. The sol-gel method is advantageous for different reasons. The most important are that, temperatures required for all stages are low, different shapes can be given easily to the formed gel and by controlling the aging and drying conditions, further pore size and mechanical strength control may be achieved [15]. Moreover and in order to improve the osteoconductivity of the obtained HA, two different drying methods for the HA precursor gels are proved: lyophilization and aerogel production. In the other hand, polymers are widely used in bone/cartilage implants, both, as polymeric materials themselves and as a polymeric surface on a different substrate. Concerning the later, and in order to improve the biocompatibility of the material, surface modification techniques appear to be quite interesting for this subject. Thus, surface modification techniques become a good choice to improve the biocompatibility of the material. Specially, plasma surface modification has been used as a promising technique for this purpose [16-17]. Acrylic acid deposition by plasma polymerization with a radiofrequency source has been studied in this work. The conditions of power, pressure and reactor design are very important because they affect the polymerization process and, thus, the final polymeric layer properties obtained. The next step will be to modify HA scaffolds surface in order to attach interesting biomolecules, such as growth factors, or to improve cell adhesion, biocompatibility, and bioactivity.

Therefore, the work will focus on the production of HA scaffolds by a sol-gel method using different drying processes, and on the study of the plasma polymerization technique to design modified HA scaffolds for bone and cartilage regeneration. These modified HA scaffolds are promising substitutes for bone/cartilage repair because of its ability to give an appropriate environment for cell proliferation and, therefore, for the growth or replacement of damaged tissues.

## EXPERIMENTAL DETAILS

### Synthesis of hydroxyapatite (HA) by a sol-gel method

Triethylphosphite or triethylphosphate (Aldrich) were chosen as phosphorous precursors. Calcium Nitrate and Calcium acetate (Aldrich) were used as calcium precursors.

The reaction was carried out at room temperature in a vessel equipped with a cooling system to avoid losses of the volatile phosphorous precursors during the sol formation. First the phosphorous precursor was diluted in anhydrous ethanol and then, a small amount of distilled water was added for hydrolysis, keeping a molar ratio of water to the phosphorous precursor at 3.

A stoichiometric amount (to maintain  $\text{Ca}/\text{P} = 1.67$ ) of the calcium precursor solution (3 M solution in anhydrous ethanol) was added dropwise into the hydrolyzed phosphorous sol. The pH of the sol was maintained around 2.8. Vigorous stirring was continued for an additional 25 min after the titration. A clear solution was obtained and aged at room temperature for 24 h before drying. The solvents were then driven off at  $60^\circ\text{C}$  until a gel was obtained. Besides, an aqueous-based process was employed with distilled water as the only diluting medium [13].

The gel compositions were analyzed by EDX (Oxford Scientific) and TGA (Mettler-Toledo TGA 50).

The gel was subjected to different drying processes: calcination, liofilization and aerogel formation.

In the calcination process the gel was subjected to different temperatures, from 300 to 900 °C, for 2, 4 or 6h intervals. The presence of HA phase was evaluated using an X-ray diffractometer (Bruker D-5005).

#### Liofilization drying process

This process was performed in standard liofilization equipment. The gels for liofilization must be in aqueous medium. The rate of cooling will influence the structure of the frozen matrix. Thus, different cooling systems were used to freeze the samples: with liquid N<sub>2</sub> (-173 °C), at -78 °C with CO<sub>2</sub>/acetone and at -20°C in the freezer.

#### Aerogel production

Aerogel production was carried out in a reactor, which has the following characteristics: maximum pressure of 500 bar, maximum temperature of 400°C, heating capability of 14500W, maximum CO<sub>2</sub> flow of 40Kg/h, maximum solvent flow of 1,8 L/h and a computer aided system. The supercritical cycle was composed of 4 stages: pressure increase until 150 bar followed by temperature increase until 250 °C, where the system reaches the supercritical conditions. Then, pressure decrease until atmospheric pressure and after that, temperature decrease until room temperature. The HA aerogels were characterized by X-ray diffraction and SEM-EDX.

#### Plasma polymerization

Acid acrylic was polymerized onto glass and HA substrates through plasma polymerization technique at low pressure, with a radiofrequency source of 13,56 MHz. Different reactor designs were employed and different monomer pressures were tried. One of the apparatus used for the plasma treatment consists of a stainless steel discharge vessel (diameter 26 cm, length 24 cm) with internal electrodes which are connected to a radio frequency (RF) ACG-3XL generator at 13,56 mHz from ENI (Italy). The gases are supplied via a standard manifold with gas fluxes adjusted with needle valves. A two stages mechanical pump (D8B from Leybold (UK)) evacuates the vessel

The second one is a stainless steel vessel (diameter 60 cm, length 45 cm) equipped with three different trays (polymerization positions). These are connected to a radio frequency (RF) at 13,56 MHz. The gases are supplied via a standard manifold on the rear part of the vessel. Also a two stages mechanical pump evacuates the vessel.

The pressure were varied between 0,1-0,8 mbar and the RF power between 15-40 W.

The kinetics of the thin film growth was also studied. Layers were also characterized by IR (FTIR Nicolet Manga 560) and XPS (PH 5500 Perkin Elmer).

## **DISCUSSION**

#### Synthesis of HA by a sol-gel method

Researchers employ a number of combinations between calcium and phosphorous precursors. Besides the difference in chemical activity of the precursors, such as, hydrolysis, polycondensation,etc, the temperature that is required to form the apatitic structure depends largely on the chemical nature of the precursors [13]. In the present work, experimental conditions of HA gel synthesis have been optimized, trying different calcium and phosphorous precursors and different solvation medias, as it is explained above. The gel ageing time is also important for the solution system to stabilize, and therefore, to obtain later the HA phase.

Hydrolysis activity of triethylphosphate is relatively poor compared with the triethylphosphite one, and a higher solution temperature together with a prolonged time period is

needed to form the HA phase [15]. That could explain why results obtained in this work with triethylphosphate were not satisfactory. In the other hand, calcium acetate was found to be less soluble in the media used than calcium nitrate, and that affected to correct sol formation.

Before doing the thermal treatment to the gels in order to obtain the HA phase, they were characterized by TGA. Gel TGAs all show a first weight loss from RT to 250 °C due to solvent evaporation. Then, no weight loss was observed until 400 °C, if calcium acetate was used as calcium precursor or until 550 °C, if calcium nitrate was used. These temperatures correspond to the decomposition temperatures of calcium precursors, as TGAs of them have confirmed.

The thermal treatment consisted of heating gels at different temperatures for different periods of time in order to find the best formation conditions of HA phase. HA phase often appears accompanied of other phases that can be different depending on the precursors used, the thermal treatment temperature and the time interval, as table I shows. The more the thermal treatment time is increased, the more HA formed at one fixed temperature becomes crystalline.

The different phase transformations of calcium precursors were observed in XRDs as a temperature function. For instance, calcium acetate was transformed to calcium carbonate at 450 °C, at 700 °C carbonate was transformed to hydroxide and finally calcium oxide was obtained. TGAs of calcium precursors and gels also confirmed it. It can be concluded that HA phase formation depend on the decomposition temperature of the calcium precursor used. Thus, the degree of carbonatation can be determined by TGA analysis. This parameter is directly related with the calcium precursor used. The maximum carbonatation level (~25%) is achieved using calcium acetate.

	Calcium precursor	Thermal treatment time /h	Thermal treatment temperatures /°C						
			300	400	500	600	700	800	900
Triethylphosphate	Nitrate	2		HA, CaCO <sub>3</sub>	HA, CaCO <sub>3</sub>	HA, CaCO <sub>3</sub>	HA, CaCO <sub>3</sub>	HA, W, CaCO <sub>3</sub>	
	Acetate	2	Amorphous			W, Ca <sub>2</sub> P <sub>2</sub> O <sub>9</sub>	HA, W	HA, W, Ca(OH) <sub>2</sub> , CaO	
	Acetate	4	HA*	-	-	HA	HA, W	HA, W	HA, W, CaO
	Acetate	6	HA* W	-	-	-	HA, W	HA, W	HA, W, CaO

Table I. HA\*: poor crystalline hydroxyapatite, W: whitlockite

Calcium nitrate and triethylphosphate in aqueous media have shown better feasibility to form the sol and in the same way the gel obtained from these precursors formed crystalline HA at lower temperatures as table I shows. Although it seems not necessary to obtain very pure and crystalline HA for bone and cartilage regeneration, (mineral component of bone is formed by myriad tiny, imperfect crystals); the use of calcium nitrate as precursor allows a better control on HA crystallinity. In this sense the HA formed could be easier tailored using this precursor.

#### Liofilization drying process and aerogel production

As we stated before, the precursors chose to make these scaffolds were calcium nitrate and triethylphosphate.

Liofilization process was used to dry hydrogels in order to obtain a porous structure. If the water freezes quickly (with liquid N<sub>2</sub>), it could be expected that final product has a finer pore structure. If freezing is slower (at -20 °C in the freezer), the resultant product may have coarser pore structure. But sometimes it becomes convenient to be able to control the pore size more exactly. Then, aerogel production appears to be a quite interesting technique. Using both techniques, HA scaffolds were obtained and characterized by XRD and EDX-SEM.

The morphology of the samples, studied by SEM, shows, as it was expected, a higher open porous structure for the aerogels, with very small pores. This higher porosity of the aerogels could be important to provide osteoconductivity to the scaffold.

It is important to point out that, whereas liofilized structures need a post-thermal treatment to form the apatitic structure, in the case of aerogels (figure 2), HA accompanied of other phases was formed during the aerogel production process, as XRD of aerogels have proved (figure 1).

#### Plasma polymerization

Different RF source powers monomer pressures, polymerization times and reactors designs were studied and optimal conditions were established for acrylic acid plasma polymerization onto glass and HA substrates (Power 9W, time 5 h, monomer pressure 0,01 mbar). This yields uniform layers of 50 nm thickness with good adhesion both to HA aerogels and glass plates. The more the RF power was increased, the more the polymerization occurred and layers obtained were not uniform, regarding the thickness uniformity on glass plates. Besides, the visual aspect corroborates the lack of uniformity. Layers deposited using a lower RF source power and a higher polymerization time, were uniform and had a high degree of acidic functional groups in its surface as IR analysis show (figure 3).

## CONCLUSIONS

Promising results to design modified HA scaffolds are obtained.

Calcium nitrate works better than calcium acetate as calcium precursor for HA formation. The reactive preparation is easier to handle and the HA crystallinity can be better tailored.

The aerogel processing technique seems to be a very interesting technique to obtain osteoconductive HA scaffolds in one step with pore size control.

Plasma polymerization of acrylic acid at low RF source power leads to uniform functionalized layers with good adhesion to HA aerogels.

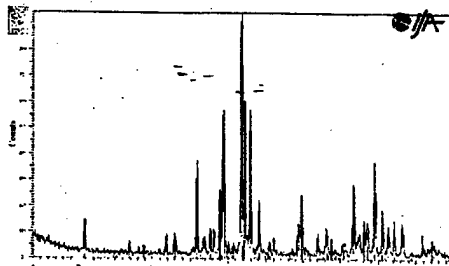


Figure 1. XRD of the aerogel  
(HA is the main phase together with CaCO<sub>3</sub>)



Figure 2. Aerogel SEM micrograph (x1500)

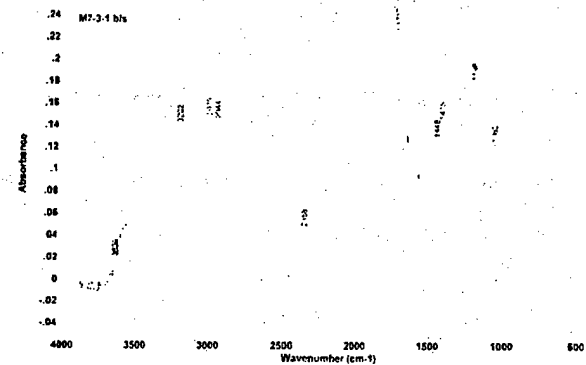


Figure 3.

#### ACKNOWLEDGMENTS

We would like to thank Dr Felicià Plana and Josep Elvira from Institut Jaume Almera -CSIC in Barcelona for performing the XRD spectra. And Dr Elias Molins and Anna Roig from ICMAB CSIC in Bellaterra (Barcelona) for carrying out the aerogel production.

#### REFERENCES

1. R. Langer, J.P. Vacanti, *Science*, **260**, 920-926 (1993).
2. W.T.Jr. Green, *Clin Orthop* **124**, 237-250 (1977).
3. Charles A. Vacanti, MD, and Joseph P. Vacanti, MD, *Tissue Engineering in Orthopedic Surgery*, vol. 31, 3, 351-355 (2000).
4. B.E. Chaitnaud, R. Langer, J.P. Vacanti, "The history of tissue engineering using synthetic biodegradable polymer scaffolds and cells". *Synthetic biodegradable polymer scaffolds*, Atala A, Mooney DJ editors. Boston: Birkhauser (1997) pp. 1-14.
5. M. Kellomaki, H. Niiranen, K. Puumanen, N. Ashammakhi, T. Waris, P. Tormala, *Biomaterials* **21**, 2495-2505 (2000).
6. D.W. Hutmacher, *Biomaterials* **21**, 2529-2543 (2000).
7. K.J.L. Burg, S. Porter, J.F. Kellam, *Biomaterials* **21**, 2347-2359 (2000).
8. V.I. Sikavitsas, J.S. Temenoff, A.G. Mikos, *Biomaterials* **22**, 2581-2593 (2001).
9. Ch.A. Vacanti, L.J. Bonassar, "Current technology- An overview of tissue engineered bone". *Clinical Orthopaedics and related research*, Lippincott Williams & Wilkins, Inc. 367S (1999) pp. S375-S381.
10. M. Itokazu, W. Yang, T. Aoki, N. Kato, *Biomaterials* **19**, pp. 817-9 (1998).
11. W. Paul, C.P. Sharma, *J Mater Sci Mater Med* **10**, pp. 383-8 (1999).
12. J.A. Jansen, J.P.C.M. Van de Waerden, J.G.C. Wolke, K. de Groot, *J Biomed Mater Res* **25**, pp. 973-89 (1991).
13. Dean-Mo Liu, T. Troczynski, W.J. Tseng, *Biomaterials* **22**, pp. 1721-30 (2001).
14. A. Jillavenkatesa, R.A. Condrate, *J Mater Sci* **33**, pp. 4111-9 (1998).
15. J.D. Wright, A.J.M. Sommerdijk, *Sol-Gel materials. Chemistry and applications*, Gordon and Breach Science Publishers (2001) pp. 3-4.
16. Thierry, M. Tabrizian, R. Sipehia, J. Silver, Y. Merhi, L. Bilodeau, L'H. Yahia, *27th Annual Meeting Transactions* **166**, Society For Biomaterials (2001).
17. Y. Wu, Y. Inoue, H. Sugimura, O. Takai, *Mat Res Soc Symp Proc* **711**, Materials Research Society (2002).

### **Antimicrobial Coatings Obtained in an Atmospheric Pressure Dielectric Barrier Glow Discharge**

Sabine Paulussen, Dirk Vangeneugden, Olivier Goossens and Erik Dekempeneer  
Materials Technology Division,  
VITO (Flemish Institute for Technological Research),  
Boeretang 200, B-2400 Mol, Belgium.

#### **ABSTRACT**

This paper addresses the development of plasma polymer coatings that should prevent bacteria from adhering to medical devices, implants, textile fibers, packaging materials, etc. The two main parameters affecting bacterial colonization onto surfaces are the surface energy and the surface roughness. Both parameters can be adjusted by the deposition of a thin plasma polymer coating in an atmospheric pressure dielectric barrier glow discharge. According to SEM, FTIR, SPM, XPS and contact angle measurements, smooth, hydrophilic plasma polymer coatings were obtained under specific plasma conditions starting from 2-hydroxyethyl methacrylate (HEMA) and ethyl diazoacetate (EDA).

#### **INTRODUCTION**

In the initial step of bacterial cell adhesion, proteins are adsorbed onto a surface [1]. Moreover, some bacteria strains produce a polysaccharide based matrix referred to as slime, which provides them with an additional mechanism for adhesion and an increased resistance to antibiotic drug therapies [2]. The reduction of protein and polysaccharide adsorption onto surfaces is therefore an important issue in the development of improved materials for medical applications such as implants, prostheses, shunts, intraocular or contact lenses and medical devices. Besides, this is also a topic in the development of food grade or medical grade plastic foil and textile fiber.

Despite the lack of a theory on the role of hydrophobicity on protein adhesion, it is reported in the literature that surfaces of low surface energy adsorb more proteins than surfaces of high surface energy [3-6]. Moreover, proteins show better adhesion to rough surfaces [7, 8].

Common low-pressure nonequilibrium plasmas represent an excellent method to deposit a very thin polymeric film (typically 2-100 nm) with mentioned desirable surface properties [9, 10]. The application of low-pressure plasmas is however limited due to the need of vacuum equipment and the low deposition rates that can be obtained.

Therefore, both the industrial and the academic world show a growing interest in plasma processes at atmospheric pressure. So far, applications were mainly situated in the area of cleaning, sterilization and activation of plastic surfaces, but currently the focus is shifting towards the deposition of organic and inorganic functional coatings on various substrates [11]. Like the low-pressure plasma techniques, atmospheric pressure dielectric barrier glow discharges allow treatment of a variety of objects, foils, fibers, etc in a sterile environment and at room temperature. In addition, the atmospheric pressure set-up allows continuous processing, which is especially interesting for the treatment of textile and plastic foil, while it allows significantly

higher deposition rates. More information on the theoretical background of this process can be found elsewhere [12-14].

## EXPERIMENTAL SETUP

The experimental setup (see figure 1) of the dielectric barrier glow discharge (DBD) consists of two parallel electrodes (160x180 mm), both covered with an insulating  $\text{Al}_2\text{O}_3$  plate of 2 mm thickness. To ensure stable plasma operation, the gap between the electrodes is limited to a few millimeters. Standard purity nitrogen and argon were used as inert carrier gases. The flow rate was controlled by mass flow controllers and set at 15 l/min. The reactive precursor is added to the inert carrier gas by means of an atomizer which generates a polydisperse submicron aerosol. In order to perform tests in a controlled environment, the electrode configuration is mounted in a closed chamber which is evacuated and subsequently filled with the carrier gas before deposition is started.

Plasma discharges were generated by a 20 kV/200 mA AC power supply with variable frequency, in this case ranging between 1 and 4 kHz.

The precursor molecules chosen in order to obtain coatings with high surface energies, are 2-hydroxyethyl methacrylate (HEMA,  $\text{H}_2\text{C}=\text{C}(\text{CH}_3)\text{COOCH}_2\text{CH}_2\text{CH}_2\text{OH}$ ) and ethyl diazoacetate (EDA,  $\text{N}_2\text{C}(\text{CO}_2\text{C}_2\text{H}_5)_2$ ) (Sigma-Aldrich, Belgium), both containing a polar functional group. Each of the precursors was polymerized in  $\text{N}_2$  and Ar plasma in runs of 2 and 6 minutes.

Double polished silicon substrates (12 x 12 mm) were used as substrates for plasma polymer deposition and placed on the lower (high voltage) electrode. The coatings obtained were analyzed by FESEM (JSM-6340F, JEOL, USA), SPM (Digital Instruments, USA), XPS (Fisons Instruments, USA) and FTIR-spectroscopy (Avatar 360 ESP, Nicolet, USA). Contact angles were measured using the sessile drop technique (SOCA 15 plus, Dataphysics Instruments GmbH, Germany).

## DISCUSSION

A first observation is that the carrier gas ( $\text{N}_2$  or Ar) has a strong influence on the polymerization process [11]. So far, it appeared however difficult to establish a correlation between the carrier gas and the details of the polymerization process. In spite of this fact, some qualitative observations could be readily made.

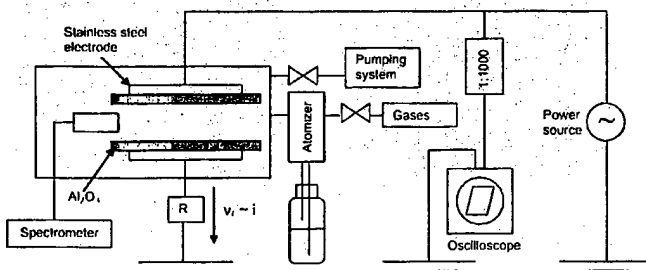


Figure 1. Experimental set-up of atmospheric pressure dielectric barrier glow discharge.

### Microscopy

Figure 2 shows the SEM cross-sections of the coatings resulting from the deposition of HEMA on silicon obtained in a N<sub>2</sub> and Ar plasma. After a deposition time of 6 minutes, both coatings showed a similar structure although the 'polymer' structure obtained in N<sub>2</sub> appears slightly more dense. Together with the difference in deposition rate this gives an indication of differences in the polymerization mechanism. The coatings prepared starting from EDA resemble the ones presented in figure 2 although thicknesses of about 400 and 550 nm were obtained in N<sub>2</sub> and Ar, respectively. The coating thicknesses obtained after 2 minutes demonstrated constant deposition rates as a function of time.

An important feature in the present context is the roughness of the coatings, which proved to be very low according to SPM measurements. Surface roughnesses between 0.20 and 0.35 nm were obtained in both Ar and N<sub>2</sub> plasma.

### Contact Angles

Contact angles of the plasma polymer coatings were determined and summarized in table 1. Under equal reaction conditions, HEMA based plasma polymers were characterized by lower contact angles than those prepared from EDA. In addition, it should be noted that the contact angles of the EDA plasma polymers remain constant, while those of the HEMA based coatings decrease somewhat after the first contact of the droplet with the surface. This could be due to the absorption of water in the coating. It is however striking that the carrier gas has more impact on the contact angle of the plasma polymers than the nature of the precursor. In N<sub>2</sub> plasma, both HEMA and EDA give rise to the deposition of coatings with contact angles lower than 20°, whereas the contact angles obtained in Ar plasma are significantly higher. XPS and FTIR analysis were necessary to gain a better insight in the present phenomena.

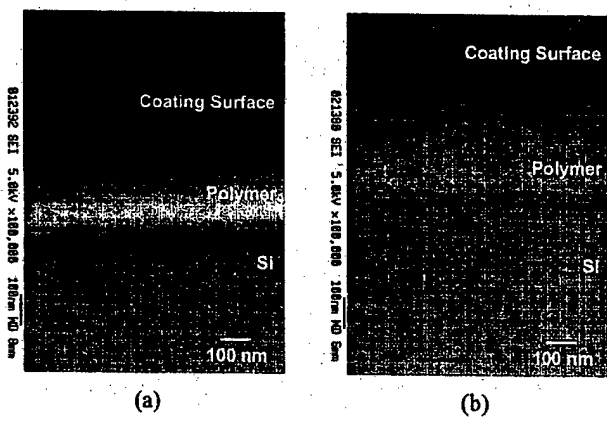


Figure 2. SEM cross sections of plasma polymer coatings obtained from HEMA in N<sub>2</sub> (a) and Ar plasma (b) after 6 minutes.

**Table 1.** Contact angles with water ( $\theta_{H2O}$ ) of plasma polymer coatings obtained from HEMA and EDA in  $N_2$  and Ar DBD glow discharges (deposition time of 6 minutes).

Precursor/Carrier Gas	$\theta_{H2O}$ (deg)
EDA / $N_2$	19.2
EDA / Ar	46.7
HEMA / $N_2$	16.1
HEMA / Ar	34.2

### XPS

X-ray photoelectron analysis was used to determine the relative amounts of C, O and N at the polymer film surfaces (Table 2). Apparently, more nitrogen is incorporated at the surface of plasma polymer coatings when  $N_2$  is used as carrier gas instead of Ar. This is manifestly demonstrated by the polymerization of HEMA, which resulted in a surface concentration of nitrogen of about 30 % in  $N_2$  plasma and 0 % when the deposition was carried out in Ar plasma. The latter can be rationalized by the incorporation of N-containing radicals present in a  $N_2$  plasma into the bulk of the plasma polymers and thus at their surface. On the other hand, stable radicals of organic origin that remain present in plasma polymer coatings after polymerization might react with  $N_2$  even in the absence of plasma conditions, e.g. during storage. Providing this interpretation is legitimate, only the upper layers of the coatings will contain the observed amounts of N. More evidence for one of these explanations may arise from FTIR measurements.

The observations made for HEMA concerning the C/N ratio of the plasma polymers also hold for the case of EDA. However, while EDA itself is characterized by a C/N ratio of 2, this ratio increased after polymerization in  $N_2$  and Ar to 6.5 and 18.1, respectively. Clearly, the diazo-group of EDA has a tendency to split off under plasma conditions. The nitrogen containing functionalities at the surface of the EDA coatings are therefore not necessarily of diazo-origin.

When comparing the contact angles of the coatings with their surface composition, it is however obvious that the high N-content should be responsible for the low contact angles obtained after polymerization in  $N_2$  plasma.

**Table 2.** XPS-data (surface mole fraction of elements excluding hydrogen in %) obtained from HEMA and EDA plasma polymer coatings prepared in  $N_2$  and Ar DBD glow discharges.

Precursor/Carrier Gas	C <sub>tot</sub>	O <sub>tot</sub>	N <sub>tot</sub>
EDA / $N_2$	65.9	24.1	10.0
EDA / Ar	63.4	33.1	3.5
HEMA / $N_2$	54.8	14.7	30.5
HEMA / Ar	69.8	30.2	0.0

### FTIR

Infrared spectra of the plasma polymers on silicon are presented in figure 3. As expected from the previous sections, the nature of the carrier gas causes some substantial differences in the FTIR spectra.

The spectrum of the HEMA based coating obtained in Ar plasma (fig. 3.a) contains the main bands typical for the monomer, including O-H stretching ( $3422\text{ cm}^{-1}$ ), C-H stretching ( $2955\text{ cm}^{-1}$ ), C=O stretching ( $1730\text{ cm}^{-1}$ ) and C-H deformation ( $1456\text{ cm}^{-1}$ ). In the spectrum obtained from the HEMA based plasma polymer deposited in N<sub>2</sub>, the weak band at  $3317\text{ cm}^{-1}$  could be attributed to O-H stretching. However, the N-H bond in amines and amides may also cause absorption in the region of  $3500\text{-}3300\text{ cm}^{-1}$ . Thus, although the low intensity of the absorption bands complicates the identification of the different functionalities, it seems reasonable to assume that amine and/or amide groups are incorporated in the HEMA based plasma polymer when N<sub>2</sub> is used as a carrier gas.

The most striking feature in the spectra of the plasma polymers obtained from EDA (fig. 3.b) is the absence of the absorption band typical for the diazo-group at  $2200\text{-}2000\text{ cm}^{-1}$ , which confirms that this group is split off from the precursor when introduced into plasma. As a result, only C-H deformation ( $1447\text{ cm}^{-1}$ ) and C-H ( $2982\text{ cm}^{-1}$ ) and C=O ( $1737\text{ cm}^{-1}$ ) stretching bands are identified in the spectrum of EDA based polymers deposited in Ar plasma. The same absorption bands are present in the spectrum of the EDA coatings that were polymerized in N<sub>2</sub>. The peaks originating from C-H stretching ( $2982\text{ cm}^{-1}$ ) are however largely covered by two bands which are typical for the N-H stretching in -NH<sub>2</sub> ( $3146$  and  $3049\text{ cm}^{-1}$ ).

In spite of their absence in these spectra, the presence of certain other functional groups at the surface of the coatings cannot be excluded as the intensity of their absorbance pattern could be too low to allow detection using common FTIR. It can however be stated that amine or possibly also amide groups are at least partly responsible for the high surface energies obtained when HEMA and EDA are polymerized in N<sub>2</sub> plasma. Ester groups, and in the case of HEMA also hydroxyl groups, are present in the coatings polymerized in both Ar and N<sub>2</sub>.

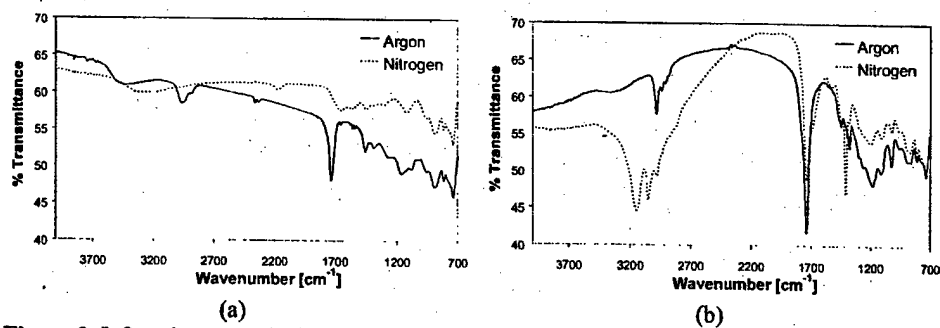


Figure 3. Infrared spectra obtained from HEMA (a) and EDA (b) in argon and nitrogen plasma.

## CONCLUSIONS

This study shows that organic coatings with low contact angles and a low surface roughness can be obtained through polymerization of HEMA and EDA in a dielectric barrier glow discharge at atmospheric pressure. Especially when N<sub>2</sub> is used as a carrier gas, contact angles lower than 20° could be obtained mainly due to the incorporation of nitrogen in the plasma polymers. The true potential of these plasma polymers as antimicrobial coatings seems therefore promising but is currently being investigated in more detail.

As the present technique allows continuous processing at low temperature and at atmospheric pressure, it is in particular interesting for the treatment of large surfaces and plastic foils or fibers.

In addition, this technique offers promising perspectives for the further development of antimicrobial coatings in that intrinsically antimicrobial substances can be mixed with the precursor and thus incorporated in plasma polymer coatings.

## REFERENCES

- [1] Y. F. Dufrêne, C. J. P. Boonaert, and P. G. Rouxhet, *Colloids and Surfaces B* **7**, 113-128 (1996).
- [2] C. R. Arciola, D. Campoccia, and L. Montanaro, *Biomaterials* **23**, 1495-1502 (2002).
- [3] B. Janocha, D. Hegemann, C. Oehr, H. Brunner, F. Rupp, and J. Geis-Gerstorfer, *Surface and Coatings Technology* **142-144**, 1051-1055 (2001).
- [4] M. Rosenberg and S. Kjelleberg, *Microbial Ecology* **9**, 353-393 (1986).
- [5] M. Quirynen, M. Marechal, H. J. Busscher, A. H. Weerkamp, J. Arends, P. L. Darius, and D. Van Steenberghe, *Journal of Dental Research* **68**, 796-799 (1989).
- [6] Z. Miqin, T. Desai, and M. Ferrari, *Biomaterials* **19**, 953-960 (1998).
- [7] P. Coussotrico, G. Clarotti, A. A. Benaoumar, A. Najimi, J. Sledz, F. Schue, and R. Quatrefages, *European Polymer Journal* **30**, 1327-1333 (1994).
- [8] G. Clarotti, F. Schue, J. Sledz, K. E. Geckeler, W. Gopel, and A. Orsetti, *Journal of Membrane Science* **61**, 289-301 (1991).
- [9] B. D. Ratner, *Journal of Biomaterials Science-Polymer Edition* **4**, 3-11 (1992).
- [10] P. Favia and R. d'Agostino, *Surface & Coatings Technology* **98**, 1102-1106 (1998).
- [11] O. Goossens, E. Dekempeneer, D. Vangencugden, R. Van de Leest, and C. Leys, *Surface and Coatings Technology* **142-144**, 474-481 (2001).
- [12] F. Massines, A. Rabehi, P. Decomps, R. B. Gadri, P. Segur, and C. Mayoux, *Journal of Applied Physics* **83**, 2950-2957 (1998).
- [13] F. Massines, R. B. Gadri, P. Decomps, A. Rabehi, P. Segur, and C. Mayoux, *AIP Conference Proceedings*, no. **363**, 306-15 (1996).
- [14] J. Salgc, *Surface & Coatings Technology* **80**, 1-7 (1996).

### Calcium Carbonate Reinforced Natural Polymer Composite For Bone Grafts

Samar J. Kalita<sup>1</sup>, Susmita Bose<sup>1</sup>, Howard L. Hosick<sup>2</sup>, Steve A. Martinez<sup>3</sup> and Amit Bandyopadhyay<sup>1</sup>

<sup>1</sup>School of Mechanical and Materials Engineering

<sup>2</sup>School of Molecular Biosciences

<sup>3</sup>College of Veterinary Medicine

Washington State University.

Pullman, WA 99164, U.S.A.

#### ABSTRACT

Challenges in tissue engineering have always-motivated scientists and engineers to develop new biomaterials that can restore the structural features and physiological functions of natural tissues. A novel ceramic-polymer composite was processed with bio-active ceramics dispersed in a natural bio-active polymer for bone graft applications. A commercially available castor bean extract polymer (CBP) was used. It is a natural polymer extracted from the oily castor beans of the dicotyledonous class. During processing of these composites, *in situ* random interconnected porosity was generated similar to natural bone. Hg-porosimetry results of these composites show that most of the pores are between 50 to 150 microns. Compression tests were performed on cylindrical samples to determine the mechanical properties. Average compression modulus was calculated as 173 MPa, while the average failure strength was 6.7 MPa. Cytotoxicity and cell proliferation studies were conducted with modified human osteoblast cell-line (OPC-1) to show that these composites are biocompatible. Composites showed good cell attachment with a continuous increase in cell growth for at least up to two weeks.

#### INTRODUCTION

During the past four decades, applications of novel materials for biomedical practices have greatly revolutionized the quality of human life. Many speciality polymers, metals, ceramics and composites have been developed for numerous applications [1]. These materials in various forms and phases are made to perform different functions in repair and reconstruction of diseased and damaged parts of the human body. Among all materials, the ceramics, and more precisely porous ceramics, are the most suitable ones for bone graft applications, primarily because bone itself is a naturally occurring porous ceramic. One of the restrictions on clinical uses of ceramics is the uncertain lifetime under the complex stress states due to poor resistance to crack propagation. Introduction of porosity increases these uncertainties to a significantly higher level. This concern has resulted in limited applications of porous ceramics.

Significant research has already taken place to develop polymer-ceramic composites as biomaterials. These composites attempt to incorporate the advantages of both the ceramic and the polymer phases. Most of the researches on polymer ceramic composites have been focused on (a) bio-inert polymer with bio-active ceramics [2, 3], and (b) bio-active polymer with bio-active ceramics [4, 5]. In our research, a novel ceramic-polymer composite was processed with bio-active ceramics dispersed in a natural bio-active polymer. Moreover, during processing of these composites, *in situ* random interconnected porosity was generated, which are similar to

natural bone. The composite material was characterized for their physical, mechanical and biological properties.

## EXPERIMENTAL PROCEDURE

A commercially available natural polymer was used for this study. The commercial name is "Polimero Vegetal Ostointegrativo". Vegetable polymer was extracted from the "Ricinus Communis" (mamona oil), oil plant belonging to the dicotiledônea class, gerianaceas order and euforbiaceas family, its ricinoleic acid structure contain 18 carbon atoms in which there is a double bond between the 9<sup>th</sup> and the 10<sup>th</sup> carbons. Calcium carbonate powder was mixed with this polymer to form a ceramic-polymer composite.

The natural polymer comes in two parts. These two parts are named as "polyol" and "prepolymero". During processing of this composite, calcium carbonate powder was added to the liquid polymer while mixing the two components prior to room temperature curing. Preparation was carried out in a clean glass beaker. Mixing was done manually. A total of 6 grams CaCO<sub>3</sub> was added to 40 ml of polymer mixture during polymerization. After 1 minute of mixing, there was an increase in material temperature to 45°C. The total curing time was between 3 to 5 minutes. The polymer was taken out of the beaker and allowed to cure in another clean glass beaker. During polymerization, *in situ* random interconnected pores were generated. After curing, the overall material resulted into a strong porous composite with three-dimensionally interconnected porosity.

Cylindrical samples were core drilled with uniform diameter of 11.5 mm. These samples were then sectioned to a length of 20 mm each to test under uniaxial compression loading. For *in vitro* testing, circular disk samples were prepared. *In vitro* samples had an average diameter of 11.5 mm and an average thickness of 1.8 mm. Biodegradation studies were carried out with *in vitro* samples in culture media. Hg-porosimetry was carried out to evaluate the pore size and their distribution.

*In vitro* testing was carried out using a human osteoblast cell-line (OPC 1). The OPC-1 cell line is a conditionally immortalized osteoprecursor cell line derived from human fetal bone tissue [6]. The OPC 1 cells were cultured in a standard medium made of McCoy's 5A (with L-Glutamine, without Phenol Red and Sodium Bicarbonate) [Sigma Chemical Co, Saint Louis, MO], supplemented with 10% fetal bovine serum, 2.2 gram/liter sodium bicarbonate, 0.1 gram/liter penicillin and 0.1 gram/liter streptomycin. The selection of a nutrient medium is strongly influenced by type of cell, type of culture and degree of necessary chemical definition. Cells were removed and split in the ratio 1:2, 3 days before use. The cells were seeded on to 15 disk samples. The cultures were incubated at 37 °C in a humidified 5% CO<sub>2</sub> atmosphere. Cell counts were taken after 3, 7, 14 and 21 days of culture. Microscopic observations revealed that the cells had attached, anchored and spread on to the porous disk samples within 3 days after seeding. A colorimetric assay (MTT assay) was used to evaluate living cell number at various times after seeding. This assay quantitates the ability of mitochondrial dehydrogenases to metabolize 3-[4,5-dimethylthiazol-2-yl]-2,5-diphenyl-tetrazolium bromide to an insoluble formazan [7]. The amount of formazan is directly proportional to the total number of living cells. This enzyme assay produces a colored product, which is quantitated in a microplate reader at a wavelength of 570 nm.

## RESULTS AND DISCUSSION

### Bulk density and mercury porosimetry

Bulk density of the composite was determined using cylindrical samples. The bulk density was found to be  $0.4 \text{ g/cm}^3$ . The composite porosity was determined using a Hg-porosimeter (Auto Porc 9400, Micromeritics, GA) and a typical result is shown in figure 1. Hg-porosimetry is a useful method for determining pore size and distribution in porous structures of many materials. It can be seen from the plot that the majority of the pores were in the range of 50-100  $\mu\text{m}$ , while some were between 200-250  $\mu\text{m}$ . The porosimetry result also indicates that the bulk density of the sample was  $0.4 \text{ g/cm}^3$  with an apparent density of  $0.51 \text{ g/cm}^3$ . The composite samples had an average total porosity of 24 vol %. Figure 2 shows an SEM micrograph of the composite. The typical pore sizes and their interconnectivity can be seen from this figure.

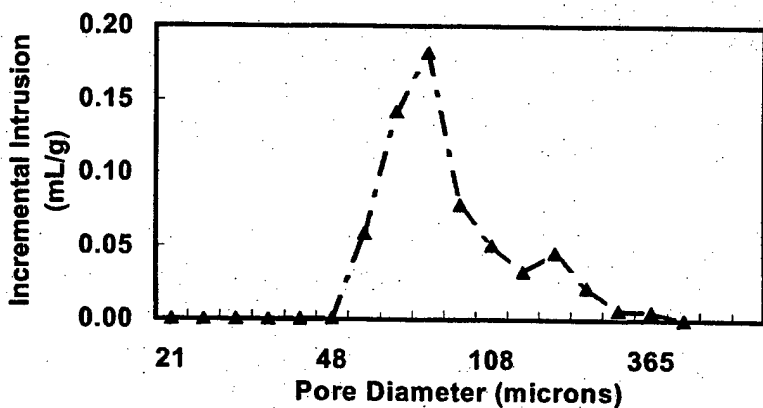


Figure 1. Hg porosimetry plot shows the variation of pore sizes in the composite.

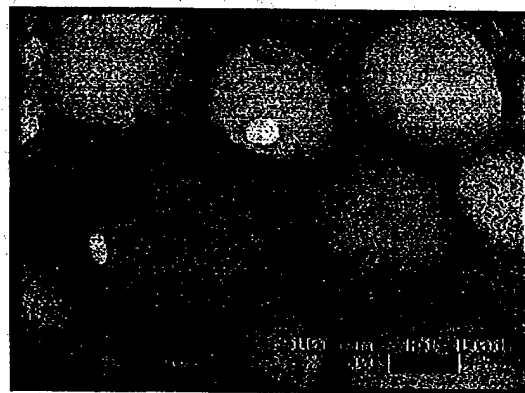


Figure 2. An SEM photograph of a composite sample shows interconnected spherical open pores in the size range of 50-100 microns.

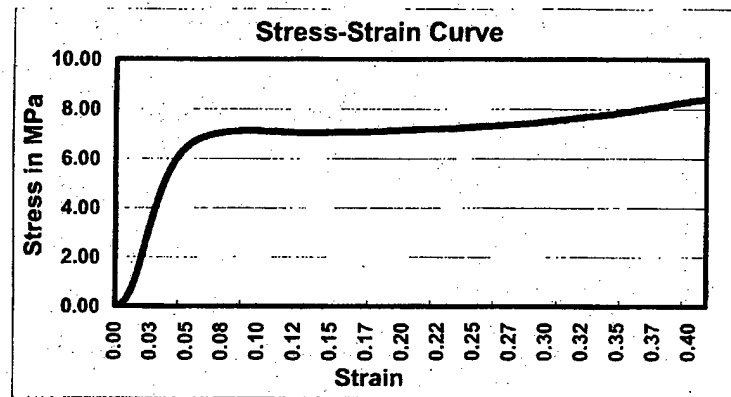


Figure 3. The stress-strain relationship of one of the compression samples

#### Mechanical testing

Uniaxial compression tests were performed on four samples of this composite to evaluate their mechanical properties. Figure 3 shows the stress-strain plot for one of the samples under compression testing. The modulus of compressibility and the stress at which failure initiates were determined from the stress-strain curves. Average compression modulus was calculated as 173 MPa (+/- 16 MPa), while the average failure strength was 6.7 MPa (+/- 0.64 MPa). The failure strength is quite comparable to human cancellous bone, which has a typical compressive strength between 0.5-14.6 MPa [8].

#### In vitro Testing

Biocompatibility is defined as the ability of a material to perform with an appropriate host response in a specific application. *In vitro* testing was done to test the biocompatibility of this composite. All the matrices were found to be non-toxic and biocompatible. Observations on the 3<sup>rd</sup> and 7<sup>th</sup> days of culture showed that the cell attachment and growth were very good. The cells were well spread and were in contact with each other. A continuous increase in cell growth was also observed up to 14<sup>th</sup> day. Cell counts on day 21<sup>st</sup> had indicated that cells had begun to detach from the matrices. Similar tests were repeated twice and the results were identical, which suggests that there was a saturation effect of cell growth in these matrices. A possible explanation for this growth behavior for cells during the third week could be due to lack of space for cells to grow. The matrix surfaces were saturated with cells after 14 days and then the cells started impinging to each other. Figure 4 shows the growth curve of OPC 1 cells on composite matrices as a function of time in days. Figure 5 shows the cell attachment on these matrices after 7<sup>th</sup> day.

Biodegradation studies were carried out on the composite using the same standard media that was used for *in vitro* testing. Fifteen samples were prepared and their dry weights were

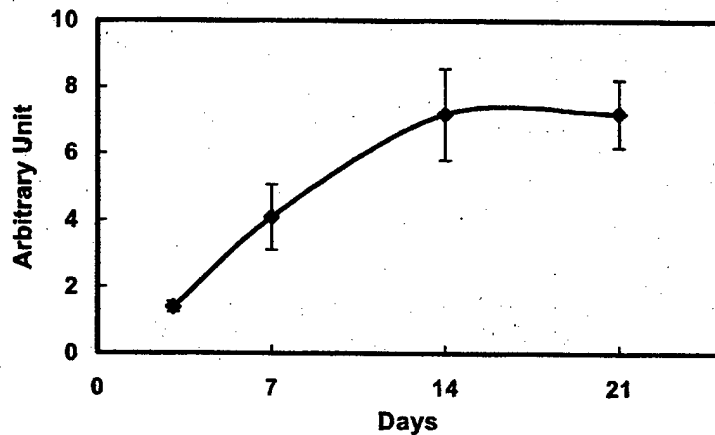


Figure 4. Growth curve of OPC 1 cells on polymer-ceramic composite matrices

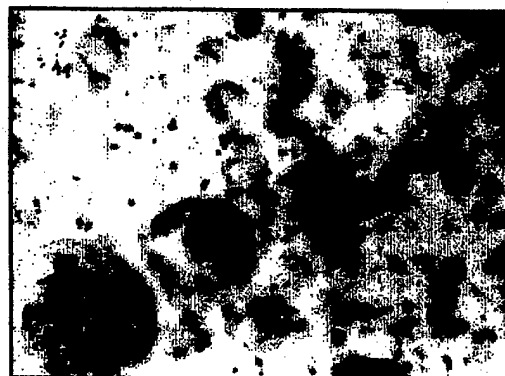


Figure 5. Cell attachment on the composite matrices on Day 7<sup>th</sup>

recorded. These samples were then immersed in the standard media and maintained at 37 °C in the incubator. Rate of dissolution was measured in terms of normalized dry weight loss. A negligible weight loss of around 1.5 weight% was recorded at the end of 28 days. The results indicate that the composite is biorecsorbable, though the degradation rate is very slow.

#### CONCLUSIONS

Porous calcium carbonate reinforced natural polymer composite has been processed and characterized. Uniaxial compression tests showed the average strength of 6.7 MPa and the

compression modulus of 173 MPa. Hg-porosimetry revealed that the majority of the pores are in the range of 50-100  $\mu\text{m}$ . *In vitro* testing with the OPC 1 cell-line showed that the composites are biocompatible. Biodegradation studies with McCoy's 5A media showed that the composite is bioresorbable as well with a fairly slow degradation rate. The results are promising for these composites to be used as bone-graft materials, though further *in vivo* tests are necessary on these materials to be used successfully in various orthopedic applications.

#### ACKNOWLEDGEMENT

The authors would like to acknowledge National Science Foundation for the financial support through NSF-CAREER grant DMI 9874971. We would also like to thank Travis Sonnett and Jens Darsell for experimental support.

#### REFERENCES

1. L. L Hench, *J of Amer Ceram Soc*, **74** [7] 1487 -510 (1991).
2. W. Bonfield, M. Wang and K. E. Tanner, *Acta Materialia*, **46**, 2509-2518 (1998).
3. K. E. Tanner, R. N. Dowens and W. Bonfield, *Br. Ceram Trans*, **93**, 104-10 (1994).
4. M. Kikuchi, Y. Suctsugu, J. Tanaka and M. Akao, *Journal of Materials Science: Materials in Medicine*, **8** [6], 361-64 (1997).
5. T. Kasuga, H. Fujikawa, Y. Ota, M. Nogami and Y. Abe, *Bioceramics II*, R. Z. LeGeros and J. P. LeGeros (Eds.), p 145 (1998).
6. S. R. Winn, G. Randolph, H. Uludag, S. C. Wong, G. A. Hair and J. O Hollinger, *J of Bone and Mineral Res*, **14**, (1999).
7. P. W. Sylvester, H.P. Birkenfeld, H.L. Hosick, K.P. Briski, *Exp. Cell. Res.*, **214**, 145 (1994).
8. Goulet et al., *J. Biomechanics*, **27**, 375-389, 1994.

**Biomimetics, Sensors and  
Nanotechnology**

### Biomimetic Networks For Selective Recognition of Biomolecules

Mark E. Byrne<sup>1,2</sup>, Kinam Park<sup>1,3,4</sup>, and Nicholas A. Peppas<sup>1,2,4</sup>

<sup>1</sup>NSF Program on Therapeutic and Diagnostic Devices

<sup>2</sup>Biomaterials and Drug Delivery Laboratories, School of Chemical Engineering

<sup>3</sup>Department of Industrial and Physical Pharmacy

<sup>4</sup>Department of Biomedical Engineering

Purdue University, West Lafayette, IN 47907-1283 U.S.A.

#### ABSTRACT

Studies of protein binding domains reveal molecular architectures with specific chemical moieties that provide a framework for selective recognition of target biomolecules in aqueous environment. By matching functionality and positioning of chemical residues, we have been successful in designing biomimetic polymer networks that specifically bind biomolecules in aqueous environments. Our work addresses the preparation, behavior, and dynamics of the three-dimensional structure of biomimetic polymers for selective recognition via non-covalent complexation. In particular, the synthesis and characterization of cognitive gels for the macromolecular recognition of D-glucose is highlighted. Novel copolymer networks containing poly(ethylene glycol) (PEG) and functional monomers such as acrylic acid, methacrylic acid, and acrylamide were synthesized in dimethyl sulfoxide (polar, aprotic solvent) via UV-free radical polymerization. Polymers were characterized by single and competitive equilibrium and kinetic binding studies, single and competitive fluorescent and confocal microscopy studies, dynamic network swelling studies, DSC, and FE-SEM. Results qualitatively and quantitatively demonstrate effective glucose-binding polymers in aqueous solvent. Due to the presence of template, the template mediated polymerization process resulted in a more macroporous structure as exhibited by dynamic swelling experiments, confocal microscopy, and SEM. Cognitive networks had a more macroporous structure with absorption of water occurring via non-fickian diffusion at a faster rate and with a higher equilibrium value. Polymerization kinetic studies suggest that the template molecule has more than a dilution effect on the polymerization, and the effect of the template is related strongly to the rate of propagation. The processes and analytical techniques presented are applicable to other biologically significant molecules and cognitive networks, in which hydrogen bonding, hydrophobic, or ionic contributions will direct recognition. Further developments are expected to have direct impact on applications such as analyte controlled and modulated drug and protein delivery, drug and biological elimination, drug targeting, tissue engineering, and micro- or nano-devices.

#### INTRODUCTION

At this stage in the evolving field of biomaterials science, major effort is being directed toward engineering the architectural design of biomaterials on a molecular level. By controlling recognition and specificity, the preparation of *synthetic macromolecular gels with designed artificial cognitive domains* is soon to be the next hurdle crossed in polymer and biomaterials development. Therefore, the next generation of biomaterials will include cognitive oriented design and intelligent complexation mechanisms that originate from specific macromolecular chemistry, itself present in the polymer matrix or surface in a controlled manner, which

manipulate the surface and bulk properties of the material in reproducible and tunable ways. The interest in this technology stems from a larger interest within our laboratory in artificially duplicating complex biological and physiological processes such as biomolecule modulated drug and protein release [1], targeted drug and protein delivery (site or ligand-specific interaction with cells and tissues), biomolecule recognition and removal of undesirable biologicals [2], ligand-directed cooperative allosteric recognition processes, directed on-off ligand binding processes, tissue engineering devices, biosensors, and novel therapeutic and micro-sensing devices, etc. For example, surface patterning of cognitive gels on silicon substrates can create micro- or nano-binding regions with areas of differing chemistry [3], which would be the basis for micro- or nano-diagnostic, drug delivery, or tissue engineering devices [4].

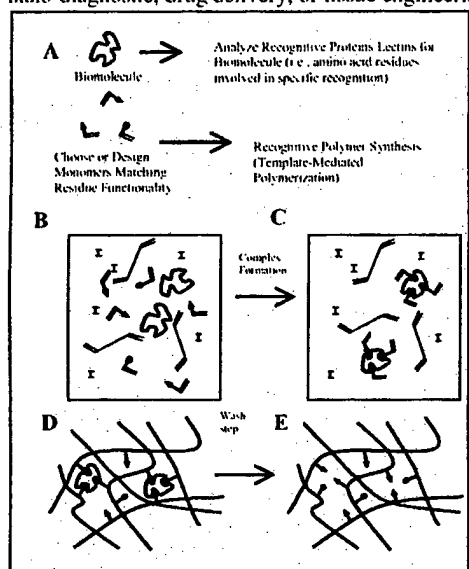


**Figure 1: Biomimetic Approach to Producing Recognitive Networks**

**A:** Mimic recognitive proteins and enzymes by analyzing the amino acids involved in binding a particular molecule and duplicating complexation interactions. **B:** Solution mixture of biomolecule (template), functional monomer(s) (triangles and circles), crosslinking monomer, solvent, and initiator (I). **C:** The pre-polymerization complex is formed via covalent or non-covalent chemistry. **D:** The formation of the network (imprinting process). **E:** Wash step where original template is removed.

Our goal, in general, is to produce stereo-specific, three-dimensional binding cavities for biologically significant molecules that function in aqueous environments. By tailoring the polymer network architecture and composition, effective biomimetic recognition sites can be created in polymer gels (Figure 1).

The network structure (polymer morphology, porosity, diffusional characteristics) depends upon the type of monomer chemistry (anionic, cationic, neutral, amphiphilic), the association interactions between monomers and pendent groups, the solvent, and the relative amounts of comonomers in the feed from which the structure is formed. Recognitive success, i.e., the ability to correlate high template binding affinity and specificity, depends on the relative amount of cross interaction between the solvent and the intended interactions. For non-covalent complexation, this translates to the strength of hydrogen bonding, hydrophobic interactions,  $\pi-\pi$  orbital interactions, ionic interactions, and van der Waals forces employed during template-monomer complex formation.

If proper complexation occurs in the pre-polymerization stage, the network formation will proceed with effective recognitive domains. For example, many binding proteins contain non-covalent binding mechanisms (e.g., hydrogen bonding, hydrophobic interactions) that bind specific molecules quite well in water

(polar, protic solvent) [5]. Our scientific rationale is based on the hypothesis that effectively designed recognition networks will have superior binding properties and directed recognition in aqueous environments by properly tuning the non-covalent pre-polymerization complexation interactions between the gel functionality and template biomolecule (increasing or decreasing macromolecular chain hydrophobicity [6], including strong hydrogen bond donors and acceptors [7], or including strong ionic directed recognition sites [8]).

## EXPERIMENTAL

### Materials

Methacrylic acid (MAA), acrylic acid (AA), acrylamide (Aam), dimethylsulfoxide (DMSO), and D-glucose were purchased from Aldrich (Milwaukee, WI). Poly(ethylene glycol) 200 dimethacrylate (PEG200DMA) was obtained from Polysciences, Inc. (Warrington, PA). Irgacure® 184, 1-hydroxycyclohexyl phenyl ketone, was purchased from Ciba Specialty Chemicals (Tarrytown, NY). Fluorescent D-glucose analogue, 2-(N-(7-nitrobenz-2-oxa-1,3-diazol-4-yl)amino)-2-deoxy-glucose (2-NBDG), was purchased from Molecular Probes, Inc.

### Methods: D-Glucose Recognition Network Synthesis

In a typical experiment involving Aam or AA as functional monomer (monomers were selected to match corresponding glucose binding protein residues of aspartate, glutamate, and asparagine), D-glucose, Aam or AA, and 2.0 mL of DMSO were mixed together. Then PEG200DMA and 1.5 wt% Irgacure® 184 were added to the mixture. Feed monomer compositions of this type varied from 20 to 80 mole% Aam per mole monomers (or 50 to 85 mole% AA) as well as from 4 to 15 mole % D-glucose. Control polymers were made with exactly the same composition except D-glucose was not added.

After preparation, the solution was placed in a nitrogen atmosphere and nitrogen was bubbled for 30 minutes. Polymerizations occurred between glass microscope slides (75 x 50 x 1mm, Fisher Scientific, Pittsburgh, PA) using 0.5 mm, 0.7mm, or 0.035 mm Teflon® spacers in a nitrogen atmosphere at a UV intensity of 10.0-15.0 mW/cm<sup>2</sup> for 15 minutes (UltraCure 100, EFOS Inc., Ontario, Canada). Polymers were placed in deionized water for 24 hours, then carefully separated from the slides, and were cut into various diameter discs using a cork borer. Discs were then placed in 50 mL conical tubes and placed on a rotating mixer (25 RPM, 70 degree angle, Glas-Col, Terre Haute, IN) and resuspended within multiple 24 hour wash steps (2 washes in acetic acid/deionized water (1:5 ratio); 8 washes in deionized water) to remove template and excess monomer. The resulting discs were then dried in air at ambient conditions and placed in a vacuum oven (T=26 °C, 28 mm Hg vacuum) until a constant weight was obtained (less than 0.1 wt% difference). The discs were then stored in a dessicator until testing.

### Methods: Recognition, Selectivity, and Dynamic Swelling Studies

In a typical binding study, a known amount of the template solution (e.g., D-glucose and D-galactose in competitive binding studies) was added to an aqueous solution containing a known amount of polymer discs. Samples were placed on a rotating mixer (70 degree angle; 25 RPM)

and supernatant was sampled at equilibrium. The time for equilibrium to occur in each system was predetermined by separate kinetic binding studies, where supernatant samples were taken at different time points. Equilibrium and kinetic-binding results were quantitatively calculated by HPLC measurements of the resulting supernatant (Phenomenex RPM monosaccharide column (300 x 7.8 mm), DI water mobile phase, 0.6 ml/min flow rate, temperature 80°C, Shimadzu RID-10A refractive index detector). Competitive binding results were visualized using a fluorescent glucose analogue: 2-NBDG (Figure 2). The analogue was added to vials containing a known amount of polymer (maximum absorption 466 nm; maximum emission 542 nm). A Nikon Labophot fluorescent microscope with a FITC filter set was used and images were acquired with an Optronics 470T CCD camera and captured using MetaMorph software from Universal Imaging. By analyzing a large amount of pixels (N=10,000) within these images, a histogram of intensity values was obtained (Adobe Photoshop). Confocal analysis was performed using a Bio-Rad MRC 1024 Confocal Microscope with an MRC 1024 system. Images, z-sections, etc. were collected using LaserSharp software and image analysis was conducted using Confocal Assistant software. The equilibrium swelling behavior of the imprinted gels was studied by weighing dry samples and placing them in a known volume of solution with and without template. The gels were weighed by removing the gels at specific periods of time and blotting with filter paper to remove excess surface solvent.

## RESULTS AND DISCUSSION

We have been successful in synthesizing novel glucose-binding gels based on non-covalent interactions (hydrogen bonding, hydrophobic interactions) formed within polar, aprotic solvent (DMSO).

For AA and Aam functional networks, a bound ratio (amount D-glucose bound/recognitive network/control network) greater than one indicates that glucose was memorized within the gel compared to a randomly polymerized network (bound ratios in water were 3.4 and 5.0 for Aam-PEG200DMA and AA-PEG200DMA networks, respectively). It is important to note that the control polymer will bind some amount of template (i.e., will contain some randomly introduced, properly positioned functional groups). For AA and Aam networks, the choice of DMSO as solvent during polymerization increased the bound ratio compared to aqueous solvents during polymerization (DMSO is aprotic and does not have the ability to be a hydrogen bond donor and interfere with complex formation).

Figure 3 provides a kinetic aqueous binding analysis of glucose-imprinted Aam-PEG200DMA copolymers prepared in DMSO. The recognitive to non-imprinted (control) bound ratio is 3.4, demonstrating the memorization of glucose within the network. Also, the equilibrium binding data was well represented by a linear isotherm at low concentration ranges (i.e., <1 mg/ml D-glucose).

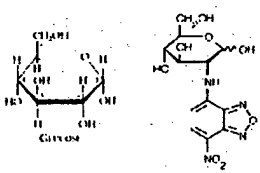


**Figure 2: D-Glucose - Template and Fluorescent Analogue.** Competitive binding results were visualized using a fluorescent glucose analogue 2-(N-(7-nitrobenz-2-oxa-1,3-diazol-4-yl)amino)-2-deoxy-glucose (2-NBDG, Molecular Probes, Inc.). In solution, glucose mutarotates between two conformations: alpha (as shown, 30-35%) and beta (65-70%) position of the carbon 1 hydroxyl group at equilibrium. D-Galactose only differs by the carbon 4 hydroxyl position.

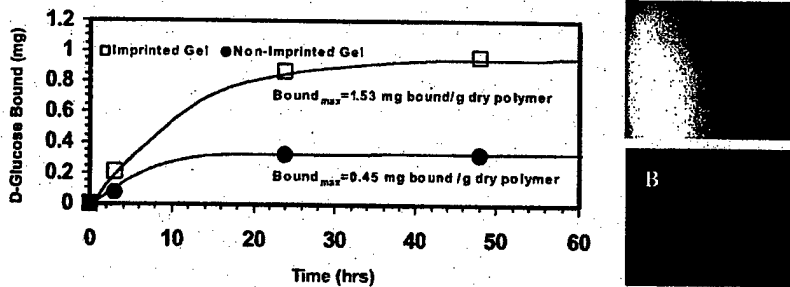


**Figure 3: Kinetic D-Glucose Binding Study in Water.** Acrylamide-PEG200DMA Copolymers of 67% Crosslinking Ratio Prepared in DMSO ( $T=24^{\circ}\text{C}$ ). Fluorescent D-Glucose Analogue Binding in Water. Acrylic Acid-PEG200DMA Copolymers with 67% Crosslinking Ratio Prepared in DMSO. **A:** Recognitive Polymer ( $I=208.84 \pm 6.48$  (10,000 pixels)). **B:** Control Polymer ( $I=36.28 \pm 1.26$  (10,000 pixels)).

Typically, the difference between recognitive and non-imprinted polymer binding values increased as the cross-linking ratio (mole crosslinking monomer/mole total monomers) increased. These results suggest that the use of PEGDMA instead of EGDMA (the average number of ethylene glycol units is 4.5 and 1 for PEG200DMA and EGDMA, respectively) can be beneficial to the diffusional character of the imprinted networks and retain memorized recognition toward template molecules.

For improved analysis of fluorescent intensities, thin polymer discs (diameter, 5.5 mm; thickness, 35  $\mu\text{m}$ ) were prepared. By analyzing fluorescent intensity values from polymer discs of equal thickness, a histogram of intensity values was obtained, which provided quantitative analysis of binding (Table I). This data contains fluorescent profiles from competitive binding analysis of Aam-PEG200DMA copolymers with varying amounts of D-glucose added to a given amount of fluorescent analogue (FITC filter cube, 1/8 integration time, 4x objective). These results were analyzed carefully by matching as many parameters as possible during analysis (excitation time, objective and field of view, camera integration time, etc.). The results demonstrate the effectiveness of fluorescent tracing in relation to a competitive analogue molecule. As glucose concentration is increased and fluorescent analogue is held at constant concentration, the fluorescent intensity of the gel decreases. Thus, glucose competed and filled binding sites once occupied by the fluorescent analogue.

**Table I. Competitive D-Glucose Substrate Binding in Water: Acrylamide-PEG200DMA Copolymers with 67% Crosslinking Ratio (prepared in DMSO).**

Competitive Substrate	Recognitive Intensity	Control Intensity
Fluorescent Analogue Only (Concentration = $F_g$ )	223 $\pm$ 11.81	50.97 $\pm$ 0.77
F. Analogue and Glucose (100 $\times$ $F_g$ )	99.44 $\pm$ 4.36	80.77 $\pm$ 3.95
F. Analogue and Glucose (3,000 $\times$ $F_g$ )	49.81 $\pm$ 1.09	48.85 $\pm$ 0.88
F. Analogue and Galactose (100 $\times$ $F_g$ )	220 $\pm$ 10.10	na
F. Analogue and Galactose (3,000 $\times$ $F_g$ )	209.06 $\pm$ 10.46	na
Fluorescent Analogue Only (PEG only network)	na	56.57 $\pm$ 0.90

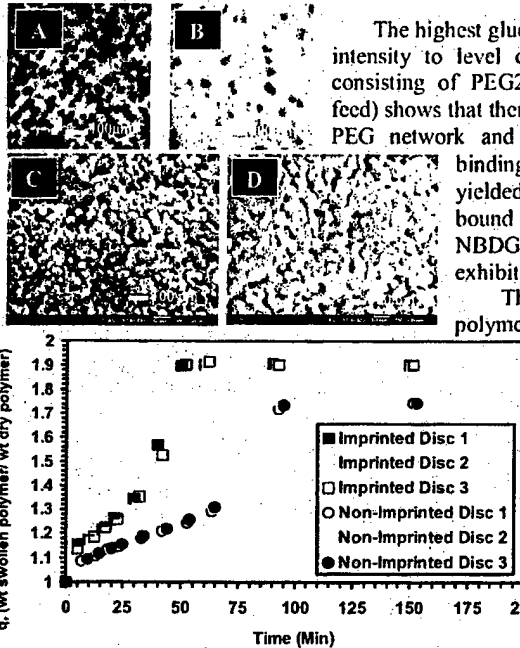


**Figure 4: Dynamic Network Swelling Study in Water and Polymer Morphology via Confocal Microscopy Transmission /FE-SEM. Acrylamide-PEG200DMA Copolymers with 67 % Crosslinking Ratio Prepared in DMSO. A. Recognitive Network. B. Control Network. C. Recognitive FE-SEM D. Control FE-SEM**

degree of translucence. The water swelling tests correlate the properties of the network (homogeneity and porosity) to the imprinting process. Due to the presence of template, the imprinting process resulted in a more porous structure as exhibited by these studies and confocal microscopy/FE-SEM (Figure 4 A, B, C, D).

The formation of a three-dimensional network is a kinetically controlled process that depends on the functionality, reactivity, and concentration of the monomeric components. Traditionally, crosslinking monomers with similar reactivities to the chain building monomer are selected to produce a homogeneous network with spatially even crosslinking density. Differences in the reactivity of the monomers can lead to structural heterogeneity. With imprinting, the template functional monomer complex influences the polymerization conditions and the resulting polymer network. The influence of the complex formation on the resulting network has not been explored and is currently being studied by our group. Polymerization kinetic studies suggest that

The highest glucose ratio ( $3,000 \times F_g$ ) drops the fluorescent intensity to level consistent with control polymer. A gel consisting of PEG200DMA only (i.e., no functionality in feed) shows that there is a low level of interaction between the PEG network and the fluorescent analogue. Competitive binding studies between D-glucose and 2-NBDG yielded conclusive results that D-glucose is bound to this polymer system and not the 2-NBDG fluorophore. AA functionalized networks exhibited similar behavior (Figure 3 A, B).

The selectivity of the Aam-PEG200DMA polymers was determined by varying concentrations of D-galactose added to a constant concentration of D-glucose fluorescent analogue (Table I). The results suggest polymers selective to D-glucose since the fluorescent intensity remained approximately unchanged.

Figure 4 shows dynamic swelling data (without template present) from Aam-PEG200DMA copolymers. The imprinted gels swelled at a faster rate than the non-imprinted gels displaying non-Fickian swelling behavior (i.e., anomalous transport since swelling process is not dominated by the polymer viscoelastic relaxation time or water diffusion) and exhibiting a higher degree of equilibrium swelling. As both systems adsorbed water, the discs became increasingly opaque, with the non-imprinted gels displaying a higher

the template molecule has more than a dilution effect on the polymerization, and the effect of the template is related strongly to the rate of propagation.

### CONCLUSIONS

The studies presented in this paper aid in further understanding and optimizing template-mediated polymerization processes for the production of novel cognitive networks for biologically significant molecules. Based on a biomimetic approach, we have synthesized novel imprinted gel structures for biomolecule recognition. In particular, we have been successful in producing and characterizing cognitive networks for the recognition of D-glucose. Equally important in this endeavor is the potential to produce cognitive networks for a wide range of biomolecules providing hydrogen bonding, hydrophobic, or ionic contributions direct recognition. Thus, these techniques and the resulting polymers can be tailored to recognize a broad range of molecules in aqueous environment. Currently, using similar techniques, our group is producing and optimizing cognitive networks for a variety of drugs and biological molecules, including proteins.

Developments of particular interest are expected to be wide and far reaching and cover a broad range of materials, such as intelligent biomolecule-modulated drug and protein delivery, nano-scale patterning and recognition of biological molecules for diagnostic and therapeutic devices, site or ligand-specific interaction with cells and tissues for targeting applications and tissue engineering, and biosensors.

### ACKNOWLEDGEMENTS

This work was supported by a grant from the National Science Foundation (DGE-99-72770). M.E. Byrne is a NSF IGERT Fellow. We thank J. Sturgis, J.P. Robinson, and D. Sherman of Purdue University for technical assistance, fluorescent microscopy equipment, and SEM, respectively.

### REFERENCES

1. M.E. Byrne, K. Park and N.A. Peppas, *Adv. Drug Deliver. Rev.* **54**, 149 (2002).
2. M.E. Byrne, K. Park, and N.A. Peppas. Non-Covalent Molecular Imprinting of Glucose: Recognition in Aqueous Media. *Society of Molecular Imprinting, 1<sup>st</sup> International Workshop on Molecular Imprinting*, Cardiff, UK, July 5, 2000.
3. M.E. Byrne, J.Z. Hilt, R. Bashir, K. Park and N.A. Peppas, *Trans. Soc. Biomater.* **28**, (2002).
4. D.A. LaVan, D.M. Lynn and R. Langer, *Nat. Rev. Drug Discovery* **1**, 77 (2002).
5. T. Li, H. Lee and K. Park, *J. Biomater. Sci. Polym. Edn.* **9**, 327 (1998).
6. C. Yu, O. Ramstrom and K. Mosbach, *Anal. Lett.* **30**, 2123 (1997).
7. C. Yu and K. Mosbach, *J. Org. Chem.* **62**, 4057 (1997).
8. K. Haupt, "Noncovalent Molecular Imprinting of a Synthetic Polymer with the Herbicide 2,4-Dichlorophenoxyacetic Acid in the Presence of Polar Protic Solvents," *Molecular and Ionic Recognition with Imprinted Polymers, ACS Symposium Series 703*, ed. R.A. Bartsch and M. Maeda (ACS, 1998) pp.135-142.

### Microcontact Printing via a Polymer-Induced Liquid-Precursor (PILP) Process

Yi-yeoun Kim and Lauric B. Gower

Department of Materials Science and Engineering, University of Florida,  
Gainesville, FL, 32611, USA

#### ABSTRACT

Our biomimetic approach for patterned crystallization is based on the combination of the Micro-Contact Printing technique and a novel mineralization process, called the Polymer-Induced-Liquid-Precursor (PILP) process, which enables the deposition of mineral films under low-temperature and aqueous-based conditions. We demonstrate that a liquid-phase mineral precursor is deposited onto specific areas templated with self-assembled monolayers of alkanethiolate on gold, and then the patterned calcitic films grow under constrained conditions via transformation of the PILP phase, leading to control over the location and morphology of calcitic films.

#### INTRODUCTION

The patterning capabilities of inorganic films derived from a biomimetic, bottom-up approach, are of interest in microelectronics and bioelectronics applications that require high performance mechanical, electrical and/or optical properties resulting from controlled nano- and microstructural design. Biomimetic processing techniques are also desirable for biomedical applications that incorporate thermally sensitive components, such as proteins or cells, into devices such as biochips for sensor applications, bioseparations, biocatalysis, and hard-tissue biomaterials. Biological mineralization differs from traditional crystallization in that the crystallization process is mediated with organic materials, leading to a high degree of control over the mineral properties. This occurs through the incorporation of both soluble proteins, which are thought to modulate crystal shape, and an insoluble matrix, which presumably regulates crystal nucleation [1], and enhances the mechanical properties of the bioceramic composite. The performance of synthetic inorganic materials could be significantly advanced by precise control over crystal size, orientation, morphology, and location, as occurs in biominerals; yet rarely can control over all of these properties be accomplished in one synthetic system [2, 3].

We have proposed that a polymer-induced liquid-precursor (PILP) process may play a fundamental role in biominerization (in both vertebrates and invertebrates) [4,5], and if the mechanisms utilized by biominerizing systems can be determined, significant advances could occur in the biomimetics field. In the PILP process, micromolar quantities of acidic polymers are added to the crystallizing solution of an inorganic salt (such as calcite), and the charged polymer sequesters the ions and generates liquid-liquid phase separation. The phase boundaries of the minor phase ultimately define the shape of the final crystal products that form upon solidification and densification of the precursor phase, thus producing a variety of non-equilibrium crystal morphologies [5,6]. The elaborate morphologies and composite structures found in biominerals have long been the envy of the materials engineer. We believe the PILP process offers a relatively simple means for mimicking such structures [7].

In addition to crystal morphology, it is the arrangement of the biominerals within the biopolymer matrix that distinguishes bioceramic composites. The design of complex macromolecular structures to serve as templates presents many challenges with respect to molecular recognition at the organic-inorganic interface due to the flexibility of the organic substrate, and the difficulty in producing patterned structures to serve as templates and matrices. Nevertheless, there have been several studies demonstrating the oriented growth of calcium carbonate crystals on self-assembled monolayers (SAMs), as well as amphiphilic and macromolecular surfaces with functionality designed to interact with the incipient nuclei [8-10]. Thin film formation of calcite by template-mediated nucleation on insoluble and relatively rigid surfaces, such as porphyrin monolayers and chitosan, has also been investigated [1, 11, 12]. Our system differs from these in that both morphological and locational control can potentially be achieved due to the shape retention that occurs when patterning a precursor phase, as opposed to controlled surface nucleation, which relies on strict control of the supersaturation and diffusional distances between patterning elements that create ion depletion zones. In the PILP process, an important distinction in terms of morphological control is that a phase segregated precursor phase can conceivably be manipulated, molded and shaped by a compartment since the precursor is in the form of a moderately viscous liquid which takes the shape of its container. In some ways, the PILP phase is analogous to sol-gel precursors used in the low temperature synthesis of ceramics, for which micromolding techniques have already been demonstrated. The difference here, though, is that the mineral precursor is not a chemical precursor, but rather a physical phase created by ion sequestration by the polyanionic additive; and a chemical by-product is not released via a condensation reaction, but rather the hydration waters are driven off (while still in solution) by the thermodynamic instability of this metastable phase.

Template-mediated nucleation of calcite from solution has provided some insight into the molecular recognition affecting the nucleation of the inorganic crystals on organic substrates. However, template-mediated nucleation of calcite crystals formed via transformation of a precursor phase might be expected to behave in an entirely different fashion than crystals nucleated from solution. The template will likely mediate where the precursor phase deposits (influencing location and morphology), and then how it transforms into the crystalline phase (influencing crystal phase, orientation, and polycrystallinity). Therefore, the influence of organic templates on the PILP process is a primary focus of our current work.

## EXPERIMENTAL

### Patterned Self-Assembled Monolayers (SAMs)

Clean fused silica cover-slips were coated with Au in thickness 500 ~ 1000 Å. (Ti underlayer is used to promote adhesion), using an electron beam evaporator. SAMs were patterned on the Au substrates using the microcontact printing technique [13]. Elastomer stamps were prepared by casting and curing Poly(dimethylsiloxane) (PDMS, SYLGARD 184 (Dow Corning)) against a silicon wafer bearing photoresist patterns formed using conventional photolithographic techniques. The resultant PDMS stamps with relief structures, such as channels and squares, were "inked" with a 1mM solution of surfactant (Mercapto-hexadecanoic acid  $\text{SH}(\text{CH}_2)_{15}\text{COOH}$  in Ethanol) and then printed onto the gold surface for 30-60s. The stamps

then were removed, and the printed substrates were washed with ethanol [8]. In the examples shown here, a follow-up dipping of a second surfactant was not utilized.

#### PILP Crystallization

The crystallization process is as follows: a 12mM  $\text{CaCl}_2 \cdot 2\text{H}_2\text{O}$  (Aldrich) solution was prepared with freshly boiled and cooled distilled water. Substrates, Au-coated cover-slips with patterned surfactants, were placed in a petri dish (3.5 cm diameter) containing a filtered 12mM  $\text{CaCl}_2 \cdot 2\text{H}_2\text{O}$  solution. Micromolar quantities of dissolved acidic polypeptides (poly-L-aspartic acid,  $M_w=8600$ , Sigma) were transferred into the dish by micropipette. The dishes were then covered with stretched parafilm®, punched with 3 needle holes, and placed in a large desiccator. A small vial cap containing crushed ammonium carbonate was also covered with stretched parafilm, punched with 3 needle holes, and placed in the same desiccator. The samples were kept at 4°C (in a refrigerator) or 23°C (room temperature) for 7 days, at which time the cover-slips were removed and gently rinsed with water and ethanol to remove any soluble salts.

The cover-slips were examined by optical microscopy, and then gold coated for scanning electron microscopy on a SEM JEOL JSM 6400 instrument [5].

#### RESULTS AND DISCUSSION

Microscopic examination of the patterned calcite in polarized light microscopy shows that crystallization without the addition of poly-aspartic acid yields rhombohedral-shaped calcite crystals, as expected. Figure 1A shows the traditional solution crystallization of calcite without a SAM template, and Figure 1B shows a linear array of crystallites patterned using a SAM template prepared with a PDMS stamp containing micro-channels. Figures 1C and 1D show that the addition of micromolar quantities of poly-aspartic acid, which induces the PILP process, cause the deposition of patterned *films* of calcite. It should be noted that some small crystalline aggregates are also present due to the incomplete inhibition of solution crystallization. The addition of magnesium ions as additional nucleation inhibitors helps to eliminate some of these undesirable crystal aggregates, but further optimization of the polymeric additive and crystallizing conditions are still needed. Nevertheless, the different effect produced by the presence of poly-aspartic acid is apparent- films, rather than discrete polycrystals, are deposited on the patterned regions of the SAM template. There may be cooperative interplay between the carboxylate groups of the SAMs and the carboxylate groups on the polypeptide, which could be adsorbed onto the surface. However, we believe that the mechanism requires most of the polymer to exist in solution in order to interact with the ions and generate the metastable phase, which then transforms into the crystalline phase. The deposition of precursor, rather than nucleation of crystals, is now dependent upon the functional head groups of the SAM template. The crystal nucleation event subsequently occurs via a precursor transformation mechanism, which is also likely modulated by the template. Regarding the deposition stage, it is not certain at this time whether PILP droplets are depositing onto the patterned regions, or if heterogeneous nucleation of an amorphous precursor phase is occurring, or both.

SAMs have found numerous applications in the realm of biomimicry. Controlled growth of crystals with specific orientation can be achieved via the functional groups on the substrate. In

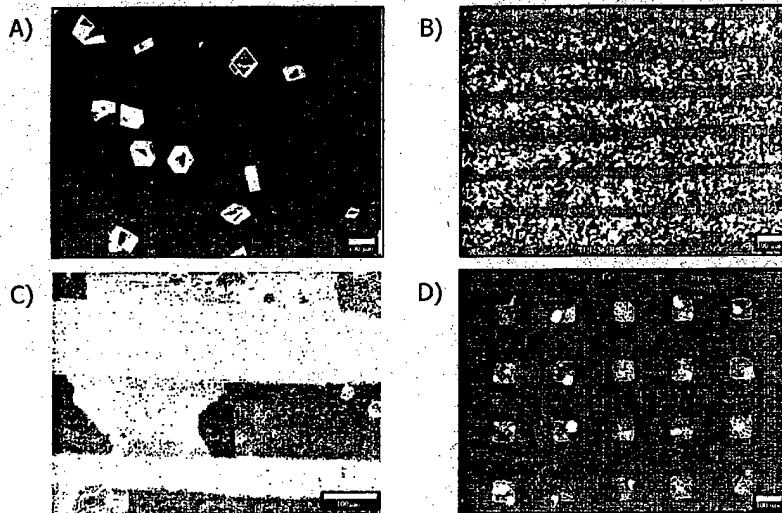


**Figure 1.** Optical micrographs of calcite crystals produced by slowly raising a 12mM  $\text{CaCl}_2$  solution in supersaturation with ammonium carbonate vapor. A) Classical rhombohedral shaped calcite crystals are produced in the control reaction, which does not contain a SAM template or soluble polymeric additive. B) Patterned nucleation of calcite crystals produced with 24mM  $\text{Ca}^{2+}$  deposited onto a SAM template patterned in the form of channels (without soluble polymeric additive). Note- the crystals are smaller here because a higher ion concentration was used, which increased the nucleation density. C) With the addition of 12  $\mu\text{g}/\text{ml}$  Poly-L-aspartic acid, the same channel-patterned SAM directed the deposition of patterned mineral films, using otherwise similar precipitation conditions. D) Likewise, square-patterned calcitic films were produced using 12mM  $\text{Ca}^{2+}$  and 12  $\mu\text{g}/\text{ml}$  Poly-L-aspartic acid. The dark objects in C) and D) are crystal aggregate side-products that form from incomplete inhibition of solution crystal precipitates. Scale bars are 100  $\mu\text{m}$ .

fact, Aizenberg has demonstrated patterned crystallization in conjunction with controlled crystallographic orientation. She suggests that the patterned calcite crystallization could be explained through a direct epitaxy nucleation in terms of diffusion-limited nucleation [9, 10]. Although her experiments demonstrate control over the initial nucleation of crystals, the growth stage is not affected by the template, thus crystal morphology is not regulated.

Figure 2 shows scanning electron micrographs of the patterned films, demonstrating both regions of smooth continuous film, as well as bumpy regions, in which the precursor droplets did not fully coalesce. In Figure 2B, bulges can be seen on the film which appear to be “dewetting” of the SAM/mineral film. Although the surface energetics of the precursor phase have not yet been examined, it has been observed that the substrate upon which these films are deposited can have a pronounced affect on the wetting behavior and adhesiveness of the films (for example, the mineral films adhere well to a glass coverslip, but tend to peel off a polystyrene petri dish).

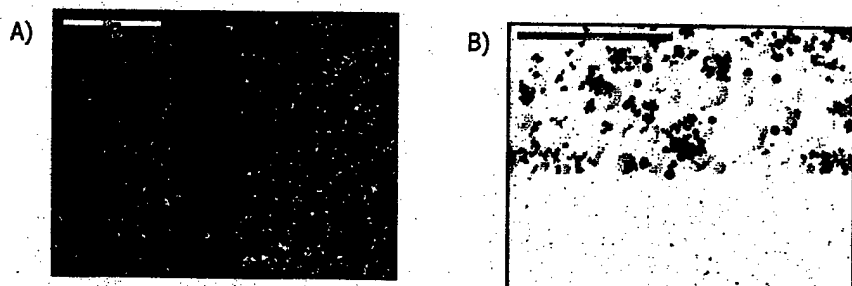


**Figure 2.** Scanning electron micrograph of patterned mineral films. A) Using 12 mM  $\text{Ca}^{2+}$  and 12  $\mu\text{g/ml}$  Poly-acrylic acid, the films appear rough due to PILP droplets which have not fully coalesced. Scale bar = 50  $\mu\text{m}$ . B) At higher magnification, it can be seen that the mineral film is relatively smooth, except for some clusters of calcitic droplets. Bulges are also seen in this film, which appear to be associated with "dewetting" of the film from the SAM substrate. Scale bar = 20  $\mu\text{m}$ .

As we expected, the crystalline films were deposited only on the regions that were functionalized. Reasonably well-defined patterned films of calcite are observed, although the fidelity is not optimal. A primary difficulty we have encountered is the formation of crystal aggregate side-products (which appear to be solution grown crystals, rather than PILP formed crystals). Likewise, no control has been exerted over the nucleation of this precursor phase (i.e. transformation via dehydration and crystallization); therefore, the patches are not always single crystalline if more than one nucleation event occurred, and specific crystallographic phase and orientation have not been addressed. It is anticipated, however, that the nucleation of the precursor phase, although different from nucleation from solution, will be amenable to regulation once the process is better understood. Nevertheless, the patterning of this PILP phase can be seen as being distinctly different than the patterning of solution grown crystals. Thus, our approach has taken the microcontact printing technique one step further, making it possible to provide some level of morphological control in patterning thin-film structures of calcium carbonate, by utilizing the synergistic interplay between a SAM template and a soluble acidic polypeptide. It should be noted that two of the crucial tools utilized in biomimetic mineralization are insoluble templates and soluble acidic proteins. We have used acidic polypeptides, such as poly-L-aspartic acid, to mimic the soluble polyanions found in biominerals, and the patterned SAMs serve the role of insoluble matrix found in biological hard tissues. One can imagine that by controlling the location of the organic template, sequential depositions of PILP phase could enable the fabrication of hierarchical composite structures, as occurs in biomimeticized tissues. A more detailed discussion of the potential relevance of the PILP process to biomimetic mineralization is discussed in more detail in our other reports [4, 7].

## CONCLUSIONS

Micro-scale patterning of calcite films via a polymer-induced liquid-precursor (PILP) process has been achieved using soluble acidic polypeptides, such as poly-L-aspartic acid (or poly-acrylic acid), in conjunction with micro-contact printing techniques. This demonstrates a

---

new strategy for the controlled deposition and patterning of inorganic thin films under benign processing conditions. Our future efforts will be directed at better controlling the precursor formation to eliminate the problem of crystal aggregates and produce patterned films with improved smoothness and higher resolution and reproducibility.

#### ACKNOWLEDGMENTS

We would like to recognize the National Science Foundation NSF "XYZ on a Chip" program (grant BES-9980795) for financial support.

#### REFERENCES

1. L.A. Gower and D.A. Tirrell, *J. Cryst. Growth* **191**, 153-160 (1998).
2. S. Mann, *J. Mater. Chem.* **5**, 935-946 (1995).
3. S. Mann, D.D. Archibald, J.M. Didymus, T. Douglas, B.R. Heywood, F.C. Meldrum, and N.J. Reeves, *Science* **261**, 1286-1292 (1993).
4. M. J. Olszta, E.P. Douglas, L.B. Gower, *Calcified Tissue International* (submitted).
5. L.B. Gower and D.J. Odom, *J. Cryst. Growth* **210**, 719-734 (2000).
6. L. Gower, "The influence of polyaspartate additive on the growth and morphology of calcium carbonate crystals", Dissertation, University of Massachusetts- Amherst (1997).
7. M. J. Olszta, E.P. Douglas, L.B. Gower, *Connective Tissue Research* (in Press).
8. J. Aizenberg, *J. Cryst. Growth* **211**, 143-148 (2000).
9. J. Aizenberg, A.J. Black, and G.H. Whitesides, *J. Am. Chem. Soc.* **121**, 4500-4509 (1999).
10. J. Aizenberg, A.J. Black, and G.M. Whitesides, *Nature* **398**, 495-498 (1999).
11. N. Hosoda and T. Kato, *Chem. Mat.* **13**, 688-693 (2001).
12. G.F. Xu, N. Yao, I.A. Aksay, and J.T. Groves, *J. Am. Chem. Soc.* **120**, 11977-11985 (1998).
13. Y.N. Xia and G.M. Whitesides, *Annu. Rev. Mater. Sci.* **28**, 153-184 (1998).

**Materials for Drug  
and Gene Delivery**

### **The Effects of Charge Separation in Quaternary Ammonium, DABCO-Containing Polymers on In Vitro Toxicity and Gene Delivery**

Theresa M. Reincke<sup>†</sup> and Mark E. Davis\*

Division of Chemistry and Chemical Engineering, California Institute of Technology  
Pasadena, CA 91107, U.S.A.

<sup>†</sup>Current address: Department of Chemistry, University of Cincinnati, Cincinnati, OH 45221-0172, U.S.A.

#### **ABSTRACT**

Polycation materials have recently emerged as promising systems for the delivery of genetic material. In this study, several DABCO (1,4-diazabicyclo[2.2.2]octane) polymers are investigated for their ability to bind and deliver plasmid DNA (pDNA) into mammalian cells. The DABCO polymers are synthesized by copolymerization of DABCO with 1,3-dibromopropane (D3), 1,4-dibromobutane (D4), 1,6-dibromohexane (D6), 1,8-dibromo-octane (D8), and 1,10-dibromodecane (D10) to form a series of quaternary ammonium polymers with increasing charge separation. Gel retardation experiments reveal that each polymer (D3-D10) binds pDNA above a charge ratio of 1.0 (polymer + / pDNA -). The polycations are examined for *in vitro* transfection efficiency and toxicity in BHK-21 cells. Results of the transfection experiments indicate that the D6 polymer had the highest transfection efficiency. Although all of the polymers are shown to have some toxicity, the D8 and D10 polymers are more toxic to BHK-21 cells; approximately 30% of the cells survive at a charge ratio of 5 +/ - as compared to the D3, D4, and D6 polymers where survival rates are about 80%.

#### **INTRODUCTION**

Cationic polymers are currently being studied as alternatives to viral systems for the delivery of therapeutic genes. Advantages of using nonviral delivery vectors over their viral counterparts include low immunogenicity, noninfectivity, and virtually no limit to the size of the foreign gene that these vectors can carry [1-3]. Polycations have the ability to self-assemble with DNA and condense it into small particles that have been denoted as polyplexes. Polyplexes have been shown to deliver DNA into cultured cells through the endocytotic pathway. Several studies on polymeric delivery vectors have indicated that small changes in the structures of polymeric vectors play a significant yet undetermined role in the delivery efficiency and toxicity of these systems [4-7]. For example, previous experiments conducted by our group have indicated that the charge separation in  $\beta$ -cyclodextrin-containing polymers has a considerable effect on both the toxicity as well as the transfection efficiency of the delivery vectors in mammalian cell lines [6]. In the current study, several DABCO-containing polymers with increasing charge separations (Figure 1) have been created to further elucidate the effect of the charge separation within polycation delivery vectors. DABCO-based polymers have been formerly studied for other applications such as structure-directing agents in zeolite synthesis [8,9]. Here, their effectiveness as gene delivery agents is considered.

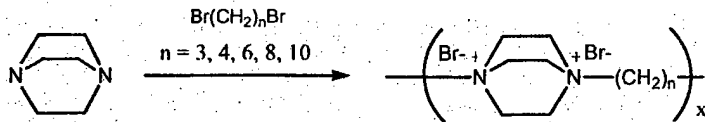


**Figure 1.** The structure of the DABCO polymers used in this study. The separation of the charge centers was varied by 3, 4, 6, 8, and 10 methylene units through copolymerization of DABCO with the corresponding dibromoalkane.

## EXPERIMENTAL DETAILS

### Polymer synthesis

All chemicals used in the synthesis of the polymers were obtained from Aldrich Chemical Company unless otherwise indicated. The polymers were synthesized by the stoichiometric copolymerization of DABCO and the corresponding dibromoalkane (1,3-dibromopropane, 1,4-dibromobutane, 1,6-dibromohexane, 1,8-dibromooctane, or 1,10-dibromodecane) in either dimethylformamide or dimethylsulfoxide and stirred at a temperature between 60°C and 70°C for 24 hours. After 24 hours, each product was purified by pipetting the reaction mixture into a Spectra/Por 1000 MWCO dialysis membrane and exhaustively dialyzing the product in Nanopure water for approximately 48 hours. The dialyzed product was then lyophilized to dryness.

### Polymer Characterization

Polymer molecular weights were determined by static light scattering. The polymers were analyzed on a Hitachi D6000 HPLC system equipped with a ERC-7512 RI detector, a Precision Detectors PD2020/DLS and a PL Aquagel-OH 30 column using 0.8M ammonium acetate pH = 2.8 with formic acid as the eluant at a 0.7 mL/min flow rate. The refractive index increment values were determined at 25°C (633 nm) in the same eluant above.

### Gel Retardation Experiments

Each polymer was examined for its ability to bind pDNA through gel electrophoresis experiments as previously described [10]. 1 µg of pGL3-CV (10 µL of a 0.1 µg/µL in DNase free water) was mixed with an equal volume of polymer at the appropriate charge ratios. Each solution was incubated for approximately 30 minutes. 2 µL of loading buffer was added to each sample and then 10 µL of each sample was pipetted into the wells of a 0.6% agarose gel containing 6 µg of ethidium bromide/100 mL TAE buffer (40 mM Tris-acetate, 1 mM EDTA) and electrophoresed.

### Cell Culture Experiments

Plasmid DNA, pGL3-CV (Promega, Madison WI), containing the luciferase gene under the control of the SV40 promoter was amplified by *Escherichia Coli* strain DH5 $\alpha$  and was then purified using Qiagen's Endotoxin-free Megaprep kit (Valencia, CA). 60 µL of cationic polymer

dissolved in DNase free water (Gibco BRL) was added to 60  $\mu$ L of pDNA (0.1 mg/mL in DNase free water at charge ratios of 5, 10, 15, 20, 25, 30 (polymer + / pDNA -)). The mixtures were incubated for 30 minutes before cell transfection. BHK-21 cells were purchased from ATCC (Rockville, MD) and maintained in Dulbecco's Modified Eagle Medium (DMEM) supplemented with 10% FBS, 100 units/mg penicillin, 100  $\mu$ g/mL streptomycin, and 0.25  $\mu$ g/ml amphotericin at 37°C and 5% CO<sub>2</sub>. Media and supplements were purchased from Gibco BRL (Gaithersburg, MD). BHK-21 cells were plated at 50,000 cells per well in 24 well plates and incubated for 24 hours. Cells were transfected with 1  $\mu$ g of pGL3-CV complexed with each of the polymers above (D3, D4, D6, D8, D10) at the various charge ratios in triplicate in serum free media. After 4 hours, 800 mL of DMEM was added to each well. 24 hours after transfection, the media was replaced with 1 mL of DMEM. 48 hours after transfection, cell lysates were analyzed for luciferase protein activity with results reported in relative light units (RLUs). Toxicities were determined by the Lowry protein assay as previously described [6,10].

## DISCUSSION

### Polymer Synthesis and Characterization

The DABCO polymers were synthesized as previously described through quaternization of the tertiary amines on the DABCO units with the corresponding dibromoalkane [8,9]. As shown in Table 1, the molecular weight values and degrees of polymerizations are all within normal parameters for this class of polymers as determined by static light scattering [8]. The data given in Table 1 show degrees of polymerization for these polymers between 10 and 20 with the D4 polymer having the largest chain length and the D10 polymer having the lowest degree of polymerization.

Gel retardation experiments were completed for each DABCO polymer (D3-D10) and reveal that all polymers bound pDNA (a requirement for cellular uptake) as expected above a charge ratio of 1.0 +/- . An example of this experiment is shown in Figure 2, where the naked pDNA migrates in response to the electric field but when pDNA is bound by the polymer at and above a charge ratio of 1.0, the migration of pDNA is retarded indicating polymer binding. This experiment is a qualitative determination of pDNA binding but does not give quantitative information on polymer binding strength.

**Table 1.** The refractive index increment, molecular weight, polydispersity, and degree of polymerization data for the DABCO based polymers as determined by static light scattering.

Polymer	D3	D4	D6	D8	D10
<b>dn/dc</b>	0.138	0.138	0.138	0.146	0.163
<b>Mw (kDa)</b>	5.10	6.70	4.82	6.44	4.41
<b>Mw/Mn</b>	1.22	1.34	1.22	1.29	1.23
<b>Degree of Polymerization</b>	16	20	14	17	11

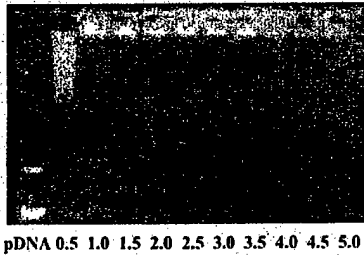


**Figure 2.** Example of gel retardation results. In this experiment, the D4 polymer was tested for binding to pDNA. The numbers, 0.5-5.0, represent the charge ratio (polymer + / pDNA -) used in the analyses. Polymers D3-D10 were all examined similarly, and bound pDNA at and above a charge ratio of 1.0 +/- (electrophoresis results were very similar to what is shown here).

#### **Transfection and Toxicity Experiments**

The polyplexes formed by all of the DABCO polymers are able to transfect BHK-21 cells *in vitro* at several charge ratios. Transfection experiments reveal that the polymers have some toxicity and complete cell death is found above a charge ratio of 20 +/- as determined by the Lowry protein assays. As shown in Figure 3, the D3, D4, and D6 polymers are only slightly toxic at a charge ratio of 5 +/- with cell survivals of approximately 80%, and the D4 gives the lowest toxicity. Polymers D8 and D10 are found to have the highest toxicity at all charge ratios. At a charge ratio of 5 +/-, only 30% of the cells survived for the polymers D8 and D10. This result is inconsistent with what was observed in a previous structure-property study conducted in our lab. Using  $\beta$ -cyclodextrin polymers ( $\beta$ CDPs), the polyplexes formed by the polymer with a charge separation of 8 methylene units had the lowest toxicity [6].

All of the DABCO polyplexes are able to transfect BHK-21 cells with differing degrees of efficiency as determined by luciferase protein activity. As shown in Figure 4, the transfection is the most efficient for all of the polyplexes at a charge ratio of 10 +/- . The highest transfection efficiency is achieved by the D6 system. This result is consistent with the  $\beta$ CDPs in the previously mentioned study where a charge separation of 6 methylene units between the  $\beta$ -cyclodextrin monomers had the highest transfection efficiency in BHK-21 cells.

Although the current study was carried out in order to verify the relationship between charge separation, toxicity, and transfection efficiency, the DABCO based polymers are not ideal models. Even though the charge separation can be modified similar to the  $\beta$ CDPs, using different dibromoalkane spacers, each DABCO polymer contains 2 quaternary ammonium charges closely spaced on the DABCO units as pictured in Figure 1. However, in the  $\beta$ CDPs (Figure 5), the amidine charge centers are spaced far apart by both the  $\beta$ -cyclodextrin monomers as well as by the various lengths of methylene units. These structural differences as well as variations in the water solubility could account for the disagreement in toxicity that was observed between the  $\beta$ CDPs and the DABCO polymers.

#### **CONCLUSIONS**

Many questions remain unanswered regarding the structure-property relationships for polycationic gene delivery vectors. The current study was completed in order to reveal how the

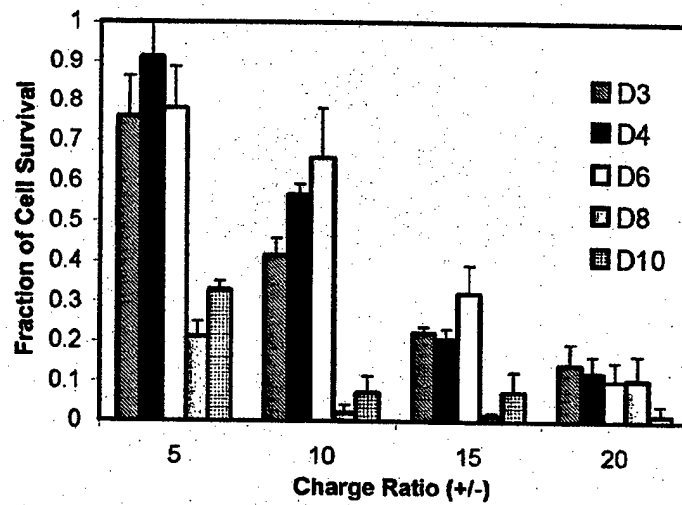


**Figure 3.** Comparison of the relative toxicities of the DABCO polyplexes at charge ratios of 5, 10, 15, and 20 +/- with BHK-21 cells. Cell Survival was determined by assaying for total protein concentration and normalizing each sample with the protein concentration for untransfected cells. The data are reported as a mean  $\pm$  SD of three samples.

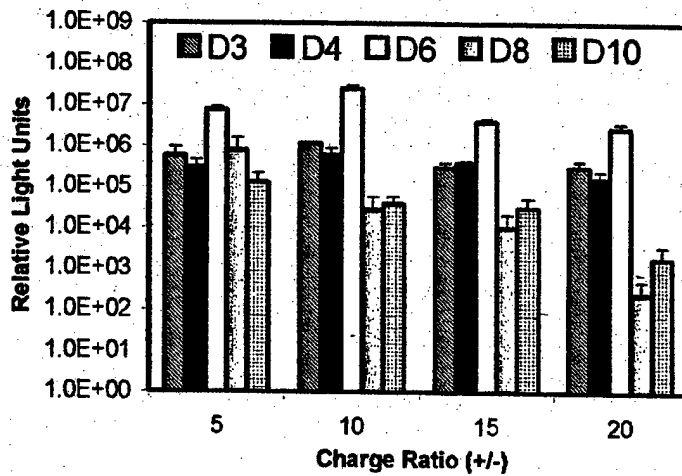


**Figure 4.** Comparison of transfection efficiencies of the DABCO polyplexes at charge ratios of 5, 10, 15, and 20 +/- with BHK-21 cells as determined by luciferase protein activity. Data are presented as a mean  $\pm$  SD of three replicates.

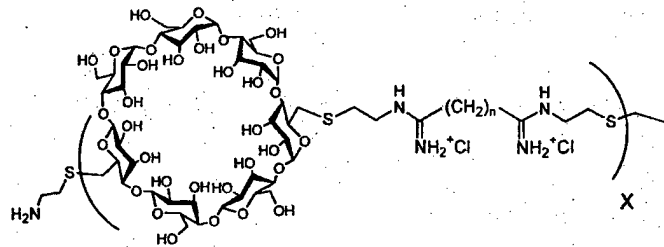


**Figure 5.** The structure of the  $\beta$ CDPs that were studied previously to elucidate structure-property relationships. The charge separation was varied by  $n = 4, 5, 6, 7, 8$ , and 10 methylene units between the amidine charge centers [6].

charge separation in polymeric vectors affects delivery efficiency and toxicity. These experiments also allowed for comparison of previous results regarding structure-property relationships that were examined using  $\beta$ -cyclodextrin polymers [6]. Here, several DABCO polymers were prepared and tested for their ability to bind and deliver pDNA in BHK-21 cells. Results indicated that all of the polymers studied bound pDNA and that the charge separation significantly affected both the transfection efficiency and the toxicity of these systems. The D3, D4, and D6 polymers were shown to have lower toxicity than the D8 and D10 polymers at charge ratios of 5, 10, and 15 +/- . In addition, the D6 polymer was consistently more efficient at gene delivery. This result coincides with previous findings in which the  $\beta$ CDP with 6 methylene units between the charges had the highest delivery efficiency. Further studies are currently being completed that are utilizing other models to more accurately elucidate the structure-property relationships for polycationic gene delivery vectors.

#### ACKNOWLEDGEMENTS

We would like to thank Insert Therapeutics Inc. for partial support of this project. T.M.R. would like to thank the NIH for a National Research Service Award (1-F32 GM64919-01).

#### REFERENCES

1. S. Han, R. I. Mahato, Y. K. Sung, S. W. Kim, *Molecular Therapy* **2**, 302-317 (2000).
2. S. J. Hwang, M. E. Davis, *Curr. Opin. Mol. Ther.* **3**, 183-191 (2001).
3. R. I. Mahato, L. C. Smith, A. P. Rolland, *Adv. Genet.* **41**, 95-156 (1999).
4. P. Ferruti, S. Manzoni, S. C. W. Richardson, R. Duncan, N. G. Pattrick, R. Mendichi, M. Casolaro, *Macromolecules* **33**, 7793-7800 (2000).
5. N. A. Jones, I. R. C. Hill, S. Stolnik, F. Bignotti, S. S. Davis, M. C. Garnett, *Biochim. Biophys. Acta* **1517**, 1-18 (2000).
6. S. J. Hwang, N. C. Bellocq, M. E. Davis, *Bioconjugate Chem.* **12**, 280-290 (2001).
7. M. X. Tang, F. C. Szoka, *Gene Therapy* **4**, 823-832 (1997).
8. R. H. Daniels, G. T. Kerr, L. D. Rollmann, *J. Am. Chem. Soc.* **100**, 3097-3100 (1978).
9. T. Takewaki, L. W. Beck, M. E. Davis, *Micropor. Mesopor. Mat.* **33**, 197-201 (1999).
10. H. Gonzalez, S. J. Hwang, M. E. Davis, *Bioconjugate Chem.* **10**, 1068-1074 (1999).

### Oral Administration of Chemotherapeutic Agents Using Complexation Hydrogels

James Blanchette<sup>1</sup>, Kinam Park<sup>1,2</sup> and Nicholas A Peppas<sup>1,3</sup>

<sup>1</sup> Department of Biomedical Engineering

<sup>2</sup> School of Industrial and Physical Pharmacy

<sup>3</sup> School of Chemical Engineering

Purdue University

West Lafayette, IN, 47907, USA.

#### ABSTRACT

Carriers were synthesized to target delivery of a chemotherapeutic agent, bleomycin, to the upper small intestine in response to the pH shift when entering the upper small intestine from the stomach. Complexation hydrogels capable of pH-responsive swelling were used to form these carriers. Hydrogel nanospheres composed of methacrylic acid (MAA) and poly(ethylene glycol) (PEG) were loaded with bleomycin. Loading of bleomycin was performed by *in situ* polymerization and release of bleomycin from the nanospheres was measured by UV spectrophotometry. Results showed that bleomycin release from the nanospheres was responsive to the pH of the environment surrounding the nanospheres. In addition to pH-responsive release of bleomycin, the hydrogel nanospheres are also able to enhance the permeability of an *in vitro* model of the intestinal epithelium. Increasing the permeability of the intestinal epithelium could aid in transport of bleomycin from the lumen of the small intestine out into the bloodstream.

#### INTRODUCTION

There are numerous potential advantages that oral administration of chemotherapeutic agents has over other methods of administration such as injection [1]. Some of these advantages include increased efficacy, lower toxicity, increased flexibility of dosing schedule and higher patient comfort. Recent studies comparing oral administration of a variety of different chemotherapeutic agents to intravenous administration found decreased toxicity and comparable, if not improved, efficacy [2-4]. The harsh environment of the gastrointestinal tract and the potential toxicity of chemotherapeutic agents requires that our carriers selectively deliver the drugs to a site promising for absorption into the bloodstream with low toxicity. During the development of these carriers, studies have focused on the use of a single chemotherapeutic agent, bleomycin. Bleomycin is a glycopeptidic antibiotic used in chemotherapy for approximately 30 years [5]. In the future, other chemotherapeutic agents will be studied to expand the potential uses for these carriers to include a variety of drugs from different classes of chemotherapeutic agents.

Successful development of the carriers requires fulfillment of a number of requirements. A delivery vehicle capable of being loaded with bleomycin and subsequently releasing it, with attention focused to the efficiency of each process, must first be developed. The pH increase that occurs when passing from the stomach to the upper small intestine is the trigger to initiate release so this carrier must be able to selectively release bleomycin in response to a pH shift used to simulate this physiological event. The kinetics of release from the carrier must be appropriate given the projected residence time for the carrier particles in the region of the digestive tract most suitable for absorption of bleomycin. The final property of our carriers to be analyzed is

the ability to enhance the permeability of an *in vitro* model of the intestinal epithelium as this should aid transport of bleomycin out of the intestinal lumen.

## EXPERIMENTAL DETAILS

### Nanosphere synthesis

Hydrogel nanospheres were formed from a diluted monomer mixture by UV-initiated free radical polymerization. The monomer mixture was composed of MAA (Polysciences, Warrington, PA), poly(ethylene glycol) monomethyl ether monomethacrylate (molecular weight 1000) (PEGMA) (Polysciences), tetraethylene glycol dimethacrylate (TEGDMA) (Polysciences) and Irgacure 184® (1-hydroxy-cyclohexyl-phenylketone (HCPK)) (CIBA-GEIGY, Hawthorne, NY). Prior to use in the reaction, MAA was vacuum distilled at 54 °C and 25 mm Hg to remove the hydroquinone that was used as an inhibitor.

The monomer solution has a 1:1 ratio of MAA to ethylene glycol units. Because the PEGMA has approximately 23 ethylene glycol units to give it a molecular weight of 1000, the molar ratio of PEGMA to MAA is therefore 1:23. A total weight of 2.0 g of PEGMA and 3.6 g of MAA yields the desired ratio and a total of 0.043 moles. For a typical reaction, a TEGDMA concentration of 1.5 mol% was added to the monomer mixture and 0.1 wt% HCPK was added to initiate the reaction.

This concentrated monomer solution was diluted in deionized water to create the working solution that was used to form the hydrogel. The working solution contained 800 µL of concentrated monomer solution for every 100 mL of deionized water. Because oxygen will inhibit the free radical-initiated polymerization, the polymerization was carried out in an oxygen-free environment. To create these conditions, the working solution was sealed with a rubber stopper in an Erlenmeyer flask and nitrogen was bubbled through the solution for 30 minutes. The sealed flask was then exposed to a UV lamp (Efos Acticure™ Ultraviolet/Visible spot cure system, Mississauga, Ontario) providing an intensity of 45 mW/cm<sup>2</sup> for 15 minutes.

The polymerization yielded a suspension containing hydrogel nanospheres. This nanosphere suspension was then washed where noted. The washing procedure involved placing the nanosphere suspension in a cellulose dialysis membrane with a molecular weight cut-off of 25,000 (Spectra Por® 7, Spectrum Laboratories Inc., Rancho Dominguez, CA) and then placing this membrane in a low pH (pH = 2.0) bath. The washing duration was typically 10 min.

After the wash was completed, the suspension was removed from the dialysis membrane, placed in a 50 mL conical tube and frozen for at least 24 h at -20 °C. To obtain the hydrogel nanospheres, the frozen solution was lyophilized at -50 °C under vacuum (Labconco Model 77500, Kansas City, MO) until only the dry nanospheres remained.

### Bleomycin loading

Bleomycin loading into the hydrogel carriers was achieved through *in situ* polymerization. Bleomycin was dissolved in the deionized water used to dilute the concentrated monomer solution prior to nitrogen purge at concentrations ranging from 0.01 – 0.05 mg/mL. As the poly(methacrylic acid) grafted with poly(ethylene glycol) (P(MAA-g-EG)) nanospheres form in the monomer solution, some of the bleomycin becomes trapped within the nanospheres.

The efficiency of bleomycin loading was measured by UV spectrophotometry (Perkin Elmer Model Lambda 10, Norwalk, CT). Bleomycin was diluted at various concentrations ranging from 0.001 to 0.1 mg/mL and the relation between the absorbances of these solutions at 300 nm and the bleomycin concentration was determined. Using the intensity of the absorbance at 300 nm, the amount of bleomycin incorporated into the nanospheres during polymerization was measured.

Before placing the samples in the UV spectrophotometer, the samples were run through a filter using a syringe (Monoject®, Sherwood Medical, St Louis, MO) attached to a 0.2  $\mu$ m nylon filter. Because the absorbance for bleomycin is in the UV range, quartz cuvettes were used with a sample volume of 2mL added to the cuvette. Samples are scanned over a range of wavelengths and the intensity at 300 nm is used to determine the bleomycin concentration present.

#### **Release studies**

Release experiments were performed with a dissolution apparatus (Distek model 2100B, North Brunswick, NJ). Bleomycin-loaded nanospheres were added to a vessel containing 100 mL of solution stirred at 100 rpm and maintained at 37 °C. For release studies done at a constant pH, 3 mL samples were taken from the release vessel, filtered through the 0.2  $\mu$ m filter and stored for later analysis by UV spectrophotometry. The 3 mL of solution removed was replaced with solution of the appropriate pH and this loss of initial solution is accounted for in later analysis. Studies done at high pH were done in a phosphate buffered saline (PBS) solution at a pH of 7.4. Both studies were carried out for a duration of 90 minutes.

To better simulate the environment of the gastrointestinal tract, some studies were done with a pH shift from low to high to better mimic the passage from the stomach into the duodenum. For these studies, the initial solution was again hydrochloric acid diluted in water to a pH of 2.0. After a period of 60 minutes, 5M NaOH and PBS were added to raise the pH to 7.0 and samples were taken for an additional 120 minutes. The necessary volume of NaOH and PBS to raise the pH of the vessel from 2.0 to 7.0 was determined prior to the release experiment with the same solutions to be used in the release experiment.

The time points at which samples were taken were close together at the beginning of the experiment and again after the pH increase to measure the release initially and after nanosphere swelling. As with the constant pH release experiments, the absorbance of all samples at 300 nm was measured by UV spectrophotometry to measure the bleomycin concentration in the release vessel.

#### **Transepithelial electrical resistance (TEER) measurements**

Caco-2 cells (human colon adenocarcinoma) were seeded on Transwell® plates at low density and allowed to grow and differentiate over the course of 21-24 days. Hank's Balanced Salt Solution (HBSS) (Hyclone South Plainfield, NJ) was added to the cells 1 hour before the TEER measurements are taken to allow the cells to equilibrate. P(MAA-g-EG) nanospheres, with no bleomycin loaded, were added to the apical side of the well at different concentrations ranging from 5-20 mg/mL and TEER measurements were taken with a 2 prong electrode (EVOM, World Precision Instruments, Sarasota, FL) over the course of 2 hours. While the measurements were being taken, the cells were placed on a heating mat to maintain the

temperature at 37 °C as the resistance value is exponentially related to the temperature. Control cells remained in HBSS without any nanospheres.

## RESULTS

### Nanosphere synthesis and bleomycin loading

Formation of the nanospheres was dependent on the ratios of the components used in the monomer mixture, the exposure time to the UV light and the conditions of the low pH wash. Increasing the amount of crosslinking agent and extending the duration of either the UV exposure or the low pH wash led to agglomeration of the nanospheres rather than formation of a homogeneous suspension. Dissolution of bleomycin within the concentration range given did not inhibit the formation of nanospheres. The loading efficiency of the *in situ* polymerization was found to be 76% (+/- 9% n=3).

### Release studies

Release studies done at a constant pH showed more release of bleomycin from nanospheres at high pH. These results were anticipated, as bleomycin should pass more readily from the nanospheres in a swollen state. The maximal release occurred after 90 minutes for both pH values with the release at pH 2.0 only 45% of that observed at pH 7.4 ( $M_t/M_\infty = 0.442 +/- 0.115$  n=3). These experiments were performed with nanospheres that had not been washed at a low pH prior to lyophilization. The crosslinking density of these nanospheres was also lower than that given in the nanosphere synthesis protocol as only 0.75 mol% TEGDMA was used. Changes to the nanosphere synthesis protocol, matching the conditions listed above, were made to reduce the amount of bleomycin released at low pH and improve the release kinetics at the high pH.

Experiments where the pH was shifted during the release experiment were used to better simulate the *in vivo* environment when passing from the stomach into the small intestine. Results showed some release occurring at the low pH used to simulate the gastric pH with the remaining bleomycin released after the pH was raised. The results of the bleomycin release studies done with the pH change are shown in Figure 1. Release of bleomycin at pH 2.0 quickly reached values of approximately 25% of the total release with a plateau established before the pH increase ( $M_t/M_\infty$  at 60 min =  $0.268 +/- 0.030$  n=3). The residence time in the upper small intestine was estimated as 2 hours and release of bleomycin was controlled over this duration.

### TEER studies

P(MAA-g-EG) nanospheres were added to the apical side of a Caco-2 monolayer with the concentration ranging from 5-20 mg/mL. The effect of the nanospheres on the electrical resistance across the Caco-2 monolayer was measured for a duration of 2 hours. Initial studies have shown a decrease in resistance, indicating an increase in permeability, for those cells treated with the nanospheres relative to control cells. The results of these studies are shown in Figure 2. The largest decrease in resistance was seen for the highest concentration of nanospheres, 20 mg/mL, with a maximal decrease of 55% relative to the control cells.

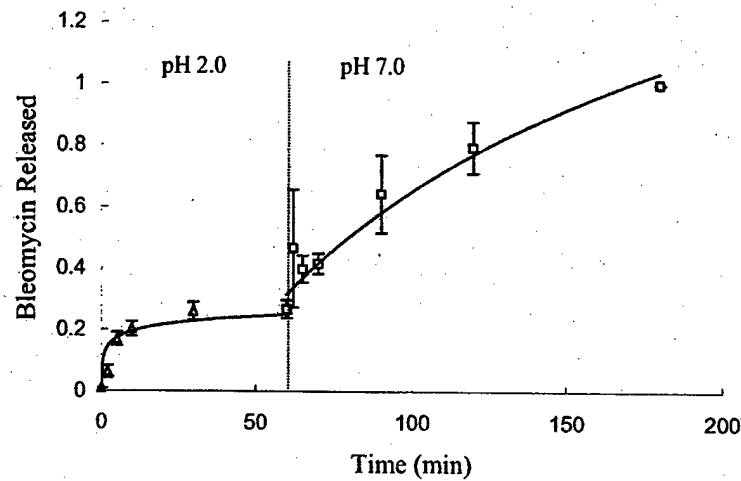


Figure 1: Bleomycin release, expressed as  $M_t/M_0$ , over three hours in a release vessel. The pH of the vessel was changed from 2.0 to 7.0 after 60 minutes to simulate passage from the stomach into the small intestine.

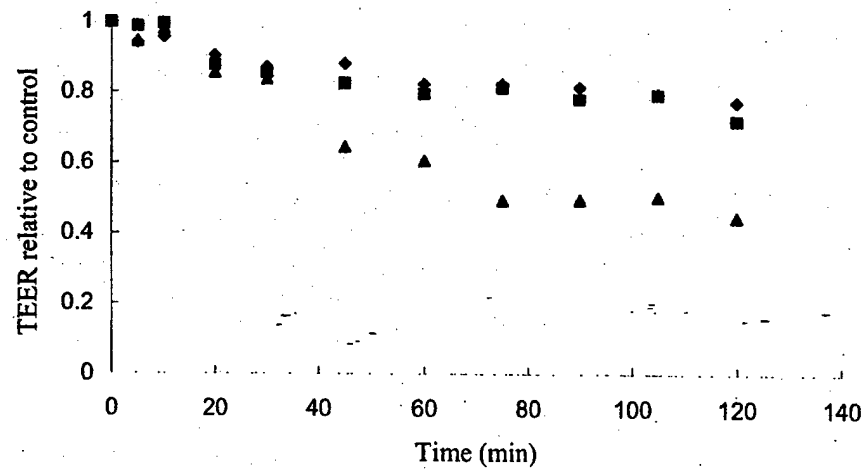


Figure 2: The value of the transepithelial electrical resistance of Caco-2 monolayers over two hours. Three different concentrations of P(MAA-g-EG) nanospheres were used, 5mg/mL (diamond), 10 mg/mL (square) and 20 mg/mL (triangle). The TEER value is given relative to the value for control cells at the same time.

## CONCLUSIONS

The studies completed show the ability to form P(MAA-g-EG) nanospheres in the presence of bleomycin resulting in loading of bleomycin by *in situ* polymerization. The pH-responsive decomplexation and swelling of these nanospheres can be used to selectively release bleomycin in response to a pH shift similar to that seen when passing from the stomach to the upper small intestine. The nanospheres are also able to increase the permeability of an *in vitro* model of the intestinal epithelium, which could aid in transport of bleomycin out of the intestinal lumen and therefore increase the bioavailability.

## REFERENCES

1. A. Sparreboom, M.J.A. de Jonge and J. Verweij, *Eur J Cancer* **38**, 18-22 (2002).
2. M. Gori, A. Oza, G. Rustin, J. Malfetano, H. Calvert, D. Clarke-Pearson, J. Carmichael, G. Ross, R.A. Beckman and S.Z. Fields, *Eur J Cancer* **38**, 57-63 (2001).
3. J. von Pawel, U. Gatzemeier, J.L. Pujol, L. Moreau, S. Bildat, M. Ransom, G. Richardson, C. Steppert, A. Riviere, I. Camlett, S. Lanc and G. Ross, *J Clin Oncol* **19**, 1743-9 (2001).
4. P.M. Hoff, R. Ansari, G. Batist, J. Cox, W. Kocha, M. Kuperminc, J. Mauron, D. Walde, C. Weaver, E. Harrison, H.U. Burger, B. Osterwalder, A.O. Wong and R. Wong, *J Clin Oncol* **19**, 2282-92 (2001).
5. H. Umezawa, K. Maeda, T. Takeuchi and Y. Okami, *J Antibiot (Tokyo) Ser A* **19**, 200-9 (1966).

## **Tissue Engineering II**

### Poly(glycerol sebacate) — A Novel Biodegradable Elastomer for Tissue Engineering

Yadong Wang,<sup>1</sup> Barbara J. Sheppard,<sup>2</sup> Robert Langer<sup>1</sup>

<sup>1</sup>Department of Chemical Engineering and <sup>2</sup>Division of Comparative Medicine,  
Massachusetts Institute of Technology, Cambridge, MA 02139, U.S.A.

#### ABSTRACT

Biodegradable polymers have significant potential in biotechnology and bioengineering. However, for some applications, they are limited by their inferior mechanical properties and unsatisfactory compatibility with cells and tissues. A strong, biodegradable, and biocompatible elastomer could be useful for fields such as tissue engineering, drug delivery, and *in vivo* sensing [1,2]. We designed, synthesized, and characterized a tough biodegradable elastomer from biocompatible monomers. This elastomer forms a covalently crosslinked three-dimensional network of random coils with hydroxyl groups attached to its backbone. Both crosslinking and the hydrogen bonding interactions between the hydroxyl groups likely contributes to the unique properties of the elastomer. *In vitro* and *in vivo* studies show the polymer has good biocompatibility. Subcutaneous (SC) polymer implants are absorbed completely within 60 days with restoration of the implantation sites to their normal architecture.

#### INTRODUCTION

The current surge of research in tissue engineering (TE) underlines the urgent need for novel biomaterials designed specifically for TE. The current benchmark biodegradable polymer is polyglycolide, polylactide, and their copolymer poly(glycolide-*co*-lactide) (PLGA). These polymers were originally designed for biodegradable sutures, and have a number of drawbacks for applications in TE: (1) inferior physical property — they are rigid and brittle; (2) heterogeneous degradation — they often lose mechanical strength and crack in the early stage of degradation; (3) limited affinity for cells — they often require surface modification for wettability and cell attachment; (4) fibrous encapsulation — often an avascular fibrous capsule forms around the implant [3-6]. Here we show a novel elastomeric and strong biodegradable polymer with high affinity for cells and excellent biocompatibility.

#### EXPERIMENTAL DETAILS

**Synthesis and characterization of the polymer.** The polymer was synthesized by polycondensation of glycerol and sebamic acid. KBr pellet of newly prepared polymer was used for FTIR analysis on a Nicolet Magna-IR 550 spectrometer. DSC is measured by Perkin-Elmer DSC differential scanning calorimeter. Elemental analysis on vacuum-dried samples was performed by QTI Inc. Water-in-air contact angle was measured at room temperature using the sessile drop method and an image analysis of the drop profile with VCA2000 video contact angle system on slabs of polymer fixed on glass slides.

**Mechanical properties.** Tensile tests were performed on six 25x5x0.7 mm polymer strips cut from polymer sheets according to ASTM standard D 412-98a on an Instron 5542 mechanical tester equipped with a 50 N load cell. Deflection rate was kept at 50 mm/min. The samples were elongated to failure.

**In vitro degradation.** Slabs of dry polymer (5x5x2 mm) were weighed and transferred to 15 ml centrifuge tubes filled with PBS. After 60 days, the samples were removed and washed with D.I. water. The surface water was removed by Kimwipe, and the samples were weighed after drying.

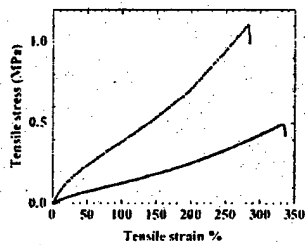


**Figure 1.** Stress strain curves of PGS (solid line), vulcanized rubber (dashed line). Both PGS and vulcanized rubber are marked by low modulus and large elongation ratio, indicating elastomeric and tough materials.

at 40 °C in an oven for 7 days. The degree of degradation was determined by dry weight change. **In vitro biocompatibility.** Nine glass petri dishes (60mm diameter) were coated with 1,3-dioxolane solution of the prepolymer (1%). The coated dishes were transferred into vacuum oven after evaporation of the solvent in air. The prepolymer was crosslinked into the elastomer after 24 hr. at 120 °C and 120 mTorr. Nine control dishes were coated with 1%  $\text{CH}_2\text{Cl}_2$  solution of PLGA (50:50, carboxyl ended, MW 15,000), and the solvent was evaporated in 24 hr in air. The coated dishes were sterilized by UV radiation for 15 min. Each dish was soaked in growth media for 4 h, replaced with fresh media and soaked for 4 h before cell seeding to remove any unreacted monomers or residual solvents. Each dish was seeded with 100,000 NIH 3T3 fibroblast cells and 8 ml of growth medium. The cells were incubated at 37 °C with 5%  $\text{CO}_2$ . Cell density was measured by MTT assay [7]. Media exchange was performed every 48 h. At day 6, phase contrast images were taken for both the polymer wells and the control wells on a Zeiss Axiovert 200 microscope equipped with a Dage 240 digital camera.

**In vivo biocompatibility.** Autoclaved PGS slabs of approximately 6x6x3 mm, and ethylene oxide sterilized PLGA disk (2 mm thick, 12.5 mm diameter) were implanted SC. in 15 seven-week-old female Sprague-Dawley rats (Charles River Laboratories) by blunt dissection under deep isoflurane/ $\text{O}_2$  general anesthesia. The surface area/volume ratio were kept the same for both PGS and PLGA implants. Two implants each of PGS and PLGA were implanted symmetrically on the upper and lower back of the same animal. Every implantation site was marked by 2 tattoo marks 2 cm away from the implantation center. The animals were randomly divided into 5 groups. At each predetermined time point, one group of rats was sacrificed, and

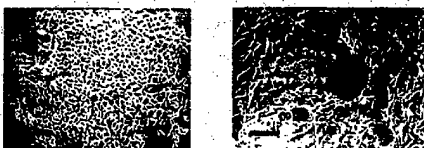


**Figure 2.** Comparison of NIH 3T3 fibroblast cell morphology and number in PGS sample wells (left) and PLGA control wells (right) 6 days after seeding. The PGS wells had more adherent cells and the cell morphology appeared normal, while those in the control well adopted a long thin thread like shape. Scale bar = 200  $\mu\text{m}$ .

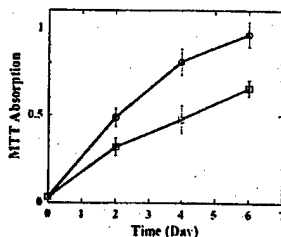


**Figure 3.** Comparison of growth rate of NIH 3T3 fibroblast cells in PGS (○) wells and PLGA (□) wells. MTT absorption measured at 570 nm, normalized value shown.

tissue samples ( $\sim 15 \times 15$  mm) surrounding the implants were harvested with the intact implant. The samples were prepared by standard methods.

## RESULTS AND DISCUSSION

PGS features ester cross-links and hydroxyl groups directly attached to the backbone [8]. The C=O stretch at  $1740\text{ cm}^{-1}$  in Fourier transformed infrared (FTIR) spectrum confirms the formation of ester bonds. FTIR also shows an OH stretch at  $3448\text{ cm}^{-1}$ , which reflects the presence of hydrogen bonded hydroxyl groups in the molecule. Elemental analysis confirms the composition of PGS as approximately 1 glycerol:1 sebatic acid. PGS is very hydrophilic due to the hydroxyl groups attached to its backbone. The water contact angle of PGS is  $32^\circ$ . Since PGS is hydrophilic by nature, unlike PLGA, surface modification is unnecessary to make it wettable.

Appropriate cross-link density renders PGS elastomeric and tough. Tensile tests on PGS strips reveal a stress-strain curve characteristic of a soft and strong material (Fig. 1). The shape of the stress-strain curve is similar to that of vulcanized rubber [9] and tendon [10]. In the elongation test, the samples can be elongated repeatedly up to at least 300% of its original length without rupture. The total elongation is unknown, as grip breaks occurred at about  $267 \pm 59.4\%$  strain. Compression tests indicate that the material can be compressed up to 70% repeatedly without rupture.

PGS also appears to be biocompatible both *in vitro* and *in vivo*. NIH 3T3 fibroblast cells were seeded homogeneously on PGS coated glass petri dishes with PLGA coated dishes as controls. The cells in PGS sample wells are viable and showed normal morphology with higher growth rate than the control, as tested by MTT assay [11] (Fig. 2A, Fig. 3). Cells in PLGA wells tend to form clusters, and the number of floating cells are higher, furthermore, most of the attached cells adopted a long thin thread-like morphology (Fig. 2B). These experiments suggested that PGS is at least as biocompatible as PLGA *in vitro*.

SC implantation in Sprague-Dawley rats was used to compare the *in vivo* biocompatibility of PGS and PLGA. These PGS and PLGA implants have the same surface area/volume ratio ( $1.33 \pm 0.04$ ). Both PGS and PLGA samples were implanted symmetrically on the back of the same animal. The inflammatory responses subsided with time for both polymer implants. In the first three weeks, the inflammatory response of PLGA implantation sites were about 16% thinner than that of PGS (Fig. 4). The thickness of the inflammatory zone in both implantation sites were approximately the same at week 4 and 5. Fibrous capsules surrounding PLGA

implants developed within 14 days, and their thickness hovered around 140  $\mu\text{m}$ . Collagen deposition did not appear around PGS implants until 35 days. The collagen layer was highly vascularized and was only about 45  $\mu\text{m}$  thick. The inflammatory response and fibrous capsule

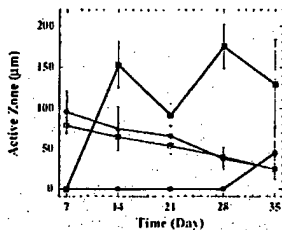


**Figure 4.** Change of thickness of the immune responses with time for PGS and PLGA. The inflammatory response decreased with time for both polymers, which had similar inflammatory zone thickness. While the thickness of fibrous capsules surrounding PLGA was consistently and significantly larger than that of PGS. Inflammatory zone: PGS, ○, PLGA, □; fibrous capsule: PGS, ●, PLGA, ■.

formation observed for PLGA is similar to those reported in the literature[12,13]. Thick fibrous capsules block mass transfer between the implants and surrounding tissues, which can impair implant functions. In an *in vivo* study with PGS alone, the SC implantation sites were undetectable despite repeated sectioning of the specimens at multiple levels in 60 days (2 implantation sites each in 3 animals). The implants were completely absorbed without granulation or scar tissues, and the implantation site was restored to its normal histological architecture. Overall, the inflammatory response of PGS is similar to that of PLGA. However, unlike PLGA, PGS barely induces any significant fibrous capsule formation.

The degradation characteristics of PGS are examined both *in vitro* and *in vivo*. Agitation for 60 days in phosphate buffered saline solution (PBS) at 37 °C causes PGS to degrade 23%. In fetal bovine serum (FBS), the degradation is 39% under the same conditions. The degradation rate is the slowest for PBS, faster for FBS, and fastest *in vivo*. This suggests that enzyme degradation occurred in the latter two cases, and the action of macrophages in the body causes PGS to degrade even faster. The PGS explants maintain their square shape and sharp edges up to at least 31 days. Furthermore, preliminary test of the explants with a nano-indenter indicates that the decrease of mechanical strength parallels that of the mass. Both suggest PGS most likely undergoes surface erosion.

## CONCLUSIONS

Compared with existing biodegradable elastomers, PGS appears to be tougher, inexpensive, and more flexible. In the models tested, the material is biocompatible both *in vitro* and *in vivo*. The polymer's properties, such as hydrophilicity, degradation rate and pattern can potentially be tailored by grafting hydrophobic moieties to the hydroxyl groups[14,15]. To further control or regulate polymer interaction with cells, biomolecules could be coupled to the hydroxyl groups or integrated into the polymer backbone[16-18].

## ACKNOWLEDGEMENTS

The authors thank Dr. David LaVan and Dr. Daniel Anderson for advice and discussions. This work was supported by NIH grant 5-R01-HL60435-02.

## REFERENCES

1. N. A. Peppas & R. Langer. *Science* **263**, 1715-1720 (1994).
2. R. Langer. *AIChE J.* **46**, 1286-1289 (2000).
3. R. F. Storey, S. C. Warren, C. J. Allison & A. D. Puckett. *Polymer* **38**, 6295-6301 (1997).
4. E.-S. Park, M. Maniar & J. C. Shah. *J. Controlled Release* **48**, 67-78 (1997).
5. J. M. Anderson & M. S. Shive. *Adv. Drug Deliv. Rev.* **28**, 5-24 (1997).
6. J. M. Anderson. *Eur. J. Pharm. Biopharm.* **40**, 1-8 (1994).
7. M. B. Hansen, S. E. Nielsen & K. Berg. *J. Immunol. Methods* **119**, 203-210 (1989).
8. Rigid, totally crosslinked polymer has been synthesized from glycerol and sebacic acid (glycerol/sebacic acid molar ratio: 2/3) under different conditions. See: Nagata, M., *et al.* Synthesis, characterization, and enzymatic degradation of network aliphatic copolymers. *J. Polym. Sci., Part A: Polym. Chem.* **37**, 2005-2011 (1999).
9. K. Nagdi. *Rubber as an Engineering Material: Guideline for Users* (Hanser, Munich, 1993).
10. P. Fratzl *et al.* *J. Struct. Biol.* **122**, 119-122 (1998).
11. S. J. Northup & J. N. Cammack. in *Handbook of Biomaterials Evaluation* (ed. von Recum, A. F.) 325-339 (Taylor & Francis, Philadelphia, 1999).
12. J. A. Cadee, L. A. Brouwer, W. den Otter, W. E. Hennink & M. J. A. Van Luyn. *J. Biomed. Mater. Res.* **56**, 600-609 (2001).
13. M. van der Elst, C. P. A. T. Klein, J. M. de Blieck-Hogervorst, P. Patka & H. J. T. M. Haarman. *Biomaterials* **20**, 121-128 (1999).
14. K. N. Jayachandran & P. R. Chatterji. *Eur. Polym. J.* **36**, 743-749 (2000).
15. A. Laschewsky, E. D. Rekai & E. Wischerhoff. *Macromol. Chem. Phys.* **202**, 276-286 (2001).
16. D. A. Barrera, E. Zylstra, P. T. Lansbury, Jr. & R. Langer. *J. Am. Chem. Soc.* **115**, 11010-11011 (1993).
17. J. L. West & J. A. Hubbell. *Macromolecules* **32**, 241-244 (1999).
18. B. K. Mann, A.-S.-Gobin, A. T. Tsai, R. H. Schmedlen & J. L. West. *Biomaterials* **22**, 3045-3051 (2001).

### Honeycomb Films of Biodegradable Polymers for Tissue Engineering

Takehiro Nishikawa, Keiko Arai, Junko Hayashi, Masahiko Hara, and Masatsugu Shimomura  
Spatio-Temporal Function Materials Research Group,  
The Institute of Physical and Chemical Research (RIKEN),  
Hirosawa 2-1, Wako, Saitama, 351-0198, JAPAN.

#### ABSTRACT

We report that microporous films (honeycomb films) can lead various types of cells to tissue formation. The honeycomb films were fabricated by applying a moist air to a spread polymer solution containing biodegradable polymers (poly(L-lactic acid) (PLLA) and poly( $\epsilon$ -caprolactone) (PCL)) and an amphiphilic polymer. Hepatocytes were cultured on a self-supporting honeycomb film of PLLA. The hepatocytes formed a single layer of columnar shape cells with a thickness of 20  $\mu$ m. The tissue formation of hepatocytes specifically occurred on the honeycomb film of PLLA, not on a flat film of PLLA. Three dimensional tissue structures were formed, when cells were cultured on both sides of the self-supporting honeycomb film. Double layers of hepatocytes were obtained by the method. Striated tissues such as heart and blood vessel could be reconstructed by utilizing a stretched honeycomb film of PCL.

#### INTRODUCTION

The tissue engineering is a technology for reconstruction of living tissues. Various matrices such as gels and porous materials have been developed to realize ideal tissue formation [1]. Matrix surface, so called "bio-interface" is an important place where cells are initially attached, because the cell-matrix interaction significantly influences the subsequent cell-cell interactions [2]. In this sense, the bio-interface should be designed to cause proper cell adhesion. It is well known that surface chemistry and surface morphology are two major points to note for the design of bio-interface [3-5]. The bio-interface to be issued in this report is a microporous film of degradable polymers. Honeycomb films are microporous films of polymers which are formed spontaneously by evaporating a polymer solution in a humid atmosphere [6]. We report the honeycomb films of degradable polymers, the control of cell spreading and cell alignment on the honeycomb films, and the application of the honeycomb films to three-dimensional cell culture system.

#### EXPERIMENTAL DETAILS

##### Fabrication of honeycomb films

Honeycomb films are formed, when moist air (75% r.h. at 20°C) is applied to a droplet of polymer solution spread onto water surface. Solutions containing 1 g/L of degradable polymers ((poly(L-lactic acid): Sigma, (PLLA: Figure 1 (a)) and poly( $\epsilon$ -caprolactone): Birmingham Polymers, Inc., (PCL: Figure 1 (b))) and 0.1 g/L of an amphiphilic polymer (Figure 1 (c)) were prepared for the film fabrication. Benzene was utilized as a solvent for the amphiphilic polymer and PCL. Chloroform was utilized as a solvent for PLLA. One hundred  $\mu$ L of the

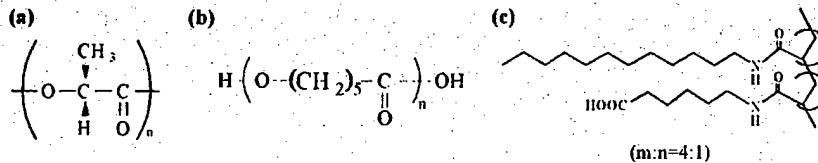


**Figure 1** Polymers used for the preparation of honeycomb films. (a) poly(L-lactic acid) (PLLA). (b) poly( $\epsilon$ -caprolactone) (PCL). (c) amphiphilic polymer.

polymer solution was spread onto the water surface in a  $\phi$ 9 cm petri-dish and evaporated by blowing the moist air at 1200 mL/min. A polymer film floating on the water surface was transferred onto a hole that was punched in a 15 mm  $\times$  15 mm of Teflon plate. Honeycomb films of PCL were stretched uniaxially with the both ends of the floating films gripped by a pair of tweezers. The honeycomb films were observed by scanning electron microscopy (S-3500N, Hitachi). For cell culture experiment, the honeycomb films were sterilized by exposing to ethylene oxide gas at 40°C.

#### Cell culture experiment

Hepatocytes (HEPs) were isolated from rat liver (male Wistar rats of 8 weeks old; Japan SLC, Inc) by modified Seglen's perfusion method [7]. HEPs were cultured with a Williams' E medium containing dexamethasone (1  $\mu$ M, Sigma), ascorbic acid (0.28 mM, Sigma), insulin (0.57 mg/L, Sigma), epidermal growth factor (0.02 mg/L, Sigma), gentamicin (48 mg/L, Schellingplau), and aprotinin (5000 KIU/L, Sigma). Cardiac myocytes (CMYs) were isolated by enzyme treatment of minced heart tissues of 19-day rat embryos (Sprague Dawley rats; Japan SLC, Inc) [8]. CMYs were cultured with a Hepes-buffered Hams F10 medium containing 0.5 % insulin-transferrin-selenium-X (Gibco) and 3 % fetal calf serum (Gibco). Bovine aortic endothelial cells (ECs) and smooth muscle cells (SMCs) were purchased as cryopreserved samples from BioWhittaker. After the frozen cells were thawed at 37°C, the cells were resuspended into a supplemented culture medium (SmGM-2; BioWhittaker). ECs and SMCs were cultured with the supplemented medium. HEPs were cultured on a one side or both sides of honeycomb film and flat film of PLLA at the density of  $1.0 \times 10^5$  cells/cm $^2$ . CMYs were cultured on both sides of a stretched honeycomb film of PCL at the density of  $1.0 \times 10^5$  cells/cm $^2$ . ECs and SMCs were co-cultured by seeding SMCs on one side of a stretched honeycomb film and then seeding ECs on another side of the film at 6 hr after the initial plating of SMCs. The initial cell density was  $2.0 \times 10^4$  cells/cm $^2$ .

#### Fluorescent labeling of cells

Filamentous actin of HEPs and CMYs was stained by rhodamine-conjugated phalloidin (Molecular Probes) after fixation with paraformaldehyde (Sigma) and treatment with Triton X-100 (Sigma) at 20°C. Von Willebrand factor of ECs and  $\alpha$  smooth muscle actin of SMCs were stained by immunological method using primary antibodies (rabbit anti-Von Willebrand factor IgG; DAKO and mouse anti- $\alpha$  smooth muscle actin IgG; Sigma) for each antigen and fluorescence labeled secondary antibodies (fluorescein labeled goat anti-rabbit IgG (Cappel) and rhodamine labeled goat anti-mouse IgG (Cappel)). For immunostaining, cells were fixed by

immersing into cold methanol (-20°C) for 10 min and permeabilized with 0.1% Triton X-100 for 5 min at 20°C. Fluorescence images of cells were taken by confocal laser scanning microscope (FV300; Olympus). Projected areas of cells were measured using computerized image analysis (image-pro Plus ver. 4.0; Media Cybernetics).

## DISCUSSION

### Self-supporting honeycomb films for cell culture substrates

Figure 2 (a) shows the scanning electron microscope (SEM) image of a honeycomb film of poly(L-lactic acid). This film has some structural features: (1) micropores with diameter of several micrometer, (2) hexagonal arrays of the micropores, (3) single layer of the array with several micrometer thickness. The honeycomb film was prepared by applying moist air to a spread polymer solution on the water surface. The porous structure is molded from the two dimensional array of water microspheres. The microspheres are formed by condensation of moist air on the surface of the spread polymer solution. The microspheres are prevented from fusing by the surfactant effect of the amphiphilic polymer.

The reasons for choosing the honeycomb film as cell culture substrates are followings: firstly, cell behavior can be controlled by porous morphology and down sized cell adhesive sites, secondly, cells can be cultured on both sides of the film, thirdly, this three dimensional culturing enables cells to interact with each other laterally on the film and also vertically via porous structure. The cell alignment is one of the typical features observed in some tissues such as muscles and blood vessels. In case of using a honeycomb film, cells cannot find a specific direction for their movement on the honeycomb film, because the honeycomb film exhibits an isotropic hexagonal pattern. An idea for the cell orientation is that a honeycomb film of an elastic polymer can be stretched and anisotropic arrays of micropores can be formed. For preparation of an elastic honeycomb film, poly( $\epsilon$ -caprolactone), PCL was applied. The PCL exhibits elastic property at around 20°C [9]. Therefore a self-supporting honeycomb film of PCL can be stretched at this temperature. After uniaxial stretching, arrays of elongated micropores were observed in the stretched honeycomb film shown in figure 2 (b). The arrays of the stretched micropores are applicable to guiding cell alignment.

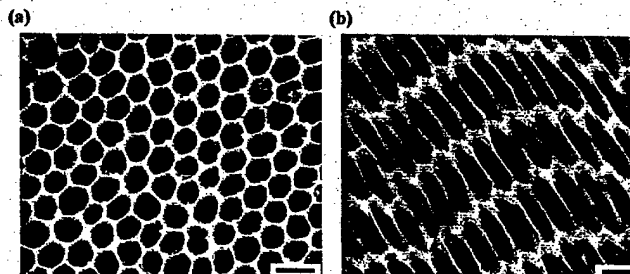
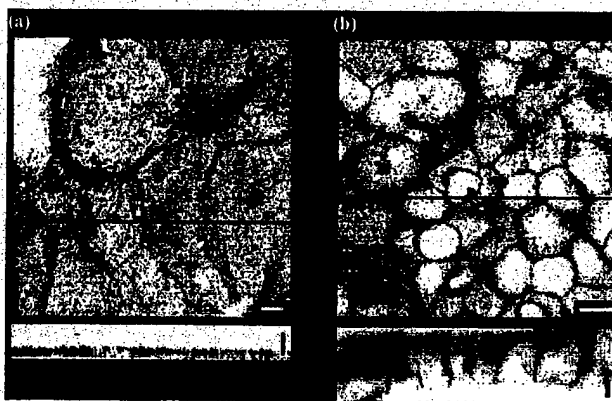


Figure 2 Scanning electron microscope images of (a) self-supporting honeycomb film of PLLA and (b) self-supporting stretched honeycomb film of PCL. Scale: 5  $\mu$ m.

### **Cell adhesion to the honeycomb film**

D. Ingber found that the total area available for cell adhesion is a key factor governing the cell spreading [10]. For the cell culture experiments, they utilized discrete micropatterns where cell adhesive islands are stamped in nonadhesive region. Our honeycomb film can be regarded as continuous micropattern of cell adhesive region. The honeycomb pattern gives reduced area for cell adhesion, compared with a flat cast film of the same polymer. Hepatocytes (HEPs) were cultured on a self-supporting honeycomb film (pore size: 4  $\mu\text{m}$  and thickness: 2  $\mu\text{m}$ ) and a flat film of PLLA. A flat film of PLLA was fabricated by evaporating a PLLA solution on a glass plate. Figure 3 shows confocal laser scanning microscope images of filamentous actin of HEPs. Cell spreading was considerably restricted on a self-supporting honeycomb film. On a flat film, HEPs formed stress fibers of actin filaments and flat shape with thickness of less than 6  $\mu\text{m}$  (Figure 3 (a): top view of cells and cross sectional image (bottom)). The average size of HEPs was 2000  $\mu\text{m}^2/\text{cell}$ . On the other hand, HEPs did not form stress fibers when they were attached to the honeycomb film. The average cell size of HEPs was 900  $\mu\text{m}^2/\text{cell}$  on a honeycomb film. Although cell detachment was observed on a flat film at day 5 of the culture, HEPs were not detached from a honeycomb film even at 2 weeks of the culture. On a honeycomb film, the HEPs formed a single layer of columnar shape cells with a thickness of 20  $\mu\text{m}$  (Figure 3 (b): bottom). The cellular aggregates of HEPs are quite resemble to the tissue structure of liver *in vivo* where HEPs are adhered to adjacent cells each other via cell adhesion proteins. The tissue formation of hepatocytes specifically occurred on the honeycomb film of PLLA, not on a flat film of PLLA. The artificial tissue of HEPs secreted albumin several times more than the HEPs cultured on the flat film (data not shown).



**Figure 3** Difference in cell shape of HEPs: (a) on a flat film and (b) on a honeycomb film of PLLA. Cross sectional images (bottom) were obtained along the line depicted in each X-Y plane image (top). Scale: 10  $\mu\text{m}$ .

### **Three dimensional culture system for tissue formation**

The self-supporting honeycomb film is a two sided substrate. Based on the feature of the honeycomb film, we expect that cells can be cultured on both sides of the film and they can contact with each other laterally and also vertically through the micropores. In order to prove this hypothesis, various types of cells were cultured on both sides of a honeycomb film. At first, cardiac myocytes (CMYs) were cultured on both sides of a honeycomb film of PLLA. For comparison, a flat film was utilized for culture substrate of CMYs. Cardiac contraction was observed at the day 7 of the cultures. On a flat film, contraction rhythm of CMYs was random. This indicates that cell-cell contact is insulated by the polymer film. On a honeycomb film, CMYs contracted in a synchronized rhythm. This suggests that the vertical contacts of CMYs are achieved through the micropores of a honeycomb film.

The three dimensional cell culture system can be applied to the various cell types such as hepatocytes, endothelial cells, and smooth muscle cells. Figure 4 (a) shows that liver HEPs form layer structure with a thickness of 20  $\mu\text{m}$  at each side of a honeycomb film. In case of using a stretched honeycomb film, CMYs are attached to both sides of the film and aligned along the stretching direction of the honeycomb film (Figure 4 (b)). Even co-culture system was established by culturing endothelial cells and smooth muscle cells on a stretched honeycomb film. Figure 4 (c) shows that each cell type was adhered separately onto each side of a stretched honeycomb film and aligned along the arrays of micropores. Heterotypic cell-cell interaction is expected in the artificial multicellular tissue.

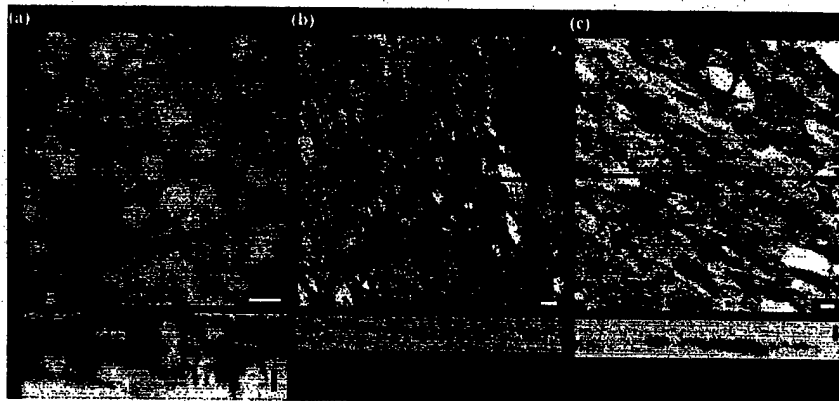


**Figure 4** Three-dimensional culture of (a) HEPs, (b) CMYs, and (c) ECs (bright) and SMCs (dark) by utilizing both sides of porous films for cell attachment. The images were taken by confocal laser scanning microscopy. Cross sectional images (bottom) were obtained along the line depicted in each X-Y plane image. Scale: 10  $\mu\text{m}$ .

## CONCLUSIONS

In the present study, we focused on the application of microporous films to the cell culture substrates for tissue engineering. The microporous films (honeycomb films) of degradable polymers were fabricated by evaporating a polymer solution in a humid atmosphere. Anisotropic arrays of micropores were formed by stretching uniaxially a honeycomb film of an elastic polymer. Microporous surface of the honeycomb film suppressed the spreading behavior of hepatocytes. Hepatocytes on a honeycomb film formed columnar shape and layered aggregate expressing higher secretion level of albumin. The honeycomb films could be utilized for three dimensional cell culture systems. Double layered cellular aggregates were formed on the honeycomb films from hepatocytes and cardiac myocytes respectively. Even multicellular tissues like a blood vessel wall could be reconstructed by co-culturing endothelial cells and smooth muscle cells on a stretched honeycomb film. The anisotropic arrays of the stretched micropores worked as a micropattern for guiding cell alignment. As a result, the honeycomb films of degradable polymers can lead basic cell behavior, such as cell adhesion, cell movement, and cell-cell interaction to a correct way of tissue formation.

## REFERENCES

1. E. Bell, "Organotypic and Histotypic Models of Engineered Tissues," W. Saltzmann, "Cell Interactions with Polymers," J. Hubbel, "Matrix Effects," R. Thomson, A. Shung, M. Yaszemski and A. Mikos, "Polymer Scaffold Processing," *Principles of Tissue Engineering*, ed. R. Lanza, R. Langer and J. Vacanti (Academic Press, 2000) pp.181-194, pp.221-236, pp.237-250, pp.251-262.
2. K. Dee, D. Puleo and R. Bizios, *Biomaterials Today* 3, 7 (2000).
3. K. McClary and D. Grainger, *Biomaterials* 20, 2435 (1999).
4. D. Mooney, L. Hansen, J. Vacanti, R. Langer, S. Farmer and D. Ingber, *J. Cell. Physiol.* 151, 497 (1992).
5. A. Curtis and C. Wilkinson, *Biomaterials* 18, 1573 (1997).
6. N. Maruyama, T. Koito, J. Nishida, T. Sawadaishi, X. Cieren, K. Ijiro, O. Karthaus and M. Shimomura, *Thin Solid Films* 327-329, 854 (1998).
7. P. O. Seglen, *Exper. Cell Res.* 74, 450 (1972).
8. M. Denyer, M. Riehle, J. Hayashi, M. Scholl, C. Sproessler, S. Britland, A. Offenheusser and W. Knoll, *In Vitro Cell. Dev Biol.-Animal* 35, 352 (1999).
9. I. Engelberg and J. Kohn, *Biomaterials* 12, 292 (1991).
10. C. Chen, M. Mrksich, S. Huang, G. Whitesides and D. Ingber, *Science* 276, 1425 (1997).

## AUTHOR INDEX

Acosta-Avalos, Daniel, 113  
Ahmed, Awad, 167  
Apkarian, Robert P., 161  
Arai, Keiko, 229  
Aranda-Manteca, F.J., 123  
Arias, José I., 3  
Arias, José L., 3  
Arruda, Ellen, 129  
Arsenault, Jennifer, 69

Baird, Barbara A., 57  
Bandyopadhyay, Amit, 185  
Basiuk, V.A., 117  
Blanchette, James, 215  
Borrós, S., 173  
Bose, Susmita, 185  
Bucio, L., 117, 123  
Byrne, Mark E., 193

Calve, Sarah, 129  
Cazalis, Chrystelle S., 43  
Cernicchiaro, Geraldo R., 113  
Chakravartula, A.M., 95  
Chawan, A.D., 95  
Clark, Theodore G., 57  
Colominas, C., 173  
Conticello, Vincent P., 43, 161  
Cooper, Alan, 161  
Coradin, Thibaud, 147  
Coupé, Aurélie, 147  
Craighead, Harold G., 57

Dauskardt, Reinhold H., 27  
Davis, Mark E., 209  
Dekempeneer, Erik, 179  
Dennis, Robert, 129

Esquivel, Darci M.S., 113  
Esteve, J., 173

Fernández, María S., 3  
Fernández, T., 173  
Fincham, A.G., 103  
Fuenzalida, Víctor M., 3

Garcia, B.E., 113

García-Garduño, M.V., 117  
Garreta, E., 173  
Gates, Richard S., 69  
Gliko, Olga, 141  
Gomez-Cortes, A.L., 123  
Goossens, Olivier, 179  
Gower, Laurie B., 201  
Grosh, Karl, 129

Haberstroh, Karen M., 51  
Halevy, Revital, 153  
Hancock, Robert E.W., 153  
Hara, Masahiko, 229  
Hayashi, Junko, 229  
Heldt, Nicole, 167  
Heredia, A., 117, 123  
Holowka, David A., 57  
Hosick, Howard L., 185

Iijima, M., 103

Jagota, Anand, 75  
Jang-Cho, H., 123  
Jelinek, Raz, 153

Kalita, Samar J., 185  
Kempf, L., 173  
Kim, Yi-yeoun, 201  
Kolusheva, Sofiya, 153  
Komvopoulos, K., 95

La, Hongly, 69  
Laibinis, Paul E., 63  
Langer, Robert, 223  
Lee, Seok-Won, 63  
Li, Musen, 135  
Li, Yuzhuo, 167  
Livage, Jacques, 147  
Lozano, L.F., 117, 123  
Lustig, Steven R., 75

Martínez, A., 117  
Martinez, Steve A., 185  
Martinez-Matias, C.A., 117  
Matsunaga, Tadashi, 11  
McMillan, R. Andrew, 161

Meuse, Curtis W., 69  
Miller, Derick C., 51  
Moradian-Oldak, J., 103  
Moriwaki, Y., 103  
Nishikawa, Takehiro, 229  
Ocotlán-Flores, J., 123  
Okamura, Yoshiko, 11  
Orozco, E., 117, 123  
Orth, Reid N., 57  
Oyarzún, Alejandro, 3  
Panitch, Alyssa, 37  
Park, Kinam, 193, 215  
Pasyk, Krystyna, 129  
Paulussen, Sabine, 179  
Peña-Rico, M.A., 117, 123  
Peppas, Nicholas A., 193, 215  
Pruitt, L.A., 95  
Reincke, Theresa M., 209  
Ries, M., 95  
Rodriguez, Renato, 3  
Rodriguez-Hernández, A., 117  
Seal, Brandon L., 37  
Seong, Jiehyun, 63  
Sheppard, Barbara J., 223  
Shimomura, Masatsugu, 229  
Silin, Vitalii, 69  
Slack, Gregory, 167  
Song, Yunjing, 135  
Takagi, T., 103  
Thapa, Anil, 51  
Vanderah, David J., 69  
Vangeneugden, Dirk, 179  
Van Osdol, William W., 27  
Vekilov, Peter G., 141  
Vergara, Italo, 3  
Villarreal, E., 117, 123  
Wajnberg, Eliane, 113  
Wang, Min, 83  
Wang, Yadong, 223  
Webster, Thomas J., 51  
Wen, H.B., 103  
Wen, Shulin, 135  
Wiff, Juan P., 3  
Wright, Elizabeth R., 161  
Wu, Kenneth S., 27  
Wu, Min, 57  
Zhou, J., 95

## SUBJECT INDEX

aerogel, 173  
amelogenins, 103  
antibacterial coating, 179  
antimicrobial peptides, 153

bacterial magnetic particles, 11  
barnacles, 3  
bee abdomens, 113  
biocompatible, 223  
biodegradable, 223  
polymers, 229  
biomaterial(s), 57, 83  
biomimetic(s), 37, 201  
imprinting, 193  
biomineralization, 3  
biopolymers, 147  
biosilicification, 147  
bleomycin, 215  
block copolymers, 161

calcium  
carbonate, 185, 201  
phosphate, 103  
calorimetry, 123  
CD, 43  
cells, 51  
collagen, 129  
composite bone graft, 185  
continuous rotational isomeric state  
theory, 75  
cross-linking, 95  
crystal elongation, 103

dielectric barrier glow discharge, 179

elastin-mimetic, 161  
peptide, 43  
elastomer, 223  
ethylene glycol, 63

failure, 27  
ferritin, 141  
fluorescence, 167  
free-radical photopolymerization, 193  
FTIR, 43

gene delivery, 209

7/2 helical conformation, 69  
honeycomb film, 229  
hydrogel(s), 37, 161, 215  
hydroxyapatite (HA), 135, 173

immunology, 57

ligand-receptor, 153  
liposome, 167

magnetic bacteria, 11  
manufacture, 83  
mechanical properties, 27  
microcontact printing, 201  
molecular recognition, 193  
Monte Carlo simulation, 75

nanofabrication, 57  
nanoparticles, 113  
nano-sized powder, 135  
natural polymer, 185  
NMR, 43  
nonviral, 209

oral administration, 215  
ostrich eggshell, calcite, 117

performance, 83  
phase-shifting interferometry, 141  
phospholipid, 167  
plasma polymerization, 173, 179  
polycation, 209  
polydiacetylene, 153  
polymer, 51  
protein adsorption, 63  
proteoglycans, 3

selective polypeptide-substrate  
binding, 75  
self-assembled monolayer(s), 63, 69  
self-assembly, 37, 43  
SEM, 117  
silica, 147

silk-mimetic peptide, 43  
sol-gel method, 135  
stratum corneum, 27  
SUID magnetometry, 113  
  
TEM, 117  
tendon, 129  
thermal  
    expansion, 117  
    stability, 123  
1-thiaoligo(ethylene oxide) segments,  
    69  
  
tissue engineering, 129, 229  
type I collagen, 123  
  
ultra-high molecular weight  
    polyethylene, 95  
  
vascular, 51  
  
wear, 95  
  
x-ray powder diffraction, 117